The Pennsylvania State University

The Graduate School

College of Earth and Mineral Sciences

LASER-FIRED CONTACT FORMATION ON METALLIZED AND PASSIVATED

SILICON WAFERS UNDER SHORT PULSE DURATIONS

A Dissertation in

Materials Science and Engineering

by

Ashwin S. Raghavan

© 2014 Ashwin S. Raghavan

Submitted in Partial Fulfillment
of the Requirements
for the Degree of

Doctor of Philosophy

August 2014

The dissertation of Ashwin S. Raghavan was reviewed and approved* by the following:

Tarasankar DebRoy
Professor of Materials Science and Engineering
Dissertation Co-Adviser
Co-Chair of Committee

Todd A. Palmer
Associate Professor Materials Science and Engineering
Dissertation Co-Adviser
Co-Chair of Committee

Suzanne E. Mohney
Professor of Materials Science and Engineering
Chair of Graduate Program

S. Ashok
Professor of Engineering Science

E.W. Reutzel
Department Head, Laser System Engineering and Integration
Applied Research Laboratory, Penn State University
Special Member

*Signatures are on file in the Graduate School.

ABSTRACT

The current process used to fabricate localized aluminum-silicon (Al-Si) ohmic contacts on the rear side of dielectrically passivated Si-based photovoltaic (PV) devices has a negative impact on manufacturing throughput and yield. Laser processing is an alternative, non-contact method that can be used to rapidly fabricate laser-fired contacts (LFCs) without sacrificing energy conversion efficiency. However, laser firing is a highly transient process governed by a number of complex physical phenomena, such as rapid heating, melting, and alloying element vaporization, that occur simultaneously over extremely short time and length scales. Therefore, determining the impact of laser processing on LFC formation is not a trivial undertaking.

Recent development of the LFC process has centered on the use of nanosecond pulse durations, despite the need for costly control systems, to prevent significant ablation of the Al metallization layer. The use of laser systems capable of microsecond laser pulses can be used to mitigate these issues. In addition, longer pulse durations can be used to form larger, more heavily-alloyed LFCs while preventing significant liquid metal expulsion when laser parameters are carefully selected. In order to assess the viability of using microsecond pulse durations for LFC formation, it is important to determine the influence that laser processing parameters have on contact geometry and passivation layer quality since these factors will directly impact device performance. In addition, due to the complexity of the simultaneously occurring physical processes, a quantitative framework is required to evaluate the physical phenomena occurring during contact formation over a wide range of processing parameters without the need for costly experimentation.

The objective of this work is to develop a comprehensive understanding of the physical processes governing LFC formation under microsecond pulse durations. Primary emphasis is placed on understanding how processing parameters influence contact morphology, passivation layer quality, alloying of Al and Si, and contact resistance. In addition, the research seeks to develop a quantitative method to accurately predict the contact geometry, thermal cycles, heat and mass transfer phenomena, and the influence of contact pitch distance on substrate temperatures in order to improve the physical understanding of the underlying processes. Finally, the work seeks to predict how geometry for LFCs produced with microsecond pulses will influence fabrication and performance factors, such as the rear side contacting scheme, rear surface series resistance and effective rear surface recombination rates.

In order to achieve these objectives, a combination of experimental characterization and numerical simulations are employed. Advanced materials characterization tools are used to section, polish, and determine the impact of laser processing on the LFC and the surrounding passivated regions. Electrical

analysis is performed using physical measurements of contact resistance as well as device simulations to evaluate the influence that laser processing and contact geometry have on contact resistance. In addition, a heat transfer and fluid model is developed to quantitatively understand how changes in processing parameters affect the LFC geometry, temperature, velocity, and concentration fields. Finally, in order to predict the impact of contact geometry on device performance, analytical expressions are developed to account for the contacts produced using microsecond pulses that have with larger interfacial contact areas to determine the rear surface series resistance and effective rear surface recombination velocities.

The characterization of LFC cross-sections reveals that the use of microsecond pulse durations results in the formation of three-dimensional hemispherical or half-ellipsoidal contact geometries. The LFC is heavily alloyed with Al and Si and is composed of a two-phase Al-Si microstructure that grows from the Si wafer during resolidification. As a result of forming a large three-dimensional contact geometry, the total contact resistance is governed by the interfacial contact area between the LFC and the wafer rather than the planar contact area at the original Al-Si interface within an opening in the passivation layer. By forming three-dimensional LFCs, the total contact resistance is significantly reduced in comparison to that predicted for planar contacts. In addition, despite the high energy densities associated with microsecond pulse durations, the passivation layer is well preserved outside of the immediate contact region. Therefore, the use of microsecond pulse durations can be used to improve device performance by leading to lower total contact resistances while preserving the passivation layer.

A mathematical model was developed to accurately predict LFC geometry over a wide range of processing parameters by accounting for transient changes in Al and Si alloy composition within the LFC. Since LFC geometry plays a critical role in device performance, an accurate method to predict contact geometry is an important tool that can facilitate further process development. Dimensionless analysis was also conducted to evaluate the relative importance of heat and mass transfer mechanisms. It is shown that convection plays a dominant role in the heat and mass transfer within the molten pool. Due to convective mass transfer, the contacts are heavily doped with Al and Si within 10 µs after contact formation, which contributes to the entire resolidified region behaving as the electrically active LFC. The validated model is also used to determine safe operating regimes during laser processing to avoid excessively high operating temperatures. By maintaining processing temperatures below a critical temperature threshold, the onset of liquid metal expulsion and loss of alloying elements can be avoided. The process maps provide a framework that can be used to tailor LFC geometry for device fabrication.

Finally, using various geometric relationships for the rear side contacting scheme for photovoltaic devices, it is shown that by employing hemispherical contacts, the number of LFCs required on the rear

side can be reduced 75% while doubling the pitch distance and increasing the passivation fraction. Reducing the number of backside contacts required can have a noteworthy impact of manufacturing throughput. In addition, the analytical models suggest that device performance can be maintained at levels comparable to those achieved for planar contacts when producing three-dimensional contacts. The materials and electrical characterization results, device simulations, and design considerations presented in this thesis indicate that by forming three-dimensional LFCs, performance levels of Si-based photovoltaic devices can be maintained while greatly enhancing manufacturing efficiency. The research lays a solid foundation for future development of the LFC process with microsecond pulse durations and indicates that device fabrication employing this method is a critical step moving forward.

TABLE OF CONTENTS

LIST OF FIGURES

x

LIST OF TABLES

ACKNOWLEDGEMENTS

Chapter 1

INTRODUCTION

1.1 Background

In order to develop a more sustainable future, we need to reduce our dependence on conventional energy sources, such as oil, nuclear, and coal. These sources of energy are limited, exhaustible, and have been linked to rises in global mean temperatures [1] and several recent environmental disasters, such as the British Petroleum Deepwater Horizon oil spill in 2010 and the Fukushima Daiichi nuclear power plant incident in 2011. Renewable energy sources, such as wind, hydroelectric, and solar power, offer clean alternatives that can aid our efforts to dramatically reduce our environmental impact while meeting our ever-increasing energy demands. To date, however, renewable energy sources account for less than 10% of all the energy consumed in the United States due to the costs associated with development and implementation [2]. In order for renewable energy sources to become more mainstream, major technological advances are required to make them economically viable and profitable.

Solar power is one renewable energy source that has gained traction over the last 15 years, growing nearly 33% per year since 1997 with projections toward a $140 billion industry by the 2020s [3]. In order for solar energy to continue to grow, photovoltaic (PV) cell costs need to be reduced considerably with primary emphasis placed on the development of cost-effective crystalline silicon (Si) solar cells, which account for nearly 90% of the current market share [4]. Although crystalline Si PV module prices have dropped by almost 40% over recent years, significant cost reductions are still required to reach grid parity. At present, 50% of crystalline Si PV cell production costs are directly related to the Si wafers and additional cell materials [5], such as performance-enhancing coatings. In order to reduce the expenditures associated with these device components, thinner wafers and novel manufacturing methods are required. The PV industry is therefore focused on the development of low-cost manufacturing processes that are compatible with thinner Si wafers and high-efficiency structures.

Solar cells are made up of three basic components: a semiconductor substrate, a p-n junction, and front and backside metal/semiconductor contacts. The focus of this work is on the backside metal/semiconductor contact. In the past, backside metal/semiconductor ohmic contact has been achieved using a full area aluminum (Al) metal layer in direct contact with the Si semiconductor. This type of structure, however, led to low energy conversion efficiencies due to high electron-hole pair recombination rates at the metal/semiconductor back surface interface. The high efficiency crystalline Si passivated emitter rear cell (PERC) device is a novel alternative. It utilizes localized metal-semiconductor point

contacts surrounded by a dielectric passivation layer, which improves performance by enhancing internal reflection and reducing recombination rates of minority and majority carriers [6]. Traditionally, rear-side ohmic contacts in the PERC device have been formed by multi-step patterning and photolithography to generate openings in the passivation layer, followed by Al evaporation and high temperature annealing. However, these steps are time-consuming, and high temperature processes can adversely impact fabrication because they increase both production costs and the risk of breaking thin wafers.

In fabricating these high-efficiency PV devices, lasers have been routinely used for various applications, such as etching [7], scribing [8] and doping [9,10], to streamline production while improving or maintaining energy conversion efficiency levels. Over the last decade, lasers have also been investigated for the processing of laser-fired contacts (LFCs) [11,12]. LFCs are localized ohmic point contacts between the Al metallization layer and the bulk Si wafer through the dielectric passivation layer [13-15]. Using this method, ohmic contacts can be fabricated without the use of photolithography and high temperature annealing, thereby improving manufacturing throughput and reducing the risk of wafer breakage during high temperature processing [16-23]. Furthermore, this laser-based approach allows devices to achieve the 22% energy conversion efficiencies observed in current PERC photovoltaic devices [19].

LFCs are currently processed using Q-switched Nd:YAG lasers operating at 1064 nm wavelength with pulse durations in the nanosecond regime [11-24]. Nanosecond pulses are used because many researchers believe that the low energy density associated with extremely short pulse durations will minimize damage to the surrounding passivation layer and the crystalline Si substrate. However, since the laser first interacts with the Al metallization layer, which has much lower melting and boiling points than Si, significant ablation of the Al has been observed [25-29]. Moreover, since the alloying of Si and Al is required for proper contact formation [11], the depletion of Al can lead to inadequate alloying in the contacted region and low or unpredictable contact quality. Furthermore, although high energy conversion efficiencies can be achieved in a laboratory setting using nanosecond laser pulses, extremely precise and costly control systems are required for to generate robust, fault-tolerant LFCs.

In order to improve LFC quality and generate a larger operating window, millisecond pulse durations have been used. The use of millisecond pulses has been demonstrated in laser spot micro-welding of various material systems to result in large, hemispherical contact regions without metal expulsion when the laser parameters are appropriately selected [30-32]. In addition, the use of millisecond duration pulses for LFC formation has been shown to result in pronounced melting and mixing of Al and Si up to depths greater than 20 μm [33,34]. By forming these large contacts that are heavily alloyed with Al and Si, the

total contact resistance is reduced considerably [34]. However, longer millisecond duration pulses have a negative impact on the ability to meet manufacturing throughput requirements.

1.2 Motivation

For the LFC technology to become a commercially viable approach, it is important to create a robust, scalable process capable of maintaining or improving current energy conversion efficiencies. Achieving this target has been difficult when using nanosecond and millisecond pulse durations. The use of microsecond pulses may provide a method to improve contact quality over a wider range of processing parameters by forming larger, more thoroughly mixed contacts, which can improve device performance [14,34]. In addition, higher powered lasers with longer exposure times can be used with specialized beam delivery systems and diffractive optics to simultaneously process multiple contacts to rapidly fabricate LFCs and meet throughput requirements in an industrial environment [35-36].

When forming a laser-fired contact, the following factors are important to consider: 1) the extent of alloying between the Al and Si in the contact region, 2) the preservation of the passivation layer outside of the contact region, and 3) the impact of contact geometry on total contact resistance. Proper alloying between the Al and Si is required to ensure that the LFC is sufficiently doped to form a metal-semiconductor contact. Preservation of the passivation layer is required because it enhances internal reflection and reduces recombination rates at the backside surface/wafer interface. If the surrounding passivation layer is damaged during laser processing, device performance will suffer. Thirdly, the total contact resistance needs to be low to prevent parasitic resistive losses and to maximize the total achievable output power of the device. The impact that forming LFCs with microsecond pulse durations has on these factors is unknown. Therefore, a comprehensive study is required to develop a fundamental understanding of the process, which can be used to further optimize the process.

Advanced materials characterization techniques, such as focused ion beam milling, are now available that can be used to accurately determine the impact of laser processing on LFC geometry, alloying of Al and Si in the molten zone, and the surrounding passivation layer. Recently, materials characterization studies have been used to show that the use of nanosecond pulses results in two-dimensional, planar, lightly-doped contacts [22], whereas the use of millisecond pulses results in three-dimensional, heavily-doped hemispherical contacts [34]. Due to the higher dimensionality of the LFCs produced with millisecond pulse durations, the contact resistance is significantly lower when considering two LFCs with the same top surface diameter [34]. Unfortunately, the characterization methods used were inadequate to thoroughly evaluate the impact of laser processing on the extent of alloying between the Al and Si within the LFC and the quality of the passivation layer. The work done with millisecond pulses [34], for

instance, only revealed the general size of the LFC, but could not show the extent of alloying and the quality of the surrounding passivation layer. In order to understand the influence that laser processing has on these aspects of LFC formation, more directed materials characterization efforts are required.

It is also important to develop a quantitative method to study the LFC process. A quantitative framework provides a means to develop a fundamental understanding of the underlying physical processes that occur during laser firing. During laser firing, the interaction between the heat source and the substrate will result in rapid heating, melting, and flow of the molten material within the melt pool. The material properties and the processing parameters will strongly influence the way the laser interacts with the material. In addition, the flow of molten material will impact the temperature, velocity, and Al concentration profiles within the pool, which will impact the geometry, composition, and structure of the solidified contacts. Little effort has been made to understand the physical processes governing contact formation under short microsecond pulse durations and micron-sized length scales. Since the contacts are formed under extremely short pulses, insufficient time for temperature measurements of heating and cooling rates is available. Therefore, numerical methods should be employed to understand the physical phenomena governing LFC formation.

Over the past 20 years, great strides have been made in using numerical simulations to understand the thermal cycles and evolution of laser spot weld geometry [30,31,38-40]. Validated mathematical models have been extensively used to obtain quantitative information about how changes in processing parameters directly influence temperature profiles, velocity flow fields, cooling rates, and spot weld geometry. However, most of these studies involved longer, millisecond pulse durations and completely different material systems. During laser-fired contact formation, the laser first interacts with an Al metallization layer before the underlying Si substrate, which makes the laser-material interaction behaviors significantly different than interaction with an alloy system of uniform composition prior to processing. Furthermore, the Al-Si system is governed by a large two-phase region that will impact alloy formation and thermal cycles. In order to determine how laser processing impacts contact formation, a mathematical model specific to the LFC process is required.

A phenomenological understanding of the influence that laser processing parameters have on LFC formation behavior is required to determine the viability of using microsecond pulses for LFCs. In order to develop this fundamental knowledge base, a combination of advanced materials characterization and mathematical modeling is required. The application of similar tools has already been demonstrated at Penn State [33,34,38-40] and can be used to develop the LFC process using microsecond pulses.

1.3 Research Objectives

The overall objective of this research is to develop an improved understanding of the important physical phenomena governing laser-firing of Al-Si ohmic contacts under microsecond pulse durations. In order to meet this objective, experimental characterization is combined with high-powered numerical simulations to study the laser-firing process. Experimental characterization is required to understand how changes in laser processing parameters impact the Al-Si alloying behavior within the contact, the quality of the passivation layer post-processing, and the total contact resistance as a function of contact geometry. Mathematical modeling is required to develop a thorough understanding of the heat transfer and mass transfer mechanisms. The numerical simulations will also provide detailed understanding of the process regarding the evolution of the three-dimensional temperature and velocity fields, the Al concentration profiles, the contact geometry, and the influence of changes in contact pitch distance on substrate temperatures.

1.3.1 Experimental Characterization

The impact of laser processing on the alloying of Al and Si, the degradation of the passivation layer, and the total contact resistance are of primary importance for device performance. In order to understand these factors, the following tasks need to be completed.

1. Determine how Al is incorporated into the laser-fired contact during processing and the influence that the presence of Al has on the solidification behavior. In order to accomplish this, a reliable method to section, polish, and characterize the presence of Al within the solidified contact must be developed to characterize the contact geometry and Al and Si mass transfer within the contact.

2. Evaluate the influence that processing has on the quality of the passivation layer, the size of the opening in the passivation layer post-processing, and the physical phenomena governing the breakdown of the passivation layer. The size of the opening in the passivation layer and the quality of the passivation layer will influence device performance and can be identified through materials characterization.

3. Investigate the influence that variations in contact geometry have on total contact resistance. A combination of physical measurements of total contact resistance and device simulations will be utilized to understand how changes in contact geometry as a function of changes in laser processing parameters will influence total contact resistance.

1.3.2 Mathematical Modeling

The influence that processing parameters have on the evolution of the contact geometry, the temperature fields, and concentration profiles is important to further develop the LFC process. In order to quantitatively understand these factors, it is necessary to use mathematical modeling.

1. Develop a numerical model that can be used to evaluate the LFC formation process. Using this model, analyze the heat transfer and mass transfer mechanisms governing contact formation to understand how contact geometry and concentration profiles evolve in response to changes in laser processing parameters. Dimensionless analysis needs to be carried out to determine how convection and diffusive heat and mass transfer influence the laser firing process.

2. Contact geometry has been shown to directly influence device performance. Therefore, it is important to use the mathematical model to develop process maps that relate the important laser processing parameters (laser power, beam radius, and pulse duration) to contact geometry. Using these process maps, end users can appropriately select laser parameters to tailor contact geometry for a specific rear contacting scheme.

3. Evaluate the impact of contact geometry and contact pitch on various device performance metrics, such as effective rear size recombination velocity and rear side series resistance. Various analytical relationships have been developed and utilized in device research that can be modified and coupled with the numerical simulations to make important conclusions about the influence of processing parameters on device design to optimize performance.

1.4 Thesis Structure

The use of microsecond pulse durations for LFC formation may be an important processing space that can be used to develop a robust, industrially-viable contacting method. This research seeks to develop a fundamental understanding of the physical phenomena governing laser-fired contact formation when using microsecond pulse durations that can be used to further optimize the process. The content of the work is divided into six chapters.

In Chapter 1, the context for the research project, the motivation for this undertaking, the research objectives, and the contents of the thesis are described.

In Chapter 2, a comprehensive review of the current research on the laser-fired contact process is presented. In addition, the physical phenomena governing laser processing and laser spot micro-welding are explained. Finally, a review of the current mathematical models used to simulate heat transfer, mass

transfer, fluid flow, and weld pool geometry is performed. Based on a critical review of the relevant literature, gaps between the available knowledge and the purpose of the current research are identified.

In Chapter 3, LFCs are generated on an industrially-relevant substrate configuration and a combination of advanced materials characterization tools, theoretical calculations, and device simulations are employed to develop a phenomenological understanding of the various factors governing contact formation when using microsecond pulse durations. Primary emphasis is placed on understanding how changes in laser processing parameters impact the onset of liquid metal expulsion, breakdown of the SiO_2 passivation layer, alloying of Si and Al within the LFC, solidification microstructures, and total contact resistance. The results obtained in this chapter generate a valuable understanding of how processing with microsecond pulse durations impacts contact formation and total contact resistance.

In Chapter 4, a description of the mathematical models used in the present study is provided. The framework for the model is described in terms of the model input parameters, applicable boundary conditions, and solution methodology. The procedure used for calculating the heat transfer and fluid flow behavior is thoroughly explained.

In Chapter 5, the development of the heat transfer and fluid flow model as relevant to the processing of laser-fired contacts is explained. Using the model, the evolution of contact geometry and temperature, velocity, and concentration fields is studied. The model is validated using experimental data for contact geometry and concentration profiles. In addition, dimensionless analysis is carried out to determine the primary heat transfer and mass transfer mechanisms governing contact formation. The impact that changes in processing parameter have on total contact resistance as a function of contact geometry and doping of the LFC by Al is also determined. Finally, the influence that contact pitch distance has on substrate temperature fields and contact geometry is evaluated since pitch and contact geometry will directly influence overall device performance. The theoretical results generated in this chapter develop a fundamental knowledge base required for future process development and optimization.

In Chapter 6, the impact of employing different contact geometries on the backside LFC array design and device performance is analyzed. Relationships between LFC array area, contact pitch distance, and contact area fraction for planar contacts are used to determine the impact of contact dimensionality on the pitch distance and the number of contacts required for a given contact area fraction. In addition, analytical models are developed to account for various contact geometries to predict the rear side series resistances and the effective rear surface recombination rates. The results presented in this chapter provide a fresh perspective on how LFC geometries can be tailored to optimize the rear contacting scheme for high efficiency, Si-based solar cells.

In Chapter 7, the summary and conclusions of the research are presented. In addition, based on the new knowledge generated from this body of work, future areas for research are suggested.

1.5 References

1. "Turn down the heat", November 2012, The World Bank, Washington DC.
2. U.S. Energy Information Administration (EIA), "Annual Energy Review," U.S. Department of Energy, Washington D.C., 2011, pp. 3-11.
3. W. Hoffman, PV solar electricity industry: market growth and perspective, Solar Energy Materials and Solar Cells 90 (18-19), 2006, pp. 3285-3311.
4. G.P. Willeke, Thin crystalline silicon solar cells, Solar Energy Materials and Solar Cells 72 (1-4), 2002, pp. 191-200.
5. A. Goodrich, P. Hacke, Qi Wang, B. Sopori, R. Margolis, T.L. James, M. Woodhouse, Solar Energy Materials and Solar Cells 114, 2013, pp. 110–135.
6. E. Urrejola, K. Peter, H. Plagwitz, G. Schubert, Silicon diffusion in Al for rear passivated solar cells, Appl. Phys. Letters 98, 153508, 2011.
7. C. Canizo, G. Coso, W.C. Sinke. Crystalline silicon solar module technology: Towards the 1€ per watt-peak goal, Prog. in Photovoltaics 2009; 17: pp 199–209. DOI: 10.1002/pip.878.
8. K.L. Chopra, P.D. Paulson, V. Dutta, Thin film solar cells: an overview, Prog. in Photovoltaics 12, 2004, pp 69–92. DOI: 10.1002/pip.541
9. S. Wang, A. Lennon, B. Tjahjono, L. Mai, G. Vogl, S. Wenham, Overcoming over-plating problems for PECVD SiNx passivated laser doped p-type multi-crystalline silicon solar cells, Solar energy materials and solar cell 99, 2012, pp. 226-234, DOI: 10.1016/j.solmat.2011.12.003
10. J.J. Blecher, T.A. Palmer, T. DebRoy, Laser-silicon interaction for selective emitter formation in photovoltaics. I. Numerical model and validation, J. Appl. Phys., 112 (11), 2012, #114906.
11. E. Schneiderlochner, R. Preu, R. Ludemann, S.W. Glunz, Laser-fired rear contacts for crystalline silicon solar cells, Prog. in Photovoltaics 10, 2002, pp. 29-34, DOI: 10.1002/pip.422.
12. O. Schultz, S.W. Glunz, G.P. Willeke, Multicrystalline Silicon Solar Cells Exceeding 20% Efficiency, Prog. in Photovoltaics 12 (7), 2004, pp. 553-558, DOI: 10.1002/pip.583.
13. D. Kray, S. Glunz, Investigation of laser-fired rear-side recombination properties using an analytical model, Prog. In Photovoltaics 14 (3), 2006, 195-201, DOI: 10.1002/pip.660.
14. A. Wolf, D. Biro, J. Nekarda, S. Stumpp, A. Kimmerle, S. Mack, R. Preu, Comprehensive analytical model for locally contacted rear surface passivated solar cells, J. Appl. Phys. 108, 2010, 124510.
15. J. Mueller, K. Bothe, S. Gatz, F. Haase, C. Mader, R. Brendel, Recombination at laser-processed local base contacts by dynamic infrared lifetime mapping, J. Appl. Phys. 108, 2010, 124513.

16. M. Tucci, E. Talgorn, L. Serenelli, E. Salza, M. Izzi, P. Mangiapane, Laser fired back contact for silicon solar cells, Thin Solid Films, 516, 2008, pp. 6767-6770, DOI: 10.1016/j.tsf.2007.12.079.

17. E. Schneiderlochner, A. Grohe, C. Ballif, S.W. Glunz, R. Preu, G. Willeke, Investigations on laser-fired contacts for passivated rear solar cells, IEEE Photovoltaic Specialists Conference 2002; 0-7803-7471-1, pp. 300-303.

18. W. Brendle, V.X. Nguyen, A. Grohe, E. Schneiderlochner, U. Rau, G. Palfinger, J.H. Werner, 20•5% efficient silicon solar cell with a low temperature rear side process using laser-fired contacts, Prog. in Photovoltaics 14, 2006, pp. 653-662, DOI: 10.1002/pip.696.

19. U. Zastrow, L. Houben, D. Meertens, A. Grohe, T. Brammer, E. Schneiderlochner, Characterization of laser-fired contacts in PERC solar cells: SIMS and TEM analysis applying advanced preparation techniques, Appl. Surface Science 252 (19), 2006, pp. 7082-7085.

20. E. Van Kerschaver, G. Beaucarne, Back-contact solar cells: a review, Prog. In Photovoltaics 14, 2006, pp. 107-123. DOI: 10.1002/pip.657.

21. B. Fischer, Loss analysis of crystalline silicon solar cells using photoconductance and quantum efficiency measurements, Dissertation, Universitat Konstanz, 2003.

22. P. Ortega, A. Orphella, I. Martin, M. Colina, G. Lopez, C. Voz, M.I. Sanchez, C. Molpeceres. R. Alcubilla, Laser-fired contact optimization in c-Si solar cell, Prog. in Photovoltaics 20 (2), 2012, pp. 173-180. DOI: 10.1002/pip.1115.

23. I. Martin, M. Labrune, A. Salomon, P. Roca i Cabarrocasb., R. Alcubilla., Laser fired contacts applied to the rear surface of heterojunction silicon solar cells, Solar Energy Materials and Solar Cells 95 (11), 2011, pp. 3119–3123, DOI: 10.1016/j.solmat.2011.06.049.

24. R. Preu, E. Schneiderlöchner, A. Grohe, S.W. Glunz, G.P. Willeke, Laser-Fired Contacts - Transfer of a Simple High Efficiency Process Scheme to Industrial Production. Photovolt. Spec. Conf.: Conf. Record of the Twenty-Ninth IEEE. 2002; pp. 130-133. DOI: 10.1109/PVSC.2002.1190473.

25. J.H. Yoo, S.H. Jeong, R. Greif, R.E. Russo. Explosive Change in Crater Properties During High Power Nanosecond Laser Ablation of Silicon, J. Appl. Phys. 88(3), 2000, pp 1638-1649. DOI: 10.1063/1.373865.

26. A. Miotello, R. Kelly. Laser-Induced Phase Explosion: New Physical Problems When A Condensed Phase Approaches the Thermodynamic Critical Temperature, Appl. Phys. A: Mat. Sci. and Proc. 69(7), 1999, S67-S73. DOI: 10.1007/s003399900296.

27. D.J. Lim, H. Ki, J. Mazumder, Mass Removal Modes in the Laser Ablation of Silicon by a Q-Switched Diode Pumped Solid-State Laser (DPSSL), J. Phys. D: Appl. Phys. 39, 2006, pp. 2624-2635. DOI: 10.1088/0022-3727/39/12/023.

28. C. Molpeceres, M.I. Sanchez-Aniorte, M. Morales, D. Munoz, I. Martin, P. Ortega, M. Colina, C. Voz, R. Alcubillia, Influence of wavelength on laser doping and laser-fired contact processes for c-Si solar cells, Proc. Of SPIE 8473, DOI: 10.1117/12.929456.

29. A. Grohe, E. Schneiderlochner, M. Hermle, R. Preu, S.W. Glunz, G. Willeke, S. Walz, Characterization of laser-fired contacts processed on wafers with different resistivity, Proceedings of the 3rd World Conference on Photovoltaic Energy Conversion 2, 2003, pp 1032-35.

30. X. He, J.W. Elmer, T. DebRoy, Heat transfer and fluid flow in laser microwelding, J. Appl. Phys. 97, 084909, 2005, DOI: 10.1063/1.1873032.

31. X. He, T. DebRoy, P.W. Fuerschbach, Alloying element vaporization during laser spot welding of stainless steel, J. Phys. D.: Appl. Phys, 36, 2003, pp 3079-3088, DOI: 10.1088/0022-3727/36/23/033.

32. V.V. Semak, G.A. Knorovsky, D.O. MacCallum, On the possibility of microwelding with laser beams, J. Phs. D: Appl. Phys. 36, 2003, pp. 2170-2174.

33. B. DeCesar, Investigation of process parameter optimization of laser-fired back contact silicon solar cells, MS Thesis Penn State University, 2010.

34. B. Hedrick, Characterization of laser fired contacts, laser doped emitters and fixed charge passivation for improved silicon solar cells, MS Thesis Penn State University, 2011.

35. Z. Hua, E.W. Reutzel, L. Zou, Beam delivery techniques for laser fired contacts, ICALEO 2010, #M1101.

36. V. Schutz, A. Horn, U. Stute, High-throughput process parallelization for laser surface modification on Si-Solar cells: determination of the process window, Proceedings of SPIE Vol. 8244 (2013).

37. W. Zhang, G. G. Roy, J. Elmer and T. DebRoy, J. Appl. Phys., 93(5), 2003, pp. 3022-3033.

38. W. Zhang, C. L. Kim, and T. DebRoy, J. Appl. Phys. 95, 2004, pp. 5220-5229.

39. J.J. Blecher, T.A. Palmer, E.W. Reutzel, T. DebRoy, Laser-silicon interaction for selective emitter formation in photovoltaics, II. Model applications, J. Appl. Phys. 112, 2012, 114907.

40. B. Ribic, R. Rai, T. DebRoy, Sci. and Tech. of Weld. and Join. 13(8), 2008, pp. 683-693.

Chapter 2

BACKGROUND

2.1 Introduction

The purpose of this chapter is to provide a critical review of the relevant literature in laser-fired contact formation on Si-based solar cells. Much of the existing literature related to laser-fired contacts has focused on empirical studies designed to optimize process capabilities, such as device performance efficiency and electronic properties, without emphasis on the laser-material interaction behavior associated with contact formation. In the following sections, the ongoing research about the laser-firing process as a method to achieve backside ohmic contact on solar cell devices is critically reviewed. In addition, the physical processes associated with laser firing and laser spot micro-welding, such as heat transfer, mass transfer, fluid flow, and laser-material interaction behavior, are examined. Finally, the application of mathematical models to understand laser-spot micro welding and laser doping, which are of direct relevance to the laser-fired contacting process, is analyzed to provide a framework for the current research approach. Based on the literature, research areas that govern the formation of laser-fired contacts fabricated using a range of laser pulse durations are identified.

2.2 Solar Cells and Laser-fired Contacts

2.2.1 Passivated Emitter Rear Cell Structure

Photovoltaic devices are comprised of: a semiconductor substrate, a p-n junction, and front and backside metal/semiconductor contacts [1]. A doped semiconductor substrate, such as Si, absorbs photons from the solar wavelength spectrum and generates electron-hole pairs that are subsequently transported to opposite directions to produce a photocurrent. When strictly talking about Si semiconductors, negative charge carriers (n-type) and positive charge carriers (p-type) base are introduced through diffusion of phosphorus (P) and boron (B), respectively, into the substrate. Due to the valence states of P and B, bonding of the dopant atom with the Si atoms in the crystal lattice will result in electron or hole charge carriers within the doped semiconductor substrate. n-Type semiconductors have electrons as the majority carrier, whereas p-type semiconductors have holes as the majority carrier. When n-type and p-type semiconductors are placed in intimate contact, a p-n junction forms.

The p-n junction is required for separation of the photogenerated charge carriers for current collection. During solar cell operation, a space charge region forms in the p-n junction that separates electrons and holes for collection due to an inherent electric field that drives charge carriers in specific directions [2]. Lastly, metal/semiconductor contacts are present on both the front and backside of the

device to collect photogenerated carriers and facilitate current flow to an external load. Silver and Al are most often used for front and backside metal contact materials due to work function requirements, high electrical conductivity, and limited diffusivity in Si at device operating temperatures [3]. A schematic diagram of a simplified solar cell device that identifies these regions is shown in Figure 2.1 [4]. To enhance device performance, coatings are often used such as an anti-reflection layer to enhance light trapping, and a surface passivation layer is used to prevent electron-hole pair recombination losses [5,6].
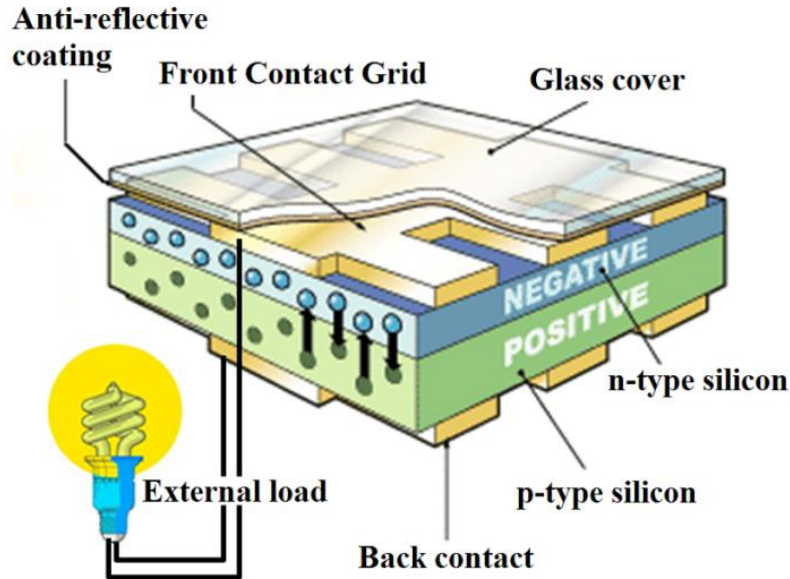
Figure 2.1. Schematic of basic components in silicon solar cell device. Adapted from [4].

One area that represents a critical need in future commercialization of Si-based solar cell technology is the backside metal/semiconductor contact. Traditionally, backside metal/semiconductor contacts have been achieved using a full area Al metal layer in direct contact with the Si semiconductor [7]. This structure, however, led to lower energy conversion efficiencies due to high electron-hole pair recombination rates at the metal/semiconductor interface. One family of crystalline Si-based solar cells that has addressed these device performance issues by improving the backside metal/semiconductor contact is the Passivated Emitter Rear Cell (PERC) structure. In order to improve performance efficiency, the PERC solar cell device replaces the full area metal back contact with localized rear-side Al-alloyed ohmic point contacts surrounded by a dielectric passivation layer between the Al metallization and the Si wafer [8,9]. The dielectric passivation layer reduces recombination rates at the Al-Si interface and enhances internal reflection, leading to higher open circuit voltages and short circuit currents, respectively [5,6,10].

Due to the thinness of Si solar cells, it is also critical to improve light-trapping, and a rear side dielectric passivation layer, such as SiN_x or SiO_2, can act as an optical back-surface mirror that results in higher internal reflectance and leads to more opportunities to generate additional photogenerated carriers. At each contact point produced in the passivation layer, there are also heavily Al-doped regions that form beneath the contact as a result of solid-state diffusion of Al into Si. The heavy Al doping makes the collection process of majority carriers more efficient due to the formation of a local back surface field (BSF) and a p-p+ junction at the contact-wafer interface [11,12]. Since a large number of the photogenerated carriers that are created in the near-surface region must travel to the contact to be collected, the BSF inhibits movement of the minority carriers to the rear surface, thereby achieving lower recombination rates. As a result of these improvements, PERC devices have demonstrated energy conversion efficiencies of greater than 23% [13].

Despite the clear performance enhancements associated with the PERC solar cell structure, creating point contacts on the backside of the wafer is a cumbersome process involving a number of steps [7,8], as shown in Figure 2.2(a) [14]. After deposition of the dielectric passivation layer on the backside of the Si wafer, multi-step patterning, photolithography, and chemical etching steps are required to create localized openings at specific locations within the passivation layer. The openings are defined based on the carrier mobility within the substrate and their relative diffusion lengths. After the openings are created, Al is deposited on the rear surface of the wafer via screen-printing or electron beam deposition methods, and high temperature annealing is performed to form the metal/semiconductor ohmic contacts between the Al metallization layer and the lightly-doped Si semiconductor. A typical furnace heat treatment cycle can be observed in Figure 2.2(b) [15]. The high temperature annealing treatment that is required to form the Al-Si contact can result in wafer warpage and breakage due to the thinness of the Si wafers, typically on the order of 100 to 200 μm [16]. Furthermore, these processing steps that are required to form the rear side ohmic contacts add significant handling costs to the overall fabrication process.

Therefore, innovative, cost-effective manufacturing methods are required to fabricate the backside Al-Si point contacts in order for the PERC solar cell device structure to become a commercially viable technology. Lasers are an important tool in photovoltaic device fabrication and are routinely used for various applications, such as etching [17], scribing [18], and doping [19]. By utilizing laser technology in a similar approach to laser doping in which P is incorporated into a Si wafer to form a shallow emitter, lasers can be used to rapidly and economically produce localized, Al-Si backside ohmic contacts on the PERC solar device [20,21]. These ohmic contacts are typically called laser-fired contacts.
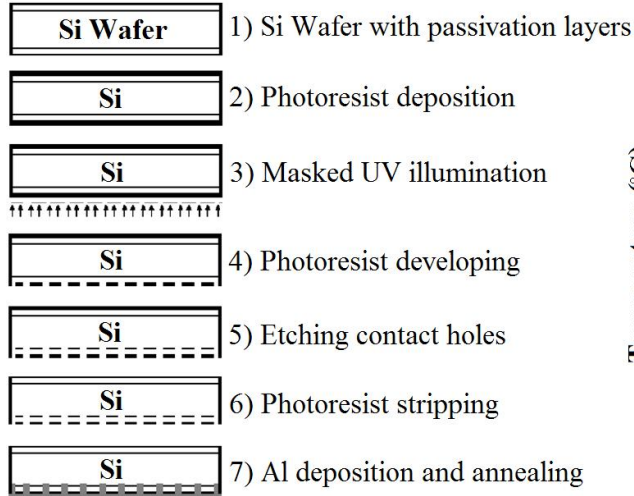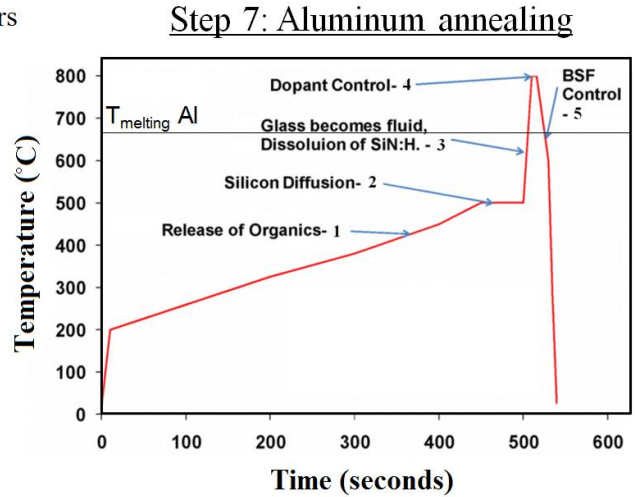
Figure 2.2. (a) Process map for Al-Si backside contact formation and (b) schematic diagram of Al-Si annealing step. Adapted from [14,15].

2.2.2 Laser-fired Contacts (LFCs)

During the processing of laser-fired contacts (LFCs), highly localized regions of the Al metallization layer and the rear-side dielectric passivation layer are rapidly heated and melted to create Al-Si point contacts with the underlying Si wafer in a single step. Using this method, it is not necessary to create individual contact openings in the dielectric passivation prior to depositing the Al metallization layer. Therefore, this contacting technique presents an incredible opportunity to transform the fabrication process and eliminate the use of photolithography, chemical etching and thermal annealing to produce backside point contacts without any loss in energy conversion efficiency. Figure 2.3(a) shows the process map used for laser-firing of backside contacts, and Figure 2.3(b) shows a closer view of the LFC between the Al contact layer and Si wafer (formed through the optical reflection and passivation layers).
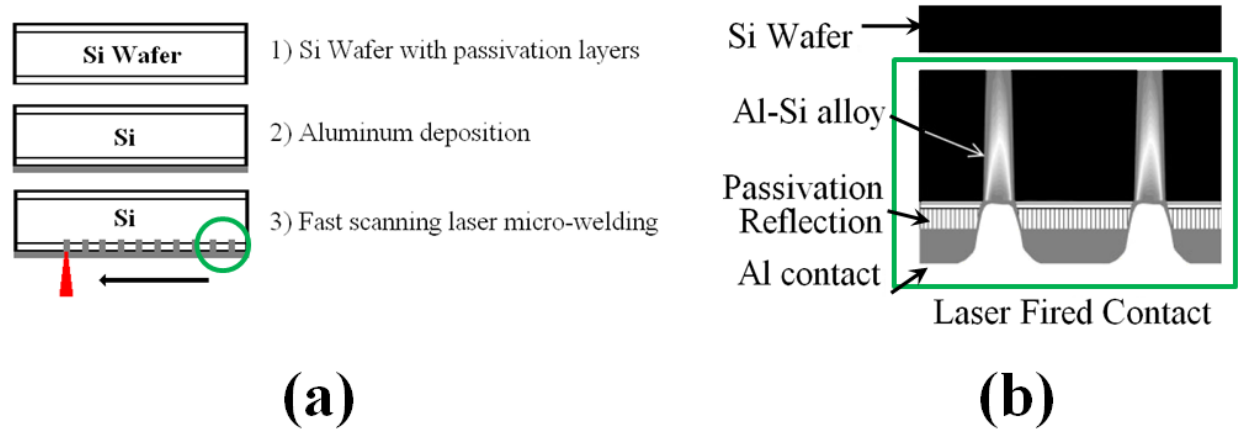
Figure 2.3. Schematic diagrams of (a) LFC process map and (b) backside of solar cell. Adapted from [14].

When used on the PERC solar cell structure, the LFC process can also result in the formation of localized back surface fields through solid-state diffusion of Al into the unmelted crystalline Si wafer. The localized doping of the Si wafer, which results in the formation of a p^+ Al doped region beneath the contact, has a positive impact by reducing recombination of photogenerated minority carriers at the rear contact surface [22]. Since the diffusion of Al into the crystalline Si directly outside of the contact region will result in an increased negative charge around the contact, the BSF prevents electron diffusion to the rear surface contact, thereby inhibiting electron-hole recombination losses that are observed in standard Al-Si rear side contacts. With the integration of LFCs into the PERC device, energy conversion efficiencies greater than 20% on various Si solar cells have been achieved [21, 23-25]. These efficiency levels are a significant improvement over commercially produced thin film Si solar cells with energy conversion efficiencies around 10-15%.

In order to maintain overall device performance efficiency requirements when creating an LFC, the processing of LFCs must meet the following requirements:

1) Minimize damage to the Si crystal lattice since photogenerated carriers originate from the bulk, and defects in the lattice can serve as prime recombination sites for minority and majority charge carriers;

2) Preserve the passivation layer outside of the immediate LFC reason since the dielectric passivation is required to reduce recombination rates and increase internal reflection;

3) Form a localized BSF around the contact region to prevent recombination close to the metal/semiconductor contact interface through which charge carriers are collected, and;

4) Generate contacts that exhibit low total contact resistance.

Therefore, when developing LFC technology, it is important to understand how the introduction of large amounts of energy from a laser heat source over a short pulse duration and within a small interaction

volume can structurally damage the surrounding bulk material. Since concentrated laser energy can introduce defects into the single crystal Si lattice and potentially degrade the surrounding passivation layer, careful selection of laser processing parameters is imperative. In addition, the impact of changes in laser processing on these material properties must be comprehensively evaluated to develop a robust manufacturing process.

2.2.2.1 Nanosecond Pulsed LFC Processing

Recent research on the LFC process has focused primarily on Q-switched Nd:YAG lasers operating at 1064 nm with short, nanosecond pulse durations [21,23,24,26]. Using these conditions, researchers have reported solar cell conversion efficiencies up to 22.4% [6,20]. Lasers operating in the infrared wavelength spectrum are used due to higher absorption depths in Si, which can improve alloying of Al and Si during the short pulse. It is likely that nanosecond pulses are the preferred choice because the low energy densities associated with extremely short pulse durations can minimize the extent of damage to the surrounding passivation layer and the crystalline Si substrate. However, excessive laser intensity combined with extremely short pulse durations has been shown to cause significant ablation of Si during laser processing [27-29]. Since the laser first interacts with the Al metallization layer, which has significantly lower melting and boiling points than Si, ablation of the Al can be expected, thereby preventing interdiffusion of Al and Si required for proper contact formation [8].

Electron dispersive spectroscopy has confirmed that contacts formed with nanosecond pulse durations exhibit little presence of Al within the contact region after firing with nanosecond pulse durations [12]. In addition, significant metal expulsion results in large craters in the substrate and microcracks in the contacted region [29,30], likely due to the rapid cooling rates and large recoil force associated with high power densities and nanosecond pulses. Despite the complexity of the laser-material interaction behavior associated with contact formation, the LFC process has typically been studied with primary emphasis on device performance metrics, such as open circuit voltage, short circuit current, fill factor and conversion efficiency. Few groups have performed materials characterization of the impact of laser processing on LFC formation to understand how changes in laser processing parameters influence LFC formation.

Zastrow, et al. [12] and Grohe, et al. [31] used a Q-switched Nd: YAG 1064 nm wavelength laser emitting in the TEM_{00} to generate laser fired contacts on Si wafers that were passivated with 100 nm thick SiO_2 and then metallized with 2 μm thick layer of Al. Characterization of the impact of laser processing parameters on the incorporation of Al into the laser-affected region was performed using Scanning Electron Microscopy (SEM), Secondary Ion Mass Spectroscopy (SIMS), Electron Dispersive X-ray Spectroscopy (EDX) and Transmission Electron Microscopy (TEM). The contacts produced had two

distinct, circular regions, as shown in Figure 2.4: 1) an outer region where the Al metallization was expelled and the passivation layer remained and, 2) an inner crater where Al was lightly alloyed with Si.
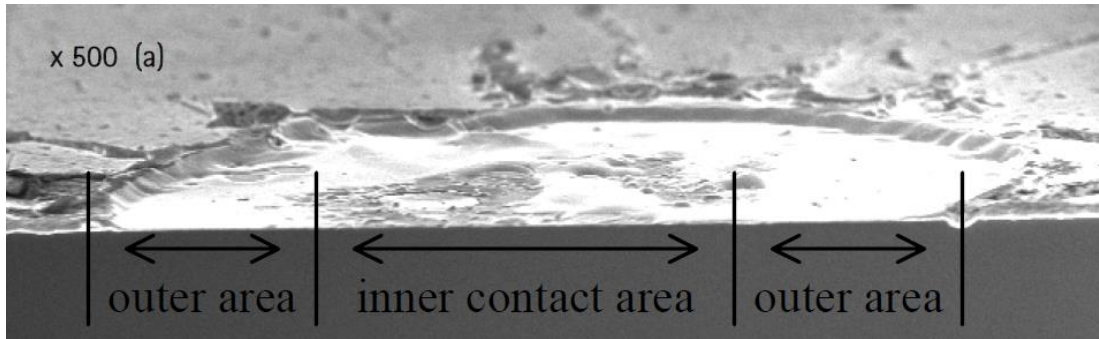
Figure 2.4. Inner and outer crater regions observed in LFCs processed with nanosecond pulse durations [31].

The top surface diameter of the outer contact region typically varied from 80 to 100 μm. This region was devoid of Al, which was completely removed by ablative mechanisms associated with the short pulse duration and high power density, and the underlying passivation layer was exposed. The interior crater region was less than 50 μm in diameter and represented the region where the dielectric passivation had been ablated and was removed. Within this region, TEM and diffraction patterns revealed the formation of a eutectic Al-Si mixture. This two-phase region constituted where the contact formed and Al was incorporated up to 1 μm in depth at a concentration on the order of 10^{19} cm^{-3}. SIMS profiling suggested that Al had also diffused into the undisturbed Si crystal lattice up to a few hundred nanometers. Although the formation of the Al-Si region was characterized, the mechanism by which contact formation occurred was not identified. In particular, since the two-phase Al-Si eutectic region was found in the 50 μm diameter crater region within the opening in the ablated dielectric passivation layer, and no Al was present within the outer crater region, which itself had a diameter of 80 μm, it is unclear how physical contact was made between the inner crater and the unaffected Al metallization layer to form the LFC.

Grohe, et al. [32] also processed LFCs on n-type Si wafers with different base resistivities using a Q-switched Nd:YAG laser system and nanosecond pulse durations with similar processing parameters [14]. They utilized Laser Secondary Neutral Mass Spectroscopy (L-SNMS) and Electron Beam Induced Current (EBIC) current measurements to study the laser alloying process of Al into the Si during contact formation. In the LFCs formed, there were also two clearly discernible regions: an inner crater and outer annular area, as observed by Zastrow, et al [12]. L-SNMS results demonstrated very low detection rate of Al in the outer ring area where the metallization layer was ablated and the dielectric passivation layer remained. Within the inner crater, Al was detected to appreciable levels relative to the Si detection rates.

However, the data for detection rate is given in arbitrary count units, making it difficult to determine the exact dopant concentration of Al within the inner crater.

EBIC results performed from the top surface as well as on a cross-sectional area through the center of a contact further confirm that alloying of Si and Al only takes place within the inner crater region. Since Al is a p-type dopant that has solubility on the order of 10^{19} cm^{-3} in Si [33,34], its incorporation into a p-type crystalline Si during LFC formation results in the formation of a p+ Si region. On an n-type Si wafer, however, when the Si is doped with Al, a p-n junction will form at the interface between the doped Al region and the undoped crystalline Si. The EBIC method utilizes an electron beam to stimulate electron-hole pairs in a semiconductor, and an electric field can be detected by an external probe. The presence of an electric field was used to identify the presence of a p-n junction and, therefore, determine whether alloying of Al and Si had taken place at the back contact. This study along with a similar investigation [35] demonstrated the presence of Al within the volume of the inner crater contact region up to a depth of approximately 1 µm. Although informative, the mechanism by which LFC formation occurs was not clearly identified in these studies. Furthermore, with the separation between the top surface Al metallization and the inner crater Al-Si alloyed region by the insulating dielectric passivation, the means by which contacting occurs is unclear for these short pulse durations. Without a robust method to form an LFC with adequate doping of the Si by the Al and proper contact between the metallization layer and the Al-doped contact, the firing process will introduce variability into the quality of the contacts formed.

An investigation by BP Solar International [36] sought to identify the mechanism by which contact formation occurs between the metallization layer and the doped contact region after laser-firing under short nanosecond pulses. LFCs were generated on Si wafer substrates that had an 80 nm thick Si nitride passivation layer and a 1 µm thick silver (Ag) metallization layer. Figure 2.5 shows images for two contacts that were generated. In Figure 2.5(a), it can be seen that there are three distinct regions: 1) the Ag-alloyed central contact region, 2) the outer annular, dielectric ring region where the Si nitride is exposed due to laser ablation of the Ag metallization, and 3) the unaffected Ag metallization layer. This particular contact exhibited extremely high resistance values, suggesting poor contact due to lack of conductive paths between the Ag metallization and the doped Si crater in the center.

Figure 2.5(b) shows a contact that exhibited lower resistances. The difference between the two contacts is the presence of regions where the Ag-doped Si material was ejected from the center of the contact due to ablation and has come in physical contact with Ag metallization. Using scanning transmission electron microscopy, it was shown that alloying of the central Si crater region by the Ag metallization took place. Furthermore, it is believed that the ablated material is a mixture of Si and Ag,

which makes it extremely conductive. Therefore, as the number of conductive paths increases through more ablation due to the use of higher energy laser pulses, the contact quality can improve. Few groups have undertaken efforts to understand the means by which contact formation occurs when utilizing short, nanosecond pulses.
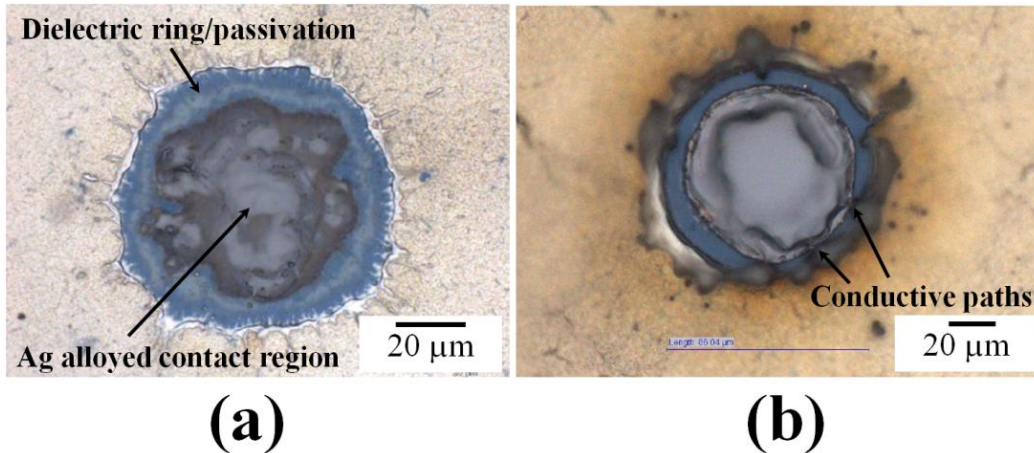
Figure 2.5. Optical microscope images showing (a) Ag-Si alloyed region contact at center surrounded by Si nitride dielectric ring, and (b) Conductive paths formed between Ag metallization and alloyed contact region. Adapted from [32].

Using EDX measurements of the top surface of the LFCs generated with short pulse durations, Molpeceres, et al. [29] also evaluated the mechanism by which contact formation occurs. EDX and optical profilometry were used to study the impact of laser processing parameters on the laser-material interaction behavior associated with LFC formation. Figure 2.6 shows large craters greater than 5 μm in depth in the Si substrate, which are formed by significant ablation of Al and Si. In related work, craters greater than 8 μm were observed during contact formation [30,37]. The EDX measurements shown in Figure 2.6 demonstrate how Al and Si are incorporated into the LFC, also suggesting that the incorporation of Al into the ejected material is critical for contact formation to occur. It can also be observed that the Al metallization has been completely removed from the central crater region. However, the impact on the quality of the passivation layer and ablation of the metallization above the passivation was not addressed nor quantified via EDX measurements. In addition, there was no clear dielectric region observed in these contacts.

In this study, the best electrical results in terms of specific contact resistance were obtained for contacts that exhibited a higher presence of Al within the crater regardless of the choice of laser wavelength. Furthermore, changes in the laser wavelength did not impact the quality of the contact as long as the Al concentration was maximized, suggesting that the most important criteria for higher quality contacts is the alloying of Al and Si into the central crater region. It was shown, however, that the use of

the 355 nm laser wavelength laser, which has a shallower absorption depth in Si, resulted in slightly improved electrical performance, likely due to the minimization of thermal damage to the material during processing. In all cases shown, the highest achieved concentration of Al in the contact within the crater was 1.1 at. %. In addition, the formation of the contact can again be attributed to the physical contact between the metallization and crater region, as observed by BP Solar International.
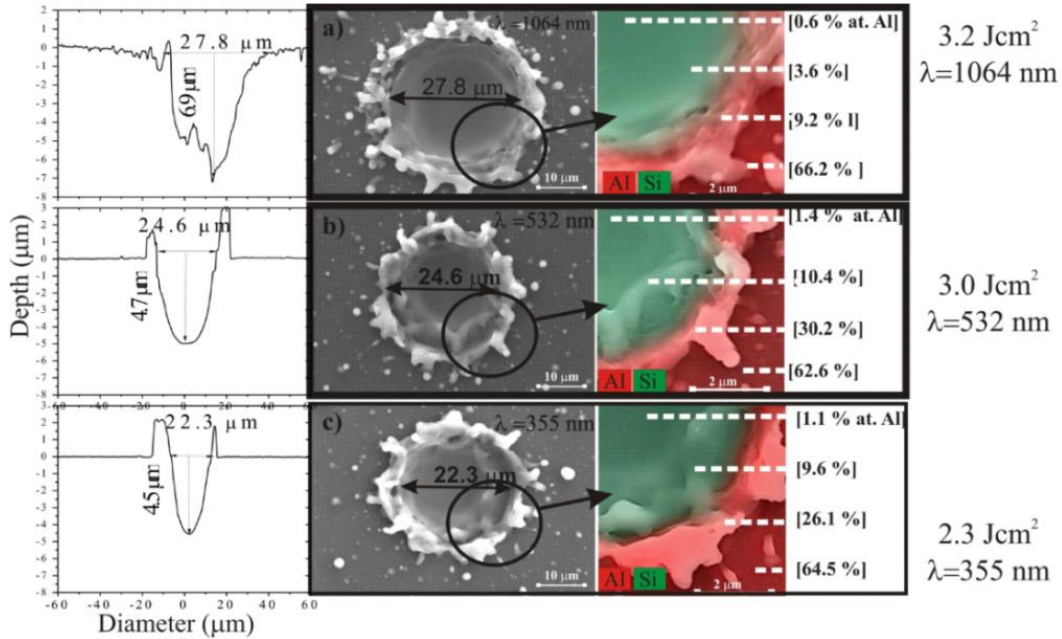
Figure 2.6. Crater and concentration profiles when processing with nanosecond pulses and different laser wavelengths [25].

In the work to date, researchers have focused on nanosecond pulse durations and have not investigated the relationship between the selection of laser processing parameters and the resulting laser-material interactions and its impact on contact formation. However, the use of longer pulses has not been extensively reported on for fabricating LFCs despite the potential benefits to reduce ablation and enhance the melting and mixing of the Al with the Si during laser processing. Although microsecond or millisecond pulse durations are substantially longer than nanosecond pulses and thousands of LFCs have to be processed per second, lasers capable of millisecond and microsecond pulses are available at much higher powers, which means that an incoming beam can be split into a large number of beams to simultaneously process multiple LFCs [38-39]. The use of millisecond pulse durations has already been investigated [43,44], and the results are promising.

2.2.2.2 Millisecond Pulsed LFC Processing

Longer pulses can be used to promote greater mixing of the Al and Si to form larger contacts that can lower the contact resistance and improve performance. Millisecond pulses have been used extensively in

laser spot micro-welding of various material systems. The resulting spot welds are characterized by well-mixed fusion zones without metal expulsion when the laser parameters are appropriately selected [40-42]. In order to investigate this pulse duration regime for LFC processing, DeCesar [43] and Hedrick [44] performed extensive experimentation and characterization of contacts produced using millisecond pulses over a wide range of laser processing parameters. LFCs were generated on p-type and n-type Si wafers that were passivated with two different passivation stacks. The p-type wafers were used to conduct the majority of the experiments since this doping levels is typical of what is conventionally used on the backside of the wafer. The n-type wafers were used for development of a p-n junction delineation technique used to view LFC cross-sectional geometry. LFCs were processed with an IPG Photonics 1070 nm single mode fiber laser with a beam diameter of approximately 46 μm at focus and laser beam power was varied from 18 to 50 W with pulse durations from 4 to 19 ms.

DeCesar [43] correlated changes in power, energy, and pulse duration to contact morphology and electrical resistivity. By characterizing the top surface of the contacts produced, he showed that ablation could be eliminated with the use of longer pulse durations, as shown in Figure 2.7. There is little spatter and liquid metal expulsion observed over a wide range of processing parameters on two different passivation stacks, which suggests that the Al metallization layer is completely incorporated into the LFC. As a result, there should be direct contact formed between the metallization and the contacted region without discontinuities between the metallization layer and the alloyed region as observed with processing with nanosecond pulses [36]. In addition, by changing processing parameters to increase the LFC top surface diameter, there was a marked reduction in total contact resistance. However, the characterization of the contact size was based solely off the top surface of the LFC, which provided little information about the cross-sectional contact geometry. From his work, it was unclear whether the sub-surface size of the LFC influenced the observed changed in contact resistance with increasing top surface diameter. Furthermore, no characterization of the mixing of Al and Si through EDS was performed to understand how both elements are incorporated into the contact during processing.
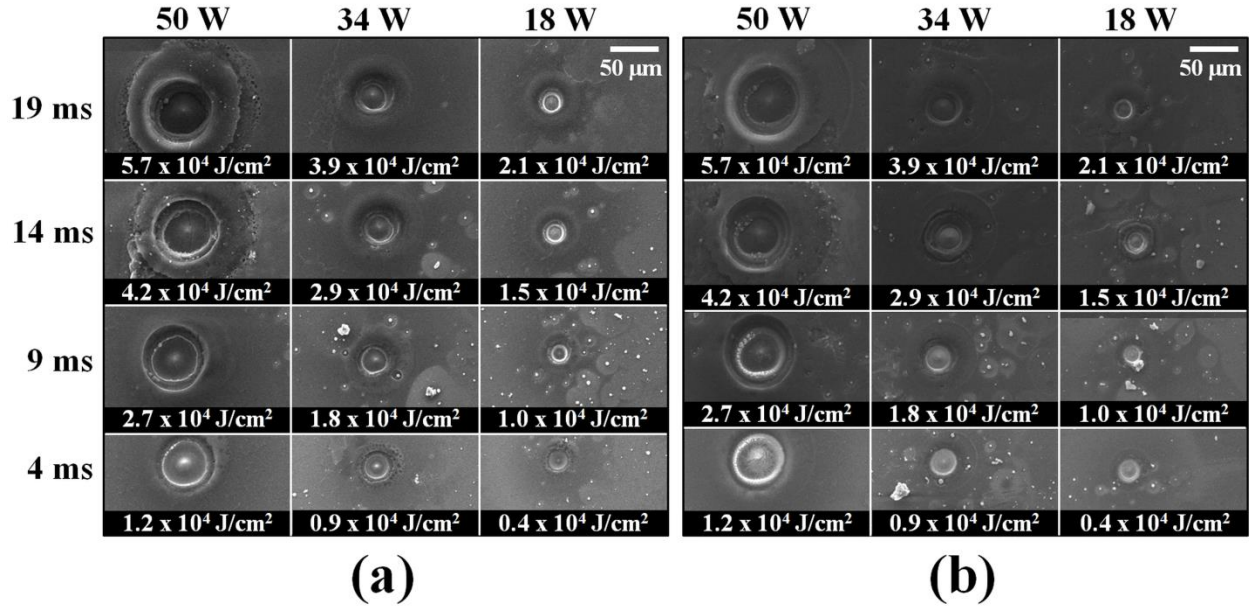
Figure 2.7. SEM micrographs of LFCs processed with IPG 1070 nm single mode fiber laser on (a) dual stack passivation sample, and (b) single layer passivation sample. 30 μm scale bar applies to all micrographs. Adapted from [27].

Hedrick [44] went a step further to develop a method to determine the cross-sectional geometry of the contacts processed with these longer pulse durations. The LFCs were produced on the n-type wafers, and since Al is a p-type donor, a p-n junction was produced at the interface between the Al-doped contact region and the Si substrate. By detecting where this junction forms, the size of the contact was determined. Hedrick [44] showed that the contacts produced with the millisecond pulses exhibited a three-dimensional hemispherical geometry with heavy Al doping of the Si to depths greater than 20 μm, as shown in Figure 2.8. The alloying depth is much greater than that produced with nanosecond pulsed lasers, which is generally less than 1 μm [12,31,32]. However, using this method, it is not possible to gain an accurate estimation of the p-doping levels of the Si by the. Furthermore, the impact on the passivation layer is not clear since the surface was too rough to determine if the passivation remained intact. Therefore, a different characterization method is required to more clearly identify the impact of laser processing on LFC formation.

Hedrick [44] also utilized carrier transport device simulations to investigate the impact of a hemispherical geometry and various doping densities on total contact and spreading resistances. It was demonstrated that the three-dimensional geometry can account for the changes in resistance observed by DeCesar as a function of LFC top surface diameter. Therefore, the use of longer pulse durations can have the advantage of creating larger contact with greater LFC/wafer interfacial area than that produced with nanosecond pulses. The larger interfacial area will effectively reduce the spreading resistance for an

individual contact. It is unclear if the use of microsecond pulses will exhibit the same contact geometry. In addition to contact resistance measurements, qualitative measurements of carrier lifetime were made using microwave photoconductive decay measurements to determine if millisecond pulses degrade the passivation layers. Although high carrier lifetime measurements suggest that the passivation layer remains intact with longer pulse durations, there were a number of data points processed with the same laser processing conditions that exhibited entirely different lifetimes [43]. Therefore, the reliability of the study is questionable since the contact area fraction used for the study was extremely low, which would make the sensitivity of the measurements extremely low.
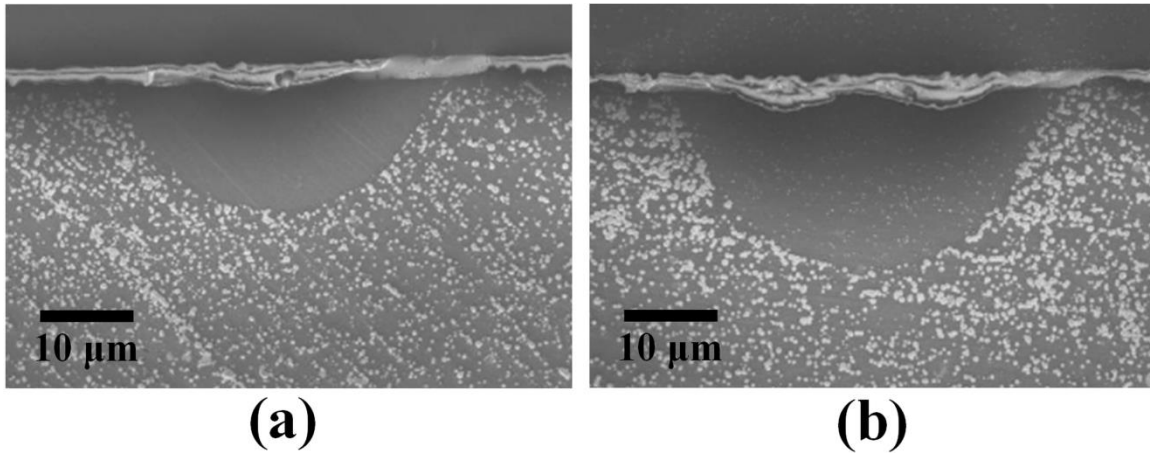
Figure 2.8. SEM micrographs of LFC cross sections after junction delineation when processing with IPG 1070 nm fiber laser with (a) 22 W laser power and 19 ms pulse duration on n-type a-Si:H sample and, (b) 45 W laser power and 4 ms pulse duration on n-type dual stack passivation sample. Adapted from [43].

One area that has received little attention is the use of microsecond pulses to form LFCs, despite the fact that substantially less processing time will be required that that for millisecond pulses. Since millisecond pulses have been shown to result in a well-mixed Al-Si LFC without extensive ablation, it is important to also evaluate the use of microsecond pulse durations on contact formation. Microsecond pulse durations may also offer a means to improve processing efficiencies with significantly shorter pulse durations while still operating in the melting regime. By producing LFCs without excessive liquid metal expulsion, the Al from the metallization layer can be preserved to improve electrical conductivity of the LFC and device performance. In order to develop an understanding of LFC formation, an understanding of the complex behaviors associated with laser processing is required.

2.3 Physical Phenomena Governing Laser Processing

As shown in Figure 2.3(a), the formation of an LFC is essentially a laser spot micro-weld formed between the Al metallization and the Si substrate. Therefore, the ensuing review and discussion will treat

LFC fabrication in the context of laser spot micro-welding in order to explain the important physical processes associated with the laser processing of LFCs.

2.3.1 Energy Absorption during Laser Heating

When a concentrated laser beam irradiates the surface of a material, a number of complex physical phenomena occur. First, the energy of the photons from the laser beam will be either reflected by the surface or transmitted. The transmitted energy is absorbed by the electrons and then redistributed through lattice vibrations, which gives rise to heat conduction [45]. The amount of energy transferred by the material is important because it directly affects the heating of the substrate, the formation and maintenance of a liquid pool, the time-dependent temperature fields within the molten pool, and the resultant microstructure and properties of the solidified material [46].

In order to determine how a material is impacted by the laser energy incident on its surface, it is important to quantify the total absorbed energy in terms of its spatial distribution across the surface. The power density distribution is affected by the beam size and the peak power of the laser. In general, laser welding is performed within the Rayleigh range, which is the distance over which the beam divergence is minimal enough that processing at any point within this range can be considered as processing at focus [47]. Furthermore, the minimum achievable laser beam size at the focal point is controlled by the focusing optics and the laser radiation characteristic wavelength [48]. The power density distribution of a Gaussian laser heat source can be represented by the following equation [49]:

$$P_d = \frac{f \eta P_t}{\pi r_b^2} \exp\left(-f r^2 \Big/ r_b^2\right)$$

(2.1)

where f is the distribution factor, η is the absorptivity, P_t is the total power of the heat source, r_b is the radius of the laser beam at the focal point, and r is the radial distance from the center point of the heat source. For Gaussian laser beam profiles, the beam intensity is highest at the center and the distribution factor f is typically taken as 3 for conduction mode laser beam welding [50]. The absorptivity coefficient, η, has been related to the substrate resistivity and the wavelength of the laser radiation [51]:

$$\eta(T) = 0.365\left(\frac{\alpha}{\lambda}\right)^{1/2} - 0.0667\left(\frac{\alpha}{\lambda}\right) + 0.006\left(\frac{\alpha}{\lambda}\right)^{3/2}$$

(2.2)

where α is the electrical resistivity of the material at a given temperature and λ is the wavelength of the laser. Both a clean metal surface and no influence of a plasma plume (typical in keyhole mode welding)

on the laser beam absorption are assumed. In conduction mode welding, the energy absorbed is directly dependent on the laser wavelength and the material.

Depending on the material, the absorptivity in laser beam welding can be very low. For instance, as much as 95% of the laser energy generated by an Nd:YAG laser operating at 1064 nm wavelength incident on a polished surface of Al will be reflected [50].   The reflectivity can be significantly reduced through surface modifications, such as coatings or the presence of surface oxides [52]. As shown in Equation (2.2), the absorptivity is directly affected by the electrical resistivity of the material, which is dependent on temperature.   In general, as the temperature of a material increases, the material will exhibit higher absorptivities. The absorptivity can also change dramatically after a material undergoes a phase change from solid to liquid. In general, after melting, the absorptivity will increase significantly [54]. For laser processing of LFCs, it is important to understand how an incident laser beam interacts with a material under various laser processing conditions since the beam will interact with both Al and Si at various points during processing and the amount of energy absorbed will impact the evolution of the molten pool.

2.3.2 Forces Driving Liquid Metal Flow

During conduction mode laser spot micro-welding, a material will be heated by the incident laser radiation at a certain rate depending on its specific heat and density. Once sufficient energy has been absorbed by the material to raise its temperature to the melting point, the material will undergo a phase change from solid to liquid when sufficient energy is supplied to overcome its inherent latent heat of fusion. At this point, a region of molten material will exist that will be influenced by a number of forces, such as the buoyancy force, Marangoni surface tension force, and vapor recoil force. A schematic diagram of the forces acting on a pool is shown Figure 2.9(a).

The buoyancy force is caused by variations in density due to temperature and composition gradients within a molten pool. Due to the laser beam power density distribution on the surface of a molten pool as calculated by Equation (2.1), the temperatures at the center of the pool will be the highest. In general, higher temperature liquids are less dense than lower temperature liquids, as shown in Figure 2.9(b). Therefore, the liquid metal will tend to sink along the periphery of the molten pool and rise at the center due to the local variation of density caused by the temperature differences. The buoyancy force can be approximated as:

$$F_b = -\rho \, g \, \beta \left(T - T_{ref} \right) \tag{2.3}$$

where ρ is the density of the liquid metal, g is the acceleration due to gravity, β is the thermal expansion coefficient, T is the temperature of the liquid metal, and T is a reference temperature. In Equation (2.3), the buoyancy force is assumed to vary linearly with temperature when assuming a constant density, as is typically done in mathematical modeling of laser spot welding [55]. As a result of the buoyancy force, the liquid metal will tend to flow from the center to the periphery, as shown in Figure 2.9(c). This liquid metal convection will contribute to heat transfer within the melt pool.
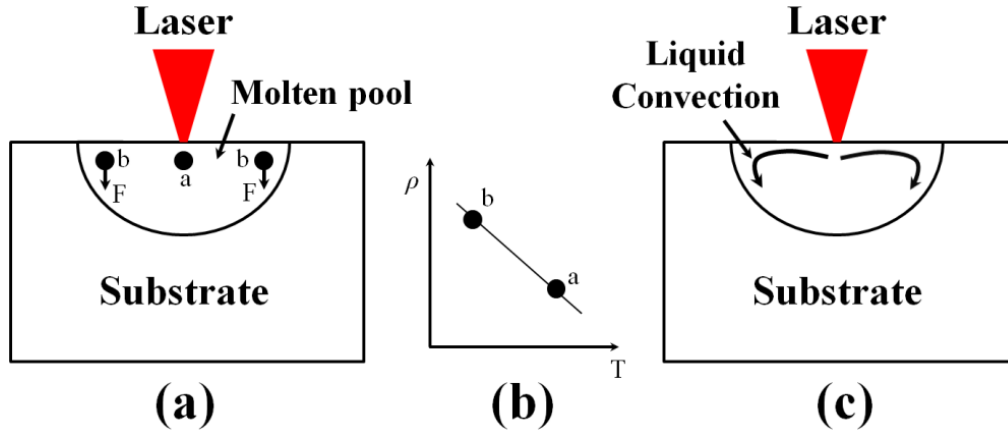
Figure 2.9. Schematic diagram of influence of (a) buoyancy forces, F, acting on molten pool, (b) density versus temperature, and (c) liquid metal convection that is caused by force imbalance.

Another force that plays a more prominent role in liquid metal convection is the Marangoni Force. Surface tension, γ, is a thermo-physical material property of liquid metal that is temperature dependent. The spatial variation of surface tension across the surface of a melt pool results in the formation of a shear stress at the liquid/gas interface, known as the Marangoni shear stress, τ. The Marangoni shear stress arises due to the spatial variation of temperature and composition and can be expressed as:

$$\tau = \frac{\partial \gamma}{\partial T}\frac{\partial T}{\partial r} + \frac{\partial \gamma}{\partial C}\frac{\partial C}{\partial r} \tag{2.4}$$

where T is temperature, r is the radial distance from the center of the heat source along the surface of the molten pool, and C is concentration of a surface active element, such as oxygen or sulfur. The influence of the concentration gradient is largely dependent on the concentration of surface active elements within the molten pool, which is usually insufficient to affect the shear stress. Therefore, the concentration gradient term in Equation (2.4) is typically negligible.

Figure 2.10(a) shows a schematic diagram of the forces acting on a molten pool due to the Marangoni shear stress along the top surface. In this case, the temperature coefficient of surface tension, $d\gamma/dT$, is

negative, which means that the surface tension decreases with increasing temperature, as shown in Figure 2.10(b). Since the temperature at locations 'b' in Figure 2.10(a) will be lower than the temperature at 'a', the surface tension will be greater at the periphery of the pool. Therefore, the liquid metal will flow radially outward, since the hotter liquid metal with lower surface tension near the center of the molten pool will be pulsed outward by the cooler metal with higher surface tension [56]. The liquid metal convection flow patterns are shown in Figure 2.10(c) where the liquid metal is transported outwards from the center of the melt pool to the periphery and will rise through the center. These convective flow patterns have been shown in laser processing of Si to strongly influence mass transfer dynamics of alloying elements, resulting in compositional variations within the melt pool [57,58].
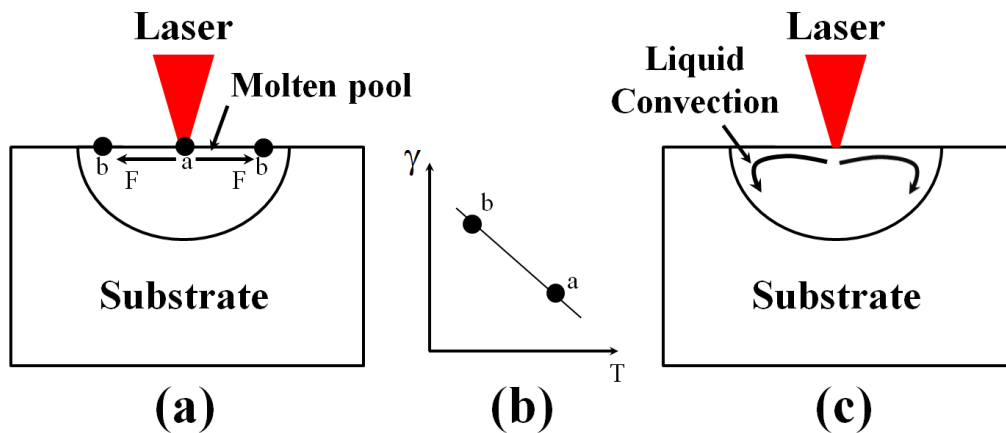
Figure 2.10. Schematic diagram of influence of (a) Marangoni forces, F, acting on molten pool surface when temperature coefficient of surface tension is negative, (b) surface tension versus temperature, and (c) liquid metal convection.

The presence of small amounts of surface active elements, such as sulfur and oxygen, which change the temperature coefficient of surface tension from negative to positive, however, can change the direction of the Marangoni shear stress on the surface of the melt pool. When there is a sufficient concentration of surface active elements within the molten pool, the temperature coefficient of surface tension, $d\gamma/dT$, will be positive, as shown in Figure 2.11(b). This means that the surface tension increases with increasing temperature. As a result, when the peak temperature is at the center of the pool, the forces acting on the surface of the pool will be in the opposite direction, as shown in Figure 2.11(a). The resulting flow pattern from the periphery to the center is shown in Figure 2.11(c) and will result in a larger penetration depth as the Marangoni shear stress drives fluid flow towards the center of the melt pool. The cooler metal with lower surface tension will flow from the edge of the pool towards the center of the pool where the surface tension is larger due to higher molten pool temperatures. Since Al is not known to be a surface active element in Si, however, this behavior should not influence laser-fired contact formation and the evolution of the molten pool during laser processing.
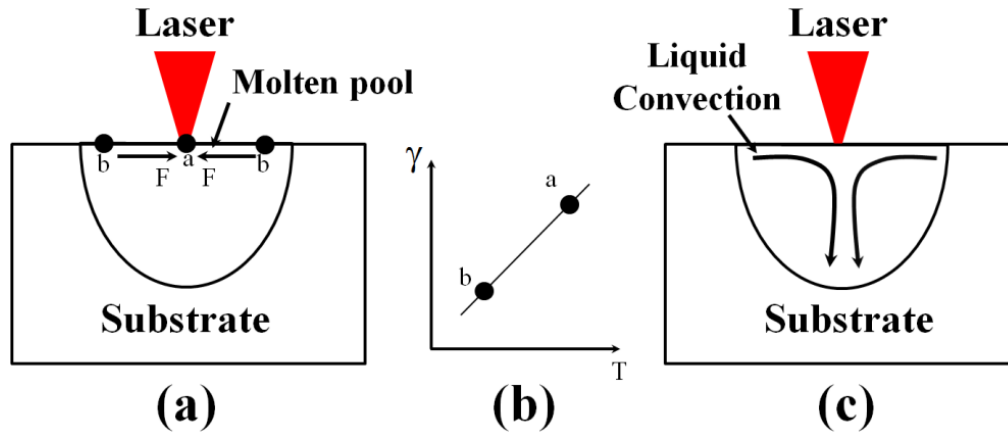
Figure 2.11. Schematic diagram of influence of (a) Marangoni forces, F, acting on molten pool surface when temperature coefficient of surface tension is positive, (b) surface tension versus temperature, and (c) liquid metal convection.

2.3.3 Vaporization and Metal Expulsion

Vaporization and liquid metal expulsion are the primary causes for material removal during laser processing. Vaporization occurs during conduction mode welding and liquid metal expulsion is caused by a vaporization-induced recoil pressure that causes material to be physically removed from the molten pool. During laser processing of materials and alloys, the high energy density associated with the process can cause the molten pool surface temperatures to rapidly exceed the boiling points of the alloying elements [59-62]. When the molten pool peak temperatures exceed the boiling point, significant vaporization of the alloying elements occurs since the partial pressures of the vaporizing elements is strongly dependent on temperature. Figure 2.12 shows experimental data for the equilibrium vapor pressure for various elements as a function of temperature [63]. Laser fired contacts are formed by the mixing of Al and Si in the melt pool. From the plot, it can be observed that Al has a vapor pressure of approximately 1×10^{-12} atm at its melting point of 933K. However, the vapor pressure increases 9 orders of magnitude to 1×10^{-3} atm around 2000K. Si has a vapor pressure of 1.3×10^{-7} atm at its melting point, and its equilibrium vapor pressure increases 2 orders of magnitude by 2000K. The drastic changes in the partial vapor pressure of the alloying elements with temperature, and the pressure difference between atmospheric, ambient pressure and the partial vapor pressures will lead to vaporization and metal expulsion, which can influence composition of the solidified metal.
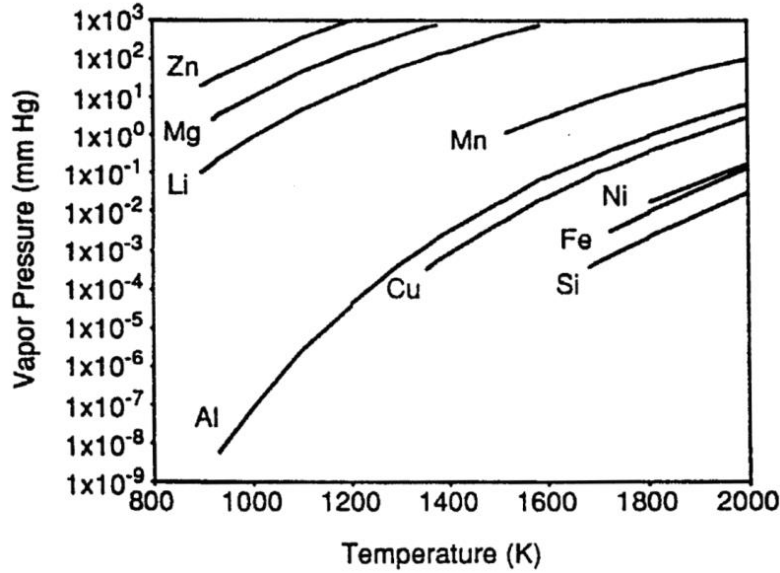
Figure 2.12. Equilibrium vapor pressure as a function of temperature for various pure elements [63].

The selection of laser processing parameters can have a large impact on the rate of vaporization. Changes in laser power, laser beam radius, and welding velocity can alter the temperature profiles on the surface of the melt pool and lead to high vaporization rates. It has been shown that laser power density and welding velocity are the most important process parameters that must be controlled to reduce the vaporization rate [41,64]. The vaporization flux, J_i, of a pure metal, i, in a vacuum is given by the Langmuir equation [68]:

$$J_i = \frac{\lambda P_i^0}{\sqrt{2 \pi M_i R T}}$$ (2.5)

where λ is a factor that accounts for condensation and collision of vaporized particles, P_i^0 is the vapor pressure of i over the pure liquid, M_i is the molecular weight of the vaporizing element, R is the gas constant and T is the temperature. The vaporization rate is proportional to the equilibrium vapor pressure of the vaporizing element. For an alloy in which multiple elements are present, the vaporization rate for each alloying element is calculated separately, and the overall vaporization rate for the alloy is the sum of the vaporization rates for each constituent. In laser spot welding, previous researchers [41,64] have assumed that the alloy behaves like an ideal gas at high temperatures according to Raoult's Law [66]. As a result, the individual vapor pressure for each component can be calculated as:

$$P_i = P_i^0 \times x_i$$ (2.6)

29

where x_i is the mole fraction of element *i* in the alloy. The Langmuir equation is accurate at very low pressures where significant condensation of the vapor does not take place. Therefore, when laser welding is conducted at one atmosphere, Equation (2.6) will predict a much higher vaporization rate than what is actually present. In order to account for these higher vaporization rates, researchers have demonstrated during laser welding of stainless steels that the actual vaporization rates are approximately one-sixth of those given by Equation (2.5) [67-69]. In order for vaporization to occur from the surface of the melt pool, part of the supplied laser energy is used for the vaporization process. The energy associated with vaporization can impact the surface temperatures based on the following equation:

$$h_v = \sum_{i=1}^{n} J_i \, \Delta H \qquad\qquad (2.7)$$

where h_v is the energy required for vaporization, J_i is the vaporization flux of element *i*, and ΔH_i is the enthalpy of vaporization. In order to vaporize a given amount of material, a significant amount of energy is required. In fact, the energy required to vaporize a given volume of material is approximately one-quarter of that required for liquid metal expulsion [70]. Therefore, liquid metal expulsion often dominates the laser-material interaction behavior at temperatures above the boiling point of a material.

During laser processing, when the surface temperatures of a melt pool exceed the boiling point of the material, there are extremely high equilibrium vapor pressures on the surface of the melt. These pressures tend to push liquid metal from the center of the melt pool to the periphery. The surface tension between the liquid metal and gas interface exerts a force on the pool that will hold the liquid metal in place. The surface tension force, F_s, can be calculated as:

$$F_s = 2\pi r_0 \, \sigma \qquad\qquad (2.8)$$

where r_0 is the radial distance at which the molten pool temperature is equal to the melting temperature of the material and σ is the surface tension coefficient at the melting point. As a result of the high vapor pressures on the surface of the material, there will also be a large vapor recoil force, F_r, caused by the pressure difference between the local equilibrium vapor pressure and the atmospheric pressure, $\Delta P(r)$. The vapor recoil force can be calculated as:

$$F_r = 2\pi \int_0^{r_b} r \, \Delta P(r) \, dr \qquad\qquad (2.9)$$

where r_b is the radial distance at which the surface temperature reaches the boiling point. For metal expulsion to occur, the vapor recoil force must exceed the surface tension force [71]. An understanding of the impact on alloying element vaporization and metal expulsion during the formation of laser fired contacts is critical to understand how Al and Si are contained within the melt during processing.

Many recent experiments for electronic and photonic materials (particularly Si) have focused on laser ablation. Although ablation is outside the scope of this thesis, ablation is observed in processing of laser-fired contacts with extremely short pulse durations. Ablation is associated with the rapid ejection of large particles from the melt. The selection of laser processing parameters, such as irradiance (or power density distribution), pulse shape, wavelength and fluence, influence the extent of ablation. Both Yoo *et al* [26] and Lim *et al* [28] demonstrated that explosive (homogeneous) boiling in Si is the dominant mechanism for mass removal above a certain energy density threshold (10^{10} - 10^{11} W/cm^2) for wavelengths of 266 nm and 1064 nm. These thresholds will be highly dependent on material properties and the material systems under consideration. As the material is heated above the boiling point, a transparency layer forms that permits the laser irradiation to superheat the liquid layer below it. As the liquid layer approaches the critical temperature, the vapor phase present below the transparency layer can act as nucleation sites for bubbles, which will expand rapidly and cause the expulsion of micron-sized particulates.

Experiments by Yoo *et al* [26] demonstrated that ablation begins above the homogeneous boiling temperature, which is defined as approximately 90% of the critical temperature [27]. Homogeneous nucleation requires the formation of vapor nuclei, which occurs as the liquid temperature approaches the critical temperature and the probability of the stable vapor nuclei formation increases. However, the relationship between the temperature fields and laser processing parameters is not known, especially at temperatures that are much greater than the boiling point of the material. Conditions for laser ablation require the presence of a free surface, confinement of the molten material in the lateral direction, and large spatial and temporal variations of temperature and pressure.

These highly non-uniform and non-equilibrium conditions make the understanding of the connection between the ablation threshold and temperature dependence for homogeneous nucleation complicated. Heterogeneous nucleation of vapor particles, on the other hand, requires the presence of pre-existing vapor nuclei within the liquid material, such as gas bubbles or vapor-filled cavities at the fusion boundary or surfaces. Although heterogeneous nucleation is a much more thermodynamically favorable condition, Miotello *et al* [72] showed that with sufficiently short pulses on the order of nanoseconds or less,

heterogeneous boiling cannot be a dominant process for mass removal since a large temperature difference between the vapor and melt does not exist [72].

The threshold temperatures, which can be related to the laser processing parameters to predict heterogeneous and homogeneous boiling, are different. Heterogeneous boiling occurs at temperatures slightly above the melting point, whereas homogeneous boiling occurs closer to the critical temperature [27]. Due to short processing times, the temporal and spatial variation temperatures of the molten Si pool as a function of laser processing parameters have not been properly investigated. By calculating these temperatures, relationships between the driving forces for observance of ablative behavior and processing parameters can be determined. In order to predict vaporization and metal expulsion, it is important to get accurate estimations of the surface temperatures on the molten pool. In order to do this, various methods of numerical simulations can be employed.

2.4 Mathematical Modeling to Understand Laser Processing

2.4.1 Temperature and Velocity Fields

High energy density processes, such as electron or laser beam welding, are associated with extremely high temperatures and fluid flow rates. The temperature and velocity fields in these high energy density processes have been shown to dramatically influence the final weld geometry, microstructure, composition, and mechanical properties of the weld [73,75,76]. Reliable experimental measurements of the temperatures and velocities within the molten pool during laser firing of contacts or laser spot welding can be extremely difficult to obtain due to the highly transient nature of the process. Several researchers [77-80] have utilized methods to measure the temperature and velocity field fluid during steady-state arc and linear laser welding processes.

Farson *et al* [77] utilized infrared (IR) optical pyrometry measurements in conjunction with thermocouples to sense and quantify the base metal temperatures during welding. However, due to the significant arc and electrode radiation interference with the IR temperature measurements, it was not possible to accurately determine the temperature at the center of the weld pool even with the use of various optical filters. Numerous other researchers [78-80] have utilized IR sensing of temperature along the top face of a weld pool for tailoring weld pool geometry during processing. Despite success with process monitoring applications, the inability to precisely know the emissivity of the molten material, which itself is highly temperature and phase-dependent, makes accurate determination of molten pool temperatures extremely difficult. In the cases for arc welding and laser linear welding, the welding has often reached a steady-state condition during process monitoring, which allows for more time to process

and sense the changes in surface temperatures. For highly transient welding conditions, such as laser spot welding, these methods will not be suitable for accurately determining molten pool temperatures.

Schauer *et al* [56] also utilized infrared radiation pyrometry to measure the temperature distributions during keyhole formation when electron beam welding several different Al, steel and tantalum alloys. They were able to able to correlate peak temperatures within the melt pool to the different material systems to estimate the impact of changes in processing parameters on temperature. Kraus [81] utilized a non-contact laser reflectance measurement technique to determine the surface temperature profiles during Gas Tungsten Arc Welding (GTAW) of various steels. However, the pool temperatures were extrapolated from temperature/time data obtained after the arc was extinguished, assuming a transient temperature profile [65]. In terms of extracting fluid flow velocities from the molten pool, Heiple and Roper [82] utilized high speed video to track the motion of particles within the melt to estimate surface flow velocities during GTAW. The size of the weld associated with arc welding and the steady-state nature of the processes has provided a means to utilize various techniques to measure temperature and fluid flow with a molten pool. However, laser spot welding is highly transient and these types of methods are not able to provide an accurate estimation of the temperatures and velocities within the pool. Therefore, in the absence of reliable, cost-effective experimental methods, numerical simulation has been used.

Over the past twenty years, various groups have utilized mathematical models to understand the heat transfer and fluid flow behavior associated with arc and laser welding. Using these models, accurate calculations of molten pool temperatures and velocities have allowed researchers to predict the microstructural evolution of a material during processing. Furthermore, with the advancement of computational hardware and software, data can be obtained relatively quickly and validated with experimental measurements. A number of transport phenomena based models have been developed to determine temperature and velocities fields during laser welding by simultaneously solving the governing equations for mass (2.10), momentum (2.11) and energy (2.12):

$$\frac{\partial \rho}{\partial t} + \frac{\partial (\rho u_i)}{\partial x_i} = 0 \tag{2.10}$$

$$\rho \frac{\partial \left(\rho u_j \right)}{\partial t} + \rho \frac{\partial \left(\rho u_i u_j \right)}{\partial x_i} = \frac{\partial}{\partial x_i} \left(\mu \frac{\partial u_j}{\partial x_i} \right) + \frac{\partial p}{\partial x_i} + S_{ui} \tag{2.11}$$

$$\rho \frac{\partial (\rho h)}{\partial t} + \rho \frac{\partial (\rho u_i h)}{\partial x_i} = \frac{\partial}{\partial x_i} \left(\frac{k}{C_p} \frac{\partial h}{\partial x_i} \right) + S_h \qquad (2.12)$$

where ρ is the density, u_i is the velocity component in the i, j, of k direction, μ is the effective viscosity of the liquid, k is the thermal conductivity, C_p is the specific heat, and h is the sensible heat, S is a source term, and t is the time.   Cline and Anthony [83] utilized a heat conduction model not considering convective heat transfer to study the effects of laser spot size, welding velocity and laser power level on the temperature profiles within the melt pool, surface rippling effects, the cooling rate and the depth of penetration during laser welding of 304 Stainless Steel. Frewin and Scott [84] utilized finite element modeling of heat transfer under pulsed laser beam welding. Using their model, they were able to calculate transient temperature profiles and dimensions of the fusion zone and heat affected zone [84]. Bennett, *et al* developed a numerical model to understand the fluid flow dynamics associated with the use of extremely short nanosecond pulses when laser texturing of magnetic, Ni-P disks to demonstrate that a competition between the Marangoni surface tension and compositional gradient driven flow resulted in various types of surface morphologies [85].

Within the field of laser spot micro-welding, He *et al* [73] utilized a finite difference model based on the control volume method [86] to accurately predict fusion zone geometries of various weldments. They also demonstrated the influence that changes in laser process parameters, such as pulse duration and power, have on the solidification microstructure. In addition, they used numerical simulations to accurately predict thermal cycles within different portions of a laser-spot weld, as shown in Figure 2.10. The numbers on the figure represent various locations on the top surface (Figure 2.13(a)) and within the cross-section of the weld (Figure 2.13(b)) where the temperatures have been calculated. Basu and DebRoy [87] evaluated the conditions during laser micro-welding that would lead to significant increases in temperature fields and metal expulsion within a laser weldment experimentally and theoretically for a number of pure materials and calculated the critical radius for metal expulsion.

Semak, *et al* [88] demonstrated that the impact of extremely high energy densities associated with laser welding on a small, micron-sized weld pool can significantly alter the fluid flow rates and melt hydrodynamics due to high temperatures within the melt. High molten pool temperatures can lead to rapid deviation from purely conduction-mode welding behavior. Blecher *et al* [58] utilized laser welding methodologies and numerical simulations to analyze the influence that changes in laser processing parameters have on the heat transfer and mass transfer dynamics in a molten pool. They demonstrated that changes in the laser welding velocity and power levels can drastically impact temperature profiles

and fluid flow velocities and ultimately influence the extent of phosphorus doping that can be achieved within a molten Si pool.

A number of important findings have been uncovered about the influence of changes in laser processing parameters on temperature and velocity fields through numerical simulations, which have been related to microstructural evolution during processing and the resulting mechanical properties. Numerical, transport phenomena-based models provide a means to correlate the calculated data to real-world phenomenological behavior. In considering the formation of LFCs, these models can be applied to study the evolution of contact geometry as a function of laser processing parameters. Since contact geometry has been shown to strongly influence device performance [30,33], the use of numerical modeling to understand this phenomena will be a valuable tool.
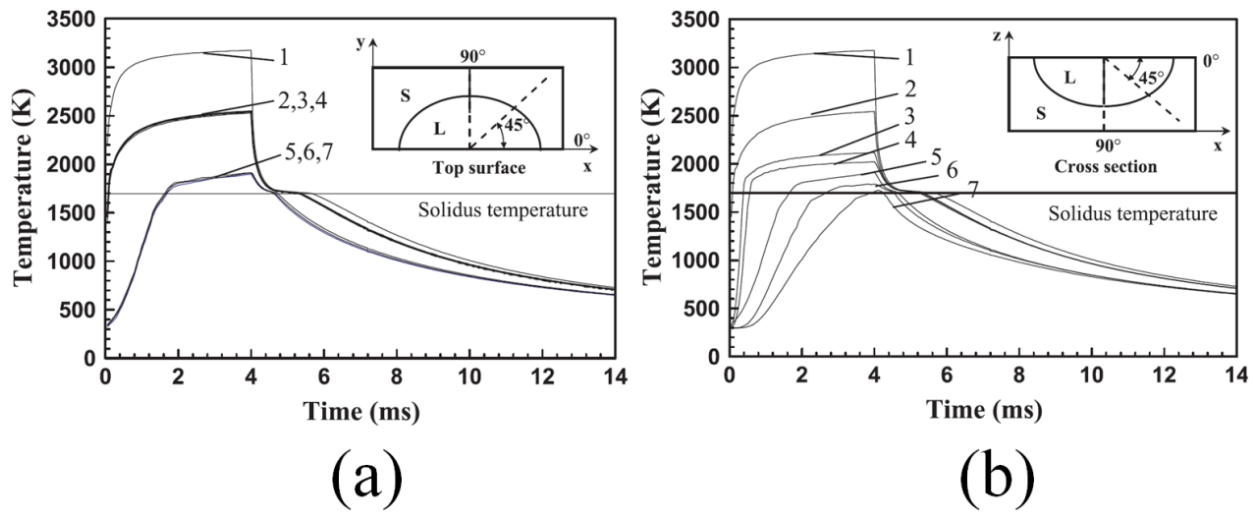
Figure 2.13. Thermal cycles calculated through numerical simulations for a laser spot weld (a) on top surface at various locations and (b) within weld pool. Locations identified here [70].

2.4.2 Relative Importance of Driving Forces

In order to understand the relative importance that various forces have on the heat transfer and fluid flow within a molten pool, a number of dimensionless numbers have been used [73]. These dimensionless numbers have been used to evaluate the influence that surface tension and buoyancy have on the size of the molten pool during laser processing and to determine the size of the fusion zone and heat affected zone of various weldments.

The Grashof number, Gr, is a ratio of the buoyancy force to the viscous force and can be calculated as:

$$Gr = \frac{g\, \beta\, L_b^3\, \Delta T\, \rho^2}{\mu^2}$$

(2.13)

where L_b is the characteristic length for the buoyancy force in the liquid pool and is approximated as one-eighth the length of the pool radius [74], ΔT is the temperature difference between the peak temperature within the molten pool and the solidus temperature, μ is the viscosity of the liquid material, and all other terms have been previously defined.

The surface tension Reynolds number, Ma, describes the ratio of the surface tension gradient force to the viscous force and is calculated as:

$$Ma = \frac{\rho\, L_R\, \Delta T\, \frac{\partial \gamma}{\partial T}}{\mu^2}$$

(2.14)

where L_R is the characteristic length of the weld pool and is assumed to be equal to half of the weld pool width. Using the dimensionless Ma number, He *et al.* [73] demonstrated that in laser spot welding of a 304 stainless steel with micron sized beam diameters and high power densities, that the surface tension force will be two orders of magnitude greater than the viscous force.

The relative importance of the buoyancy force and surface tension force can be conceptualized by combining the Equations (2.13) and (2.14) in the following form, $R_{s/b}$:

$$R_{s/b} = \frac{Ma}{Gr}$$

(2.15).

Using this dimensionless number, He *et al.* [73] also demonstrated that in laser spot welding over millisecond pulse durations that the surface tension force will be five orders of magnitude greater than the buoyancy force. In order to estimate the influence of convection on LFC formation, a back-of-the-envelope calculation of $R_{s/b}$ for molten Si based on LFC sizes observed in the literature [43,44] can be performed. Taking ρ as 2.51 g/cm^3, $d\gamma/dT$ as -0.13 mN/m, β as 2.1 x 10^{-5}/K, ΔT as 1000K, and L_R as 35 μm, $R_{s/b}$ is calculated as approximately 1 x 10^8. Therefore, it can be expected that the liquid flow will be driven mainly by Marangoni convection and the influence of the buoyancy force will be minimal. In order to develop a more comprehensive understanding of the LFC process over these short pulse durations and small length scales, it will be important to evaluate the forces that are competing within the molten pool to understand the heat and mass transfer dynamics during laser processing.

2.4.3 Heat Transfer and Mass Transfer

The mode of heat transfer within the molten pool can influence the size of the LFC while the mode of mass transfer can influence how Al is distributed throughout the molten region. Heat is transported throughout a melt pool by heat conduction and convection driven by fluid flow. The mechanism of heat transport within the weld pool will determine the width and depth of the pool [89]. In general, heat transport dominated by convection leads to a wider and shallower molten pool compared to transport by conduction, which produces more hemispherical pools.

In order to gauge the influence of factors on weld pool evolution, it is important to evaluate the relative importance of each mechanism, which can be done using the heat transfer Peclet number, Pe_h:

$$Pe_h = \frac{heat\ convection}{heat\ conduction} = \frac{u\,\rho\,C_p\,\Delta T}{k\,\Delta T/L_R} = \frac{u\,\rho\,C_p}{k} \tag{2.16}$$

where u is the average velocity, L_R is the characteristic length taken as the melt pool radius along the top surface, k is the thermal conductivity and all other terms have been previously defined. When the value for Pe_h is large, then heat transfer by convection dominates within the melt pool. When the value of Pe_h is small, however, then heat transport is driven by conduction [90]. Using this relationship, He $et\ al$ [73] demonstrated for laser spot welding of stainless steel that the Pe_h number increases significantly over the course of a 4 ms pulse as shown in Figure 2.14. It was shown that at the beginning of the pulse, heat transfer is driven by conduction, which leads to slower growth of the molten pool. As convective heat transfer becomes more dominant over the course of the pulse, the molten pool grows at a much higher rate.

A back-of-the-envelope calculation for Si material properties reveals that Pe_h should be approximately 90 when assuming u is 200 cm/s, k is 1.2 cal s^{-1} cm^{-1} K^{-1}, and C_p is 0.217 cal g^{-1} K^{-1}. Depending on the temperature gradients within the pool, which will be influenced by the spatial variation of temperature over the extremely small molten pool size, the value of u can change significantly. In addition, since LFCs are processed with much shorter pulses (microseconds or shorter versus milliseconds used here) and higher energy densities, it is unclear how heat transfer will be affected. Furthermore, since the contact resistance is often related to the size of a contact [30,91], determining LFC size over the course of processing with short pulses will be critical for further development of the process.
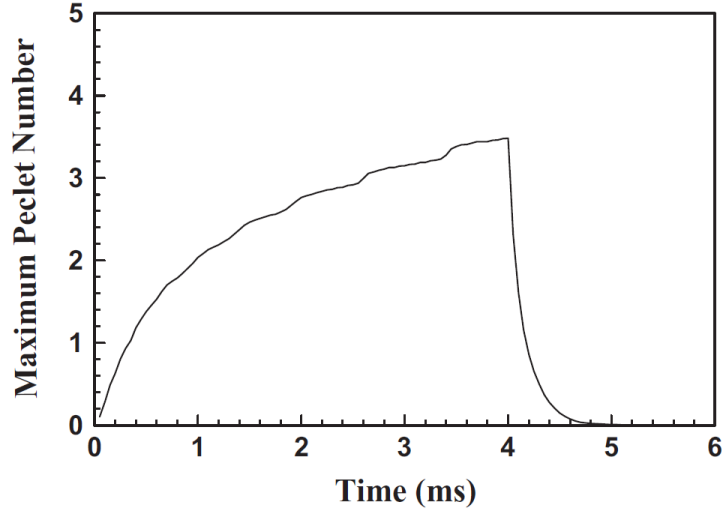
Figure 2.14. Variation in Pe_h number with time during laser spot welding of Stainless Steel using laser power of 530 W, 4 ms pulse duration and beam radius of 0.159 mm [54].

In the processing of LFCs, Al needs to be incorporated into the molten Si to form a contact. Therefore, it is also important to evaluate the relative influence that convection and diffusion will play on mass transfer. Convection driven fluid flow moves a dopant atom, such as Al, throughout the molten metal. Diffusion driven mass transfer, on the other hand, involves the random motion of atoms through the bulk and is affected by a concentration gradient in the bulk. Similar to heat transfer, a dimensionless mass transfer Peclet number, Pe_m, has been defined to understand the relative importance of mass transfer by diffusion and convection. The mass transfer Pe_m number can be calculated using the following equation:

$$Pe_m = \frac{mass\,convection}{mass\,diffusion} = \frac{u\,L_R}{D} \tag{2.17}$$

where D is the diffusion coefficient and all other terms have been previously defined. If Pe_m is greater than unity, then mass transfer is dominated by convection. If Pe_m is less than unity, then diffusion will be the primary mass transfer mechanism. Blecher *et al* [57,58] used numerical simulations of heat transfer and fluid flow to understand the relative importance of mass transfer by convection and diffusion when laser doping Si wafer with phosphorus to create selective emitters. The influence of variations in laser processing parameters, such as travel speed and laser power, was evaluated to determine the factors that influence dopant profiles within a melt pool. Figure 2.15(a) [57] shows a calculated dopant distribution for an emitter processed with 15 W laser power at a travel speed of 4 m/s where the concentration contours represent a fraction of the initial surface concentration, which was 2.7 x 10^{16} atoms/mm^3.

38

Figure 2.15(b) shows a plot [58] of the mass transfer Pe_m number plotted as a function of travel speed for various powers. Increases in power caused significant increase in convective mass transfer while a reduction in travel speed had a similar impact. A calculation of Pe_m for Si reveals that its value should be approximately 7000 when assuming a mass diffusivity for Al in Si on the order of 1 x 10^{-4} cm^2/s [58], suggesting that mass transfer will be dominated by convection rather than diffusion. However, an accurate determination of the Pe_m value will be highly dependent on the molten pool size and fluid flow velocities, which are highly dependent on the processing parameters. The use of the dimensionless quantities, Pe_h and Pe_m, will be important to understand how Al is distributed within the Si. Furthermore, since the process considered here was for steady-state laser doping, it will be necessary to consider the transient nature of laser firing to understand the influence that temporal variations in velocity and temperature have on heat transfer and mass transfer.

(a) (b)
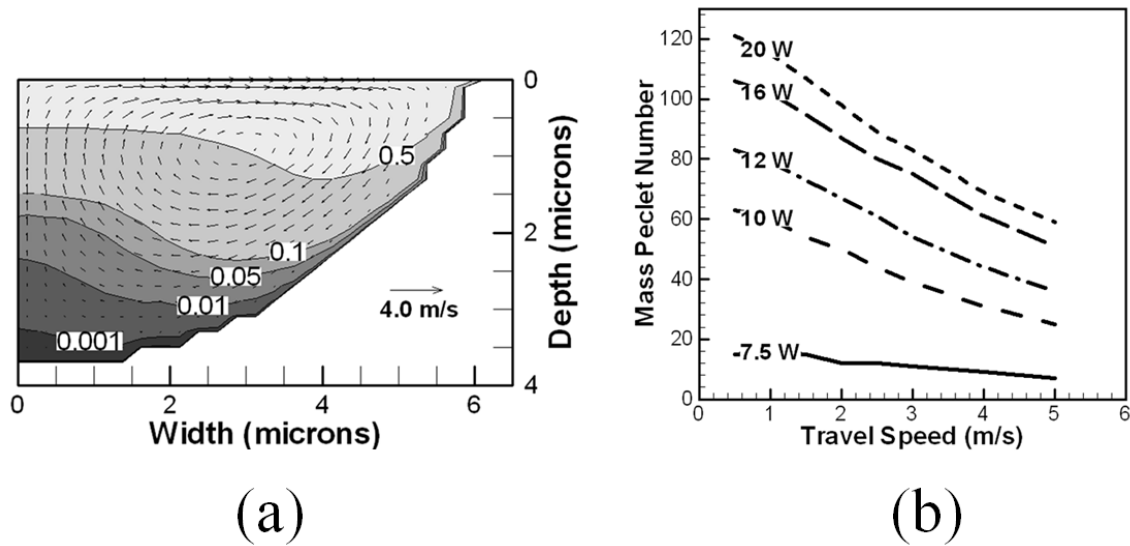
Figure 2.15. (a) Phosphorus dopant concentration profile when laser doping Si at 15 W laser power and 4 m/s travel speed, values represent fraction of surface concentration, 2.7 x 10^{16} atoms/mm^3 and (b) Pe_m versus travel speed and laser power.

2.4.4 Solidification Behavior

LFCs form due to the mixing of Al and Si. However, a laser-fired contact is different from other laser spot welding situations in that the Al layer is not alloyed with the Si prior to laser processing. Therefore, during the course of processing and as Al is mixed into the molten pool, the influence that its presence has on solidification has not been studied. Numerical simulations provide a method to understand how variations in transport phenomena during high energy density welding affect solidification behavior. Several [57,92-95] groups have utilized heat transfer and fluid flow models to understand the influence that changes in laser processing parameters have on solidification behavior for various alloy systems. Rai

et al [92,93] calculated the temperature gradient (G), solidification rate (R), the cooling rate (GR), and the solidification morphology parameter (G/R) at the trailing edge of a weld pool for titanium, vanadium and stainless steel alloys to predict changes in solidification behavior when changing laser processing parameters. Blecher *et al* [94] also calculated these parameters to predict solidification morphologies during keyhole mode laser welding on Alloy 690, a high chromium nickel base alloy and determine a critical G/R parameter to predict the transition from cells to dendrites within various regions of a weld. These studies, however, were focused on keyhole mode welding whereas a laser-fired contact should be a conduction mode weld to avoid significant penetration and damage to the crystalline Si wafer.

Tan *et al* [95] calculated temperature fields during conduction mode laser spot welding of a 304 stainless steel to calculate various solidification characteristics, such as morphology and grain growth direction. They combined phase field modeling with cellular automata to identify grain density and dendrite arm spacing at the fusion line and demonstrated the influence of different cooling rates within various regions of the molten pool on grain structure. He *et al* [55,73] extensively analyzed the influence of laser processing parameters on solidification behavior during laser spot welding of a 304 stainless steel. They calculated various solidification parameters, such as G, R, GR and G/R at the interface between the liquid and the two-phase region to understand how these values change at various locations within a weld pool to influence final morphology.

Figure 2.16 shows a series of plots for G, R, GR and G/R as a function of time during cooling that were calculated for a weld produced with 530 W laser power, a 4 ms pulse duration, and a 159 μm beam radius. It was shown that the value of G/R decreases from the fusion line to the weld centerline, which suggested a change in solidification morphology from a cellular microstructure at the fusion line to cellular-dendritic microstructures closer to equiaxed-dendrites at the pool center. In addition, they showed that the morphologies that are present will vary along the top surface as opposed to through the center from the bottom of the weld. In these cases, however, the material system was a multi-crystalline, homogeneous alloys versus that of an LFC. Laser spot micro-welding of an Al-Si contact requires melting of a single crystal Si and then the incorporation of Al into the molten region. Therefore, it is unclear how the presence of Al in the Si will influence the solidification of the fusion zone and the potential implications on device performance.
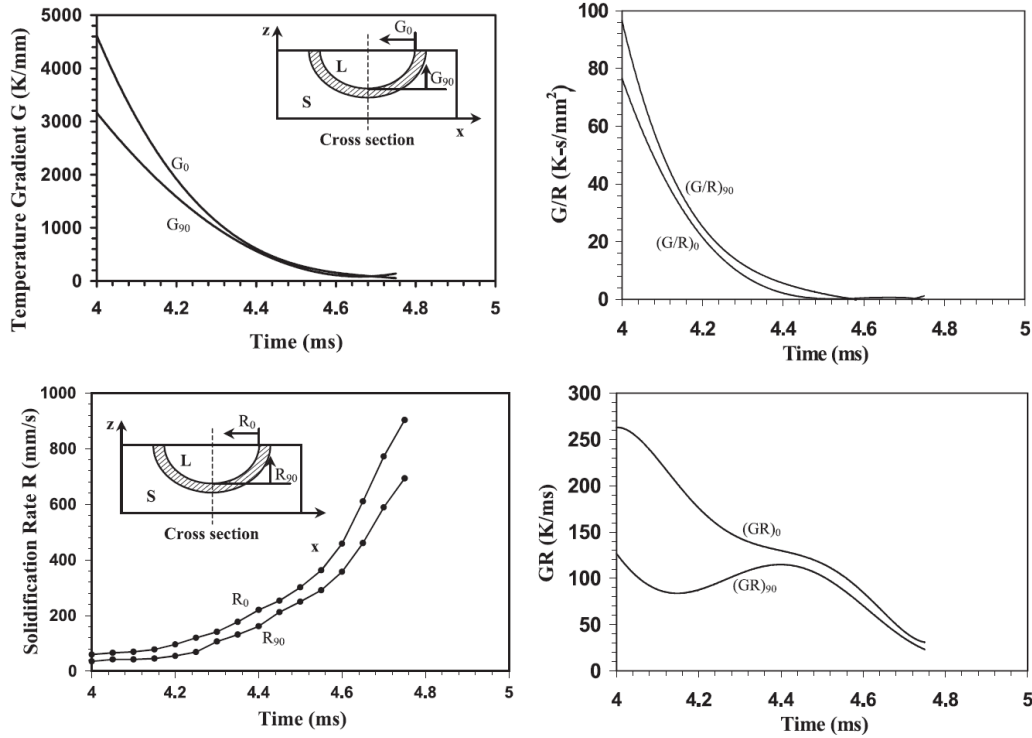
Figure 2.16. G, R, G/R and R plots for laser spot weld on 304 SS using 530 W laser power a 4 ms using a 159 μm beam radius.

2.4.5 Vaporization and Expulsion

The vaporization and expulsion of Si and Al during laser processing is important to consider during LFC formation. A number of groups have utilized computational methods to understand how changes in laser processing parameters impact vaporization and metal expulsion [59,62,68,96]. Mundra and DebRoy [59] calculated the vaporization rate during laser welding using the Langmuir Equation and compared their simulated results with experimental data to determine that the calculated vaporization rate is significantly higher than what is experimentally observed. Theoretical approaches have also been used by other researchers to investigate this behavior [97-100].

Aden *et al* [97] investigated the laser-induced vaporization from the surface of an irradiated material by a Nd:YAG laser. They identified a critical laser intensity above which expansion of the escaping vapor no longer occurs. However, the model did not account for convective heat transfer within the molten pool, which can have a significant impact on surface temperatures during laser processing [64]. Dilthey *et al* [98] studied the vaporization of alloying elements from the surface of a melt pool during laser keyhole mode welding by analyzing the diffusion of alloying elements from the interior to the surface of the melt pool and subsequent vaporization, but did not consider the influence of condensation. In order overcome these shortcomings, researchers [56,92] have developed laser-induced vaporization

models that account for vapor temperature, density, velocity and the extent of condensation based on derivations by Anisimov [99] and Knight [100].

Previous micro-joining work has shown that small changes in the laser processing parameters significantly affect the molten pool geometry, temperature profiles, the evaporation rates of compositional elements and the occurrence of metal droplet ejection [42,64]. He *et al* [64] used these models to understand the impact that vaporization has on compositional changes in the molten material during laser spot welding of a 304 stainless steel. Using electron microprobe analysis, they studied the concentration of vaporized particulates and used these values to validate calculated temperatures. Using the validated model, they demonstrated that the temperatures within the center of the molten material can often exceed the boiling point of the material depending on the power density and pulse duration. Furthermore, the extent of vaporization will increase significantly as the power density is increased, since the peak temperatures at the center of the pool will increase exponentially. They also predicted the vaporization rates and change in weld metal composition with good agreement. By predicting these compositional variations, it was possible to understand how mechanical and microstructural properties evolved during laser processing. Compositional variations in contact formation may influence device performance and numerical models will provide a means to evaluate these changes.

Researchers have also used computer simulations to understand the influence that laser processing parameters have on liquid-metal expulsion. Using experimental methods and numerical modeling, Basu and DebRoy [87] used a combination of experiments and calculations to demonstrate that vaporization and liquid metal expulsion take place when the vapor recoil pressure exceeds the surface tension force of the molten metal at the periphery of the weld pool. Additional simulations of laser-spot microwelding [71] have utilized the results from Semak and Matsunawa [101], where the role of recoil pressure in the energy balance during materials processing was analyzed. Figure 2.17 shows various results generated for numerical simulations that demonstrate the impact of changes in processing parameters, such as pulse duration, laser beam power and beam size, on metal expulsion. Figure 2.17(a) and Figure 2.17(b) show two plots for recoil pressure and surface tension as a function of time during laser spot welding of a 304 stainless steel [71]. The plots were generated when spot welding with 1967 W laser power and a 3 ms pulse using various beam sizes. Figure 2.17(a) corresponds to a beam size of 0.835 mm whereas Figure 2.17(b) corresponds to a beam size of 0.651 mm. He *et al* [71] demonstrated that by decreasing the beam size less than 20%, the high peak temperature can increase significantly and cause the recoil force to exceed the surface tension during laser welding. As a result, metal expulsion can be predicted from the melt pool.

Figure 2.17(c) shows the relationship between power density and pulse duration for laser spot welding of 304 stainless steel [71]. The points on the graph represent experimental results and the solid line represents the critical power density at which expulsion begins. For a given pulse duration an increase in the power density leads to intermittent or heavy expulsion. Both the calculated and experimental results show that metal expulsion can take place at a lower critical power density with an increase in the pulse duration. An increase in power density caused a significant increase in temperature fields. As the temperature exceeded the boiling point, vaporization of alloying elements occurred due to pressure and concentration gradients. Longer pulse durations provide more time for the interaction between the laser and the substrate, which lead to higher weld pool temperatures and higher recoil pressures. Predicting the threshold levels for metal expulsion during laser processing of LFCs can help prevent loss of Al and Si during processing. However, as a particular energy density threshold is reached, more advanced ablation of the substrate is observed and the mechanisms change that drive the laser-material interaction behavior.
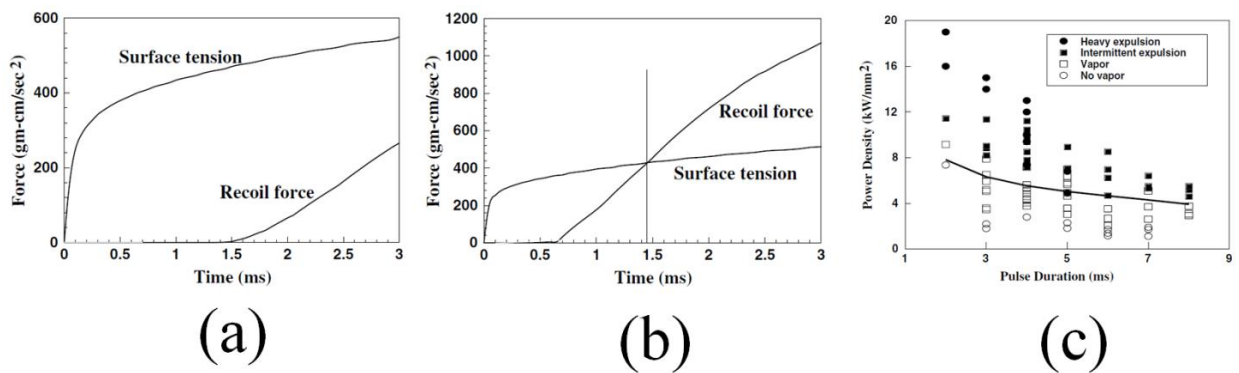
Figure 2.17. Recoil and surface tension force versus time for laser weld processed with 1967 W power, 3 ms pulse and (a) 0.651 mm, (b) 0.835 mm beam diameters; and (c) Vaporization and expulsion threshold levels for various processing parameters.

2.5 Summary

Laser-fired contacts on the PERC structure have been traditionally generated with nanosecond pulses despite significant ablation and loss of the Al metallization, which makes direct contact between the metallization and Al-doped Si semiconductor difficult. The use of longer millisecond pulse durations has demonstrated that larger LFCs can be generated without significant loss of alloying elements. Furthermore, millisecond pulses are likely too long to meet throughput requirements. Therefore, one area that needs to be investigated is the use of microsecond pulses to form laser fired contacts without significant metal expulsion while obtaining a low-resistance contact. In particular, it is of critical importance to determine the impact of laser processing with microsecond pulse durations on the passivation layer quality, the formation of crystalline defects, and the size of the contacted regions.

Minimizing damage to the passivation layer and crystalline Si wafer is necessary to maintain performance benefits that have been realized with point-contacted structures that utilize LFCs. In order to understand the impact of laser processing on the contacting process, further experimentation is required to characterize Al doping within the Si, the degradation of the passivation layer, and damage to the crystalline wafer under microsecond pulse durations.

Since the laser-firing process is highly transient with pulse durations are on the order of tens to hundreds of microsecond, cost-effective experimental methods are not available to accurately predict substrate temperatures, fluid flow velocities, and the evolution of contact geometry as a function of processing parameters. The large temporal and spatial variations of temperature of the extremely small LFC size will have a significant impact on the heat and mass transfer behavior during contact formation. Since contact geometry has been shown to have a large impact on device performance metrics, such as the effective rear surface recombination rates, tailoring geometry through the appropriate selection of processing parameters is a critical need. Therefore, numerical methods must be employed to develop a more comprehensive understanding of the mechanism governing LFC formation to optimize the process. By leveraging computer simulations, a more comprehensive understanding of the LFC formation process can be made to add to the body of knowledge currently available.

2.4 References

1. S.J. Fonash Solar cell device physics. 2nd ed. Burlington, MA: Academic Press/Elsevier; 2010.
2. S.O. Kasap, P. Capper. Springer handbook of electronic and photonic materials. New York, NY: Springer; 2006.
3. E.V. Kerschaver, G. Beaucarne, Back-contact solar cells: A review, Progress in Photovoltaics Research Applications 14(2), 2006, pp 107-23.
4. http://www.comerfordsolar.com/basics.html
5. S.W. Glunz, New concepts for high-efficiency silicon solar cells, Solar Energy Materials and Solar Cells 90 (18-19), 2006, pp 3276-84.
6. M. Hofmann, S. Janz, C. Schmidt, S. Kambor, D. Suwito, N. Kohn, J. Rentsch, R. Preu, S.W. Glunz, Recent developments in rear-surface passivation at Fraunhofer ISE, Solar Energy Materials and Solar Cells 93 (6-7), 2009, pp 1074-8.
7. A.W. Blakers, A. Wang, A.M. Milne, J. Zhao, and M.A. Green, 22.8% efficient silicon solar cell, Appl. Phys. Letters (55), 1989, pp 1363-1365.
8. E. Urrejola, K. Peter, H. Plagwitz, G. Schubert, Silicon diffusion in aluminum for rear passivated solar cells, Appl. Phys. Letters 98, 2011. #153508.

9. K. Muller, R. Borges. Simulation in photovoltaics: From solar cells to full-scale arrays. Solar Industry Magazine 1(10), 2010.

10. B. Hoex, S.B.S. Heil, E. Langereis, M.C.M van de Sanden, W.M.M. Kessels, Ultralow surface recombination of c-si substrates passivated by plasma-assisted atomic layer deposited Al_2O_3, Appl. Phys Letters 89 (4), 2006. #042112.

11. O. von Roos, A simple theory of back-surface-field (BSF) solar cells. J. Appl Phys 50 (8), 1979, pp 5371-5374.

12. U. Zastrow, L. Houben, D. Meertens, A. Grohe, T. Brammer, E. Schneiderlöchner, Characterization of Laser-Fired Contacts in PERC Solar Cells: SIMS and TEM Analysis Applying Advanced Preparation Techniques. Applied Surface Science 252, 2006, pp 7082–7085.

13. J. Zhao, A. Wang, P.P. Altermatt, S.R. Wenham, M.A. Green. 24% Efficient PERL silicon solar cell: recent improvements in high efficiency silicon cell research, Solar Energy Materials and Solar Cells, 1996, pp 87-99.

14. E. Schneiderlochner, R. Preu, R. Ludemann, S.W. Glunz, Laser-fired rear contacts for crystalline silicon solar cells, Prog. in Photovoltaics 10, 2002, pp 29-34.

15. B. Sopori, V. Mehta, d. Guhabiswas, R. Reedy, H. Moutinho, B. To, A. Shaikh, A. Rangappan, Formation of a back contact by fire-through process of screen-printed solar cells, IEEE, 2009. pp 1963-1968.

16. P. Stallhofer, Why are silicon wafers as thick as they area?, Ultra-thin chip technology and applications, 2011, pp 3-12. DOI: 10.1007/978-1-4419-7276-7_1.

17. C. Canizo, G. Coso, W.C. Sinke. Crystalline silicon solar module technology: Towards the 1€ per watt-peak goal, Prog. in Photovoltaics 2009; 17: pp. 199–209, DOI: 10.1002/pip.878.

18. K.L. Chopra, P.D. Paulson, V. Dutta. Thin film solar cells: an overview, Prog. in Photovoltaics 2004; 12: pp. 69–92, DOI: 10.1002/pip.541.

19. S. Wang, A. Lennon, B. Tjahjono, L. Mai, B. Vogl, Wenham, S., Overcoming over-plating problems for PECVD SiNx passivated laser doped p-type multi-crystalline silicon solar cells, Solar energy materials and solar cell 2012; 99, pp. 226-234, DOI: 10.1016/j.solmat.2011.12.003

20. W. Brendle, V.X. Nguyen, A. Grohe, E. Schneiderlochner, U. Rau, G. Palfinger, J.H. Werner, 20.5% efficient silicon solar cell with a low temperature rear side process using laser-fired contacts, Prog. In Photovoltaics Research Applications 14(7), 2006, pp 653-62.

21. D. Suwito, U. Jager, J. Benick, S. Janz, M. Hermle, S.W. Glunz, Industrially feasible rear passivation and contact scheme for high efficiency n-type solar cells yielding a V_{OC} of 700 Mv, IEEE Transactions on Electron Devices 57(8), 2010, pp 2032-36.

22. R. Preu, E. Schneiderlöchner, A. Grohe, S.W. Glunz, G. Willeke. Laser-Fired Contacts - Transfer of a Simple High Efficiency Process Scheme to Industrial Production. Photovolt. Spec. Con.: Conf. Record of the Twenty-Ninth IEEE. 29, 2002, pp 130-133.

23. O. Schultz, S.W. Glunz, G.P. Willeke, Multicrystalline Silicon Solar Cells Exceeding 20% Efficiency. Prog. In Photovolt.: Research and Apps. 12, 2004, pp 553.

24. A. Grohe, B. Fleischhauer, R. Preu, S.W. Glunz, G.P. Willeke, Boundary Conditions for the Industrial Production of LFC Cells. Conf. Record of the 2006 IEEE 4th World Conf. on Photovolt. Energy Conversion 1, 2006, pp 1032.

25. M. Tucci, E. Talgorn, L. Serenelli, E. Salza, M. Izzi, P. Mangiapane. Laser Fired Back Contact for Silicon Solar Cells, Thin Solid Films 516, 2008, pp 6767-6770.

26. J.H. Yoo, S.H. Jeong, R. Greif, R.E. Russo. Explosive Change in Crater Properties During High Power Nanosecond Laser Ablation of Silicon, J. Appl. Phys. 88(3), 2000, pp 1638-1649.

27. A. Miotello, R. Kelly. Laser-Induced Phase Explosion: New Physical Problems When A Condensed Phase Approaches the Thermodynamic Critical Temperature, Appl. Phys. A: Mat. Sci. and Proc. 69(7), 1999, pp S67-S73. DOI: 10.1007/s003399900296.

28. D.J. Lim, H. Ki, J. Mazumder, Mass Removal Modes in the Laser Ablation of Silicon by a Q-Switched Diode Pumped Solid-State Laser (DPSSL), J. Phys. D: Appl. Phys. 39, 2006, pp 2624-2635.

29. C. Molpeceres, M.I. Sanchez-Aniorte, M. Morales, D. Munoz, I. Martin, P. Ortega, M. Colina, C. Voz, R. Alcubillia, Influence of wavelength on laser doping and laser-fired contact processes for c-Si solar cells, Proc. Of SPIE 8473, DOI: 10.1117/12.929456.

30. P. Ortega, A. Orphella, I. Martin, M. Colina, G. Lopez, C. Voz, M.I. Sanchez, C. Molpeceres, R. Alcubilla, Laser-fired contact optimization in c-Si solar cell, Prog. in Photo. 2012, 20 (2): pp 173-180.

31. A. Grohe, U. Zastrow, D. Meertens, L. Houben, W. Brendle, G. Bilger, E. Schneiderlo¨chner, S.W. Glunz, R. Preu, G. Willeke, Progress in characterization pf laser-fired contacts, Proc. 20th European Photovoltaic Solar Energy Conference, Barcelona, (2005), p. 1158.

32. A. Grohe, E. Schneiderlochner, M. Hermle, R. Preu, S.W. Glunz, G. Willeke, S. Walz, Characterization of laser-fired contacts processed on wafers with different resistivity, Proceedings of the 3rd World Conference on Photovoltaic Energy Conversion 2, 2003, pp 1032-35.

33. D. Kray, S. Glunz, Investigation of laser-fired rear-side recombination properties using an analytical model. Prog Photovoltaics Research Application 2006; 14(3): pp 195-201.

34. F.A. Trumbore, Solid Solubilities of Impurity Elements in Germanium and Silicon, The Bell System Technical Journal, 1960, pp 205-233.

35. O. Krause, H. Ryssel, Determination of aluminum diffusion parameters in silicon, J. Appl. Phys 91(9), 2002, pp 5645-5649. DOI: 10.1063/1.1465501.

36. D.W. Cunningham, BP Solar International, Reaching Grid Parity Using BP Solar Crystalline Silicon Technology A Systems Class Application, DOE Award Number: DE-FC36-07GO17049.006.

37. I. Sanchez-Aniorte, R. Barrio, A. Casado, M. Morales, J. Carabe, J.J. Gandia, C. Molpeceres, Optimization of lase-rfiring processes for silicon-heterojunction solar-cell back contacts, Appl. Surf. Sci. 258, 2012, pp 9443-9446.

38. Z. Hua, E.W. Reutzel, E.W., L. Zou, Beam delivery techniques for laser fired contacts, ICALEO 2010, #M1101.

39. V. Schutz, A. Horn, U. Stute, High-throughput process parallelization for laser surface modification on Si-Solar cells: determination of the process window, Proceedings of SPIE Vol. 8244 (2013).

40. X. He, J.W. Elmer, T. DebRoy, Heat transfer and fluid flow in laser microwelding, J. Appl. Phys. 97, 2007, DOI: 10.1063/1.1873032.

41. X. He, T. DebRoy, P.W. Fuerschbach, Alloying element vaporization during laser spot welding of stainless steel, J. Phys. D.: Appl. Phys, 36, 2003, pp 3079-3088, DOI: 10.1088/0022-3727/36/23/033.

42. V.V. Semak, G.A. Knorovsky, D.O. MacCallum, On the possibility of microwelding with laser beams, J. Phs. D: Appl. Phys. 36, 2003, pp 2170-2174.

43. B. DeCesar, Investigation of process parameter optimization of laser-fired back contact silicon solar cells, M.S. Thesis, Penn State University, 2011.

44. B. Hedrick, Characterization of laser fired contacts, laser doped emitters, and fixed charge passivation for improved silicon solar cells, M.S. Thesis, Penn State University, 2011.

45. W. M. Steen, *Laser Material Processing*, Springer 2003.

46. J. Mazumder and W. M. Steen, Heat transfer model for cw laser material processing, J. Appl. Phys., 51, 1980, pp 941.

47. A. E. Siegman, *Lasers*, University Science Books, Sausalito, CA. 1986.

48. W. W. Duley, *Laser Processing and Analysis of Materials*, Plenum Press, New York and London, 1983.

49. S. Kou, Welding Metallurgy, 2nd ed., John Wiley & Sons, Inc., 2003.

50. C. L. Chan, R. Zehr, J. Mazumder and M. M. Chen, Three-Dimensional Model for Convection in Laser Weld Pool, In: B. Kuo, R. Mehrabian (eds), Proceedings of the 3rd Engineering Foundation conference on modeling and control of casting and welding processing TMS-AIME, Warrendale, pp 229-246, 1986.

51. M.A. Bramson, *Infrared Radiation: a Handbook for Applications*, Plenum Press, New York, 1968.

52. J.F. Ready, editor, *LIA Handbook of Laser Materials Processing*, Magnolia Publishing, Inc., 2001.

53. J. Xie and A. Kar, Laser welding of thin sheet steel with surface oxidation, Weld. J., 78, 343s (1999).

54. S. B. Boyden, Y. W. Zhang, Journal of Thermophysics and Heat Transfer 20 (1), 9-15 (2006).

55. X. He, Heat transfer, fluid flow and mass transfer in laser welding of Stainless Steel with small length scale, PhD Thesis, Pennsylvania State University, 2006.

56. D. A. Schauer, W. H. Giedt and S. M. Shintaku, Electron beam welding cavity temperature distributions in pure metals and alloys, Weld. J., 57, 1978, pp 127s.

57. J.J. Blecher, T.A. Palmer, T. DebRoy, Laser-silicon interaction for selective emitter formation in photovoltaics, I. Numerical model and validation, J. Appl. Phys. 112, 2012. #114906.

58. J.J. Blecher, T.A. Palmer, E.W. Reutzel, T. DebRoy, Laser-silicon interaction for selective emitter formation in photovoltaics, II. Model applications, J. Appl. Phys. 112, 2012. #114907.

59. K. Mundra, T. DebRoy, Calculation of weld metal composition change in high-power conduction mode carbon dioxide laser-welded stainless steels, Me.l Trans. B 24B, 1993, pp 145-155.

60. M. von Allmen, Laser-beam interactions with materials, Spring Verlag, New York, 1987.

61. C.L. Chan, J. Mazumder, One-dimensional steady-state model for damage by vaporization and liquid expulsion due to laser-material interaction, J. Appl. Phys 62, 1987, pp 4579.

62. P.A.A. Khan and T. DebRoy, Alloying element vaporization and weld pool temperature during laser welding of AISI 202 stainless steel, Met. Trans. B 15B, 1984, pp 641-644.

63. T. Iida, I.L. Guthrie, The Physical Properties of Liquid Metals, Oxford: Clarendon Press, 1993.

64. X. He, T. DebRoy, P.W. Fuerschbach, Composition change of stainless steel during microjoining with short laser pulse, J. Appl. Phy. 96, 2004, pp 4547.

65. S. Dushman, Scientific Foundations of Vacuum Technique, Wiley publishing, New York, 1962.

66. W.D. Bancroft, H.L. Davis, Raoult's Law, J. Phys. Chemistry, 33(3), 1929, pp 361-370.

67. M.M. Collur, A. Paul, T. DebRoy, Emission spectroscopy of plasma during laser welding of stainless steels, Met. Trans. B 20B, 1989, pp 277-286.

68. M.M. Collur, A. Paul, T. DebRoy, Mechanism of alloying element vaporization during laser welding, Met. Trans. B 18B, 1987, pp 733-740.

69. T. DebRoy, S. Basu, K. Mundra, Probing laser induced metal vaporization by gas dynamics and liquid pool transport phenomena, J. Appl. Phys. 70(3), 1991, pp 1311-1319.

70. K..T. Voisey, C.F. Cheng, T.W. Clyne, Laser-Solid Interactions for Materials Processing, edited by D. Kumar, Materials Research Society, San Francisco, CA, 2001.

71. X. He, J.T. Norris, P.W. Fuerschbach, T. DebRoy, Liquid metal expulsion during laser spot welding of 304 stainless steel, J. Phys. D.: Appl. Phys. 39, 2006, pp 525-534.

72. A. Miotello, R. Kelly, Critical assessment of thermal models for laser sputtering at high fluences, Appl. Phys. Lett. 67, 1995, pp 3535-3537.

73. X. He, P. Fuerschbach, T. DebRoy, Heat transfer and fluid flow during laser spot welding of 304 stainless steel, J. Phys. D: Appl. Phys. 36, 2003, pp 1388-1398.

74. Z. Yang, PhD Thesis, Pennsylvania State University, 2000.

75. T. Zacharia, S.A. David, J.M. Vitek, T. DebRoy, Heat transfer during Nd:YAG pulsed laser welding and its effect on solidification structure of austenitic stainless steels, Met. Trans. A 20A, 1989, pp 957-967.

76. M. Rappaz, S.A. David, J.M. Vitek, L.A. Boatner, Analysis of solidification microstructures in Fe-Ni-Cr single-crystal welds, Met. Trans. A. 21A, 1990, pp 1767-1782.

77. D. Farson, R. Richardson, X. Li, Infrared measurement of base metal temperature in gas tungsten arc welding, Welding Journal, 1998, pp 396s-401s.

78. A. Bicknell, J.S. Smith, J. Lucas, Infrared sensor for top face monitoring of weld pools, Measurement Science and Technology 5(4), 1994, pp 371.

79. P. Banerjee, S. Govardhan, H.C. Wikle, J.Y. Liu, Infrared sensing for on-line weld geometry monitoring and control, J. Engineering for Industry, 117(3), 1995, pp 323-330.

80. S. Nagarajan, W.H. Chen, B.A. Chin, Infrared sensing for adaptive arc welding, Welding Journal, 1989, pp 462s-466s.

81. H.G. Kraus, Experimental measurement of stationary SS 304, SS 316L, and 8630 GTAW weld pool surface temperatures, Welding Journal 68, 1989, pp 269s-279s.

82. C.R. Heiple, J.R. Roper, Trends in welding research conference proceeding, edited by S.A.David, Metals Park: American Society for Metals, 1982.

83. H.E. Cline, T.R. Anthony, Surface rippling induced surface-tension gradients during laser surface melting and alloying, J. Appl. Phys. 48, 1977, pp 3888.

84. M.R. Frewin and D.A. Scott, Finite element model of pulsed laser welding, Welding Journal 78, 1999, 15s-22s.

85. T.D. Bennett, D.J. Krajnovich, C.P. Grigoropoulos, P. Baumgart, A.C. Tam, Marangoni mechanism in pulsed laser texturing of magnetic disk substrates, J. Heat Transfer 119, 1997, pp 589 – 596.

86. S.V. Patankar, Numerical Heat Transfer and Fluid Flow, Hemisphere Publishing Co., New York: 1980.

87. S. Basu, T. DebRoy, Liquid metal expulsion during laser irradiation, J. Appl. Phys. 72, 1992, pp 3317.

88. V. V. Semak, G.A. Knorovsky and D.O. MacCullum, On the possibility of microwelding with laser beams, J. Phys. D 36, 2003, pp 2170-2174.

89. W. Zhang, C-H. Kim, and T. DebRoy, Heat transfer and fluid flow in complex joints during gas metal arc welding – Part I: Numerical model of fillet welding, J. Appl. Phys. 95, 2004, pp 5220.

90. T. DebRoy and S.A. David, Physical processes in fusion welding, Reviews of Modern Physics 67 (1), 1995, pp 85-112.

91. R.H. Cox, H. Strack, Ohmic Contacts for GaAs Devices, Solid State Electronics 10, 1967, pp 1213-1218. DOI: 10.1016/0038-1101(67)90063-9.

92. R. Rai, G.G. Roy, T. DebRoy, A computationally efficient model of convective heat transfer and solidification characteristics during keyhole mode laser welding, J. Appl. Phys. 101, 2007. #054909.

93. R. Rai, J.W. Elmer, T.A. Palmer, T. DebRoy, Heat transfer and fluid flow during keyhole mode welding of tantalum, Ti-6Al-4V, 304L stainless steel, and vanadium, J. Phys. D: Appl. Phys, 40, 2007, pp 5753-5766.

94. J.J. Blecher, T.A. Palmer, and T. DebRoy, Solidification map of a nickel-base alloy, Metallurgical and Materials Transactions A, 2013. DOI: 10.1007/s11661-013-2149-1.

95. W. Tan, N.S. Bailey, Y.C. Shin, Numerical modeling of transport phenomena and dendritic growth in laser spot conduction welding of 304 stainless steel, J. Manufacturing Science and Engineering 134, 2012. p 041010.

96. H. Zhao, T. DebRoy, Weld Metal Composition Change during Conduction Mode Laser Welding of 5182 Aluminum Alloy, Metallurgical and Materials Transactions B 32B2001, pp 163-17.

97. M. Aden, E. Beyer, G. Herziger, H. Kunze, Laser-induced vaporization of a metal surface, J. Phys. D: Appl. Phys. 25, 1992, pp 57-65.

98. U. Dilthey, A. Goumeniouk, V. Lopota, G. Turichin, and E. Valdaitseva, Development of a theory for alloying element losses during laser beam welding, J. Phys. D.: Appl. Phys. 34, 2001, pp 81-86.

99. S.I. Anisimov and A. Kh Rakhmatulina, The dynamics of the expansion of a vapor when evaporated in a vacuum, J. Experimental and Theoretical Physics 37(3), 1973, pp 441.

100.   C.J. Knight, Theoretical modeling of rapid surface vaporization and back pressure, AAIA Journal 17(5), 1979, pp 519-523.

101.   V. Semak, A. Matsunawa, The role of recoil pressure in energy balance during laser materials processing, J. Phys. D: Appl. Phys. 30, 1997, pp 2541-2552.

Chapter 3

LASER-FIRED CONTACTS FORMED USING MICROSECOND PULSES

3.1 Introduction

Laser fired contacts (LFCs) represent an attractive means for decreasing manufacturing costs for silicon-based photovoltaic (PV) devices by providing a non-lithographic method to rapidly produce aluminum-silicon (Al-Si) backside ohmic contacts [1]. In addition to streamlining the fabrication process, the LFC technology has also been shown to form a back surface field (BSF) p^+ region containing Al-doped Si underneath the contact, which can effectively reduce recombination rates of minority and majority carriers at the metal-semiconductor interface [2]. Despite the inherent advantages of the LFC technology, its implementation has been hindered by an insufficient understanding of the process.

In order to form a high quality LFC, proper alloying of the Al and Si within the molten Si is required to form a low resistance ohmic contact. In addition, the passivation layer surrounding the contact should remain undamaged since it is vital to improving device performance by reducing rear surface recombination rates and enhancing internal reflection [3]. The majority of researchers who study the LFC process [3-6] utilize nanosecond pulses, likely because they believe that the low energy densities associated with these pulse durations will minimize damage to the surrounding passivation layer and the crystalline Si substrate. Although energy conversion efficiencies up to 22.4% have been reported with nanosecond pulses, [7,8] the use of nanosecond pulses has been shown to result in significant material ablation [9-11], loss of Al at high vapor pressures [12], and unpredictable contact resistances due to variations in the LFC quality between the Al-alloyed central region and the metallization layer [13].

Recent investigations [14,15] have been performed with longer pulse durations on the order of several milliseconds, which showed that pulse durations greater than 4 ms yield heavily-alloyed, low resistance LFCs without metal expulsion. Despite this benefit, the use of longer millisecond pulses will adversely impact manufacturing throughput [16,17]. The use of microsecond pulse durations to form LFCs may offer the benefit of sufficiently short processing times and improved contact quality by promoting the mixing of Si and Al in the contact region without significant metal expulsion. Since laser firing with microsecond pulses is a highly transient process, governed by a number of complex physical phenomena that occur simultaneously over extremely short time and length scales, such as rapid heating, melting, and alloying element vaporization, this contacting approach is not easily understood with the current knowledge base.

An in-depth investigation of the physical processes governing LFC formation is required for the use of microsecond pulses to gain acceptance within the photovoltaic community. The objectives for the work presented in this chapter[1] are to develop a fundamental understanding of the influence of laser processing parameters on the physical processes that occur during LFC formation and evaluate the impact of laser processing parameters and LFC geometry on contact resistance. In order to accomplish these objectives, LFCs generated with microsecond pulse durations are subjected to comprehensive microstructural and chemical analyses to study the LFC formation process.

Advanced materials characterization tools, such as focused ion beam (FIB) milling, scanning electron microscopy (SEM), and electron dispersive spectroscopy (EDS), are used to determine how laser processing parameters impact the top surface contact morphology, the sub-surface contact geometry, the spatial arrangement of Al, Si, and O_2 within and around the LFC, the morphology of the solidification structures, and the SiO_2 passivation layer. Electrical characterization is also performed to determine how laser processing parameters impact the total contact resistance. Due to the highly localized nature of an LFC compared to a uniformly metallized and contacted Si wafer, traditional methods of measuring contact resistance, such as the transfer length method (TLM), cannot be directly applied. Therefore, a modified method is developed and combined with electrical modeling using the Sentaurus device simulation software to enable better quantitative assessment of contact resistance as a function of contact geometry.

3.2 Experimental Details

3.2.1 Sample Preparation

LFCs were generated on an industrially relevant substrate over a wide range of processing parameters. Figure 3.1 shows a schematic diagram of the substrate configuration used for laser firing. The front-side of a 500 μm thick, 9 Ω-cm resistivity, double side polished, <100>, p-type, float zone, crystalline Si wafer was passivated with 100 nm of SiO_2 via plasma enhanced chemical vapor deposition (PECVD) using a $SiCl_3/O_2/Ar$ gas mixture in an Applied Materials P5000 system. Next, approximately 2 μm and 0.4 μm thick Al layers were sputtered on the front and backside of the wafer, respectively, using a Denton DV-502A DC magnetron sputtering tool at a base pressure below 1 x 10^{-7} torr at a rate of 1 to 2 Å/s. Prior to laser processing, electrically isolated regions (1.5 mm x 1.5 mm area) were created with lift-

---

[1] Portions of this chapter are directly excerpted from the following two manuscripts currently in review:
   1. A. Raghavan, *et al*, Employing microsecond pulses to form laser-fired contacts in photovoltaic devices, Submitted to Progress in Photovoltaics October 2013.
   2. A. Raghavan *et al*, Passivation layer breakdown during laser-fired contact formation for photovoltaic devices, for submission to Appl. Phys. Letters, 2014.

off on the front side using contact photolithography. Individual LFCs were processed on each insulated pad on the front side of the wafer, as shown in Figure 3.1.
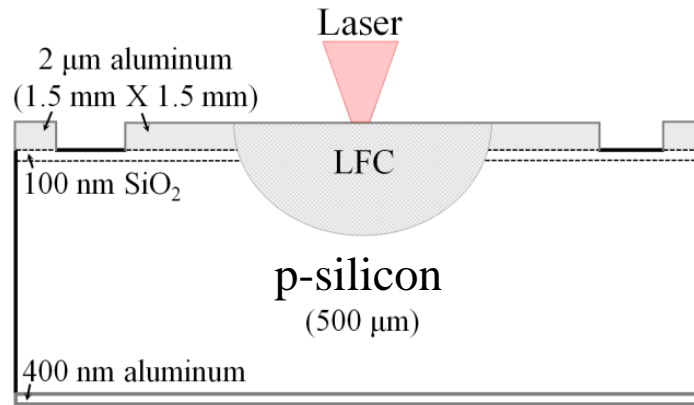
Figure 3.1. Schematic diagram of experimental substrate used for LFC investigation.

3.2.2 Laser Processing Parameters

Laser processing was performed over a large parameter space to capture a range of laser-material interaction modes from initial melting to significant metal expulsion. An IPG Photonics® YLR-LP Series 1070 nm single mode fiber laser that outputs a collimated, near-Gaussian beam emitting in the TEM_{00} mode with 500 W maximum power was used for processing. This laser system was selected because it is has a 1070 nm laser wavelength, which is most readily absorbed by the Si substrate [18], a sufficiently large range of output powers, and is capable of operating over a wide range of exposure times from a few microseconds to over 1000 ms.

In order to investigate the entire range of output powers, laser powers were varied from 65 W to 460 W and pulse durations were varied from 20 μs to 1000 μs. In order to generate industrially-relevant results, primary emphasis for characterization was placed on the shorter pulse durations (20 μs to 100 μs) and lower power levels (65 W to 260 W) since shorter pulse durations are advantageous to meet throughput requirements and higher power levels cause undesirable levels of metal expulsion and extremely large penetration depths. Pulse durations were modulated using a control system programmed with the National Instruments LabVIEW® software and confirmed via oscilloscope readings from a Newport 818-BB-21 high-speed photodiode. Figure 3.2 shows a screen shot from the oscilloscope confirming a 50 μs pulse. The x-axis is time (in μs) and the y-axis is the intensity of the detected light. As part of the 50 μs pulse, there is a 20 μs ramp-up time and 10 μs ramp-down time after the pulse. Similar ramp-up and ramp-down behavior was observed with changes in laser power and pulse duration. The laser beam diameters used for the study, which were determined from experimental measurements

prior to processing, were 50 µm and 70 µm. The 50 µm spot size is the approximate beam size at focus, and the 70 µm spot size was used to evaluate the influence of changing beam diameter on contact geometry and contact resistance.
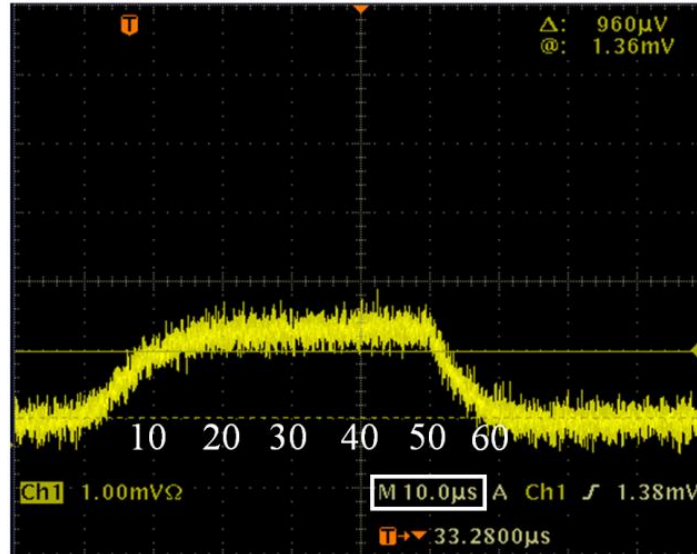
Figure 3.2. Oscilloscope reading of temporal pulse profile when processing with 230 W laser power and a 50 µs pulse duration.

3.2.3 Materials Characterization Techniques

Advanced materials characterization tools were used to quantify the impact of laser processing on the transition in laser-material interaction modes, solidification behavior, interdiffusion of Al and Si, and passivation layer quality. Top surface contact morphology was determined via SEM imaging and optical profilometry. SEM micrographs were obtained using two systems: an FEI Quanta 200 Environmental Scanning Electron Microscope SEM and a FEI NanoSEM 630 Field Emission SEM. The LFC surface topography was determined using a ZYGO NewViewTM 7300 optical profilometer and its accompanying MetroPro® Version 8.3.5 software. Figure 3.3 shows typical output data obtained when using the optical profilmetry method to measure surface deformation. Surface deformation can be used to evaluate the onset of liquid metal expulsion to determine when substrate temperatures exceed the boiling point of the alloying elements and when loss of these elements will take place. Figure 3.3(a) and Figure 3.3(c) show the type of contour plots that can be used to quantify the surface morphology after laser-firing with microsecond pulse durations.

The optical profilometry method used to quantify the extent of surface deformation and metal expulsion and was validated using multiple measurements at different angular orientations through the centerline of two LFCs, as shown in Figure 3.3(b) and Figure 3.3(d). By evaluating the error observed for

54

different angular orientations, it becomes clear that the measurements through any singular axis will serve as a good approximation to evaluate the extent of surface deformation for a given sample. For instance, although the two LFCs shown were processed with significantly different processing parameters, it can be observed in Figure 3.3(b) and Figure 3.3(d) that the measurements of surface topography exhibit little variation through the centerline of the contact when taken at different angular orientations. Therefore, the measurements presented through one centerline are representative of the entire contact when the contact is highly symmetrical. It should be noted, however, that as laser processing parameters are changed to the point where significant liquid metal expulsion occurs, the LFCs can be highly asymmetrical. Optical profilometry measurements presented in this chapter are made only for highly symmetrical LFCs where the onset of liquid metal expulsion has just initiated or little to no expulsion is observed.
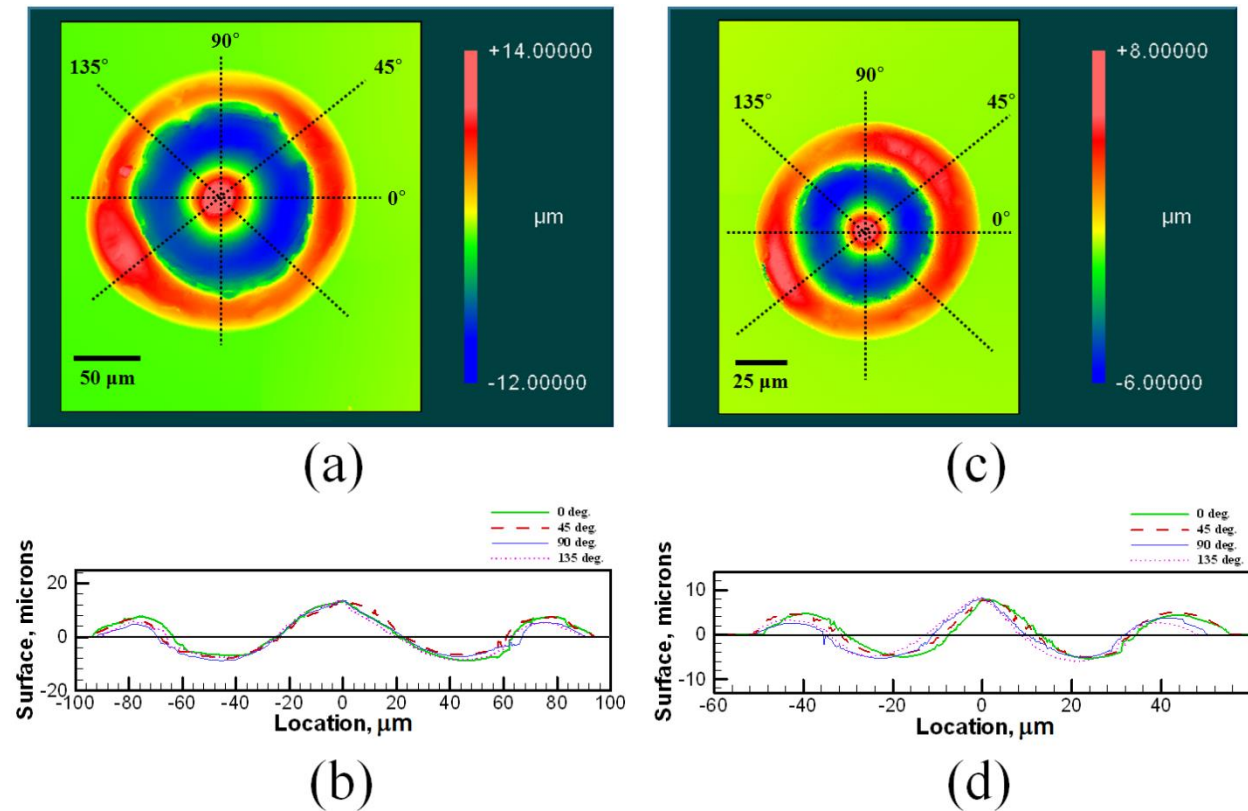
Figure 3.3. Top surface measurements and validation of centerline accuracy around symmetrical nature of contacts for contacts processed with (a),(b) 260 W, 70 μm beam diameter, and 100 μs pulse duration; and (c),(d) 159 W laser power, 50 μm beam diameter, and 50 μs pulse duration. Note: For certain cases with extreme metal expulsion, round LFC geometries may not be obtained and surface topography will vary significantly.

EDS mapping was used to determine the elemental distribution of Al, Si, and O_2 after laser-firing along the LFC top surface and cross-section. Initial EDS point analysis measurements were made with the FEI Quanta 200 Environmental Scanning Electron Microscope, which is equipped with a 10 mm^2 Si-

Li detector. Point data collected using an accelerating voltage of 5 keV and 1 μm beam size was analyzed using the Oxford INCA software to quantify the EDS measurement data. The majority of measurements were made using EDS mapping techniques. EDS mapping was performed with the FEI NanoSEM 630 Field Emission SEM, which is equipped with an X-max 80 mm^2 Si drift detector and an Xstream2 micro analytical pulse processor. The data was analyzed using the Oxford AZtec software. The working distance for most SEM imaging with the FEI NanoSEM 630 was 2 mm and imaging was performed with an accelerating voltage of 2-3 kV and a spot size of 1 μm. For EDS mapping with this system, the working distance was 5 mm with an accelerating voltage of 5 keV and a spot size of approximately 1 μm.

Contact geometry and LFC solidification structures were determined by evaluating top surface and cross-sectional SEM micrographs. Cross-sectional samples were obtaining by sectioning LFCs close to their centerline using an ADT 7100 Provectus dicing saw system with a diamond encapsulated resin blade. The cross-sections were polished using an FEI Quanta 200 3D Dual Beam FIB. Prior to FIB milling and polishing, a carbon (C) or platinum (Pt) coating was deposited on the top of the sample near the cross-sectional surface to be polished to protect the edge from deteriorating during the process. For Pt and C deposition, the beam current was varied between 1 and 5 pA/μm^2 to obtain a smooth surface layer without degrading the top surface of the sample. Due to the size of the LFC cross-sectional regions to be polished, which were often on the order of 100 μm in length by 60 μm in depth, polishing was performed at 7 nA at a working distance of 30 mm and 20 nA at a working distance of 10 mm to increase the rate of milling and polishing. Polishing was performed in a controlled fashion to ensure that LFC cross-sections were as close to the LFC centerline as possible.

3.3 Impact of Laser Processing on Contact Formation

3.3.1 LFC Morphology

Contact geometry can strongly influence the contact resistance [15,19]. Therefore, it is important to quantify the influence of laser processing parameters on LFC morphology. Previous work [20,23] has indicated that changes in laser power, power density profile, and pulse duration have a significant impact on the temperature fields, molten pool geometry, diffusion of dopant atoms, evaporation rates of various elements, and the metal ejection. As a result, the selection of appropriate laser parameters is a major challenge when fabricating LFCs. In this section, advanced materials characterization tools are used to investigate how these laser processing variables influence the evolution of LFC geometry during laser-firing with microsecond pulse durations.

For all cases where LFCs were formed, there are two distinct regions present: an inner contact/crater region and an outer ring region. These regions are annotated in Figure 3.4, which shows SEM

micrographs and corresponding surface contour plots for two LFCs. Figure 3.4(a) shows an SEM micrograph and corresponding surface contour plot for a contact that has just formed that exhibits little to no surface deformation and metal expulsion within the inner and outer ring regions, whereas Figure 3.4(b) shows a contact that exhibits significant liquid metal expulsion and surface deformation in these regions.
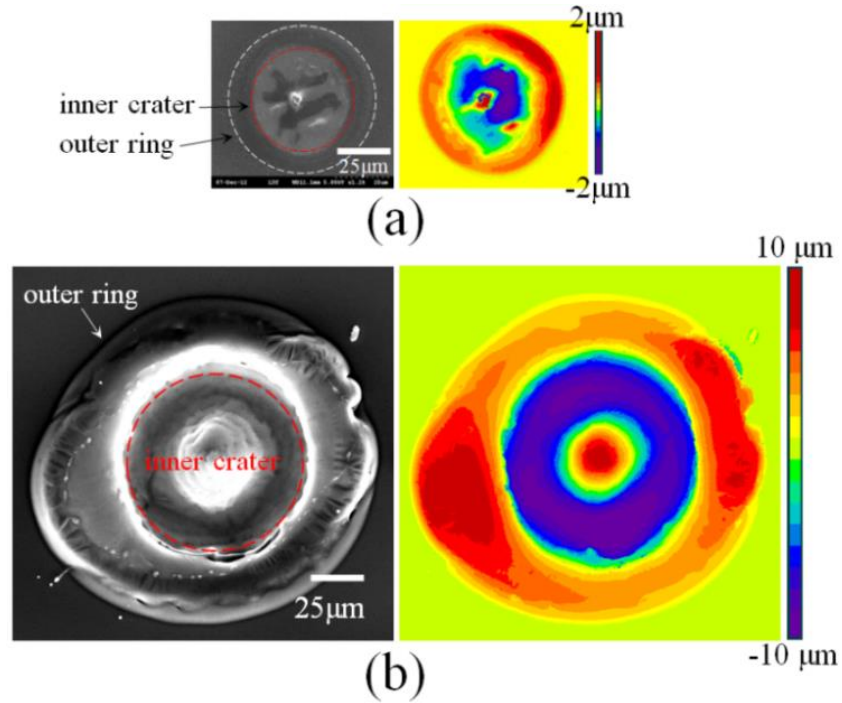
Figure 3.4. SEM micrographs and optical profilometry measurements for LFCs processed with 50 μm beam diameter and (a) 159 W, 30 μs pulse duration and (b) 260 W and 40 μs pulse duration. All images are set to the scale used on the SEM micrographs. The colors and scale bar for the contour plot refer to the surface elevation of portions of the contact.

Figure 3.5 shows top surface SEM micrographs for LFCs processed with 50 μm and 70 μm laser beam diameters over a wide range of power levels and pulse durations. It can be observed that various laser-material interaction modes from initial melting to metal expulsion are observed during LFC formation as a result of changes in processing parameters. The samples in which liquid metal expulsion occurs, which can be determined from the formation and solidification of a lip region outside of the inner crater region, are identified in each row with a red box. At power levels greater than 260 W, liquid metal expulsion was observed at 20 μs. It is clear that changes in the pulse duration, laser power, and laser beam diameter strongly influence contact morphology, which underscores the highly transient nature of this process when using microsecond pulse durations. Increases in power and pulse duration lead to significant growth in the inner crater contact diameter and can eventually result in liquid metal expulsion.
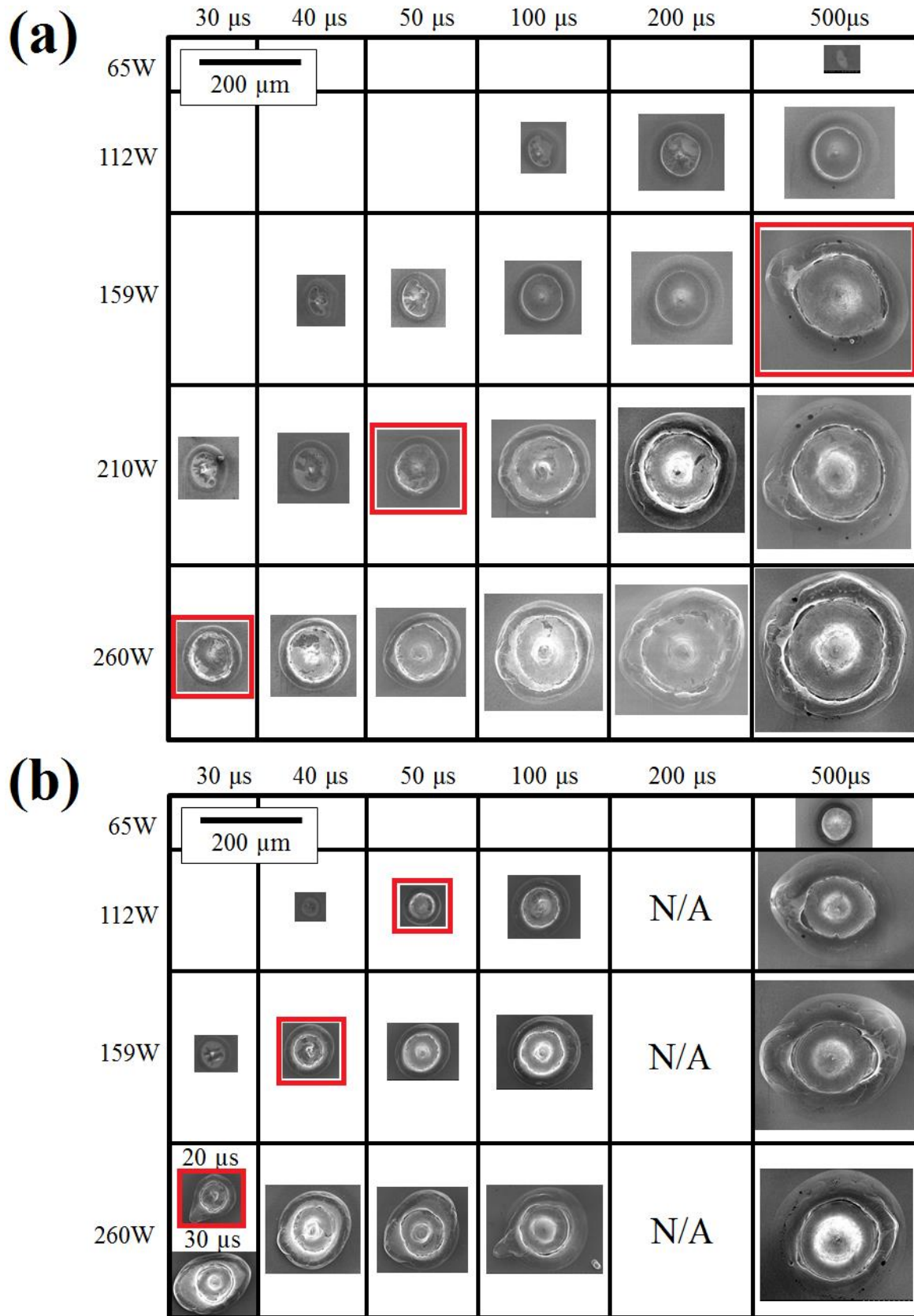
Figure 3.5. SEM top surface images as a function of pulse duration & laser power for (a) 70 μm & (b) 50 μm beam diameters.

Figure 3.6 shows a plot of the inner crater/contact size as a function of laser power and pulse duration. Inner crater size is important because it has been correlated to changes in total contact resistance in many studies [14,15,19] and is believed to constitute the electrically active LFC region. Therefore, it is instructive to understand how changes in process parameters will influence its size. The maximum standard error for multiple measurements (i.e. measurements of contact diameter for LFCs reproduced three times with identical parameters) was no greater than 10%, which correspond to the error bar values used on the plot for each measurement. For both laser beam diameters, the inner crater contact size increases with longer pulse durations and increasing laser power. The change in contact geometry and morphology in response to changes in power and pulse duration will be driven by the convective and conductive heat transfer mechanisms. The onset of the melting process and contact formation will be governed by conduction [20]. However, it has been shown through calculations of laser spot micro-welding that the dominant mechanism shortly after contact formation will be convection.
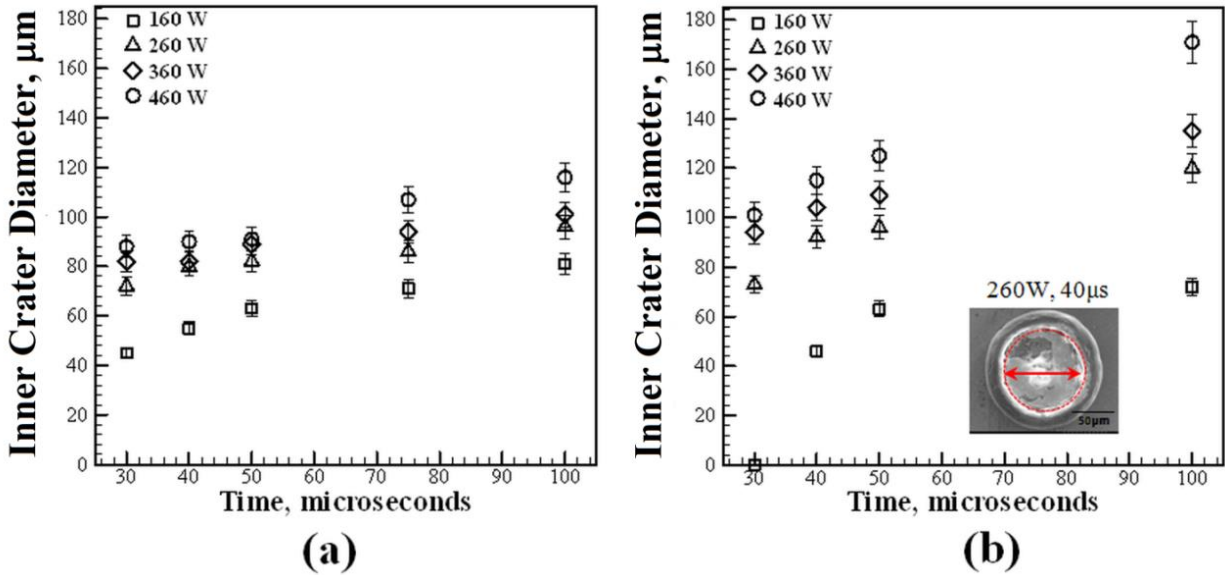
Figure 3.6. Inner crater contact size as a function of pulse duration and power level for (a) 50 μm and (b) 70 μm beam diameter.

The influence of convection is largely dependent on the spatial variation of temperature within the molten pool [20,24]. The spatial variation of temperature influences the Marangoni shear stress on the melt pool surface, which drives fluid flow from the center to the periphery of the melt pool [20]. The Marangoni shear stress, σ, can be calculated as:

$$\sigma = \frac{dT}{dx}\frac{d\gamma}{dT} \tag{3.1}$$

59

where dT/dx is the temperature gradient on the surface of the molten pool in the x-direction and $d\gamma/dT$ is the surface tension coefficient of the molten material, which is assumed to be constant. The dT/dx value can typically be approximated by dividing the difference between the peak temperature at the center of the melt and the liquidus temperature at the edge of the melt (dT) by the molten pool radius (dx). Since a contact is symmetrical, the temperature gradient on the surface of the melt will be equal in all directions assuming uniform distribution of the laser heat source in the x and y directions. In order for the Marangoni shear stress to have a strong influence on contact growth, the temperature gradient needs to increase significantly in response to changes in pulse duration and power level. Numerical calculations of the LFC process [20,24] have demonstrated that the molten pool temperature can increase over 1000K during the first 100 µs. As a result, temperature gradients on the surface of the melt pool will increase significantly, resulting in a higher Marangoni shear stress on the molten pool surface and substantial growth in contact geometry. The significant increase in inner contact size can be observed in Figure 3.6 as a function of pulse duration for all processing conditions.

The influence of power on contact size can also be observed in Figure 3.6. In all cases, an increase in the power level leads to a larger contact geometry. An increase in power level will also have a significant impact on the molten pool surface temperatures. For instance, numerical simulations of the LFC process have shown that increasing the power from 20 W to 45 W when using a laser beam diameter of 30 µm and a 2 ms pulse can cause the peak temperature to increase over 800K [24]. Therefore, there will be a much larger temperature gradient on the surface as the power level is increased, which will drive fluid from the center of the melt to the periphery at much greater velocity and lead to larger contact sizes. In addition, there will be a vapor recoil force on the surface of the melt pool as temperatures exceed the boiling point for the alloying elements, which should introduce additional forces on the molten pool surface that will drive fluid flow from the center of the melt pool towards the periphery.

Although the contact sizes all increase with increasing power and pulse duration, LFCs processed with a 70 µm beam diameter exhibit larger inner crater contact diameters when using the same laser beam power and pulse duration. It is likely that when using a larger beam size, the melting threshold for both Al and Si is reached at larger distances away from the beam center than when using a smaller beam size. Therefore, the inner crater size is larger despite the fact that the smaller beam size will have higher peak temperatures and higher fluid flow velocities within the melt.

The output beam from the fiber laser used has a Gaussian irradiance (or laser power per unit area) distribution, F, emitting in the TEM$_{00}$ mode that can be calculated using the following equation:

$$F = \frac{q f \eta}{\pi r^2} e^{-f(x^2+y^2)/r^2}$$

(3.2)

where q is the laser power, f is the distribution factor (taken here as 3 to accurately simulate the output from the fiber laser), η is the absorptivity of the laser wavelength at the substrate surface, r is the beam radius, and x and y are the distances from the beam center. From Equation (3.2), it can be seen that the intensity of the laser radiation will be highest in the center and that as the beam radius is decreased, the power density distribution for the beam will be much higher at the center of the melt pool.

The contacts processed with the small beam diameter should have larger depths of penetration because the spatial variation of the power density distribution across the surface of the melt will be substantially higher than for a larger beam diameter. Numerical simulations of the LFC process [24] confirm that when two contacts have the same top surface area, the one processed with a smaller beam diameter will have a larger depth of penetration since the laser intensity is more concentrated at the center of the molten region. As the irradiance increases through a reduction in beam size, the mode of laser processing will transition from conduction mode to keyhole mode [25], and the shape of the molten volume will change from hemispherical to ellipsoidal with large penetration depths. The impact of tailoring contact geometry on total contact resistance and other device performance metrics is discussed in more detail in Section 3.4 and in Chapter 6, respectively.

3.3.2 Alloying of Al and Si within the LFC

The size of the Al-alloyed region within an LFC has been shown to influence the total contact resistance when using both nanosecond [19] and millisecond [15] pulse durations. Therefore, it is important to understand how Al is incorporated into the LFC when processing with microsecond pulse durations in order to determine the true size of the contacted region. In this section, several contacts formed under different processing parameters are characterized to identify the extent of alloying between Al and Si within the LFC and to evaluate the impact of laser processing on solidification behavior.

3.3.2.1 Incorporation of Al and Si in the LFC

Cross-sectional micrographs taken close to the center of the two contacts processed with 112 W laser power, a 50 μm laser beam diameter, and 40 μs and 50 μs pulse durations are shown in Figure 3.7. The SEM micrographs and corresponding EDS reveal that significant alloying between Al and Si has occurred within the LFC. The corresponding EDS maps of Al confirm that the lighter-colored regions in the SEM micrographs are an Al-rich second phase. The presence of a second phase indicates that the Al

concentration within the LFC is greater than the maximum solid solubility of Al in Si [26], which was also confirmed via localized EDS measurements at various locations within the LFCs.
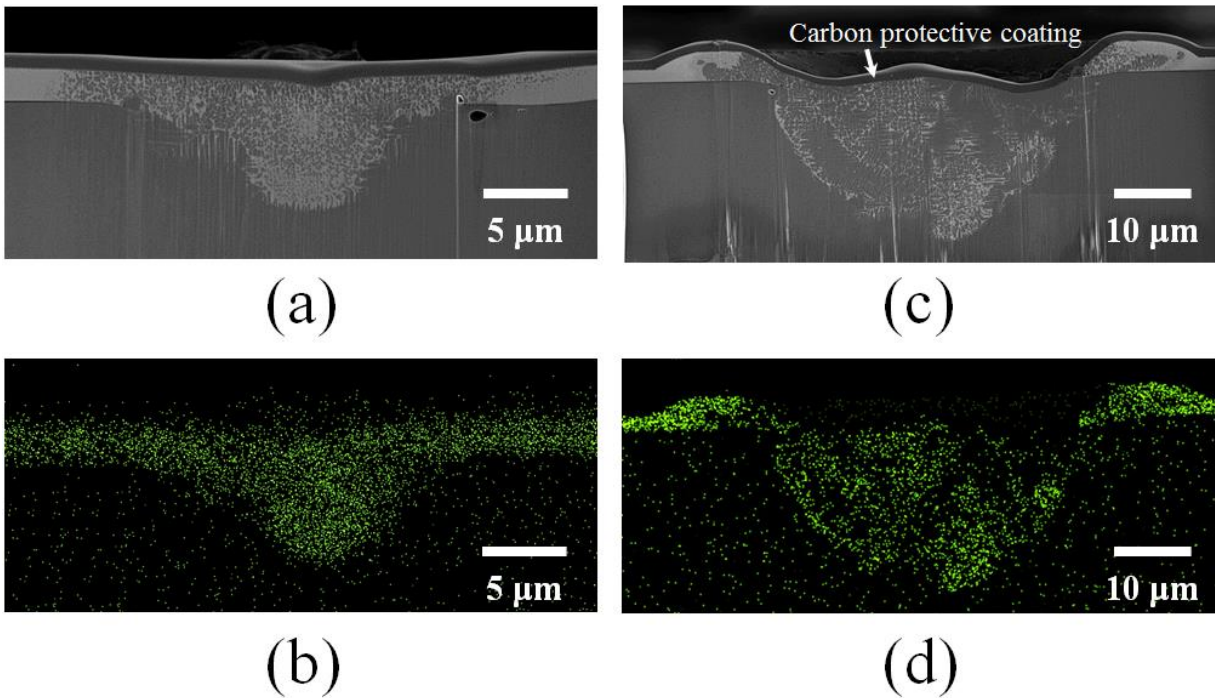
Figure 3.7. Cross-sectional SEM micrographs and EDS maps of Al (green) for contacts processed with 112W laser power, 50μm beam diameter and (a)-(b) 40μs; and (b)-(d) 50μs pulse durations.

The cross-sectional SEM micrograph for the contact processed with 112 W laser power, a 50 μm beam diameter and 40 μs pulse duration is enlarged shown in Figure 3.8. The contact shown here possesses a uniform distribution of a second, Al-rich phase within the Si matrix. In the micrographs, the white-colored region indicates a phase with higher concentration of Al, and the darker region is a Si-rich phase, which was confirmed through EDS measurements shown in Table 3.1. Since an LFC was not present when using a pulse duration of 30 μs with the other processing conditions held constant, it can be assumed that the contact has formed sometime between 30 μs and 40 μs. In laser spot micro-welding under short pulse durations [12], the initial stages of heat transfer are often driven by conduction, indicating that fluid flow is not a dominant heat transfer mechanism. With a limited influence of fluid flow, diffusion will likely play a more dominant role in mass transfer of Al and Si at these shorter pulse durations.
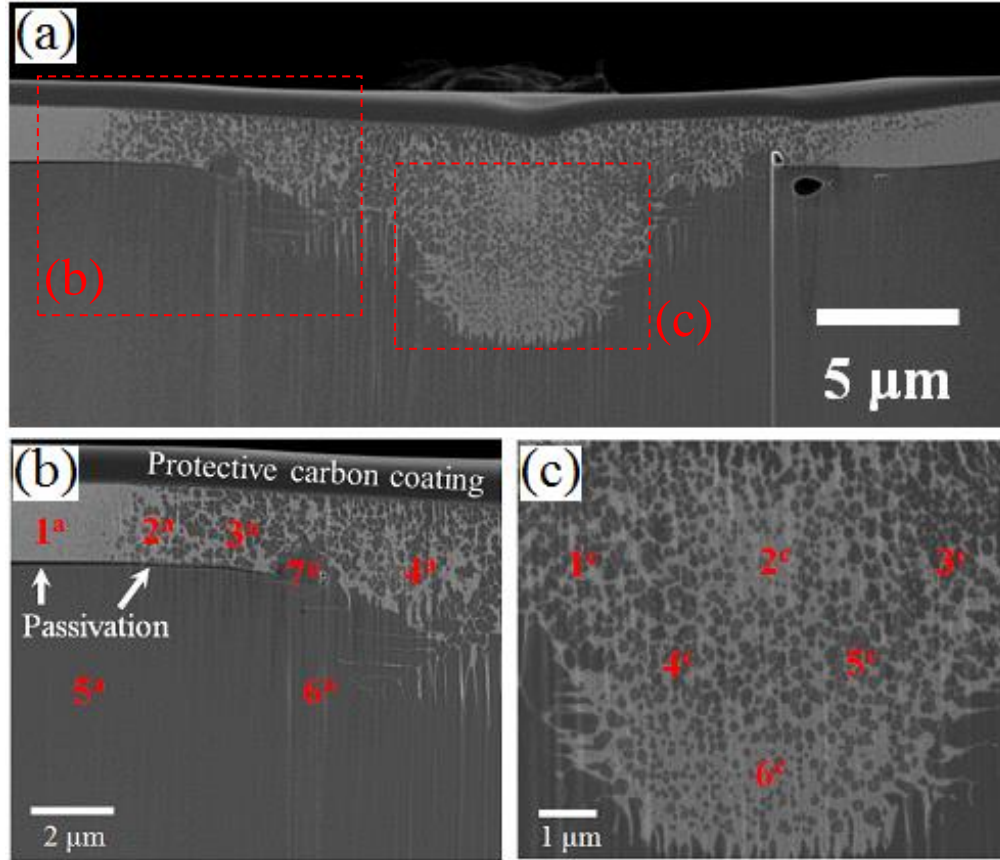
Figure 3.8. LFC processed with 112 W laser power, a 50 μm beam diameter, and a 40 μs pulse duration.

In order for diffusion to account for the distribution of Al and Si observed in Figure 3.8, extremely rapid diffusion rates are required since the original Al/SiO$_2$/Si interface has shifted to a maximum depth of approximately 6.5 μm at the center of the LFC. A back-of-the envelope calculation can be used to approximate the relative diffusion coefficient using the following equation:

$$x = \sqrt{Dt} \tag{3.3}$$

where x is the diffusion distance (6.5 μm), D is the diffusion coefficient, and t is the time (taken here as 10 μs assuming a contact forms between 30 μs and 40 μs). The maximum diffusion distance at the center of the LFC (6.5 μm) requires a relative diffusion coefficient of approximately 4 x 10^{-3} cm^2/s. This shift can be produced by the rapid diffusion of Si from the wafer into a molten LFC and/or Al metallization layer since the diffusivity of Si into a liquid will be on the order of 10^{-4} cm^2/s [27] in comparison to solid-state diffusion of Al into the Si wafer, which will be on the order of 10^{-10} cm^2/s or less [28].

Diffusion rates will also depend largely on the temperatures within the LFC. Since the laser beam used in the experiments possesses a Gaussian distribution with peak intensity at its center, substrate

temperatures will be highest at the LFC center [13]. In order for the SiO_2 layer to melt, the temperatures are likely close to 2000K and the diffusion rates of Si into the liquid phases will be orders of magnitude higher than that of Al into Si. Furthermore, with high substrate temperatures associated the LFC process, the presence of a liquid or two phase (liquid + Si) can be expected to exist near the LFC/wafer interface. The results support the idea that at the onset of contact formation, diffusion plays a significant role in distributing Al and Si within the LFC, assuming that the primary diffusing species is Si into a liquid phase at the LFC/wafer interface.

Figure 3.8(b) and Figure 3.8(c) show closer views of the distribution of Al and Si within various regions for the contacts produced with a 40 µs pulse duration. The numbers on the figures indicate regions where Al and Si concentrations have been measured by EDS over a 1 μm^2 circular area. Although EDS measurements are not extremely quantitative, the values give a good idea of the distribution of Al and Si within the LFC. The numbers and superscripts on the figures can be used to identify the measurements in Table 3.1. Close to the passivation layer/LFC boundary, the Al concentration from the unaffected metallization layer into the contact for locations 1^a, 2^a, 3^a and 4^a is 100, 78, 55 and 38 weight percent Al, respectively. The decreasing concentration of Al and increasing concentration of Si demonstrates how both elements intermix during processing. Due to the rapid interdiffusion rates of Si in Al, there is Si present above the unmelted passivation layer. Since Al has a much greater solid solubility of Si (~ 2 wt. %), Si can also be incorporated into the metallization layer without any observable phase change in the metallization far from the passivation layer/LFC fusion boundary.

At point 7^a, the concentration is 58 wt. % Al and 42 wt. % O, which indicates the formation of the Al_2O_3 as the SiO_2 passivation layer melts and breaks down. At locations 5^a and 6^a, the concentration is 100 wt. % Si, which indicates that Al has not diffused into the wafer. In addition, Figure 3.8(c) shows a higher concentration of Al within the center of the contact, which will be due to interdiffusion of Al and Si after the passivation layer has been removed through processing. The concentration measurements within the center of the contact shown in Figure 3.8(c) demonstrate a fairly uniform distribution of Al and Si, which is also clear from the microstructure. The measurements confirm that the white phase is richer in Al than the dark phase, as seen at locations 2^c and 6^c where the Al concentration is 62 and 63 wt. %, respectively. The measurements indicate that the overall composition is fairly uniform and greater than the eutectic. Therefore, since the composition of Al is high and Si has a low solid solubility of Al, as seen from the phase diagram in Figure 3.9, the Al-rich phase is present upon solidification.

Table 3.1. EDS measurements of Al and Si and at designated locations in **Figure 3.8** and **Figure 3.10**. Superscript (x) pertains to (a), (b), (c) or (d) depending on corresponding micrographs.

	(a)		(b)		(c)		(d)	
	Al	Si	Al	Si	Al	Si	Al	Si
$1^{(x)}$	100	0	100	0	54	46	8	92
$2^{(x)}$	78	22	13	87	62	38	19	81
$3^{(x)}$	55	45	73	27	37	63	--	--
$4^{(x)}$	38	62	24	76	49	51	--	--
$5^{(x)}$	0	100	0	100	52	48	--	--
$6^{(x)}$	0	100	56	44	63	37	--	--
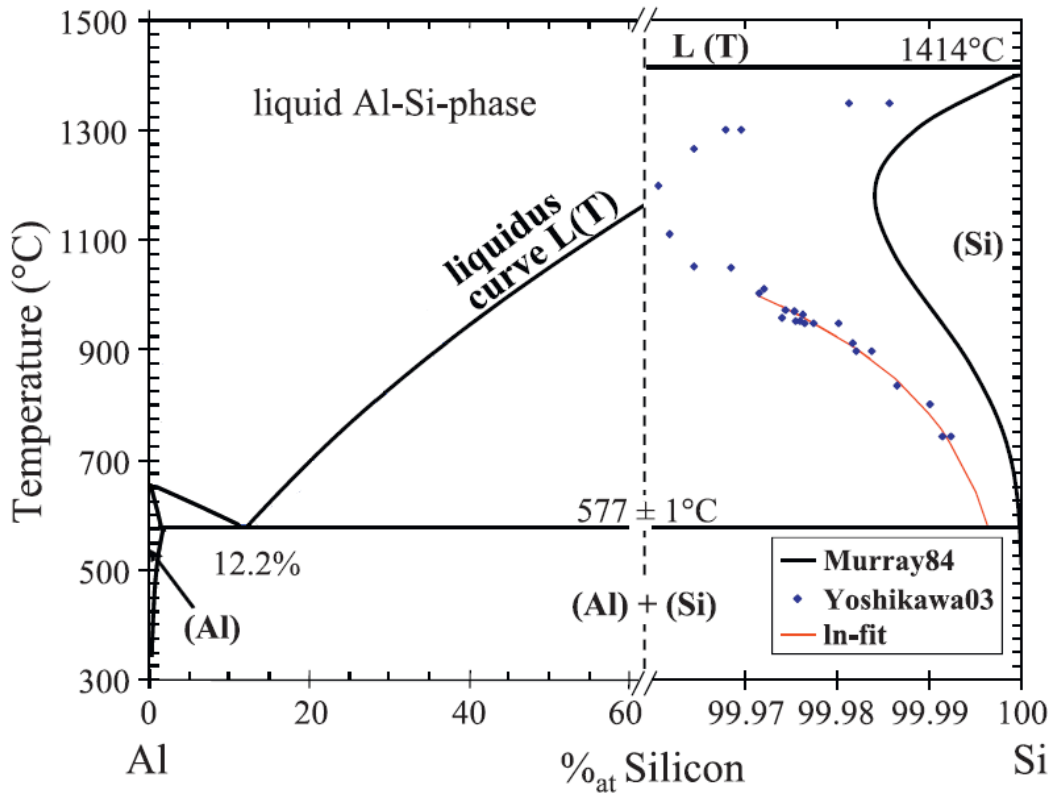
Figure 3.9. Aluminum-Silicon phase diagram, adapted from [31].

Figure 3.10 shows the impact of increasing pulse duration to 50 µs on the alloying of Al and Si. The cross section for the contact processed with a 50 µs pulse reveals an alloying depth of approximately 25 µm. In order to achieve alloying of Al and Si to these depths, mass transfer must be driven by convection, as demonstrated through numerical simulations for laser doping of Si [23]. Figure 3.10(b) shows a cross-sectional view above the passivated region for the contact produced with a 50 µs pulse duration. The Al concentration from the metallization into the contact for locations 1^b, 2^b, 3^b, and 4^b are

100, 13, 73 and 24 weight percent Al, respectively. The expulsion of the Si and Al from the center of the contact due to the vapor recoil force will result in this inhomogeneous mixing pattern within the outer ring region above the passivation layer. In addition, the alloying within the contact, as shown in Figure 3.10(c) and Figure 3.10(d), show a non-uniform distribution of Al and Si on either side of the LFC.

Although the cause for the lack of uniformity in the distribution of Al and Si is unclear, the irregularity in the mixing suggests that the beam may not have been perfectly Gaussian, leading to non-uniform heating of the substrate despite a circular beam. The non-uniformity of the beam profile at focus has been confirmed through experimental measurements made using a NanoScan Beam Profiler as shown in Figure 3.11 [29]. It can be observed that in the x- and y-axes, the beam profile is not uniform in both directions. Instead, the beam profile in the y-axis is much more uniform than the beam profile in the x-axis, which can contribute to variations in the intensity distribution at the substrate. Variations in intensity can influence temperature profiles and fluid flow velocities within the melt and impact the distribution of Al and Si within the melt pool. Furthermore, since significant Al expulsion is observed, the concentration of Al on either side of the melt pool may be different, causing a non-uniform distribution of Al and Si in the final LFC.
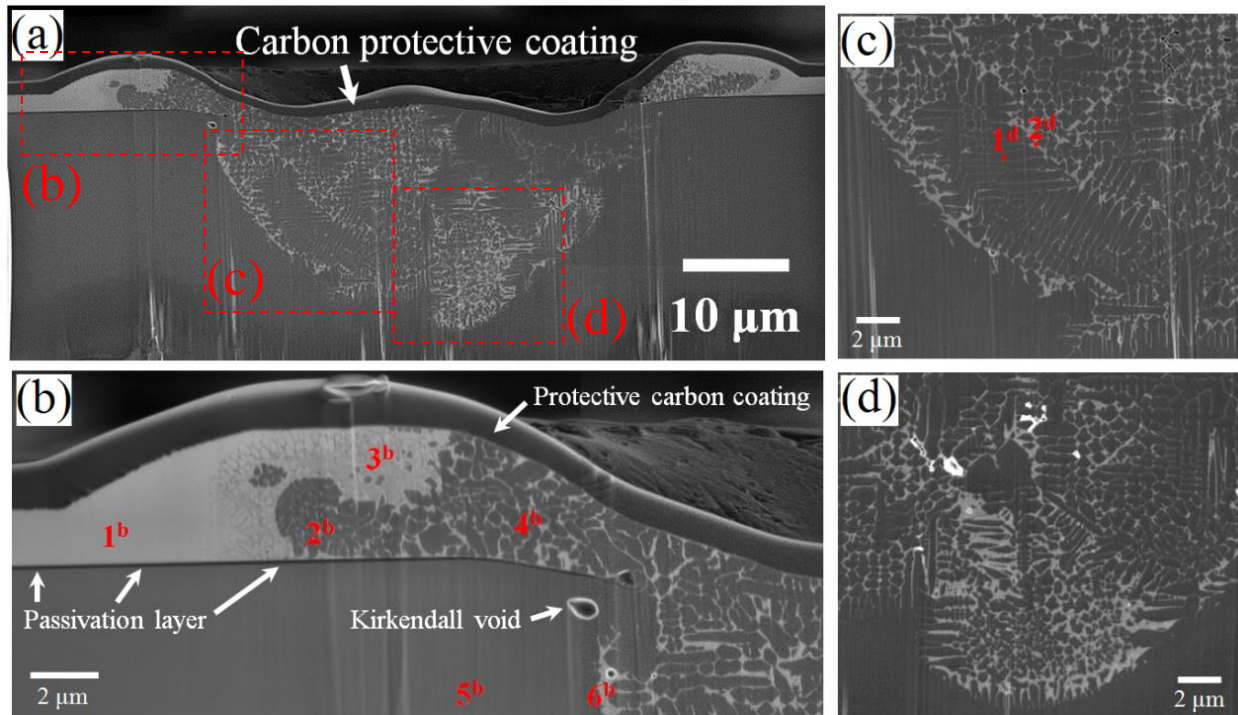
Figure 3.10. Cross section for LFC processed with 112 W laser power, 50μm beam diameter and various locations within the contacts. Numbers represents locations where EDS measurements were made and are reported as shown in **Table 3.1**.

x-axis   y-axis

Beam at Focus
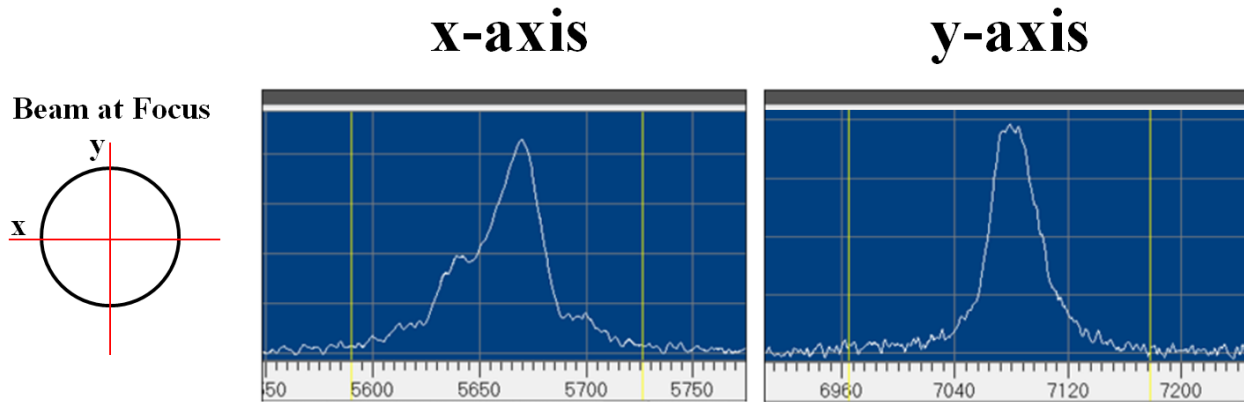
Figure 3.11. Beam Profile obtained from NanoScan Optical Profiles for LENS single mode fiber lasers using Precitec focusing optics with 200 mm collimator and 200 mm focusing optics. X-axes are in microns. Adapted from [29].

For both contacts processed with 40 µs and 50 µs pulse durations, Al and Si have mixed throughout the contact melt region, which suggests that the actual contact area is larger than typically assumed for LFCs. The impact of further increasing the pulse duration can be observed in Figure 3.12 for a contact processed with the same operating conditions (112 W laser power and a 50 µm beam diameter) and a 100 µs pulse duration. The SEM micrograph contains a clear delineation around the molten region, which may be caused by thermal stress encountered during rapid contraction and solidification of the molten material due to the rapid heating and cooling cycles associated with laser processing. The EDS map for Al provides an indication of the areas where Al has alloyed with Si within the LFC. This region is outlined with a red dotted line for clarity. The contact geometry appears to transition from the hemispherical shape observed when processing with a 50 µs pulse duration to a keyhole type geometry, suggesting a change in laser processing modes [25]. This transition can be expected as the energy density or power density is increased during processing, which can lead to molten pool temperatures above the boiling points of the alloying elements within the pool.
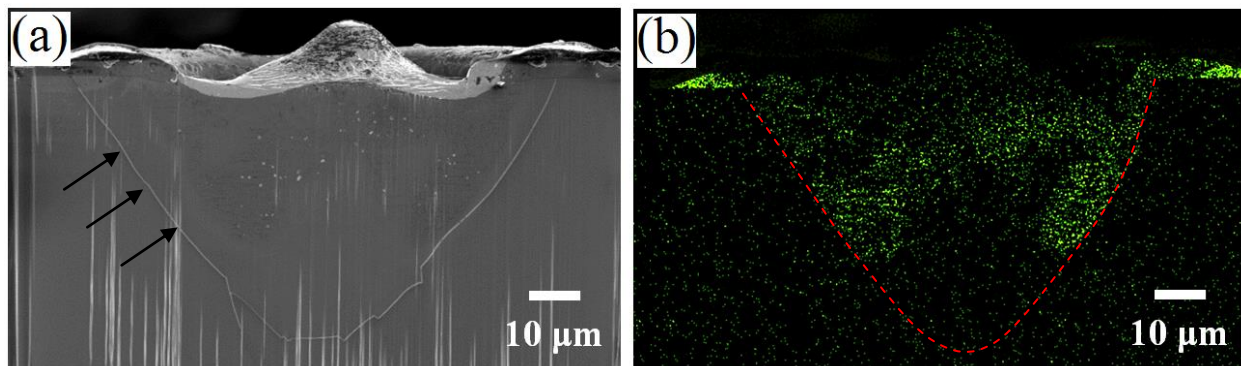
Figure 3.12. SEM micrograph (a) and corresponding EDS map for Al for contact processed with 112 W laser power, a 50 µm beam diameter, and a 100 µs pulse duration.

Previous work with nanosecond pulse durations assumes a planar Al-Si interface rather than a three-dimensional contact shape. For LFCs processed with microsecond pulses, the interfacial contact area will be larger due to the heavy alloying of the p+-Si by Al within the molten region, as observed in the cross sectional geometries and EDS maps for Al The formation of a three-dimensional contact region should have a positive influence on reducing the total contact resistance, as has been shown for three-dimensional contacts produced with millisecond pulse durations [15].

As laser intensity is increased, alloying of Al with Si in the melt pool is also affected because Al can be removed from the melt pool. The impact of metal expulsion on the mixing of Al and Si in the melt can also be observed in Figure 3.13, which shows a cross section of an LFC processed with 260 W laser power, a 40 µs pulse, and a 70 µm beam diameter (270 J/cm^2). The EDS map shows the distribution of Al within the recrystallized material. Figure 3.13(c) shows a higher concentration of Al within the left hand side inner crater region. In addition, the outer ring region also shows the presence of Al on both sides and is substantially brighter on the right hand side, indicating a higher concentration of Al. This additional Al was most likely displaced from the inner crater at the onset of processing and not adequately incorporated into the melt.

On the left hand side of the LFC shown in Figure 3.13(c), Al has clearly mixed throughout the melt, which is likely due to convective mass transfer of the Al, as has been shown for laser doping of Si with phosphorus [23]. Due to the surface tension gradient driven Marangoni flow for Si, molten material will flow along the surface from the high-temperature center region to the low-temperature periphery before returning to the center through the depth of the melt [21,22]. These flow patterns will lead to convective mixing of the Al in the molten Si, which is observed in Figure 3.13(c), in which Al is detected at a depth of approximately 25 µm. Although Al is detected throughout the molten pool, the onset of metal expulsion and/or the inhomogeneity of the beam intensity can contribute to irregular distribution of Al within the melt. Therefore, careful selection of processing parameters is required to ensure that Al is not removed from the substrate prior to sufficiently mixing with Si in the LFC.
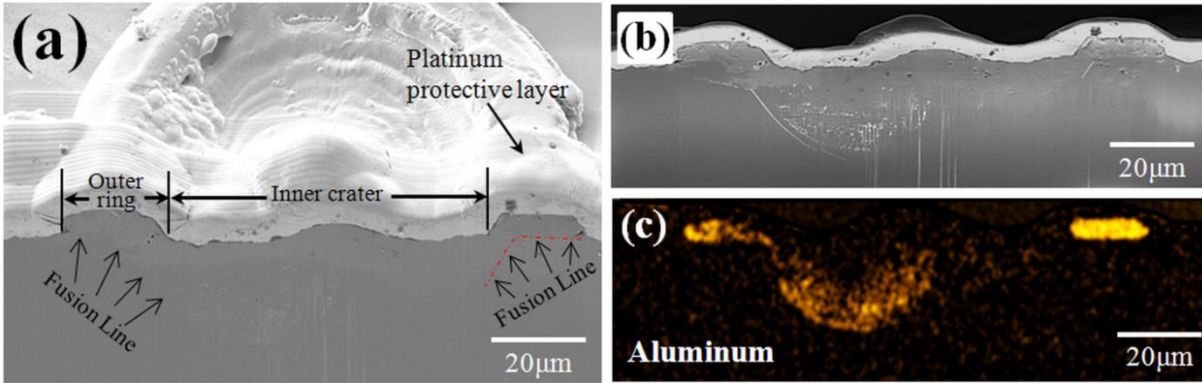
Figure 3.13. FIB polished SEM cross section for LFC processed with 260 W, 30 μs and 70 μm beam diameter (202 J/cm2 peak fluence with 469 Ω total contact resistance) at (a) 44° tilt and (b) no tilt. EDS maps for (c) aluminum (no tilt).

3.3.2.2 Solidification Structures

The solidification behavior will be dictated by the relationship between the temperature gradients and liquid/mushy zone growth rate, which will depend largely on the selection of laser processing parameters [21]. During rapid solidification of the laser-fired contact, the resulting microstructure will be dependent on the temperature gradient (G) at the liquid/mushy zone interface, the solidification growth rate (R) of this interface, the amount of constitutional supercoiling, and the alloy composition. The mushy zone represents the two-phase regions shown in the equilibrium phase diagram in Figure 3.9 [26] where liquid + Si or liquid + Al are present. Constitutional supercooling corresponds to the level to which the liquid alloy of a particular composition is cooled below its equilibrium liquidus temperature. As the level of constitutional supercooling increases, the type of solidification structure will change from planar to cellular to dendrites to equiaxed dendrites [30].

In order to understand the influence of pulse duration on the solidification structure, a comparison of the top surface regions of three contacts processed with 112 W laser power, a 50 μm beam diameter, and 40 μs, 50 μs, and 100 μs pulse durations is made. Figure 3.14 shows different solidification morphologies that are observed along the top surface of the contacts as a function of changing pulse duration. The regions that have been analyzed from the top surface micrographs in Figure 3.14(a) through (c) are outlined in the orange box. As the pulse duration is increased, the total energy density and heat input to the contact will increase. With the larger energy density associated with a 100 μs pulse duration as shown in Figure 3.14(f), the cooling rate, which is the product of G and R, will be the lowest [21]. A slower cooling rate will lead to an increase in the solidification structures. As shown in Figure 3.14(f), the lower cooling rate produces the solidification substructures that are approximately 2 times larger in width than those observed in Figure 3.14(e) when using a 50 μs pulse.
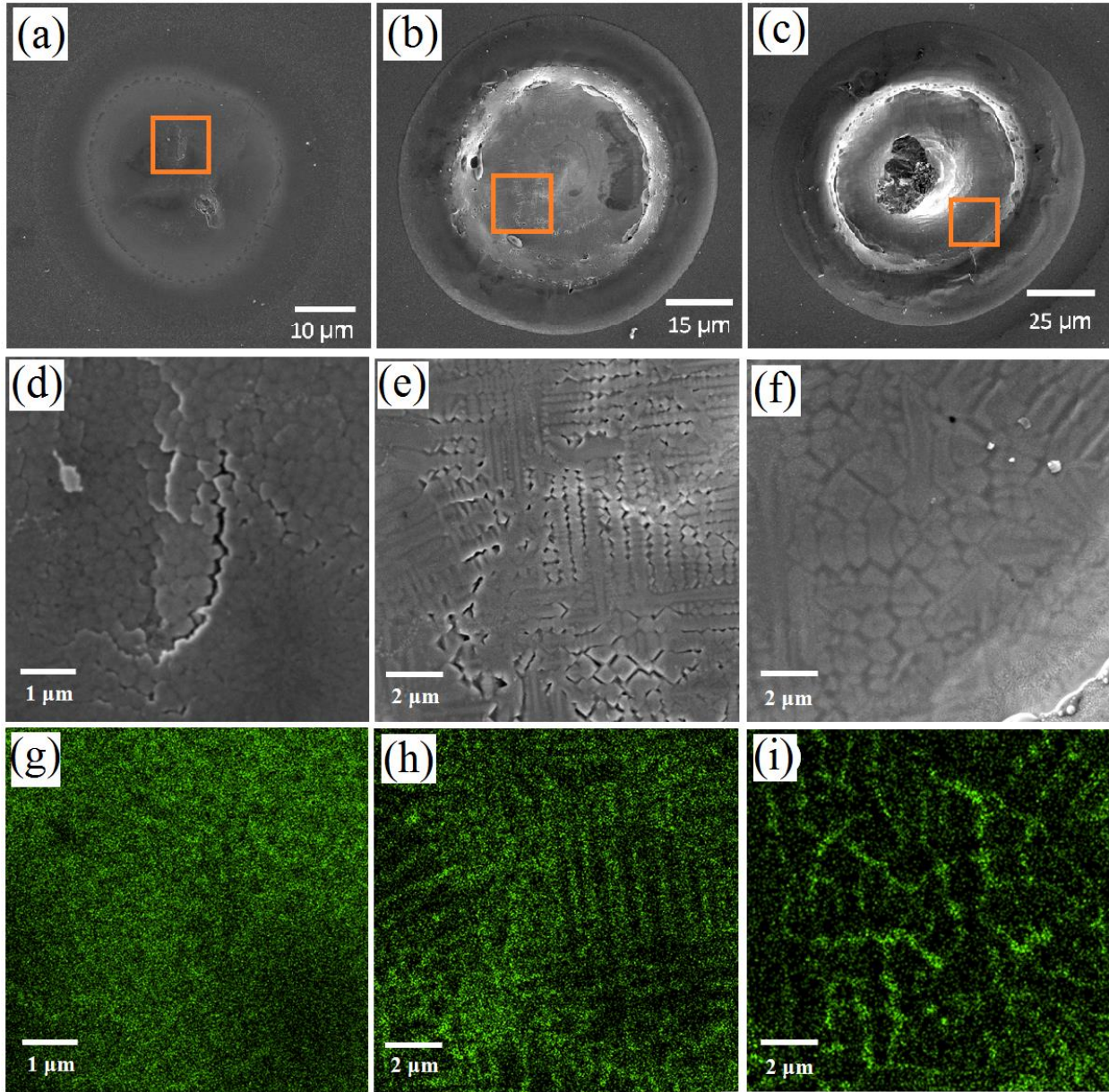
Figure 3.14. SEM micrograph and corresponding EDS map for contacts processed with 112W laser power, 50µm beam diameter and (a),(d),(g) 40µs, (b),(e),(h) 50µs, & (c),(f),(i) 100 µs. Green corresponds to aluminum and black to silicon.

The solidification morphology is dictated by the ratio of G/R, and as the value of G/R increases, the morphology will change from equiaxed dendrites to cellular-dendritic to cellular morphology [30]. In Figure 3.14(d), the solidification structure appears to be more equiaxed versus cellular dendrites and cells shown in Figure 3.14(e) and Figure 3.14(f), respectively. The size and morphology of the solidification structures may influence device performance depending on the nature of the crystalline defects, which can serve as recombination sites for electron-hole pairs. This influence needs to be determined by measuring carrier lifetimes and correlating them to the observed microstructures.

Figure 3.14(g) through Figure 3.14(i) show the corresponding EDS maps for the contacts shown in the SEM micrographs. The green and black regions correspond to Al and Si, respectively. At a pulse duration of 40 µs, shown in Figure 3.14(g), the region is primarily composed of Al with Si present at the boundaries of the equiaxed structures. At this point in processing, it is likely that Si is diffusing into the sputtered Al metallization due to rapid interdiffusion of Si into Al at elevated temperatures [28]. As Si is incorporated into the Al film, a second phase will form and the the liquidus temperature to the left of the eutectic composition will decrease, according to the equilibrium Al-Si phase diagram.

As the pulse duration is increased to 50 µs, the dendrites that form are primarily Si (black) with Al at the boundaries. During solidification of the melt pool from above the appropriate liquidus temperature, the Al will be rejected from the solidifying Si to the liquid phase until the eutectic transformation temperature is reached. In addition, due to the rapid cooling rates associated with laser processing [21], the system cannot maintain an equilibrium composition throughout the solidification process, and compositional gradients will be observed within the solidification structures. In this case, the Al becomes concentrated within the interdendritic region, due to the limited solid solubility of Al in Si as seen in the Al-Si phase diagram. For the longest pulse duration of 100 µs, similar microsegregation of the Al is observed in the EDS map. The cells are primarily composed of Si (black) whereas the intercellular regions are composed of high concentrations of Al (green).

Additional imaging of the LFC cross sections performed using an ion beam revealed no contrast in the various crystalline substructures, suggesting that the resolidification occurs as a single crystal because of epitaxial growth. Similar behavior has also been observed in high energy density welding of single-crystal nickel-based alloys [31]. The solidification substructures (i.e. dendrites and cells) will, however, possess different orientations based on the preferential growth directions of the solidifying melt pool from the fusion boundary of the contact [31]. Although more data is required to conclusively determine the influence of alloying on solidification and device performance, the results suggest that Al is heavily alloyed with Si throughout the melt pool when using microsecond pulse durations.

3.3.3 Impact of Laser Processing on Passivation Layer

In order to form an Al-Si contact, the passivation layer must first be removed during processing to allow Al and Si to mix within the contacted region. At the same time, the passivation layer should be preserved outside the LFC to achieve high energy conversion efficiencies. In this section, materials characterization methods are used to determine how laser processing parameters influence both the breakdown of the passivation layer within the LFC and the passivation layer quality surrounding the LFC.

3.3.3.1 Characterization of the Passivated Regions

Removal of the passivation layer, which is a prerequisite for mass transfer of Al and Si during LFC formation, is likely driven by reduction of the SiO_2 passivation layer by the Al metallization layer, melting and dissociation of the SiO_2 or a combination of both. It has previously been observed that accelerated breakdown of the SiO_2 dielectric passivation layer in $Al/SiO_2/Si$ structures can initiate at the Al/SiO_2 interface at temperatures as low as 500K [32] by the following reduction reaction:

$$4\,Al + 3\,SiO_2 \rightarrow 2\,Al_2O_3 + 3\,Si \tag{3.4}.$$

Although the solid-state reduction reaction (3.4) is thermodynamically favorable, possessing a negative free energy [32], Tsukada *et al* [33] and Olsen *et al* [34] demonstrated that the reduction of SiO_2 by Al is a self-limiting reaction at the Al/SiO_2 interface for SiO_2 thicknesses greater than 3.5 nm. As the SiO_2 is reduced and the interfacial Al_2O_3 becomes sufficiently thick, Al cannot diffuse to the original Al/SiO_2 interface for the reaction to continue. Although these experiments [33,34] were performed at much lower temperatures (773K) with significantly longer processing times than those expected during laser processing, the SiO_2 layer used here is nearly 100 nm, and it can be anticipated that the reaction will still be diffusion-limited upon the formation of the Al_2O_3. Therefore, this is not likely the method by which the passivation layer breaks down during contact formation.

Numerical simulations of the LFC process under microsecond pulses [24] have shown that substrate temperatures rapidly exceed the melting temperatures of Al, Si and SiO_2 due to the high energy densities associated with laser processing. In addition, the total energy required for heating and melting the respective Al, Si and SiO_2 regions assuming a hemispherical LFC shape with an LFC with a 50 µm contact radius is on the order of 10^{-7} kcal. This value is calculated considering the total energy required to heat and melt each constituent based on the corresponding mass, specific heat, and latent heat of fusion. Since sufficient energy is supplied to heat and melt the entire LFC region, the removal of the passivation layer will be governed by the melting and dissociation of the SiO_2. As the SiO_2 dissociates into Si and O_2 during contact formation, Al will react with the free O_2 to form Al_2O_3 at the periphery of the inner contact region, which can be observed in Figure 3.15. Figure 3.15(b) and Figure 3.15(c) show the passivated regions adjacent to the LFCs processed with 40 µs and 50 µs pulse durations, respectively.
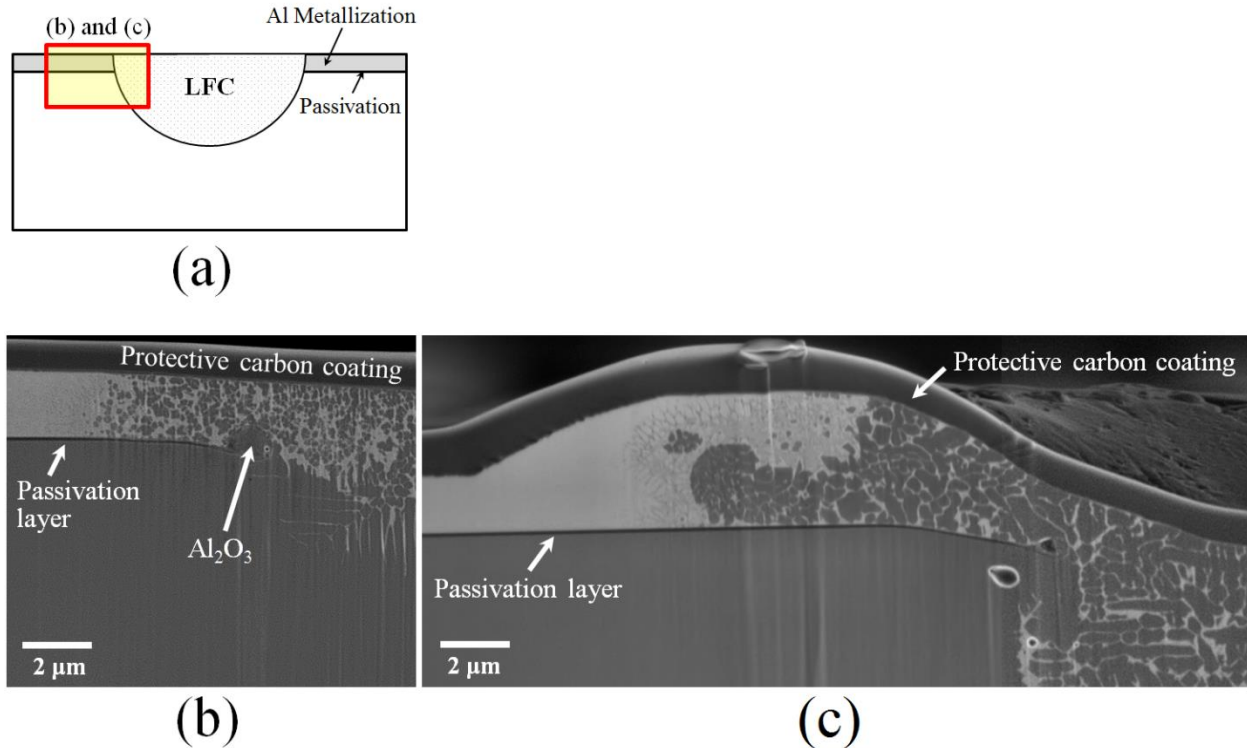
Figure 3.15. Close up of cross-sectional regions near the passivation layer, as shown in the red box within the (a) schematic, for LFCs processed with 112W laser power, a 50μm beam diameter, and pulse durations of (b) 40μs (c) 50μs.

For the contacts shown in Figure 3.15(b) and Figure 3.15(c), the passivation layer is completely removed within the LFC center, possesses a reduced thickness close to the passivation layer/LFC boundary, and retains its original form and thickness (100 nm) away from the contact center. The passivation layer terminates in Al_2O_3 that has accumulated at the passivation layer/LFC interface, as indicated on the contact processed with the 40 μs pulse. The presence of Al_2O_3 in the region where the passivation layer terminates was confirmed via EDS measurement. The formation of Al_2O_3 at the LFC/passivation layer boundary is consistent for the majority of cases considered.

Figure 3.16 shows an SEM micrograph and EDS maps for O_2, Al, and Si taken close to the right side LFC boundary for the contact processed with a 50 μs pulse, as identified in Figure 3.16(a). In Figure 3.16(a), the point marked with a cross has a concentration of approximately 53 wt.% Al and 47 wt.% O_2 (as measured by EDS), which is in excellent agreement with the expected stoichiometric balance for Al_2O_3. Figure 3.16(b) shows that O_2 is only detected at specific locations along the LFC fusion boundary and at corresponding circumferential locations on top of the outer ring. Al is also detected at the same locations, as shown in Figure 3.16(c), whereas Si is not, as shown in Figure 3.16(d). The results suggest that as the melt pool grows radially and the passivation layer is melted, the O_2 will continue to react with

73

the Al to form Al_2O_3 at the passivation layer/LFC fusion boundary since this reaction is thermodynamically favorable, possessing a lower standard free energy of formation than SiO_2 [35]. In addition, since Al_2O_3 is also present on top of the solidified LFC outer ring, Al_2O_3 particles will be ejected from the melt pool along with Al and Si as metal expulsion occurs.
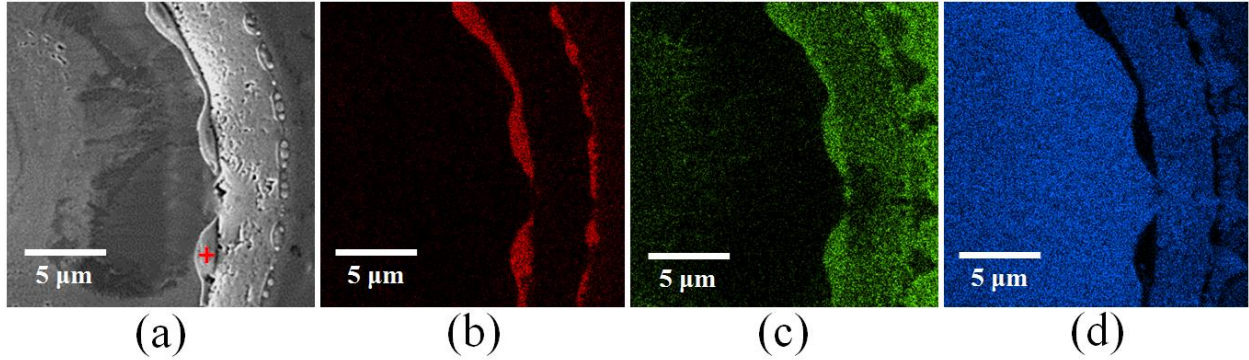
Figure 3.16. Top surface (a) SEM micrograph and EDS maps for (b) O_2, (c) Al, and (d) Si for LFC processed with 112 W laser power, a 50 μm beam diameter, and a 50μs pulse. EDS measurement at red cross corresponds to concentration of 45.7 wt.% O_2 and 54.3 wt.% Al.

The influence of laser processing on the region surrounding the passivation layer is also observed in Figure 3.17 and Figure 3.18. Figure 3.17 shows an SEM micrograph and corresponding EDS maps for O_2, Al, and Si close to the LFC/passivation layer interface for the contact processed with the 112 W laser power, a 50 μm beam diameter, and a 50 μs pulse. In this case, significant metal expulsion was observed, which indicates that operating temperatures within the molten region are greater than the boiling point for the alloying elements. Despite the high molten pool temperatures, it can be observed in Figure 3.17(b) that there is a clear red line that is present outside of the LFC region, which corresponds to the original SiO_2 passivation layer. Therefore, the passivation layer does not melt outside the LFC despite these temperatures.
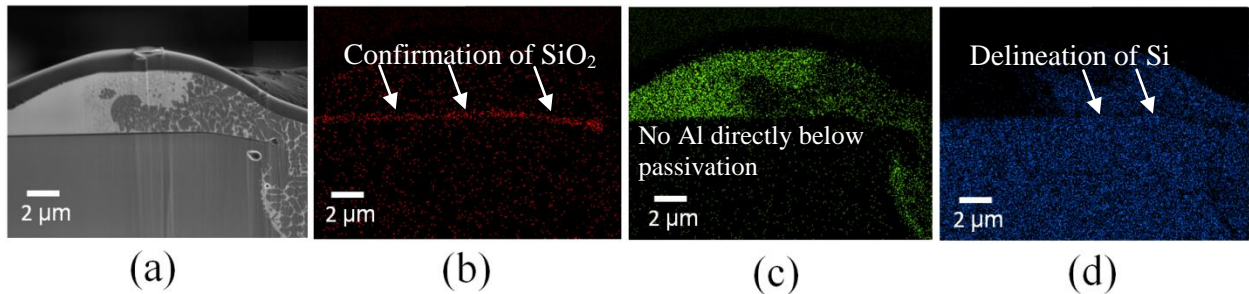
Figure 3.17. Cross section for contact shown in processed with 112W laser power, 50 μs pulse duration, and a 50 μm beam diameter of (a) SEM cross section, and EDS maps for (b) oxygen (red), (c) aluminum (green) and (d) silicon (blue).

74

The influence of processing with longer pulse durations on the passivated region outside of the molten zone can also be observed in Figure 3.18, which shows a contact processed using a 50 µm beam diameter, 65 W laser power, and a 500 µs pulse duration. Figure 3.18(c) shows a cross-sectional view of the hemispherically-shaped contact at the location indicated in Figure 3.18(a). In Figure 3.18(b), there is visible re-solidification of the doped Si region. Although there are some limitations to what can be resolved because the FIB process did not allow for a perfectly clean cross-section to be produced, certain features can be identified. For example, a close-up image of the region identified in Figure 3.18(b) near the passivation layer is shown in Figure 3.18(c).

The preservation of the passivation layer is further confirmed within the regions outside of the LFC in Figure 3.18(e) and Figure 3.18(f), which are identified in the EDS map for Al in Figure 3.18(d). The passivation layer breaks down within the regions directly under the laser heat source, yet it remains intact towards the edges of the contacted region. It can therefore be inferred that the SiO_2 passivation layer outside of the resolidified, Al-alloyed region can withstand the laser energy associated with longer microsecond pulse durations. SiO_2 has a melting temperature that is greater than those of both Al and Si. Therefore, the regions outside the LFC, which can be at temperatures no greater than the melting temperature of Si, do no melt. Since the passivation layer remains intact beneath these surrounding regions, the recombination rates at this interface should remain much lower than the metallized regions.
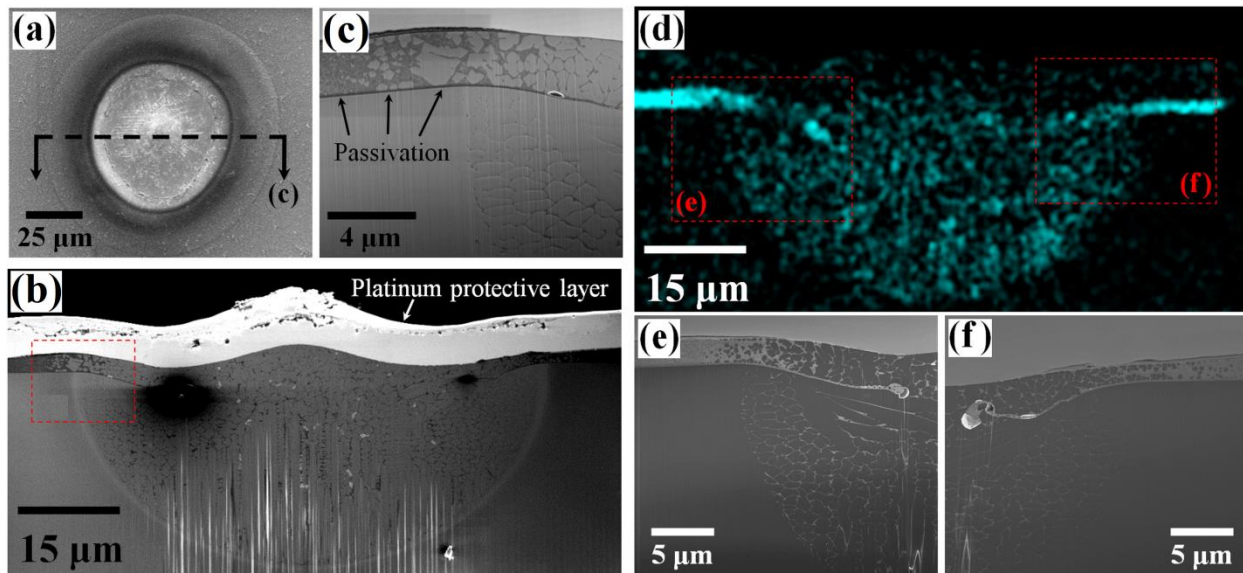
Figure 3.18. SEM micrographs of (a) top surface, (b) cross section of entire contact area, (c) zoomed in cross section of identified location in (b), (d) Al EDS map of cross section in (c). Locations (e) and (f) are zoomed in cross section locations identified in (d) however FIB polished back ~ 1 µm from the original surface in (c). LFC processed with IPG 1070 nm laser using 65 W laser power and 0.5 ms pulse on p-type silicon wafer with 100 nm SiO2 passivation and 2µm Al metallization.

75

3.3.3.3 Voiding during Contact Formation

As the passivation layer breaks down at the periphery of the LFC fusion boundary during contact formation, voiding is observed in certain samples within the crystalline Si near the LFC/wafer interface directly below the passivation layer. For the contacts processed with 112 W laser power, a 50 μm beam diameter and 40 μs and 50 μs pulse durations, voiding is observed close to the opening in the passivation layer, as shown in Figure 3.19. Voiding in diffusion couples between two metals is generally governed by the Kirkendall effect [36]. The Kirkendall effect is characterized by the formation and coalescence of vacancies in a multi-element structure caused by the difference in the diffusion rates of the various species. During laser processing, Si atoms from the crystalline Si wafer will rapidly diffuse into the liquid or two-phase (liquid + Si) microstructure present at the LFC/wafer interface. Assuming a diffusion coefficient of 10^{-4} cm^2/s [36] for Si into the liquid phase, Si can travel over 0.6 μm in approximately 40 μs. The distance from the void to the LFC/wafer interface for the contact processed with a 40 μs pulse is approximately 1 μm. Therefore, void formation is most likely governed by the Kirkendall effect since solid-state diffusion of Al into the Si crystal lattice will be much slower [27]. With a solid-state diffusion coefficient for Al in Si on the order of 10^{-10} cm^2/s [28], there will not be sufficient time for the Al atoms to fill the void formed by diffusion of Si from the crystal into the molten LFC and Al metallization layer.

Voiding was not observed close to LFC/wafer fusion boundary for the contact processed with the 100 μs pulse duration, as shown in Figure 3.19(c). Numerical simulations of the laser spot welding process [21], which should behave similarly to the LFC process, have shown that increasing the pulse duration from 1 ms to 5 ms can lead to 4 fold increase in the solidification time. With substantially longer solidification times associated with longer pulse durations, there may be sufficient time for the voids to be filled by solid-state diffusion since the regions surrounding the molten pool will remain at elevated temperatures for longer time. The idea that longer processing times leads to less voiding is also supported by a comparison of the void size for the contacts processed with the 40 μs and 50 μs pulses. The void size is approximately 0.5 μm for the longer pulse duration in comparison to 0.7 μm for the shorter pulse duration. Additional cross-sectional data are required to conclusively determine if this phenomenon can be avoided by using longer pulse durations.
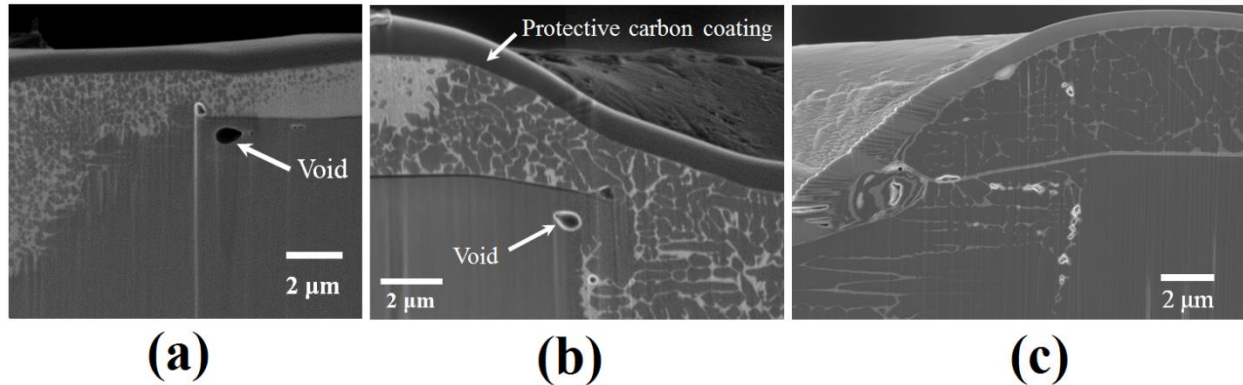
Figure 3.19. Formation of voids in crystalline Si below passivation layer for contacts processed with 112 W laser power, 50 μm beam diameter, and (a) 40 μs and (b) 50 μs pulse duration. No voids observed when processing with (c) 100 μs pulse.

3.3.3.4 Lifetime Measurements from Previous Study [14]

Previous work using millisecond pulse durations also supports the idea that the passivation layer is well preserved outside the LFC when processing with longer pulse durations. DeCesar [14] performed effective carrier lifetime mapping by microwave-photoconductive decay using a Semilab WT-2000. Prior to performing the measurements on the laser-processed samples, the Al was removed using Transcene Al Etchant Type D. Carrier lifetime mapping results were compared between LFCs processed with millisecond pulse durations varied between 4 ms and 19 ms using an IPG Photonics 1070 nm single mode fiber laser, and LFCs processed using a Coherent AVIA laser that utilized 30 nanosecond pulse durations. A brief summary of the carrier lifetime mapping results is provided here to support the idea microsecond pulse durations will not result in significant degradation of the carrier lifetime since the passivation layer is preserved outside of the immediate contact region as explained in the characterization work.

Figure 3.20 shows a carrier lifetime map for a wafer with the dual stack passivation before laser firing and then post-firing with both laser systems using millisecond and nanosecond pulse durations. Figure 3.20(a) shows that the lifetime is nearly uniform at 600 μs across the wafer prior to processing. Figure 3.20(b) shows the wafer after laser firing under various conditions, which are identified in Figure 3.21. The map shows that the lifetime has degraded significantly after processing, suggesting that the laser processing can adversely impact carrier lifetime when processing with either nanosecond or millisecond pulses. The drastic reduction in the carrier lifetimes after processing will be due to the damage to the passivation layer, which can increase surface recombination velocity, and/or the introduction of defects to the Si, which can reduce the bulk carrier lifetime.

Figure 3.21 shows the carrier lifetime map seen in Figure 3.21(b) after annealing the substrate at 275°C for 10 minutes. The laser system, processing parameters, and approximate carrier lifetimes from

the contour plots can be viewed in the included tables. The map demonstrates that the carrier lifetimes have been restored on numerous pads that were laser-fired. In addition, the maps demonstrate that carrier lifetime can be recovered post laser-processing without inflicting damage to the surrounding regions. The greatest improvements were observed on the contacts processed with the IPG 1070 nm fiber laser using millisecond pulse durations and, in the majority of cases, the values approached those for the unprocessed wafer for duplicated laser processing parameters. However, in one case, the carrier lifetime map for contacts processed with identical conditions, such as locations 5 and 6, which were processed with 45 W laser power and a 4 ms pulse duration, exhibited entirely opposite behavior. Location 5 has extremely poor lifetime whereas location 6 has excellent recovery after annealing. The low sensitivity of lifetime measurements is likely caused by the low contact area fraction used in the study, which was on average 0.2%. The use of a higher area fraction would improve the response of the measurements to the laser processing conditions.

LFCs processed with the pads fired with nanosecond pulse durations using an AVIA 355 nm frequency tripled laser [14] did not recover lifetime to the same extent as the millisecond processed contacts. The substantially lower carrier lifetime results suggest that although the contacts were processed with 30 ns pulses, the passivation layers were degraded. The processing of contacts with nanosecond pulses results in significant ablation of Si, Al, and the passivation layer from the laser-affected region, which may adversely effective carrier lifetime. In the study, however, the contact area fractions were not controlled to ensure consistency between the two studies. Although more data are required to quantitatively evaluate the impact of longer pulse durations on carrier lifetime, the results are encouraging and suggest that damage to the passivation layer and/or damage within the Si may not be as extensive as often believed. Furthermore, when considering microsecond pulse durations, all the cross-sectioned LFCs used in this study indicate that processing with microsecond pulses should not result in significant deterioration of the passivation layer outside of the inner LFC melt region. The carrier lifetime measurements support this observation.
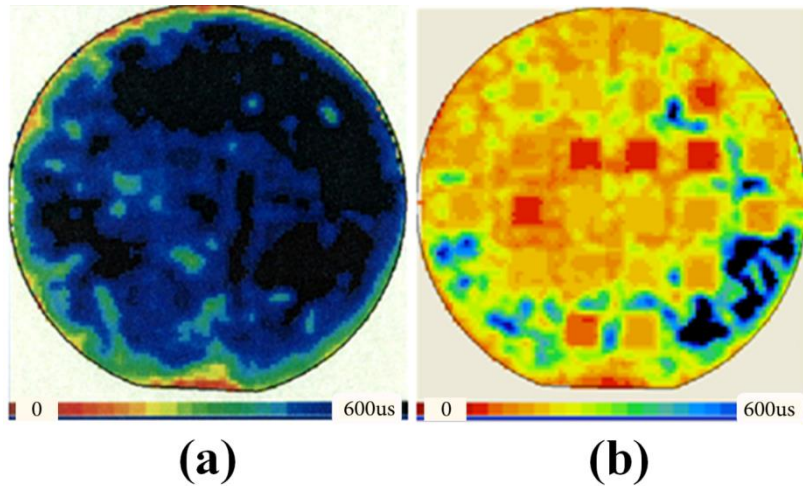
Figure 3.20. Carrier lifetime maps for substrate: (a) with passivation only (no firing), and (b) after laser firing and removal of Al layer (conditions detailed in **Figure 3.21**). [14]

| | 1070 nm | | | | 355 nm | | |
| | IPG Fiber Laser | | | | AVIA Q-Switched | | |
ID	Power (W)	Pulse (ms)	Lifetime (µs)	ID	Shots	Freq. (kHz)	Lifetime (ms)
1	23	6.5	~ 600	9	1	5	~ 600
2	23	6.5	~ 600	10	1	5	~ 300
3	23	21.5	~ 600	11	1	50	~ 270
4	23	21.5	~ 600	12	1	50	~ 330
5	45	4	~ 60	13	5	5	~ 90
6	45	4	~ 600	14	5	5	~ 540
7	50	14	~ 540	15	5	50	~ 90
8	50	14	~ 480	16	5	50	~ 120
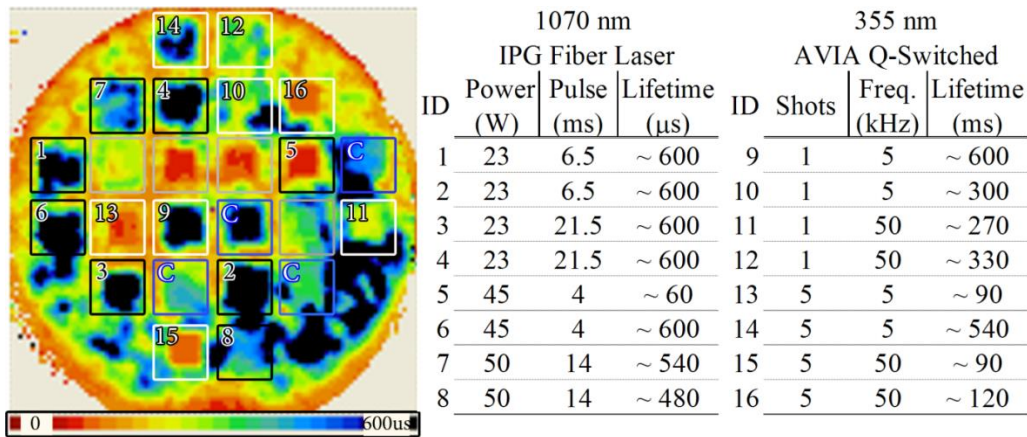
Figure 3.21. Carrier lifetime map for substrate after laser firing, removal Al and annealing at 275°C for 10 min with corresponding laser parameters. Contacts fired with 1070 nm fiber laser outlined in black with ID numbers 1-8. Contacts fired with 355 nm frequency doubled Q-switched laser outlined in blue with ID numbers 9 - 16. Other regions are not applicable. [14].

3.4 Impact of Laser Processing on Contact Resistance

It is important to form low resistance contacts to reduce the overall rear side series resistance on passivated rear surface photovoltaic devices. In this section, LFCs produced with microsecond pulses are electrically characterized via measurements of total contact resistance to determine the influence that laser processing parameters and contact geometry have on total contact resistance. In addition, device simulations are performed using the Sentaurus TCAD Software to evaluate the impact that contact geometry has on total contact resistance.

3.4.1 Total Contact Resistance Measurements

The total contact resistance, R_{LFC}, has been related to contact geometry when using nanosecond [19] and millisecond [15] pulse durations. R_{LFC} is related to the spreading resistance, R_S, and the individual contact resistance, R_C as [19]:

$$R_{LFC} = R_S + R_C \qquad\qquad (3.5).$$

The spreading resistance for an LFC processed with nanosecond pulse durations is typically calculated using the Cox-Strack relationship for a planar, two-dimensional contact [37]:

$$R_S \cong \frac{\rho_b}{2\pi r} arctan\left(\frac{2W}{r}\right) \qquad\qquad (3.6)$$

where ρ_b is the base resistivity, r is the contact radius, and W is the wafer thickness. The individual contact resistance is calculated as:

$$R_C \cong \frac{\rho_{cef}}{\pi r^2} \qquad\qquad (3.7)$$

where ρ_{cef} is the effective specific contact resistance (Ω cm^2). The value of R_{LFC} should approach the spreading resistance as the contact quality improves and the contribution from the specific contact resistance at the Al/Si interface becomes negligible.

In order to determine the total contact resistance for the LFCs generated in this study, a probe station and a Keithley 4200 semiconductor characterization system were used. For the resistance measurements between two contacts, four probes were used to eliminate the resistance contribution from the wiring and probes. Since the LFCs were processed on the front side of the substrate and it was not possible to make a low-resistance connection with the rear side of the wafer to make a through-thickness measurement, a method was developed to quantify the individual total contact resistance from the front side. The resistance between a pair of electrically-insulated contacts ($R_{x/y}$, $R_{y/z}$, or $R_{z/x}$) was measured from the front side of the wafer and can be expressed as:

$$R_{x, y, or z} + R_{x, y, or z} = R_{x, y\ or\ z/x, y\ or\ z} \qquad\qquad (3.8)$$

where $R_{x,y,or\ z}$ is the individual contact resistance, $R_{x,y,or\ z/\ x,y,\ or\ z}$ is the resistance in Ω between two pairs of contacts, and the subscripts x, y or z pertain to the two contacts in series contributing to the measured resistance ($R_{x/y}$, $R_{y/z}$, or $R_{z/x}$). Resistance contributions from the wafer base resistivity due to the distance

between contacts were assumed negligible since the measured resistances were significantly greater than the expected contribution from this quantity.

Figure 3.22(a) and Figure 3.22(b) show schematic diagrams for the method used to measure the resistance between two contacts. In Figure 3.22(a), the resistances ($R_{x/y}$ and $R_{z/x}$) are being measured between two pairs of contacts (R_x/R_y and R_x/R_z). For clarity, the contact pairing between R_y and R_z (or $R_{y/z}$) is not shown. In Figure 3.22(b), an alternative configuration for the contact pairings is shown. Alternative pairings of contacts were used to evaluate the reproducibility of the measurement method, and the standard error associated with this measurement method is reported below. Using the measured resistances for the three pairings of contacts, each individual contact resistance was back calculated by simultaneously solving the following system of three equations:

$$R_x + R_y = R_{x/y} \tag{3.9}$$

$$R_x + R_z = R_{x/z} \tag{3.10}$$

$$R_y + R_z = R_{y/z} \tag{3.11}$$

For example, from Equations (3.9) through (3.11) and the measured resistance values for the three pairs of contacts, the individual contact resistance, R_x, was calculated as:

$$R_x = \frac{R_{x/y} - R_{y/z} + R_{x/z}}{2} \tag{3.12}$$

Using the calculated contact resistance, R_x, the two remaining values were calculated using Equation (3.9) and (3.10). For example, the resistance for R_y can be calculated from Equation (3.9) as:

$$R_y = R_{x/y} - R_x \tag{3.13}$$

The total contact resistance measurements determined from the aforementioned method and corresponding processing parameters are shown in Table 3.2 and Table 3.3 for 50 μm and 70 μm beam diameters, respectively. In order to evaluate the reproducibility of this technique, measurements were made between multiple pairings of contacts processed with significantly different laser parameters. The total contact resistances determined using this calculation procedure of simultaneously solving Equations (3.9) through (3.11) are shown in Table 3.4. The results were reproducible with less than 5% variation when different contact pairings were used. Therefore, the measurement system analysis demonstrates that the technique is reproducible and the contact resistance data are reliable. The total contact resistance

measurements are expected to be indicative of the spreading resistance from the contact. In addition, the contribution of R_C to R_{LFC} is not considered and assumed negligible based on the extremely low contact resistivities of 4 x 10^{-6} Ω-cm^2 for Si heavily doped with Al [38]. For an LFC with a 50µm radius, this corresponds to a resistance of 0.02 Ω, which is much lower than the measured total contact resistances shown in Table 3.2 and Table 3.3.
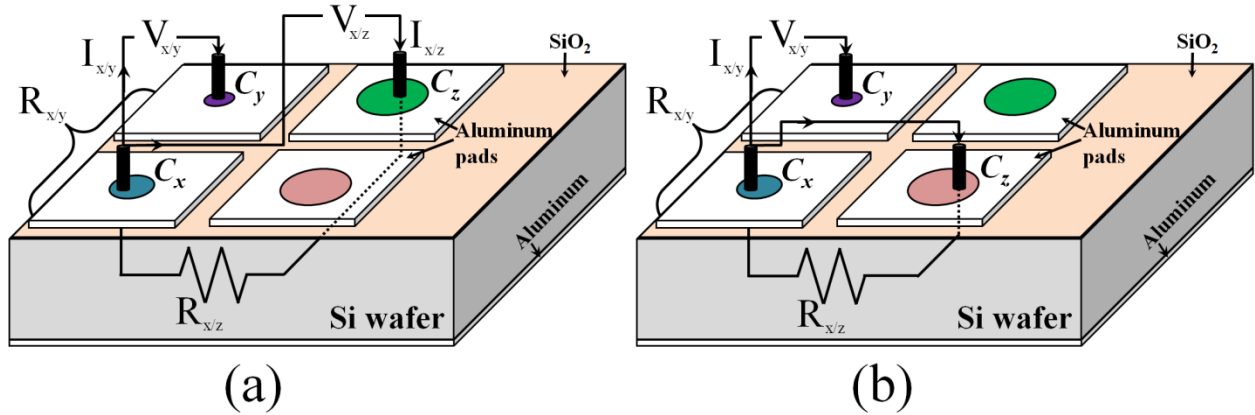
Figure 3.22. Different configurations of contact pairings used in (a) and (b) as a means to test the validity of back-calculating total contact resistance from this top surface measurement method.

Table 3.2 Measured total contact resistances (Ω) with corresponding processing parameters for 50µm beam diameter. NC signifies no contact formed with a measurable total contact resistance.

	Power (W)				
Time (µs)	112	159	260	360	460
20	NC	NC	582	477	498
30	NC	1097	347	288	348
40	NC	595	266	297	271
50	1183	358	284	263	206
75	668	296	241	223	–
100	361	263	233	204	172

* no data available for for 460 W, 75 µs pulse.

Table 3.3. Measured total contact resistances (Ω) with corresponding processing parameters for 70µm beam diameter. NC signifies no contact formed with a measurable total contact resistance.

	Power (W)					
Time (µs)	**159**	**210**	**260**	**312**	**360**	**460**
20	NC	NC	NC	NC	482	437
30	NC	783	469	393	292	--
40	1315	528	410	293	273	--
50	573	432	318	283	265	212
100	622	260	222	208	184	126

* no data available for for 460 W, 30 µs and 40 µs pulses.

Table 3.4. Standard error calculated for different contact resistance measurements.

Beam Diameter (µm)	Power (W)	Pulse (µs)	Contact Resistance Measurements (Ω)			Average (Ω)	Standard Deviation	Standard Error
			Reported	2	3			
50	112	100	361	362	362	361	0	0.09%
	360	40	297	297	298	297	0	0.14%
	360	50	263	262	264	263	1	0.32%
	460	20	498	484	487	489	6	1.26%
70	159	50	573	560	563	565	6	0.98%
	210	30	783	790	789	787	3	0.35%
	210	40	528	535	538	534	4	0.73%
	210	50	432	435	450	439	8	1.75%
	260	30	469	479	479	476	4	0.92%
	260	40	410	440	442	431	14	3.33%
	312	30	393	404	404	400	5	1.22%
	312	40	293	294	298	295	2	0.67%
	312	50	283	291	288	287	3	1.10%
	360	20	482	465	464	470	8	1.79%
	360	30	292	301	303	299	5	1.54%
	360	40	273	280	280	278	3	1.08%

3.4.2 Influence of Geometry on Total Contact Resistance

Total contact resistance is most often related to the contact geometry [15,19], and previous work [19] with LFCs has suggested that the inner crater size can be most accurately used to predict R_{LFC}. In order to understand the influence of processing parameters on R_{LFC} when using microsecond pulse durations, the total contact resistance is plotted as a function of LFC inner crater size in Figure 3.23. The spreading resistance assuming a planar contact has also been plotted as calculated by the Cox-Strack equation assuming a base resistivity of 9 Ω-cm. From Figure 3.23, it can be clearly observed that the Cox-Strack relationship for a planar contact drastically over-predicts the total contact resistance when increasing

contact diameters. Since the contacts have been shown to be heavily alloyed with Al within a three-dimensional contact area, the planar approximation for contact resistance is not valid for these contacts.
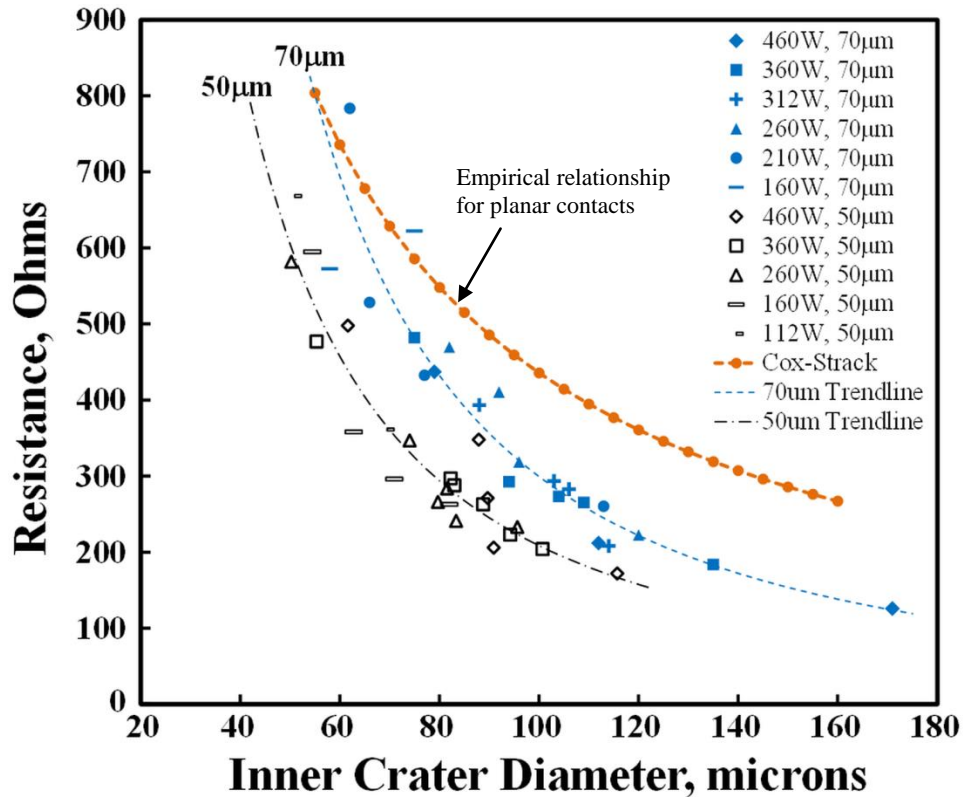
Figure 3.23. Total contact resistance as a function of inner crater diameter, laser power, pulse duration, and laser beam diameter. Trendlines for 50 μm and 70 μm beam diameters included for clarity.

It can also be observed that as the LFC inner crater diameter increases, the total contact resistance decreases when using either a 50 μm or a 70 μm beam diameter. As pulse duration and/or power is increased, the LFC inner crater diameter increases (as shown in Figure 3.6) and there will be a larger contact area regardless of beam diameter. Although the trend is the same regardless of beam size, a change in the beam diameter has a noticeable impact on the measured total contact resistance for two contacts with the same inner crater diameter. Specifically, the total contact resistance can be significantly lower for the same inner crater diameter when using the smaller 50 μm beam diameter. For instance, for an inner crater diameter of 100 μm, the contact resistance is approximately 220 Ω when using a 50 μm beam diameter, whereas it is nearly 330 Ω when using a 70 μm beam diameter. Since there is a clear difference observed in the total contact resistance despite an identical inner crater size, the results suggest that the contact area is governed by a larger region than the inner crater.

The contacts processed with a smaller beam diameter have smaller inner diameter, as observed in Figure 3.5, and should also have larger depths of penetration. It has been shown through numerical simulations of the LFC process [24] that when two contacts have the same top surface area, the one processed with a smaller beam diameter will have a larger depth of penetration since the laser intensity at the center of the beam is largest. As the irradiance increases through a reduction in beam size, the contact depth will grow, resulting in a transition in contact geometry from planar to half-ellipsoidal (with depth less than contact radius) to hemispherical (with depth equal to contact radius) to half-ellipsoidal (with depth greater than contact radius). Furthermore, the presence of Al at large depths within the resolidified Si will result in an interfacial LFC/wafer contact area that is not planar in shape. This variation in geometry is the primary contributor to the differences in the total contact resistances observed in Figure 3.23 when using different laser beam diameters despite having the same LFC top surface diameter. As the contact geometry varies, the interfacial LFC/wafer contact area will change.

The impact of the interfacial LFC/wafer contact area on the data was further evaluated by plotting total contact resistance as a function of the estimated interfacial contact area. Although the cross-sectional dimensions for the contacts are not known for all of the LFCs generated in this study, the influence of a three-dimensional surface area of the contact on total contact resistance can be predicted based on an anticipated surface area for a three-dimensional contact that possesses a hemispherical or a half-ellipsoidal shape. An approximate surface area for an ellipsoid, S, can be calculated using the Knud Thomsen approximation [39]:

$$S = 4\pi \left[\frac{d^p b^p + d^p c^p + b^p c^p}{3} \right]^{1/p} \qquad (3.14)$$

where p is a constant (1.6075), and d and b are the radii of the ellipsoid in the x and y directions, respectively, and c is the depth of the contact. When d, b, and c are equal, the surface area will correspond to that of a sphere. Due to the circular nature of top surface for the contacts produced, the values for d and b are equal and are known based on the top surface radii for the inner region of each contact shown in Figure 3.23. The surface area for our contacts calculated from Equation (3.14) will be half since we are only considering a hemisphere or half of an ellipsoid. Figure 3.24 shows a plot of the total contact resistance from Table 3.2 and Table 3.3 for 50 µm and 70 µm beam diameters, respectively, versus the estimated interfacial LFC/wafer contact area based on Equation (3.14) assuming a three-dimensional contact. The contacts produced with the 70 µm beam diameter are assumed to have a hemispherical shape (i.e. $c = d$) for a direct comparison with the contacts produced with a 50 µm beam.

The value for the depth of the contact, *c*, is plotted as equal to *d* and 2*d* for the contacts produced with a 50 μm beam to demonstrate the influence on contact depth on surface area and total contact resistance.

From Figure 3.24, it can be observed that when *c* equals *d* the trend for total contact resistance versus estimated surface area is the same as that observed in Figure 3.23 when plotting total contact resistance as a function of inner crater LFC diameter. When assuming that both contacts exhibit a hemispherical shape, the data suggests that a reduction in the beam diameter leads to a reduction in the total contact resistance. However, when the contact depth is doubled (i.e. *c* = 2*d*) for the 50μm beam diameter, the curve shifts to the right and the two data sets demonstrate excellent agreement. Previous modeling work on the contact geometry for laser-fired contacts [24] has shown that a reduction in beam diameter by 25 μm can cause the depth of penetration to increase by 1.5 times for the power levels considered in that study. Therefore, for two contacts processed with different beam diameter that have the same top surface diameter, it can be expected that the penetration depth will be larger for the contact processed with the smaller beam size. With a larger penetration depth yet similar top surface inner crater radius, the surface area of the doped recrystallization region will be greater for the contact processed with the smaller beam. As a result, the curve for the interfacial area of the contact produced with the 50 μm beam diameter shifts to the right.

Since the contacts produced with microsecond pulse durations are three-dimensional, the interfacial area between the LFC and the wafer will influence the total contact resistance in comparison to contacts produced with nanosecond pulses that exhibit planar contact areas, which can be accurately approximated using Equation (3.6). Based on the good agreement between the experiments and simulations for total contact resistance as a function of inner crater LFC diameter and the approximate interfacial contact area, it is clear that to obtain the lowest total contact resistance the contact dimensionality should be increased through appropriate selection of processing parameters. In order to more accurately study the impact of contact geometry on contact resistance device simulations have been performed.
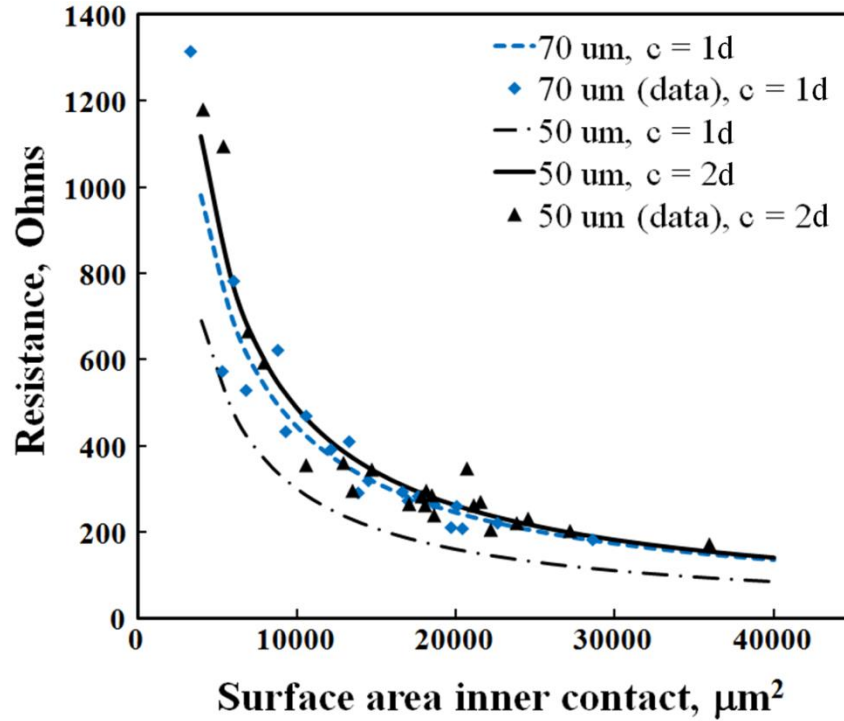
Figure 3.24. Contact resistance versus approximated inner crater spherical surface area for contacts processed with wide range of laser powers and 50μm and 70μm beam diameters.

3.4.3 Device Simulations

The influence of a three-dimensional contact geometry on total contact resistance was explored through modeling of the carrier transport by self-consistently solving Poisson's equation and the carrier continuity equation with drift-diffusion physics using the commercial software Sentaurus by Synopsis, Inc. Simulations were performed using a two-dimensional rectangular computational domain that was 500 μm thick based on the wafer thickness, and the length was equal to three times the thickness. The total contact resistances were then calculated for three-dimensional geometries using cylindrical symmetry. The substrate was modeled as doped p-type Si with a boron acceptor concentration of 1.5 x 10^{15} cm^{-3} [40] based on the known wafer base resistivity of 9 Ω-cm. The individual contact resistance, R_C, was assumed to be negligible due to the extremely low specific contact resistances on the order of 4 x 10^{-6} Ω-cm^2 known for Si very heavily doped with Al [38]. Simulations were performed assuming Al dopant densities of 2 x 10^{19} cm^{-3} based on experimental data for Al concentration in Si annealed at 800 °C [41]. Total contact resistance was determined from the slope of voltage/current plots that were generated for a DC bias of 0–2 volts between the top surface of the LFC with the bottom surface at ground.

LFC regions were modeled in two-dimensions as quarter-circles and quarter-ellipses as shown in Figure 3.25 with a contact diameter, *a*, and a contact depth, *c*. Furthermore, based on previous heat

transfer and fluid flow modeling of the transient growth of the laser-fired contact geometry which revealed that contacts processed with microsecond pulses are hemispheres or half-ellipsoids [24], the regions were cylindrically rotated within the device simulation software around the central axis to calculate the total contact resistance for a three-dimensional geometry. The heat transfer and fluid flow model revealed that a reduction in beam diameter by approximately 20 μm caused the depth of penetration to increase by 1.5 times for the power levels considered in that study, which would cause the LFC shape to change from a hemisphere to a half-ellipsoid and is the basis for using these two geometrical configurations. The contact diameter, a, was selected based on the values obtained from the experimental measurements for inner crater LFC diameter shown in Figure 3.23. For the ellipses, the depth, c, was taken as the same length as the contact diameter ($c = a$) to account for the change in penetration depth when processing with a smaller beam size as shown in the inset of Figure 3.26 .
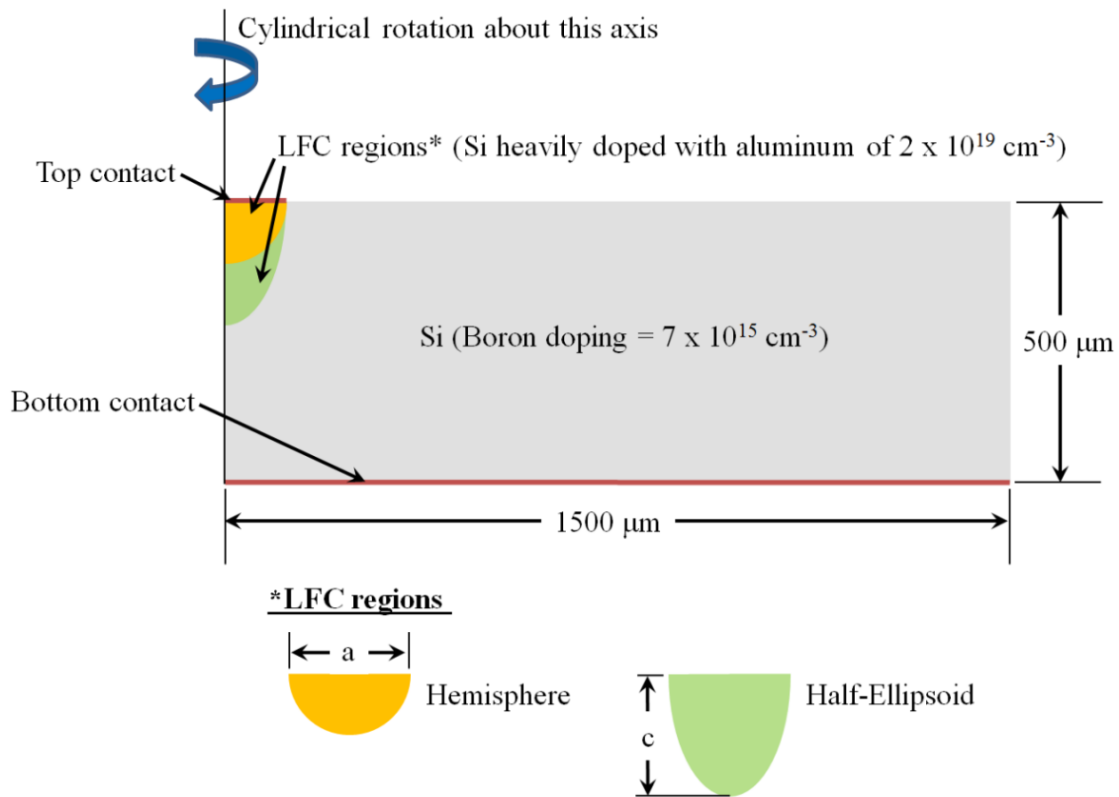
Figure 3.25. Sentaurus device simulation substrate and contact geometries, and relevant doping levels.
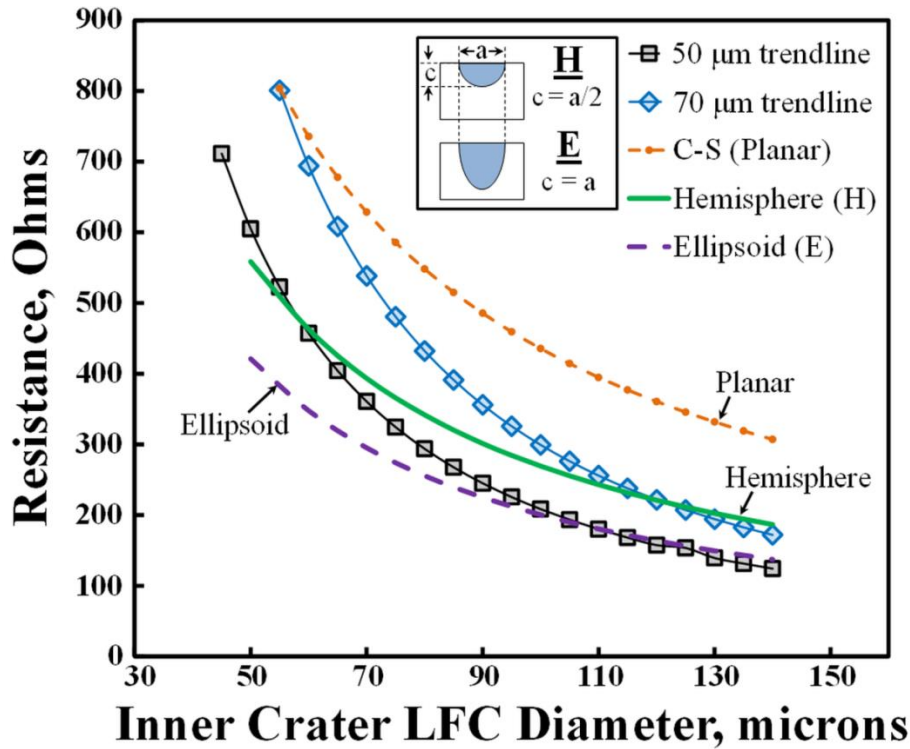
Figure 3.26. Device simulations for total contact resistance assuming hemispherical or half-ellipsoidal contact shape (with Al doping concentration of 2×10^{19} cm^{-3}) versus planar Cox-Strack (C-S) calculation and experimental values.

Figure 3.26 shows a plot of the total contact resistance for the experimental and simulated results as a function of the inner crater LFC diameter. In order to clearly distinguish the simulated results from the experimental results, experimental measurements are plotted as data points based on the trendlines shown in Figure 3.10 for the total contact resistance data for 50 μm and 70 μm beam diameters. When looking at the simulated contacts resistances for the hemispheres and the half-ellipsoids, it is clear that despite the fact that the inner crater LFC diameter is the same size, the total contact resistance is different. For instance, when the diameter is 90 μm, the contact resistance is 225 Ω for the half-ellipsoid versus 301 Ω for the hemisphere. Since the half-ellipsoid has a larger contact area at the LFC/wafer interface, the calculated spreading resistance is nearly 25% less, which explains the shift in the curves for the simulations when modeling a hemisphere versus half-ellipsoid.

The experimental total contact resistance data when processing with the 70 μm beam starts close to the planar approximation by the Cox-Strack equation [37] but deviates rapidly and approaches the values predicted for the hemisphere. Heat transfer and fluid flow modeling of the transient growth of LFCs when using microsecond pulse durations supports the idea that the contact will start off more planar but take on a more three-dimensional shape with increasing processing time [24]. At the onset of processing, the contacts processed with the larger beam will be more elliptical in shape with the depth, c, being much

smaller than the inner crater LFC diameter, *a*. Therefore, the resistance will be better predicted by a planar approximation. However, as the contact grows in size either by increasing laser power or through the use of longer pulse durations, the contact size will continue to grow into a hemispherical shape and the *c/a* ratio will increase from 0 to 0.5. As this occurs, the experimental data approaches the simulated data for total contact resistance of a hemisphere. This LFC shape has also been observed through heat transfer and fluid flow simulations in which it was shown that when processing with 25 W laser power and a 20 μm beam diameter, the *c/a* ratio was 0.2 after 1 μs and reached 0.43 by 30 μs.

Similarly, the contacts processed with the 50 μm beam diameter will take on a hemispherical shape more quickly due to the concentrated power density distribution predicted by Equation (3.1). As the duration of the laser pulse increases, the depth of penetration will increase and the *c/a* ratio will increase above 0.5. When the *c/a* ratio reaches 1, which corresponds to the simulated data for the half-ellipsoid shown, there is good agreement in total contact resistance between the experiments and simulations. Therefore, for two contacts processed with a different beam diameter yet possess the same top surface LFC inner crater diameter, it can be expected that the penetration depth will be larger for the contact processed with the smaller beam size, and total contact resistance will be lower. With a larger penetration depth yet similar top surface inner crater diameter, the contact area at the LFC/wafer interface will be greater for the contact processed with the smaller beam. As a result, we observe the shift in curves observed in Figure 3.23 when looking only at the top surface inner crater diameter.

The total contact resistance for LFCs processed with nanosecond pulse durations is best approximated by the Cox-Strack relationship [37]. For the contacts produced with the microsecond pulse durations, the total contact resistance is significantly lower depending on the contact geometry produced (i.e. half-ellipsoidal or hemispherical). When comparing the contact resistances presented in Figure 10 for planar and three-dimensional contacts, it can be observed that the total contact resistance is approximately 37% and 56% less than that predicted for planar contacts over the entire range of LFC diameters for hemispherical and half-ellipsoidal contacts, respectively. For example, for an LFC diameter of 80 μm, the total contact resistance is 541 Ω for a planar contact in comparison to 342 Ω for a hemispherical contact and 256 Ω for a half-ellipsoidal contact. Therefore, significant reductions in individual contact resistance can be achieved by employing three-dimensional contacts.

It is worth noting that with these processing conditions, the simulated data for the hemispheres and half-ellipsoids suggests that recrystallization depths with Al alloying greater than 100 μm can be achieved. Therefore, since the passivation layer remains intact outside of the inner crater region (as seen in Figure 3.10), it is possible that the larger contacts may improve carrier collection since photogenerated

carriers would not have to travel as far to reach the LFC. However, a contact that occupies a larger volume would reduce the available volume of Si for the photogeneration of carriers. Since these phenomena are at odds, it is important to experimentally quantify the impact on device efficiency. Nevertheless, based on the good agreement between the experiments and simulations for total contact resistance as a function of inner crater LFC diameter, it is clear that to obtain the lowest total contact resistance, laser processing parameters should be carefully selected when using microsecond pulse durations to optimize the *c/a* ratio while maximizing the area at the LFC/wafer interface without damaging the wafer.

3.5 Metal Expulsion during Contact Formation

As the molten pool surface temperatures exceed the boiling points for the alloying elements, metal expulsion can occur [12,22], resulting in the loss of Al and Si from the melt pool. If Al is removed from the melt pool, the contact quality may suffer due to insufficient alloying between Si and Al within the LFC. In addition, the onset of liquid metal expulsion is an indication that molten pool temperatures have exceeded the boiling points of the alloying elements. In this section, materials characterization is used to identify the conditions for the initiation of liquid metal expulsion, and theoretical calculations of the forces acting on a molten pool are used to explain the factors governing liquid metal expulsion. By understanding how processing parameters influence the onset of liquid metal expulsion, the loss of Al and Si from the contact zone can be prevented while avoiding excessively high operating temperatures.

3.5.1 Onset of Liquid Metal Expulsion

Various laser-material interaction modes from initial melting to metal expulsion are observed during LFC formation as a result of changes in pulse duration, laser power, and laser beam diameter as shown in Figure 3.5. The onset of liquid metal expulsion can be observed in the SEM micrographs shown in Figure 3.27 for two contacts processed with different power levels and a 50 μm laser beam diameter. The onset of liquid metal expulsion results in the formation of a raised lip at the periphery of the molten pool [42], which can be clearly identified from the SEM micrographs. For the contact processed with 112 W laser power, liquid metal expulsion occurs between 40 μs and 50 μs. An increase in laser power from 112 W to 159 W leads to faster onset of liquid metal expulsion between 30 μs and 40 μs. For higher power levels, liquid expulsion metal expulsion is observed at all processing conditions, as shown for the LFCs made with 260 W laser power in Figure 3.27(c). The formation of this region is a consequence of the force exerted on the molten pool surface due to rapid vaporization of alloying elements from the surface of the melt pool [22]. In order for metal expulsion to occur, the vapor recoil force on the surface of the

melt pool must exceed the surface tension force of the liquid metal at the periphery of the molten pool [14,17].
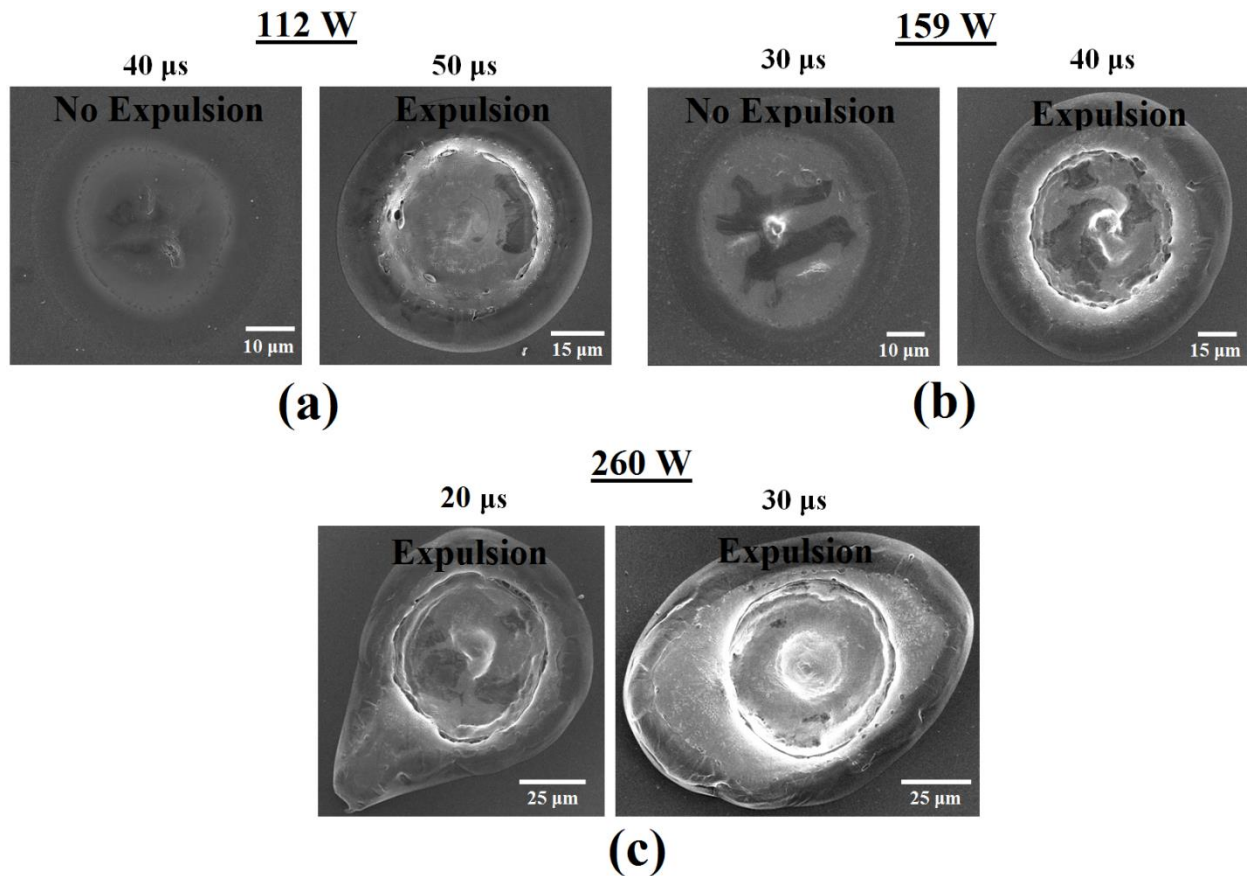
Figure 3.27. SEM micrographs indicating onset of liquid metal expulsion for contacts processed with 50 μm beam diameter and (a) 112 W laser power and pulse durations of 40 μs and 50 μs, (b) 159 W laser power and pulse durations of 30 μs and 40 μs, and (c) 260 W laser power and pulse durations of 20 μs and 30 μs.

The impact of using a larger beam diameter on the onset of liquid metal expulsion can also be observed in Figure 3.28, which shows SEM micrographs for irradiated samples as a function of laser power and pulse duration. When using 112 W laser power and 70 μm beam diameter, liquid metal expulsion is not observed experimentally regardless of the pulse duration (up to 1000 μs), as shown in the figure. The contact diameter appears to reach a steady state diameter value by 500 μs with little growth in contact diameter after this time. An increase in the power level from 112 W to 159 W leads to the onset of liquid metal expulsion between 200 μs and 500 μs. Further increasing the power levels leads to the onset of liquid metal expulsion sooner in the processing window. For example, at 360 W laser power, expulsion is observed at the lowest processing pulse duration of 20 μs.

EDS mapping provides a more complete picture of the progression of liquid metal expulsion. SEM micrographs and the corresponding EDS maps for the top surface of three LFCs formed when using 112 W laser power, a 50 µm beam diameter, and pulse durations of 40 µs, 50 µs, and 100 µs are shown in Figure 3.29. The EDS maps shown in Figure 3.29(d) through Figure 3.29(f) illustrate the top surface distribution of Al (green), Si (blue), and O_2 (red) for each contact. For the contact processed with a 40 µs pulse, the outer ring is composed primarily of Al, whereas the inner contact region is composed of both Al and Si. Alloying of Al and Si within this inner LFC region takes place after an opening in the SiO_2 passivation layer forms and will be driven by interdiffusion of Al and Si at the onset of contact formation. After initial contact formation around 40 µs, the molten pool surface temperatures should be substantially lower than the boiling points of Al and Si. With surface temperatures below the boiling points of the alloying elements, vaporization of Al and Si will not occur. With no vapor recoil force on the surface of the melt, deformation of the LFC surface and formation of the raised lip at the periphery of the melt pool are not observed, as shown in Figure 3.30, which is a plot of solidified LFC surface topography for each contact, which was obtained from the optical profilometry data.
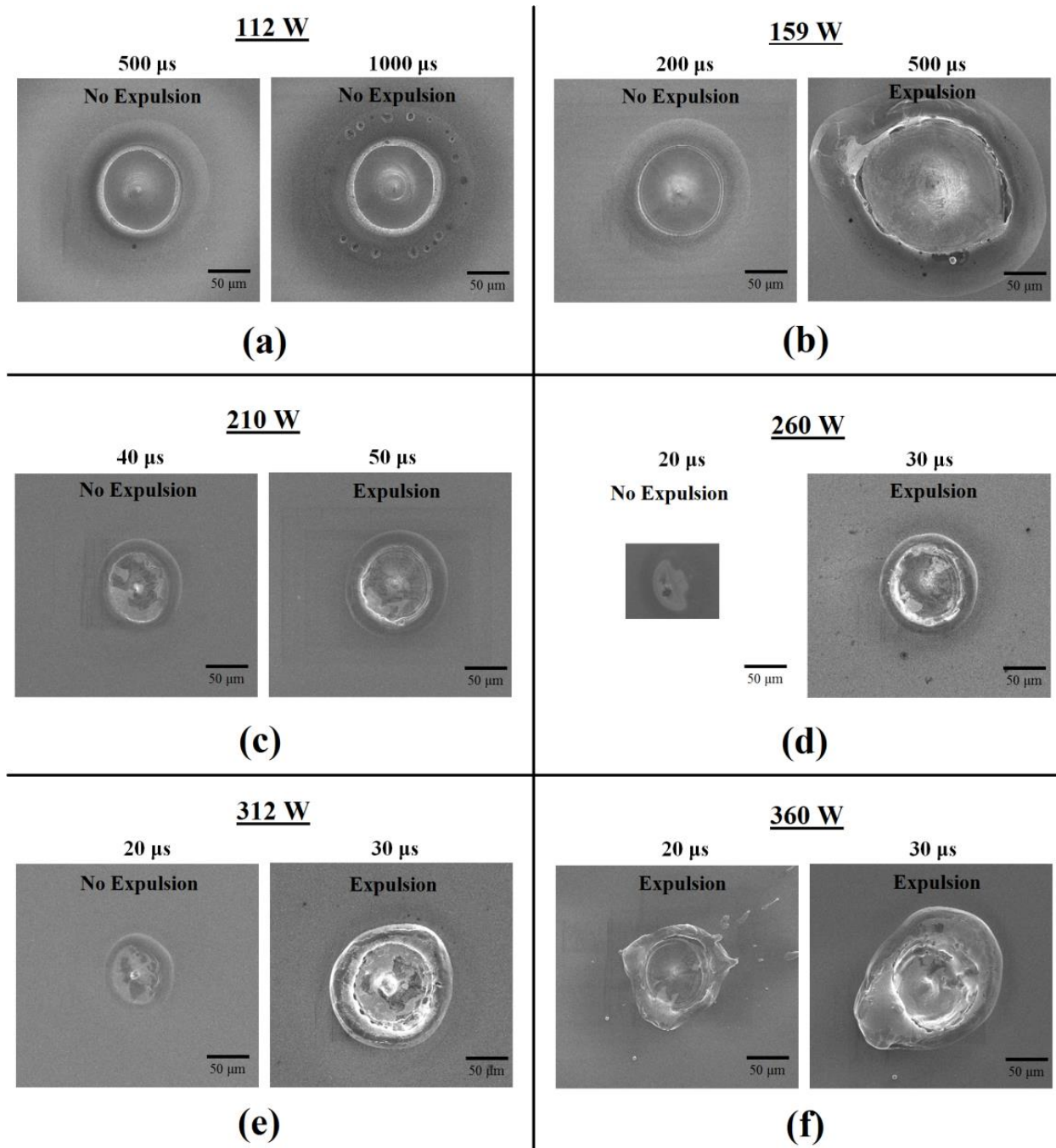
Figure 3.28. SEM micrographs indicating onset of liquid metal expulsion for contacts processed with 70 µm beam diameter and (a) 112 W laser power, 500 µs and 1000 µs pulse durations; (b) 159 W laser power, 200 µs and 500 µs pulse durations; (c) 210 W laser power, 40 µs and 50 µs pulse durations; (d) 260 W laser power, 20 µs and 30 µs pulse durations; (e) 312 W laser power, 20 µs and 30 µs pulse durations; and (f) 360 W laser power, 20 µs and 30 µs pulse durations.
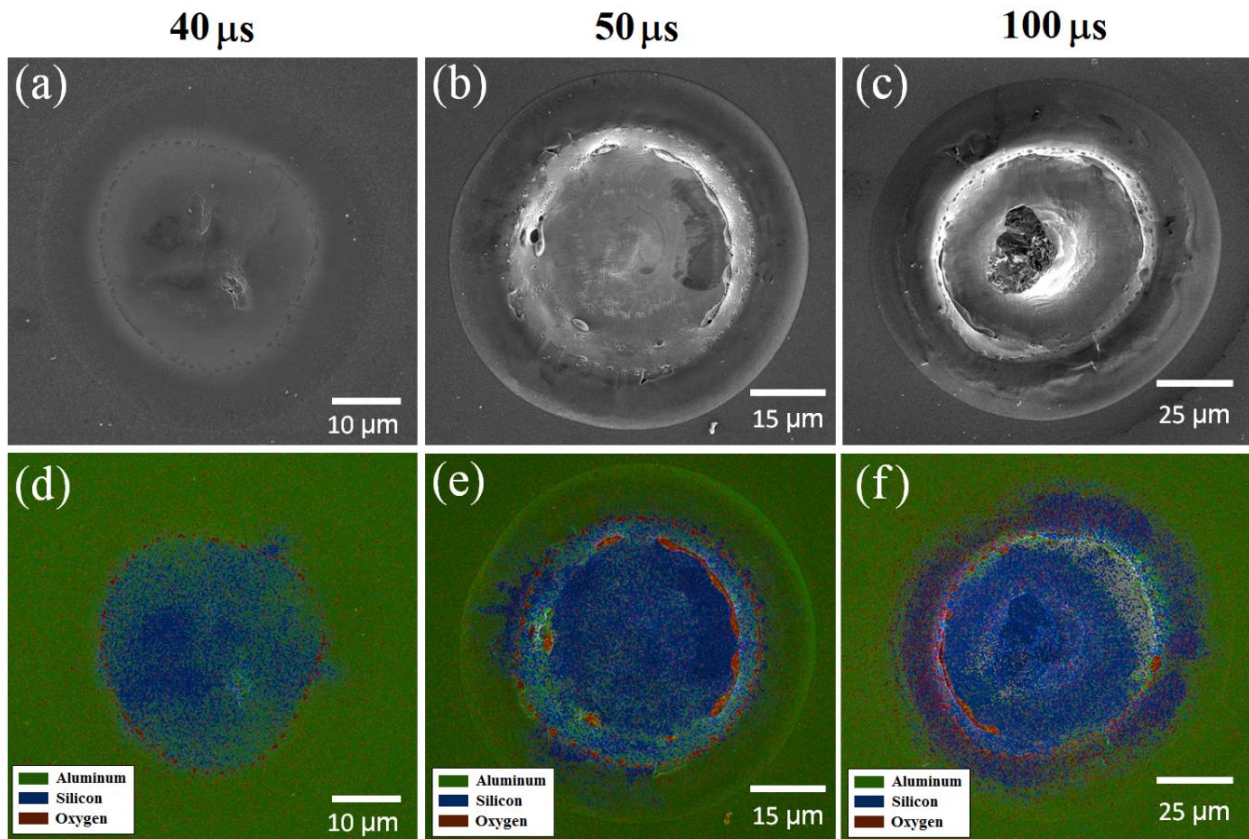
Figure 3.29. SEM micrographs and EDS maps of the top surface of LFCs processed with 112W laser power, a 50μm beam diameter and (a)-(b) 40μs, (c)-(d) 50μs, and (e)-(f) 100 μs pulse durations. Green corresponds to Al, Blue to Si and red to O_2.
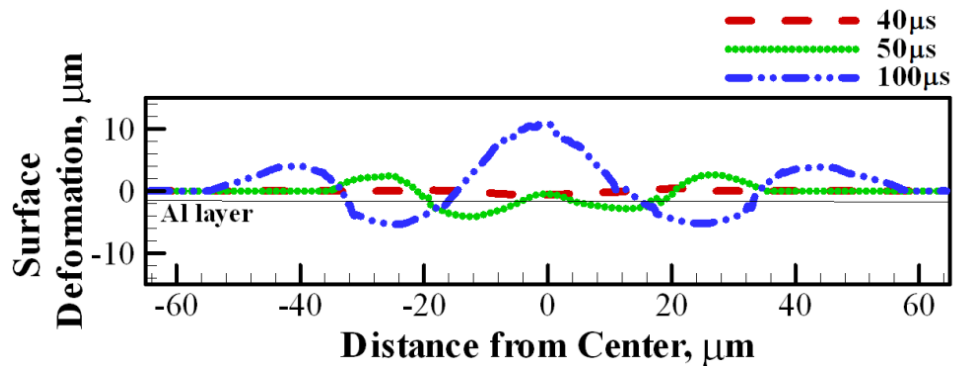
Figure 3.30. Solidified LFC surface topography through center for contacts processed with 112W laser power, 50μm beam diameter and pulse durations of 40μs, 50μs and 100μs.

An increase in the pulse duration from 40 μs to 50 μs, results in visible metal expulsion and surface deformation, as shown in Figure 3.29(e) and Figure 3.30. The EDS map shown in Figure 3.29(e) for the contact processed with a 50 μs pulse duration shows the impact of metal expulsion on the top surface distribution of Al and Si. Si (blue) is present within the inner contact region as well as around the inner

portion of the outer ring. The presence of Si within the inner portion of the outer ring occurs due to the onset of Si expulsion from the inner contact region. In addition, the outermost portion of the outer ring is composed primarily of Al, indicating that Al is expelled before the Si, which is expected since Al is the material first exposed to the laser irradiation and has much lower melting and boiling points than Si. Increasing the pulse duration to 100 µs leads to the presence of more Si along various portions of the outer ring, as observed in Figure 3.29(f), which is due to ongoing Si expulsion from the inner melt region during laser processing. There is also more pronounced surface deformation as a result of increasing the pulse duration to 100 µs, which is caused by significant liquid metal expulsion followed by re-flow of expelled material into the molten pool during solidification.

3.5.2 Factors Governing Onset of Liquid Metal Expulsion

In order to predict the transition from melting to expulsion, theoretical calculations can be used to predict the vapor recoil force and the surface tension force to determine the conditions for the initiation of liquid expulsion. In order for metal expulsion to occur, the vapor recoil force on the surface of the melt pool must exceed the surface tension force of the liquid metal at the periphery of the molten pool [14,17]. The vapor recoil force, F_R, can be calculated as:

$$F_R = 2\pi \int_0^{r_b} r\,\Delta P(r)\,dr \tag{3.15}$$

where r_b is the radial distance at which the surface temperature equals the boiling point of the material, and $\Delta P(r)$ is the difference between the local equilibrium vapor pressure and the atmospheric pressure [42]. $\Delta P(r)$ is function of both the radial distance from the center of the beam and the surface temperature at that particular location. In order to approximate the vapor recoil pressure, it is necessary to know the spatial variation of temperature on the molten pool surface. In lieu of a complicated numerical model that requires the simultaneous solution of the conservation equations for mass, momentum, and energy, the temperature distribution along the surface of a circular molten pool irradiated by a Gaussian laser beam distribution can be approximated as [42]:

$$T = T_0\,e^{-a_1 r^2} \tag{3.16}$$

where T is the temperature on the weld pool surface at a distance r from the center, T_0 is the peak temperature at the center of the pool, and a_1 is a prescribed term based on the measured value of the melt pool radius, r_0, when liquid expulsion initiates. The value of a_1 is calculated as [42]:

$$a_1 = \frac{1}{r_0^2} \ln\left(\frac{T_0}{T_m}\right)$$

(3.17)

where T_m is the melting point of the material. The melting temperature, T_m, is taken as here as the melting temperature of Si (1687K). The use of the melting temperature of pure Si is acceptable since the difference between the melting temperature of pure Si and the liquidus temperature of a binary Al-Si alloy with a low Al concentration (i.e., less than 10 wt. % Al) is less than 50K.

Values for r_0 (for the LFCs processed with a 50 μm and 70 μm beam diameters) are highlighted in Table 3.5. When using a 70 μm beam diameter, the average value for r_0 is approximately 39 μm for the contacts processed with laser powers of 210 W and higher. The contact processed with 159 W is not considered since expulsion takes place between 200 μs and 500 μs and an exact value for r_0 is not known. For the LFCs processed with a 50 μm beam diameter, the value for r_0 is assumed to be 20 μm since expulsion is observed within a 10 μs pulse duration window for both laser power levels. The value of 20 μm is close to the higher pulse duration at 112 W laser power and close to the lower pulse duration for the 159 W laser power. It is reasonable to assume that expulsion should take place close to the end of the window for the lower laser power and closer to the beginning of the window for the higher laser power level when considering a 10 μs for both cases.

Table 3.5. LFC radius before and after metal expulsion for various cases as measured from SEM micrographs. Yellow highlighted measurements represent clear onset of expulsion r_0 values. Orange highlighted region represents observed expulsion, but not at onset. Low and high pulse durations vary as observed in the SEM micrographs (**Figure 3.27** and **Figure 3.28**).

	Power (W)	Low Pulse Radius (μm)	High Pulse Radius (μm)
50 μm beam diameter	112	16	20
	159	21	27
70 μm beam diameter	112	45	49
	159	49	76
	210	35	39
	260	28	38
	312	30	43
	360	37	40

The pressure difference term, $\Delta P(r)$, in Equation (3.4), can be calculated based on the local equilibrium vapor pressure. Since Al has a lower boiling point (2792K) than Si (3514K), it is assumed that the primary vaporizing element at the onset of metal expulsion is Al. The equilibrium vapor pressure for Al, P_{Al}, in atm is calculated as [43]:

$$P_{Al} = 10^{(8.2407 - 14524.89/(T + 192.25))}\Big/760 \qquad (3.18)$$

where T is the molten pool surface temperature. In order to predict the critical peak temperature for metal expulsion, the vapor recoil force must exceed the surface tension force, F_S, at the periphery of the melt pool, which is calculated as:

$$F_S = 2\pi r_0 \sigma \qquad (3.19)$$

where σ is the surface tension of the molten material at the melting point. The surface tension, σ, is taken as 735 mN/m [44] since the molten pool has a high concentration of Si.

A comparison of the recoil and surface tension forces acting on the molten pool is shown in Figure 3.31 as a function of the peak temperature, T_0, at the center of the pool for the contacts processed with 50 μm and 70 μm beam diameters. The critical peak temperature corresponds to the temperature at which the vapor recoil force exceeds the surface tension force. The surface tension force remains constant over the temperature range since the pool size, r_0, is assumed constant. By increasing the beam diameter from 50 μm to 70 μm, the melt pool radius, r_0, at the onset of liquid expulsion nearly doubles from approximately 20 μm to 39 μm. However, the critical peak temperature for metal expulsion is 3359K for the smaller beam diameter in comparison to 3216K for the larger beam diameter.

The critical peak temperature for metal expulsion is lower for the larger beam diameter because the molten pool surface temperatures exceed the boiling point of Al over a larger area within the molten pool, as shown in Figure 3.32. When using the larger beam diameter, the molten pool temperatures are above the boiling point over a radial distance of approximately 20 μm in comparison to a 10 μm radial distance for the smaller beam diameter. Therefore, although the surface temperatures are lower for the larger contact, there will be a larger vapor recoil force over the entire surface of the molten pool since a larger area of molten material is above the boiling point of Al. When the critical peak temperature is exceeded, metal expulsion can be expected. In order to generate larger contacts over short microsecond pulses without initiating expulsion, it is necessary to use a larger beam diameter. However, the critical temperature threshold for the onset liquid metal expulsion will be lower.
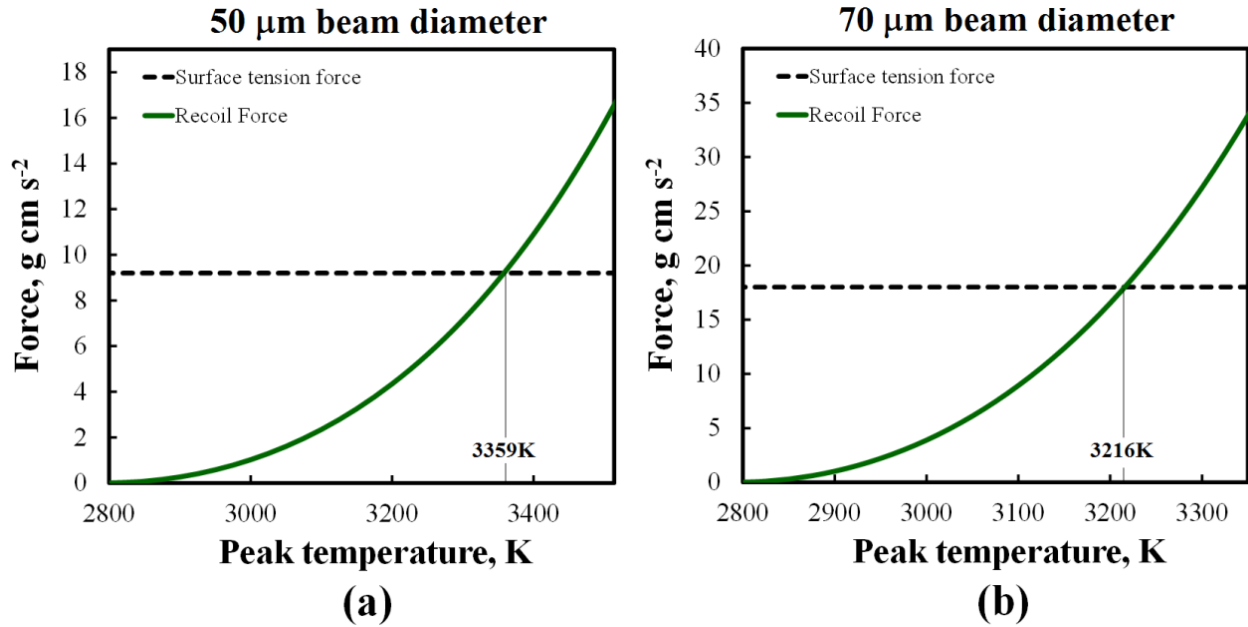
Figure 3.31. Vapor recoil force and surface tension force as a function of peak temperature for a (a) 50 μm beam diameter with $r_0 = 20$ μm and (b) a 70 μm with $r_0 = 39$ μm.
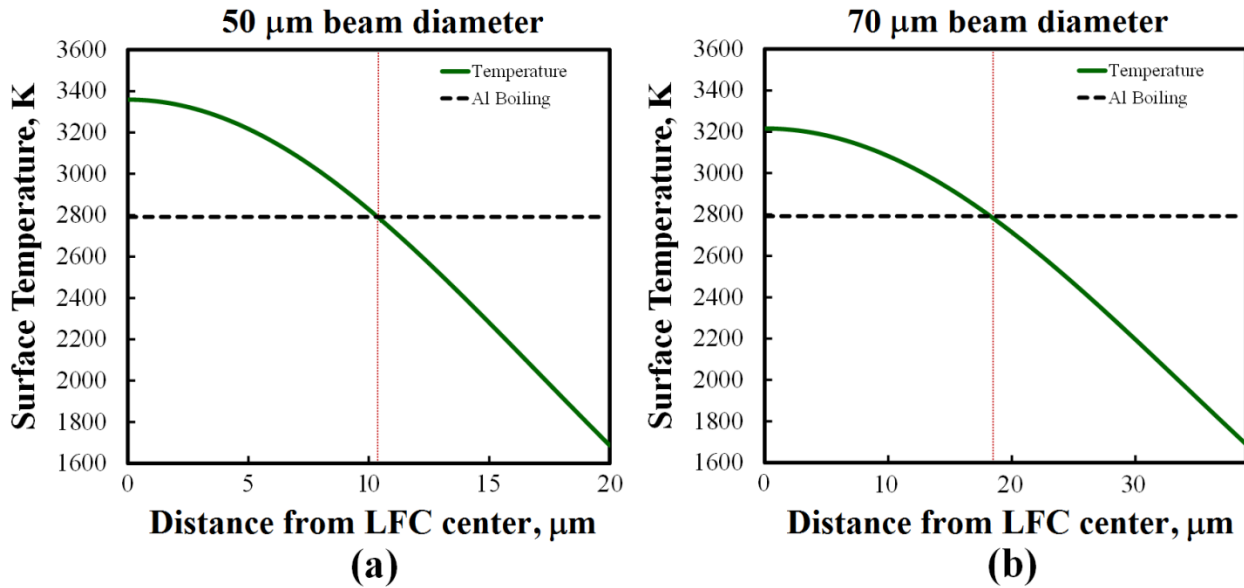
Figure 3.32. Surface temperature calculated using Equation (3.5) as a function radial distance from the LFC center for a (a) 50 μm beam diameter with $r_0 = 20$ μm and (b) a 70 μm with $r_0 = 39$ μm.

For the cases examined, the onset of liquid metal expulsion occurs within a 10 μs timeframe after initial contact formation. In order for expulsion to initiate within this time frame, the molten pool surface temperatures would have to increase at least 500K (from the boiling point of Al (2792K) to greater than the critical temperature threshold of 3359K for a 50 μm beam diameter) and at least 400K (from 2792K to

3216K) for a 70 μm beam diameter. This rapid rise in temperature will be driven by a change in the absorptivity of the laser energy due to the melting and mixing of Al and Si. The transition in the concentration distribution on the LFC top surface is observed in the EDS maps shown in Figure 3.29. As shown in Figure 3.29(d) for the contact at 40 μs, there is a larger presence of Al and Si throughout the inner contact region. At 50 μs, however, the inner contact region is primarily Si. As alloying takes place and the material exposed to the laser irradiation changes, the amount of absorbed energy will also change. The absorptivity, η, of a material has been related to the substrate resistivity and the laser wavelength [44]:

$$\eta = 0.364\left(\frac{\alpha}{\lambda}\right)^{1/2} - 0.0667\left(\frac{\alpha}{\lambda}\right) + 0.006\left(\frac{\alpha}{\lambda}\right)^{3/2} \tag{3.20}$$

where α is the electrical resistivity at a particular temperature [45] and λ is the wavelength of the laser (1070 nm). At the onset of processing, the laser will irradiate a solid Al surface, corresponding to an absorptivity of approximately 0.06 from Equation (3.3). At the melting temperature for Al (933K), the absorptivity will be approximately 0.16, and will again increase to approximately 0.26 at the melting temperature of Si (1687K). Therefore, the amount of absorbed energy will be substantially less at the onset of processing when the irradiated surface is Al, but will increase over 4 times as molten Si is exposed to the laser irradiation. Per Equation (3.20), the absorptivity will also continue to increase after melting since the resistivity tends to increase linearly as a function of temperature for both Al and Si [21]. As the absorptivity increases with time due to an increase in temperature and the irradiated material changes from Al to Si, the increase in absorbed energy will lead to a rapid rise in surface temperatures and expulsion of material from the melt when the critical peak temperature is exceeded.

The net force acting to expel the liquid metal from the melt pool is the difference between the recoil force and the surface tension force when the peak temperature is greater than the critical peak temperature. This net force must be equal to the inertia force due to the acceleration of the liquid metal. The acceleration will increase in direct proportion to the net force and can provide an indication of the tendency for liquid metal expulsion. A dimensionless acceleration term [42] can be used to understand the tendency for liquid metal expulsion above the critical peak temperature. The non-dimensional acceleration term, F, can be calculated as:

$$F = \frac{a}{g} \tag{3.21}$$

where a is the acceleration of the liquid metal and g is the acceleration due to gravity. The acceleration, a, of the liquid metal due to the net force acting on the molten pool can be calculated as:

$$a = \frac{F_R - F_S}{\frac{2}{3} \pi r_0^3 \rho}$$

(3.22)

where all terms have been previous defined. The non-dimensional acceleration term, F, is plotted as a function of the temperature difference between the molten pool peak temperature and the critical peak temperature threshold in Figure 3.33. For 50 μm and 70 μm beam diameters, the critical peak temperatures are 3359K and 3216K, respectively. The molten pool peak temperature values are increased above these values to determine the ΔT value plotted on the graph. The liquid metal acceleration increases rapidly for both beam diameters with small increases in the molten pool peak temperature above the critical temperature, which indicates that the liquid metal will be expelled almost instantly from the melt pool once this temperature threshold is reached. A reduction in the beam diameter results in a much greater increase in the acceleration of the liquid metal for the same increase in temperature above the peak temperature. This dramatic increase is largely driven by the fact that the size of the molten pool at the onset of expulsion is smaller, which will lead to greater acceleration of the liquid metal under similar net forces.
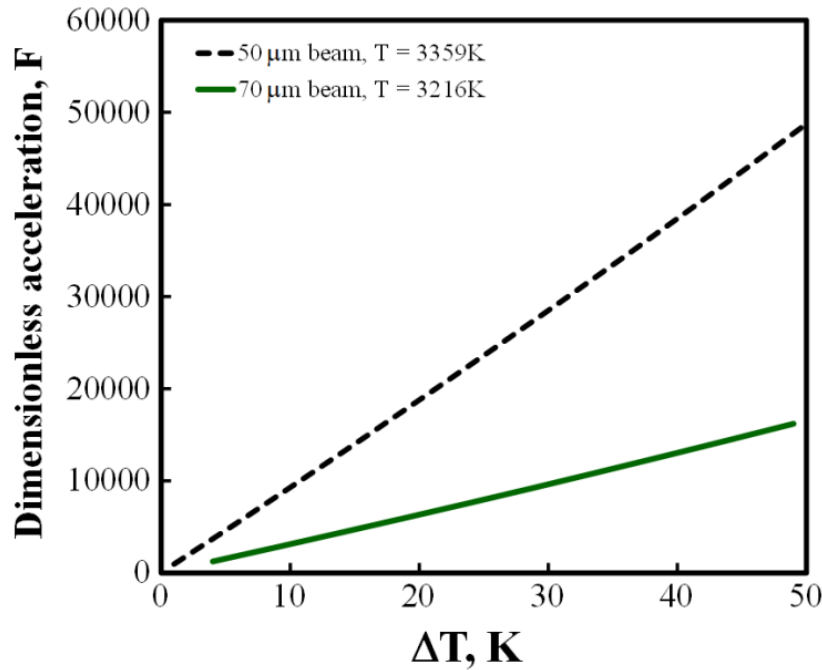
Figure 3.33. Dimensionless acceleration term of liquid metal as a function of the difference between the peak temperature and the critical peak temperature for 50 μm and 70 μm beam diameters.

The influence of changes in beam diameter on the extent of surface deformation and expulsion can be observed in Figure 3.34, which shows surface deformation profiles through the center of various contacts as a function of pulse duration and laser beam diameter with an average laser power of 260 W. The deformation profiles in Figure 3.34(a) were processed with a 50 μm beam diameter and the profiles in Figure 3.34(b) were obtained when processing with a 70 μm beam diameter. The extent of metal expulsion can be viewed in terms of the height of the peak which forms at the center of the LFC. Molten material expelled from the melt pool will flow back into the molten pool to form this central peak upon solidification. The central peak grows monotonically as a function of increasing pulse duration. Furthermore, the central peak height increases as the beam size is reduced. As observed in Figure 3.33, the acceleration of the liquid metal will be significantly higher for a smaller beam diameter as the molten pool peak temperature exceeds the critical peak temperature for liquid metal expulsion. When the evaporative vapor recoil pressure is removed at the termination of the laser pulse, the surface will rebound and molten material that was expelled from the melt pool will flow into the crater, and the central peak will form during solidification. It is important to ensure that the molten pool peak temperatures are kept below the critical peak temperature in order to avoid the loss of alloying elements by vaporization and metal expulsion. Processing parameters can be selected accordingly to avoid metal expulsion while sufficient alloying the Al and Si under short pulse durations.
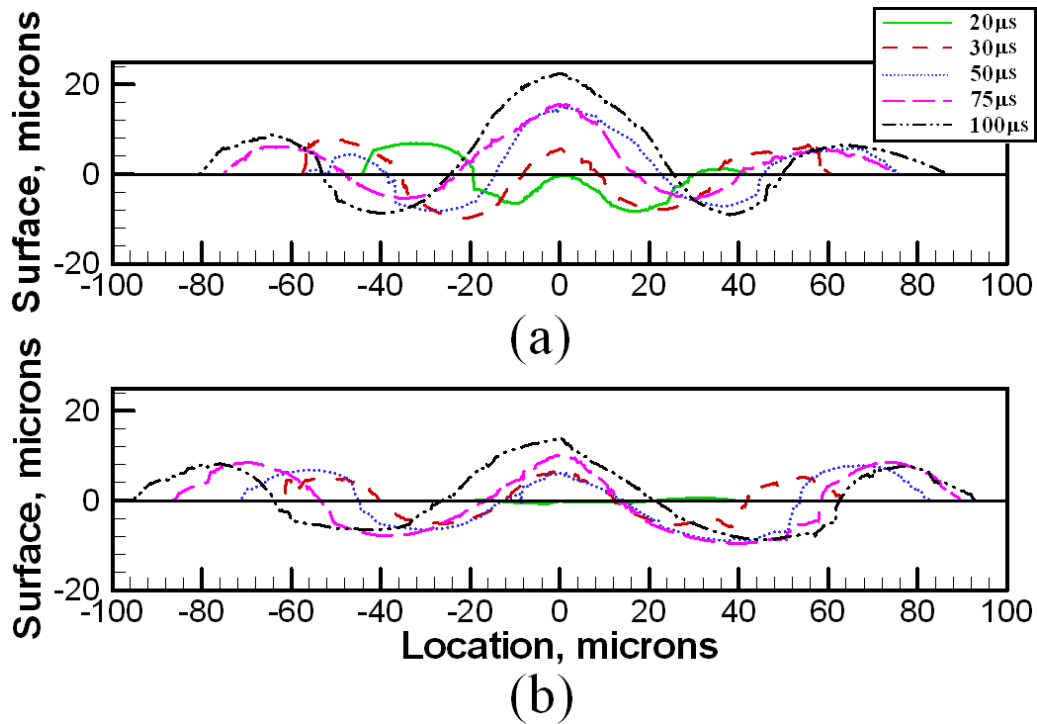
Figure 3.34. Surface deformation with respect to the original surface of the silicon wafer prior to laser processing as a function of time and power density for (a) 50 μm beam diameter and, (b) 70 μm beam diameter when processing with 260W laser power.

3.6 Summary and Conclusions

LFCs generated with microsecond pulse durations were systematically analyzed using advanced materials characterization tools and device simulations to determine the influence of laser processing parameters on LFC surface morphology, cross-sectional contact geometry, passivation layer quality, alloying element concentration, and total contact resistance. As a result of this extensive study, the following conclusions can be made:

1. LFCs processed with microsecond pulse durations exhibit three distinct features: a central peak, an inner contact/crater region and an outer ring region. The formation of these features is largely dependent on pulse duration, laser power, and beam diameter. Due to the highly transient nature of the process, small increases in pulse duration and/or laser power level can result in large changes in LFC inner contact diameters. However, when the power or energy density is sufficiently high, extensive metal expulsion and surface deformation is observed.

2. The removal of the passivation layer during contact formation is dominated by the melting of the SiO_2 layer under the laser irradiation rather than the reduction of the SiO_2 by the Al metallization layer. As the LFC grows radially outward, the SiO_2 layer dissociates into Si and O_2 at the LFC/passivation layer boundary and O_2 reacts with Al to form a highly stable Al_2O_3. After initial removal of the passivation layer, contact formation is likely driven by rapid diffusion of Si into the liquid phases within the Al metallization layer, which leads to significant migration of the original Al/Si interface.

3. The dielectric SiO_2 passivation layer is well preserved outside of the central LFC region despite the high energy densities associated with microsecond pulse durations, likely due to the high melting temperature of SiO_2. The opening in the passivation layer is restricted to the central region designated as the inner contact region even when significant metal expulsion is observed. Therefore, it is believed that recombination rates should not degrade significantly by utilizing longer pulse durations, which was also observed through microwave photoconductance measurements from a previous study [14].

4. LFCs produced with microsecond pulses are three-dimensional in nature and exhibit two distinct phases within the resolidified region regardless of processing parameters. Since the concentration of Al is greater than the eutectic composition, the two phases are a Si-rich phase and a second phase with a higher concentration of Al. The Si-rich phase forms due to limited solid solubility of the dissolved Al as seen in the equilibrium Al-Si phase diagram. Heavy doping of Si by Al within the LFC suggests that the electrically active region is governed by the surface area of the three-dimensional contact.

5. The total contact resistance is dependent on the interfacial area between the LFC and the Si wafer since the contacts are half-ellipsoidal and hemispherical when using microsecond pulses. For all contact geometries, an increase in the top surface contact diameter leads to a reduction in the total contact resistance. Over the entire range of LFC top surface diameters, the total contact resistance is 37% less for hemispherical contacts and 53% less for half-ellipsoidal contacts than that predicted for planar contact geometries from the Cox-Strack relationship.

6. Using a smaller beam diameter to produce a contact with the same inner contact area but deeper fusion zone can result in substantially lower total contact resistances since the area of the LFC/wafer interface for a three-dimensional contact will be greater with larger melt depths. For example, an LFC with an 80 µm inner contact area produced with a 50 µm beam results in a deeper doped region and a total contact resistance of approximately 300 Ω versus 450 Ω when produced using a 70 µm beam.

7. Metal expulsion is observed within tens of microsecond after contact formation due to a rapid rise in molten pool surface temperatures caused by changes in the substrate absorption coefficient and a phase change from solid Al to liquid Si. A change in the irradiated material from solid Al to molten Si results in more laser energy absorbed, which will lead to higher molten pool surface temperature and larger vapor recoil forces on the surface of the melt pool. When the recoil force exceeded the surface tension force, liquid metal expulsion initiates.

8. By increasing laser beam diameter from 50 µm to 70 µm, the critical radius for metal expulsion increases from approximately 20 µm to 39 µm, whereas the critical peak temperature decreases from 3359K to 3216K. The critical peak temperature decreases because a larger molten pool area is above the boiling point of Al at the onset of liquid metal expulsion. Decreasing the power level for a given laser beam diameter can dramatically increase the pulse duration operating window since the molten pool surface temperatures will remain below the critical peak temperature throughout laser-firing.

3.7 References

1. E. Schneiderlochner, R. Preu, R. Ludemann, S.W. Glunz, Laser-fired rear contacts for crystalline silicon solar cells, Prog. in Photovoltaics 10, 29-34, 2002, DOI: 10.1002/pip.422

2. U. Zastrow, L. Houben, D. Meertens, A. Grohe, T. Brammer, E. Schneiderlöchner, Characterization of Laser-Fired Contacts in PERC Solar Cells: SIMS and TEM Analysis Applying Advanced Preparation Techniques, Appl. Surf. Sci. 252, 2006, pp 7082–7085.

3. M. Tucci, E. Talgorn, L. Serenelli, E. Salza, M. Izzi, P. Mangiapane. Laser Fired Back Contact for Silicon Solar Cells, Thin Solid Films 516, 2008, pp 6767-6770. DOI: 10.1016/j.tsf.2007.12.079.

4. R. Preu, E. Schneiderlöchner, A. Grohe, S.W. Glunz, G.P. Willeke, Laser-Fired Contacts - Transfer of a Simple High Efficiency Process Scheme to Industrial Production. Photovolt. Spec. Conf.: Conf. Record of the Twenty-Ninth IEEE. 2002; 130-133. DOI: 10.1109/PVSC.2002.1190473.

5. O. Schultz, S.W. Glunz, G.P. Willeke. Multicrystalline Silicon Solar Cells Exceeding 20% Efficiency. Prog. Photovolt.: Research and Apps. 12, 2004, pp 553-558. DOI: 10.1002/pip.583.

6. W. Brendle, V.X. Nguyen, A. Grohe, E. Schneiderlöchner, U. Rau, G. Palfinger, J.H. Werner, 20.5% Efficient Silicon Solar Cell with a Low Temperature Rear Side Process Using Laser-Fired Contacts. Prog. Photovolt.: Research and Apps. 14, 2006, pp 653-662. DOI: 10.1002/pip.696.

7. M. Hofmann, S. Janz, C. Schmidt, S. Kambor, D. Suwito, N. Kohn, J. Rentsch, R. Preu, S.W. Glunz, Recent Developments in rear-surface passivation at Fraunhofer ISE, Solar Energy Materials & Solar Cells 93, 2009, pp 1074-1078. DOI: 10.1016/j.solmat.2008.11.056.

8. D. Suwito, U. Jager, J. Benick, S. Janz, M. Hermle, S.W. Glunz, Industrially Feasible Rear Passivation and Contacting Scheme for High-Efficiency n-Type Solar Cells Yielding a Voc of 700mV, IEEE Transactions on Electron Devices. 57 (8), 2010, pp 2032-2036.

9. J.H. Yoo, S.H. Jeong, R. Greif, R.E. Russo. Explosive Change in Crater Properties During High Power Nanosecond Laser Ablation of Silicon, J. Appl. Phys. 88(3), 2000, pp 1638-1649.

10. A. Miotello, R. Kelly. Laser-Induced Phase Explosion: New Physical Problems When A Condensed Phase Approaches the Thermodynamic Critical Temperature, Appl. Phys. A: Mat. Sci. and Proc. 69(7), 1999, S67-S73. DOI: 10.1007/s003399900296.

11. D.J. Lim, H. Ki, J. Mazumder, Mass Removal Modes in the Laser Ablation of Silicon by a Q-Switched Diode Pumped Solid-State Laser (DPSSL), J. Phys. D: Appl. Phys. 39, 2006, pp 2624-2635.

12. X. He, T. DebRoy, P.W. Fuerschbach, Alloying element vaporization during laser spot welding of stainless steel, J. Phys. D.: Appl. Phys 2003; 36, pp. 3079-3088, DOI: 10.1088/0022-3727/36/23/033.

13. D.W. Cunningham, BP Solar International, Reaching Grid Parity Using BP Solar Crystalline Silicon Technology A Systems Class Application, DOE Award Number: DE-FC36-07GO17049.006.

14. B. Decesar, Investigation of process parameter optimization of laser-fired back contact silicon solar cells, MS Thesis Penn State University, 2010.

15. B. Hedrick, Characterization of laser fired contacts laser doped emitters and fixed charge passivation for improved silicon solar cells, MS Thesis Penn State University, 2011.

16. Z. Hua, E.W. Reutzel, L. Zou, Beam delivery techniques for laser fired contacts, ICALEO 2010, #M1101.

17. V. Schutz, A. Horn, U. Stute, High-throughput process parallelization for laser surface modification on Si-Solar cells: determination of the process window, Proceedings of SPIE Vol. 8244 (2013).

18. J.F. Ready, editor, *LIA Handbook of Laser Materials Processing*, Magnolia Publishing, Inc., 2001.

19. P. Ortega, A. Orphella, I. Martin, M. Colina, G. Lopez, C. Voz, M.I. Sanchez, C. Molpeceres, R. Alcubilla, Laser-fired contact optimization in c-Si solar cell, Prog. in Photovoltaics 2012; 20 (2): 173-180, DOI: 10.1002/pip.1115.

20. X. He, P.W. Fuerschbach, T. DebRoy, Heat transfer and fluid flow during laser spot welding of 304 stainless steel, J. Phys. D: Appl. Phys. 36, pp 1388-1398 (2003).

21. X. He, J.W. Elmer, T. DebRoy, Heat transfer and fluid flow in laser microwelding, J. Appl. Phys 97, 084909 (2005).

22. X. He, J.T. Norris, P.W. Fuerschbach, T. DebRoy, Liquid metal expulsion during laser spot welding of 304 stainless steel, J. Phys. D: Appl. Phys. 39 (2006), pp 525-534.

23. J.J. Blecher, T.A. Palmer, T. DebRoy, Laser-silicon interaction for selective emitter formation in photovoltaics – Part I: Numerical model and validation, J. Appl. Phys. 112, 114906 (2012).

24. A. Raghavan, T.A. Palmer, T. DebRoy, Evolution of laser-fired aluminum-silicon contact geometry in photovoltaic devices, J. Appl. Phys. 2012; 111 (2), DOI: 10.1063/1.3675442.

25. J-H. Cho, D.F. Farson, J.O. Milewski, K.J. Hollis, Weld pool flows during initial stages of keyhole formation in laser welding, J. Phys D.: Appl. Phy 42 (2009); DOI: 10.1088/0022-3727/42/17/175502

26. J. Krause, R. Woehl, M. Rauer, C. Schmiga, J. Wilde, D. Biro, Microstructural and electrical properties of different-sized aluminum-alloyed contacts and their layer system on silicon surfaces, Solar Energy Materials & Solar Cells 95 (2011) 2151–2160.

27. H. Kodera, Diffusion Coefficients of Impurities in Silicon Melt., Jap. J. Appl. Phys. 2, 212 (1963).

28. R.C. Miller, A. Savage, Diffusion of aluminum in single crystal silicon, J. Appl. Phys., 27 (12), 1954

29. Private e-mail communication with E.W. Reutzel and D. Reiley from Ophir Optics. 11/2013.

30. S. Kou, Welding Metallurgy 2nd Edition, Jon Wiley & Sons, Inc. 2003

31. S.A. David, J.M. Vitek, Correlation Between Solidification Parameters And Weld Microstructures, Int. Mater. Rev., 34: 213, 1989.

32. E. Cavanaugh, J.I. Franco, N.E. Walsöe de Reca, Reaction between aluminum and SiO_2 in integrated circuits, Jap. J. Appl. Phys. 15 (10), 1976.

33. M. Tsukada, S. Ohfuji, In situe xray photoemission spectroscopic studies of Al/SiO_2 interface formation, J. Vac. Sci. and Tech. A. 12(1) (1994), doi: 10.1116/1.578883

34. L.C. Olsen, D.L. Barton, W. Miller, J.E. Garnier, R.P. Turcotte, Physical structure of Al-pSi metal-insulator semiconductor solar cells, J. Appl. Phys. 51 (12), 1980, pp 6393-6398.

35. H.J.T. Ellingham, reducibility of oxides and sulphides in metallurgical processes, J. Soc. Chem. Ind., (1944) pp 125-160.

36. E.O. Kirkendall, Diffusion of zinc in alpha brass, Trans. AIME 147, 104 (1942), pp 104-110.

37. R.H. Cox, H. Strack, Ohmic Contacts for GaAs Devices, Solid State Electronics 1967; 10: 1213-1218, DOI: 10.1016/0038-1101(67)90063-9.

38. T. Hara, H. Suzuki, M. Furukawa, K. Ameyiya, Contact resistance of Al/Si ohmic electrodes formed by rapid lamp sintering, Jap. J. Appl. Phys 22(6), 1983, L340-L342. DOI: 10.1143/JJAP.22.L340.

39. Xu, D., Cui, J., Bansal, R., Hao, X., Liu, J., Chen, W., Peterson, B.S., The ellipsoidal area ratio: an alternative anisotropy index for diffusion tensor imaging, Magnetic Resonance Imaging 27 (2009); 311, DOI: 10.1016/j.mri.2008.07.018

40. Sze, S.M., K.NG, Kwok, Physics of Semiconductor Devices, 3rd Ed., John Wiley & Sons, Hoboken, NJ (2007).

41. Trumbore, F.A., Solid solubilities of impurity elements in germanium and silicon, The Bell System Technical Journal, 1960, pp 205-233.

42. S. Basu, T. DebRoy Liquid metal expulsion during laser irradiation, J. Appl. Phys. 72 (1992), pp. 3317. DOI: 10.1063/1.351452.

43. C.L. Yaws, Handbook of Vapor Pressure, Houston: Gulf, 1994

44. H. Fujii, T. Matsumoto, N. Hata, T. Nakano, M. Kohno, K. Nogi, Surface tension of molten silicon measured by the electromagnetic levitation method under microgravity, Met. Trans. A 31A, 2000, pp 1585.

45. M.A. Bramson, Infrared Radiation: A Handbook for Applications (New York: Plenum), 1968.

46. Smithells Metals Reference Book, 7th ed., edited by E. A. Brandes and G. B. Brook (Butterworth Heinemann, Oxford, 1992).

47. C. Molpeceres, M.I. Sanchez-Aniorte, M. Morales, D. Munoz, I. Martin, P. Ortega, M. Colina, C. Voz, R. Alcubillia, Influence of wavelength on laser doping and laser-fired contact processes for c-Si solar cells, Proc. Of SPIE 8473, DOI: 10.1117/12.929456.

Chapter 4

MATHEMATICAL MODEL FRAMEWORK

4.1 Importance

The formation of laser-fired contacts is governed by a number of complex physical processes. Since obtaining data on the laser-material interaction behavior during laser firing is difficult due to the short time and length scales associated with the process, numerical simulations can be utilized to develop a fundamental understanding of the physical processes that occur during contact formation. A transport phenomena, finite-difference model that utilizes the control volume method [1] is used to solve the governing equations for conservation of mass, momentum and energy to accurately calculate three-dimensional contact geometry, and temperature and velocity fields. From these direct calculations, data can be generated to evaluate solidification rates, cooling rates and growth rates to understand the impact changes in laser processing parameters have on the material during contact formation.

4.2 Model Framework

The mathematical model is written in the FORTRAN programming language. The user specifies various input parameters that are then used in the program to iteratively solve the equations for the conservation of mass, momentum and energy in a three-dimensional computational space for the laser-firing process.

4.2.1 Inputs

The factors required to obtain a stable solution for the laser-fired contact formation process are the computational domain, laser processing parameters, substrate material properties, boundary conditions and numerical scheme parameters. Each of these factors is discussed in the following subsections.

4.2.1.1 Computational Domain

The computational domain is defined based on the dimensions of the part to be processed. In the research here, the LFCs were processed on circular Si wafers 4 inches in diameter and greater than 250 μm in thickness. A rectangular computational domain is defined based on the x, y, and z dimensions from the known part geometry. Figure 4.1 shows a schematic of the Cartesian coordinate system used for the calculations. The rectangular computational domain is referenced by its six faces as top, bottom, north, south/symmetry, east, or west. The computational domain is further divided into fixed non-uniform rectangular grids based on the requirements for the problems. Finer grid spacing is used beneath the heat

source due to the large temperature gradients associated with an extremely small laser beam diameter and large laser power. Grid points are indexed in the *x*-, *y*-, and *z*- direction as i, j and k, respectively.
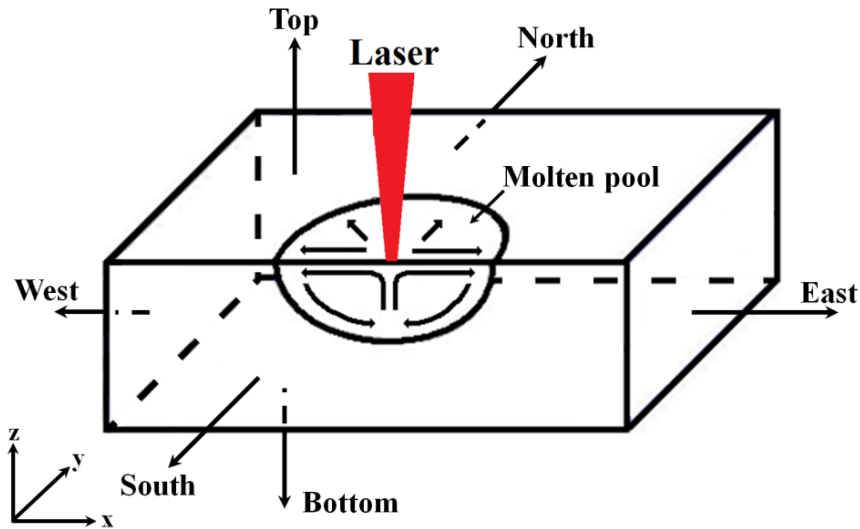
Figure 4.1. Schematic of overall computational domain for calculations.

4.2.1.2 Laser Processing Parameters

The laser processing parameters include the laser power, material absorptivity, laser beam distribution factor, and laser beam radius. Material absorptivity is determined from the laser wavelength, electrical resistivity, phase of the material (i.e. solid or liquid), and temperature of the substrate [2]. The materials considered in this work are specifically Si and Al. The laser beam distribution is based on the anticipated beam profile (e.g. Gaussian or top hat). In this work, the beam profile is assumed to be Gaussian based on empirical measurements by the laser manufacturer [3]. Laser power, laser beam radius, and linear velocity are all direct inputs that are required to calculate the incoming heat flux to the computational domain. The values for these parameters are based on the experimental values, except for the linear velocity, which is zero since laser-fired contacts are all generated with no velocity, similar to laser spot welds.

4.2.1.3 Substrate Material Properties

The substrate material properties used in the model are the density of the liquid, the solidus and liquidus temperatures, the enthalpy of the solid and liquid at the melting point, the specific heat of the solid and liquid, the thermal conductivity of the solid and liquid, and the effective viscosity of the liquid. These material properties are required to define coefficients in the discretization scheme to solve for the dependent variables and to generate an enthalpy-temperature relationship to determine temperatures

within the solution domain. In this work, the material properties are specified within the domain as those of Al or Si based on location.

4.2.1.4 Boundary Conditions

The input boundary conditions include the temperature and heat transfer coefficients at the six faces of the rectangular domain as well as velocity boundary conditions. Due to the nature of a laser-fired contact, which is symmetrical about the centerline, only half of the workpiece is considered. The incoming heat flux at the top surface is based on the incoming laser beam power distribution, and the symmetry face has no heat flux and y-velocity component. Application of the boundary conditions to the solution procedure is explained in more depth in section 4.2.4.

4.2.1.5 Numerical Scheme Parameters

The numerical scheme parameters are required to define important aspects of the calculation. With the extremely short pulse durations (less than 1 ms) used for the laser-fired contact process, the system does not reach steady state, and it is necessary to consider the transient nature of system. The numerical scheme parameters used include the time step at which calculations are performed, the maximum number of iterations per time step, and the total time for the calculation. In addition, the influence of the solution at the previous time step on the solution for the subsequent time step can be specified through the use of under-relaxation parameters for pressure, velocity (u, v and w) and enthalpy. These under-relaxation parameters are utilized to increase the rate of convergence (and decrease computation time) when solving such a large system of algebraic equations through an iterative process.

4.2.2 Governing Equations

Differential equations based on conservation principles for mass, momentum and energy are used to express the physical laws governing the heat transfer and fluid flow in the laser-fired contact formation process. The differential equations are specific to a desired dependent variable, such as mass, velocity and enthalpy and the general form of the equation for a dependent variable, ϕ, is:

$$\rho\frac{\partial\phi}{\partial t}+\rho\frac{\partial(u_i\phi)}{\partial x_i}=\frac{\partial}{\partial x_i}\left(\Gamma\frac{\partial(\phi)}{\partial x_i}\right)+S \tag{4.1}$$

where ρ is density, t is time, u_i is the liquid velocity along the i direction, x_i is the distance along the i direction, Γ is the general diffusion coefficient, and S is a source term. The four terms in Equation 4.1 are the unsteady term, convection term, diffusion term and source term, which accounts for additional factors not captured in the other three terms. In addition, depending on the dependent variable, Γ and S will have

specific meanings. For instance, if ϕ is velocity or enthalpy, Γ will be the liquid viscosity or thermal diffusivity, respectively.

The specific conservation equations for mass (4.2), momentum (4.3) and energy are (4.4) expressed as:

$$\frac{\partial \rho}{\partial t} + \frac{\partial(\rho u_i)}{\partial x_i} = 0 \tag{4.2}$$

$$\rho \frac{\partial\left(\rho u_j\right)}{\partial t} + \rho \frac{\partial\left(\rho u_i u_j\right)}{\partial x_i} = \frac{\partial}{\partial x_i}\left(\mu \frac{\partial u_j}{\partial x_i}\right) + \frac{\partial p}{\partial x_i} + S_{ui} \tag{4.3}$$

$$\rho \frac{\partial(\rho h)}{\partial t} + \rho \frac{\partial(\rho u_i h)}{\partial x_i} = \frac{\partial}{\partial x_i}\left(\frac{k}{C_p}\frac{\partial h}{\partial x_i}\right) + S_h \tag{4.4}$$

where μ is the effective viscosity of the liquid, k is the thermal conductivity, C_p is the specific heat, and h is the sensible heat. The source terms S_{ui} and S_h are given by the following expressions:

$$S_{ui} = \frac{\partial p}{\partial x_i} + \frac{\partial}{\partial x_j}\left(\mu \frac{\partial u_j}{\partial x_i}\right) - C\left(\frac{(1-f_l)^2}{f_l^3 + B}\right)u_i + \rho g \beta (T - T_{ref}) \tag{4.5}$$

$$S_h = -\frac{\partial(\rho \Delta H)}{\partial t} - \frac{\partial(\rho u_i \Delta H)}{\partial x_i} \tag{4.6}$$

where p is the pressure, f_l is the liquid fraction, B is a constant on the order of 10^{-10} to avoid division by zero, C is a constant that accounts for mushy zone formation [4], β is the coefficient of volume expansion and T_{ref} is a reference temperature (typically taken as 298K), and ΔH is the latent heat content, which is based on the following relationship between total enthalpy, H, sensible heat, and latent heat content:

$$H = h + \Delta H \tag{4.7}.$$

The sensible heat, h, is calculated as:

$$h = \int C_{p, s/l}\, dT \tag{4.8}.$$

The latent heat content is calculated as:

$$\Delta H = f_l L \tag{4.9}$$

where L is the latent heat of fusion and f_l is the liquid fraction. In a system in which modeling is performed for a pure material, the enthalpy-temperature relationship is defined within the model as shown in Figure 4.2(a), which is an enthalpy-temperature plot for melting of pure Si. In the plot, *Hlmelting* is the enthalpy of the liquid material (Si) at the melting point, *Hsmelting* is the enthalpy of the solid Si at the melting point, *Hlatent* is the latent heat of fusion, which is the difference between *Hlmelting* and *Hsmelting*, and h is the sensible heat as previously defined in Equation (4.8). The liquid fraction, f_l, shown in Equation (4.9) will be equal to 0 or 1 depending on if the material is solid or liquid, as shown in Figure 4.2(b). After melting, the molten pool is 100% liquid with a liquid fraction of 1. In arriving at a solution for the sensible heat from the conservation of energy equation, the temperature values can be directly calculated from the relationship in Equation (4.8) between sensible heat and specific heat.
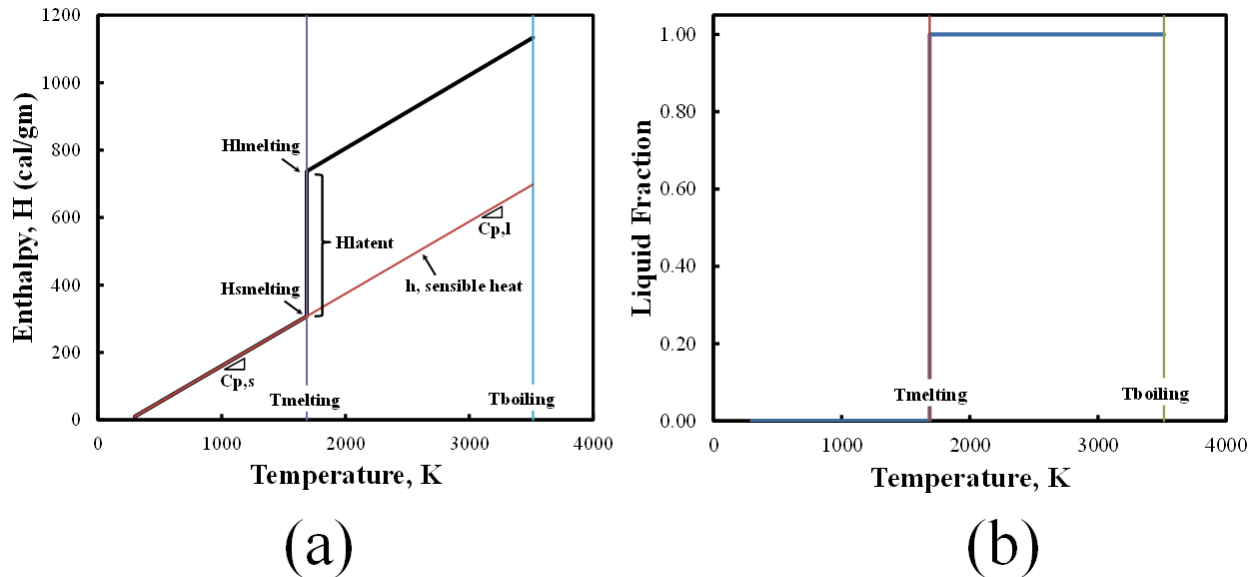
Figure 4.2. (a) Enthalpy-Temperature relationship and (b) Corresponding liquid fraction-temperature relationship.

When dealing with an alloy system, the enthalpy-temperature relationship will change because there will be a liquidus and solidus temperature rather than a single melting temperature. In the past [5], one particular methodology for the enthalpy-temperature relationship has been used when the difference between the liquidus and solidus temperatures was small (on the order of 10-50K). A binary Al and Si alloy will have a difference between the liquidus and solidus of greater than 800K. For illustrative purposes, Figure 4.3(a) shows a plot of the enthalpy-temperature relationship used for the Al-Si alloy system using the traditional approach. Two additional variables, *Hcal* and $C_{p,avg}$, have been introduced. *Hlcal* is the enthalpy of the solid at the liquidus temperature, since *Hsmelting* is the enthalpy of the solid

at the solidus temperature. C_{pavg} is the average specific heat beween the values for the liquid and the solid. With the introduction of a two-phase region, the enthalpy-temperature changes and different approaches are used to determine the liquid fraction to be used in Equation (4.9) and temperature. Based on values on the plot in Figure 4.3(a), the temperatures are calculated from sensible heat as:

$$T = \begin{cases} T_{solidus} + \dfrac{h - Hsmelting}{C_{P,S}} & \text{for } h \leq Hsmelting \\[3ex] T_{solidus} + \dfrac{h - Hsmelting}{C_{P,avg}} & \text{for } Hsmelting < h < Hlcal \\[3ex] T_{liquidus} - \dfrac{h - Hlcal}{C_{P,l}} & \text{for } h \geq Hlcal \end{cases} \qquad (4.10)$$

As can be seen from Figure 4.3(b), the liquid fraction is assumed to vary linearly with temperature as:

$$f_l = \begin{cases} 1 & \text{for } T > T_{liquidus} \\[3ex] \dfrac{T - T_S}{T_L - T_S} & \text{for } T_s < T \leq T_{liquidus} \\[3ex] 0 & \text{for } T \geq T_{liquidus} \end{cases} \qquad (4.11)$$

In Figure 4.3, the plot is constructed assuming an alloy with 80% Si, 20% Al, which would correspond to an approximate liquidus temperature of 1577K. Due to the difference in the temperatures between the liquidus and solidus on the Al-Si phase diagram, however, this method will not be suitable for modeling the laser firing process. Therefore, a new method was introduced to the model in which the he liquid fraction is assumed to vary based on the Al-Si phase diagram [6]. The method by which the Al-Si phase diagram is used in our system is explained in more detail in Chapter 5 as it has been applied to modeling of laser-fired contacts.
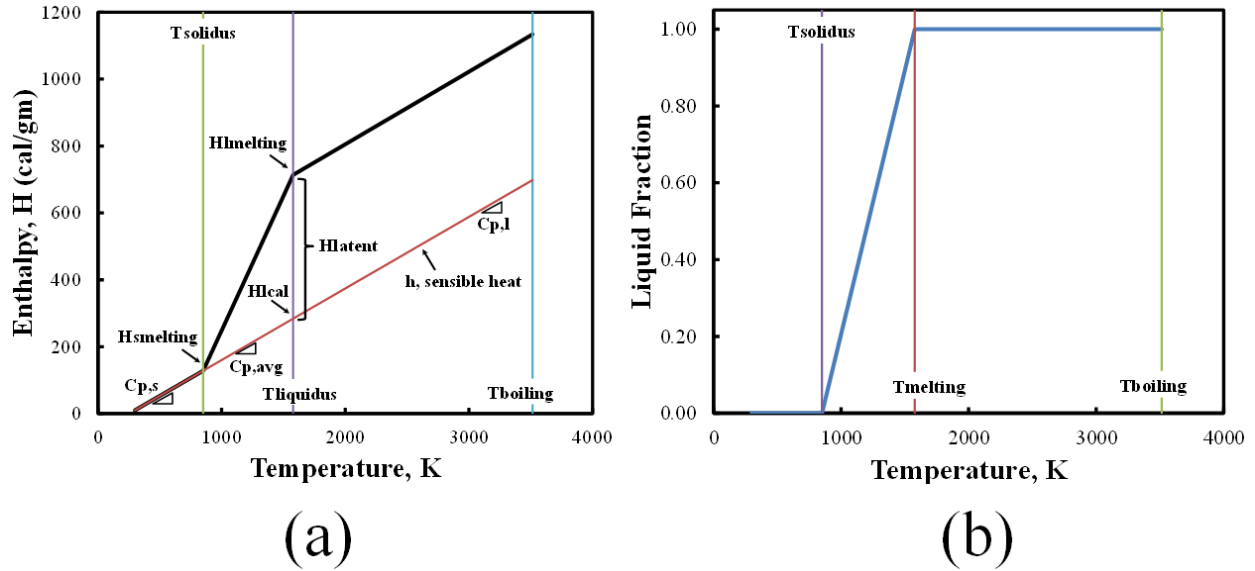
Figure 4.3. (a) Enthalpy-Temperature relationship and (b) Corresponding liquid fraction-temperature relationship for alloy.

4.2.3 Discretization Scheme

A fully converged solution is obtained by solving algebraic expressions for the governing partial differential equations (PDEs) for mass, momentum and energy. The governing equations (4.2) through (4.4) have been discretized (i.e. converted to algebraic expressions) based on the control volume method [1]. Using this method, the computational domain is divided into multiple, rectangular control volumes. Figure 4.4 shows a three-dimensional schematic for a single interior control volume with the capital letters corresponding to grid point locations at nearest neighbor control volumes in the east (E), west (W), north (N), south (S), top (T) and bottom (B) directions and lower case letters (e, w, n, s, t, and b) correspond to the faces of the control volume around grid point P in the respective directions.
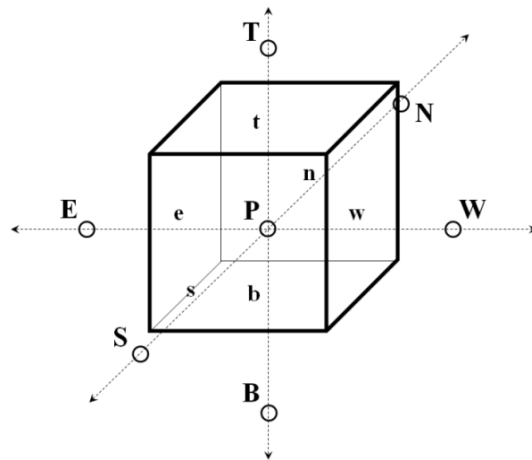
Figure 4.4. Schematic diagram of interior control volume surrounding grid point P.

114

Discretization of the PDEs is performed by integrating the governing equations over the three-dimensional control volume [1]. The discretization equation defines the dependent variable, ϕ, at one grid point, P, in terms of the values of its nearest neighbor grid points and the value at the previous time step using the following form:

$$a_P\,\phi_P = a_E\,\phi_E + a_W\,\phi_W + a_N\,\phi_N + a_S\,\phi_S + a_T\,\phi_T + a_B\,\phi_B + a_P^0\,\phi_P^0 + S_U\Delta V \qquad (4.12)$$

where a is a coefficient calculated based on the power-law scheme, the subscripts (E, W, N, S, T, and B) pertain to the nearest geometric neighbor for the grid point P, the superscript 0 pertains to the previous time step, S_U is the constant part of the source term and ΔV is the volume of the control volume. The values for the dependent ϕ variables of pressure and enthalpy are stored at scalar grid points located at the center of each control volume. Values for the velocity components are stored at different grid points using a staggered grid to ensure stability of the calculations. As a result, the control volumes for the scalar variables are staggered from those for the vector variables. The use of the staggered grid is based on discretization of the pressure term in Equation (4.3) and is based on the Semi Implicit Method for Pressure Linked Equation (SIMPLE) [1]. The coefficients can be calculated from the following expressions based on the power law scheme [1]:

$$a_P = a_E + a_W + a_N + a_S + a_T + a_B + a_P^0 + S_P\Delta V \qquad (4.13)$$

$$a_{NN} = D_{nnf}\left\| 0,\left(1-0.1\left|\frac{F_{nnf}}{D_{nnf}}\right|\right)^5 \right\| + \left\| -F_{nnf}, 0 \right\| \qquad (4.14)$$

where the subscript NN is the nearest neighbor (i.e. E, W, N, S, T or B), S_P is dependent part of the source term, and the subscript nnf is the nearest neighbor face [i.e. e, w, n, s, t or b] for the control volume around grid point P. The negative sign in Equation 4.14 for the F term does not apply when the nearest neighbor face is west (w). The values for D_{nnf} and F_{nnf} can be calculated as:

$$D_{nnf} = \frac{\Gamma_{nnf}\,A_{nnf}}{(\delta x)_{nnf}} \qquad (4.15)$$

$$F_{nnf} = \left(\rho u_{nnf}\right)A_{nnf} \qquad (4.16)$$

where A_{nnf} is the area of the respective face for each direction (i.e. e, w, n, s, t or b) for the control volume around point P and δx is the length of the nearest neighbor face. In equations 4.15 and 4.16, A_{nnf} is

calculated as the product of Δy times Δz for the east (e) and west (w) faces of the control volume around grid point P. Likewise, the product of Δx and Δy for the top and bottom faces and the product of Δx and Δz for the north and south faces will be used to obtain the appropriate A_{nnf} to be used in Equations 4.15 and 4.16. The discretized partial differential equations for mass, momentum and energy are solved iteratively on a line-by-line basis using the Tri-Diagonal Matrix Algorithm (TDMA) [1] with appropriate boundary conditions.

4.2.4 Boundary conditions

Figure 4.1shows a schematic diagram of the computational domain based on a Cartesian coordinate system. The entire domain will be divided into multiple rectangular control volumes. Enthalpy and velocity boundary conditions are applied at the faces (top, bottom, west, east, south and north) to the domain shown in Figure 4.1 to arrive at realistic solutions.

4.2.4.1 Enthalpy Boundary Conditions

The net heat flux on the top surface of the substrate is calculated as the sum of the input heat flux, F_i, radiative heat loss, F_r, convective heat loss, F_c, and any other heat loss terms, F_o, using the following equation:

$$F = F_i + F_r + F_c + F_o \tag{4.17}$$

The net input heat flux from the laser heat source can be calculated using the following equation [7]:

$$F_i = \frac{f_h Q \eta}{\pi r_b^2} \exp\left(\frac{-f_h\left(x^2 + y^2\right)}{r_b^2}\right) \tag{4.18}$$

where f_h is the laser distribution factor and is typically taken as 3 for conduction mode welding [8], Q is the laser power, η is the absorption coefficient, r_b is the laser beam radius and x and y represent the distance in these directions from the center of the laser beam along the top surface. The absorption coefficient, η, is taken as a constant or calculated using the following expression [2]:

$$\eta(T) = 0.365\left(\frac{\alpha}{\lambda}\right)^{1/2} - 0.0667\left(\frac{\alpha}{\lambda}\right) + 0.006\left(\frac{\alpha}{\lambda}\right)^{3/2} \tag{4.19}$$

where α is the electrical resistivity of the material at a given temperature and λ is the wavelength of the laser. The radiative, F_r, and convective, F_c, heat loss terms are given from the following two equations, respectively:

116

$$F_r = \sigma \varepsilon \left(T^4 - T_0^4 \right)$$ (4.20)

$$F_c = - h_c (T - T_0)$$ (4.21)

where σ is the Stefan-Boltzmann constant (5.670×10^{-12} J K^{-4} cm^{-2} s^{-1}), ε is the emissivity, T is the top surface temperature in K, T_0 is the ambient temperature and h_c is the heat transfer coefficient. The enthalpy heat flux boundary condition at the symmetry face is given as:

$$\frac{dh}{dy} = 0$$ (4.22)

Equation (4.22) is used to ensure that there is no heat flux out of the symmetry surface. For the other faces (north, west, east and bottom), the enthalpy value is specified such that the temperature at that face corresponds to 298K. This is based on an enthalpy-temperature relationship, which is the basis for converting the solution to the energy equation for the dependent variable of sensible heat to temperature values at each grid point location. The enthalpy-temperature relationship is determined from the following input variables: solidus temperature, liquidus temperature, enthalpy at the solidus temperature and enthalpy at the liquidus temperature. This methodology as it pertains to the Al-Si laser-fired contact system is explained in more detail in Chapter 5.

4.2.4.1 Velocity Boundary Conditions

In order to arrive at a solution to the discretized equation for the conservation of momentum, boundary conditions for the u, v and w velocity components for the x-, y-, and z-directions, respectively, are applied to the faces of the computational domain. The boundary conditions for the u, v and w velocities on the top surface of the substrate are, respectively, given as [9]:

$$\mu \frac{du}{dz} = f_l \frac{d\gamma}{dT} \frac{dT}{dx}$$ (4.23)

$$\mu \frac{dv}{dz} = f_l \frac{d\gamma}{dT} \frac{dT}{dy}$$ (4.24)

$$w = 0$$ (4.25)

where μ is the liquid viscosity, $d\gamma/dT$ is the temperature coefficient of surface tension (typically taken as that for Si when modeling the LFC process) and f_l has been previously defined. As shown in Equations (4.23) and (4.24), the u and v velocities are determined by the Marangoni effect and material flow is

driven by the temperature gradient on the top surface. The *w* velocity is set equal to zero because there is no material flow perpendicular to the top plane. The boundary conditions for the *u*, *v* and *w* velocities on the south/symmetry face are, respectively, taken as:

$$\frac{du}{dy} = 0 \qquad (4.26)$$

$$v = 0 \qquad (4.27)$$

$$\frac{dw}{dy} = 0 \qquad (4.28)$$

The *v* velocity is set to zero because there is no material flow perpendicular to the symmetry surface. In addition, there is no change in velocity at the south surface due to the symmetrical nature of the problem. The *u*, *v* and *w* velocities are all set equal to zero at the east, west, bottom and north faces and within region where the domain temperature is less than the solidus temperature.

4.2.5 Solution Methodology

4.2.5.1 Tri-Diagonal Matrix Algorithm (TDMA)

The discretized equations for the conservation of mass, momentum and energy are iteratively solved on a line-by-line basis using the Tri-Diagonal Matrix Algorithm [1]. The TDMA procedure used to solve the system of equations is briefly outlined below for the one-dimensional case. For the actual conditions associated with LFC processing, the problem is solved in three dimensions, which is based on the same principle. The TDMA is used to solve for values of the dependent variables, enthalpy and u, v and w velocities, at each individual grid point. Figure 4.5 shows a schematic diagram of one row of control volumes with corresponding grid points in one-dimension within a superimposed computational domain.
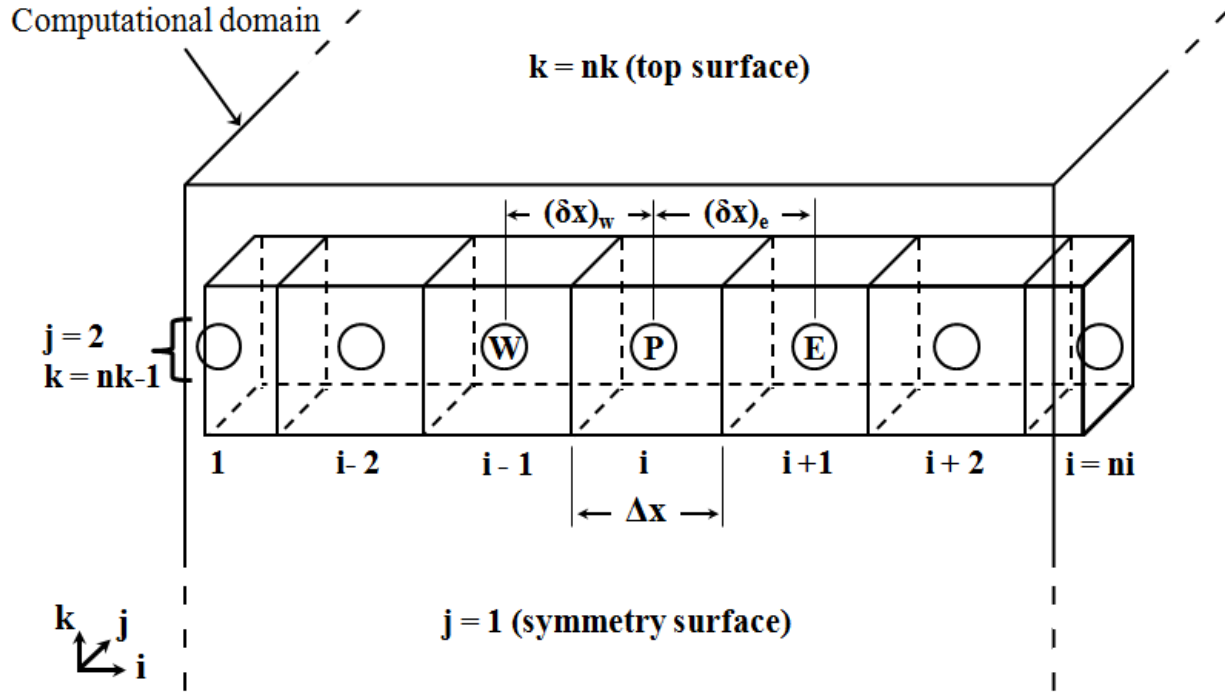
Figure 4.5. One-dimensional row of control volumes used to explain TDMA procedure.

When indexing grid points within the arrays used to store values for each dependent variable, the x-, y- and z-directions correspond to i, j, and k, respectively. The western most face in the computational domain corresponds to an index value for i of 1. The eastern face most face has an i index value of ni, where ni is based on the total number of control volumes specified in the x-direction when defining the geometry of the domain at the start of the problem. In the case shown in Figure 4.5, there are 5 total control volumes. In addition, the control volumes at the east and west faces of the computational domain have grid points that are located at the face of the individual control volumes, which are half the size a typical control volume. The same configuration will apply in the y- and z- directions in terms of indexing for j and k. In the y-direction, the j index is set to 1 at the symmetry surface as shown in Figure 4.5 and goes to nj depending on the total number of specified control volumes. In the z-direction, the k index is set to one at the bottom face and equal to nk at the top face. For the explanation of the TDMA in one dimension, we are specifically looking at the row that corresponds to indexes of j = 2 and k = nk-1. In addition, there are 5 control volumes in this row with i index values centered at the location i in Figure 4.5.

From Equation (4.12), we have the following discretization equation:

$$a_i \phi_i = a_{E,i} \phi_{i+1} + a_{W,i} \phi_{i+1} + d_i \tag{4.29}$$

where i is equal to 2, …, ni-1 and correspond to i-2, …, i+2, respectively, in Figure 4.5. At the boundary points on the east and west faces, the values for a_W and a_E will be zero, respectively, since these points do not exist in the domain. Therefore, for i = 1 and i = ni, Equation (4.27) can be rewritten as for the west and east faces in the following two forms:

$$a_1 \phi_1 = a_{E,1} \phi_2 + d_1 \tag{4.30}$$

$$a_{ni} \phi_{ni} = a_{W,ni} \phi_{ni} + d_{ni} \tag{4.31}$$

We can re-write Equations (4.29) through (4.31) in the following general forms, respectively, for one row of dependent variables:

$$a_i \phi_i - a_{E,i} \phi_{i+1} - a_{W,i} \phi_{i+1} = d_i \qquad \text{for } i = 2, \text{ni-1} \tag{4.32}$$

$$a_1 \phi_1 - a_{E,1} \phi_2 = d_1 \qquad \text{for } i = 1 \tag{4.33}$$

$$a_{ni} \phi_{ni} - a_{W,ni} \phi_{ni} = d_{ni} \qquad \text{for } i = ni \tag{4.34}$$

Equations (4.32) through (4.34) can be transferred to a system of equations that can be solved simultaneously for one row of dependent variables. This can be visualized with the following matrix:

$$
\begin{bmatrix}
a_1 & -a_{E,1} & 0 & 0 & \cdot & \cdot & \cdot & \cdot & \cdot & 0 & 0 \\
-a_{W,2} & a_2 & -a_{E,2} & 0 & & & & & & & \cdot \\
0 & -a_{W,3} & a_3 & -a_{E,3} & 0 & & & & & & \cdot \\
0 & 0 & & & & & & & & & \cdot \\
\cdot & & & & & & & & & & 0 \\
\cdot & & & & & & & & & & 0 \\
\cdot & & & & & & 0 & -a_{W,ni-1} & a_{ni-1} & -a_{E,ni-1} \\
0 & 0 & \cdot & \cdot & \cdot & \cdot & 0 & 0 & -a_{W,ni} & a_{ni}
\end{bmatrix}
\begin{bmatrix}
\phi_1 \\ \phi_2 \\ \phi_3 \\ \phi_4 \\ \cdot \\ \cdot \\ \phi_{ni-1} \\ \phi_{ni}
\end{bmatrix}
=
\begin{bmatrix}
d_1 \\ d_1 \\ d_1 \\ d_1 \\ \cdot \\ \cdot \\ d_{ni-1} \\ d_{ni}
\end{bmatrix} \tag{4.35}
$$

The first matrix is the coefficient matrix, the second is the dependent variable and the third is the source terms. The non-zero coefficients align themselves along the three diagonals in the first matrix, which is the basis for the name TDMA. From Equation (4.30) and row one of the matrix (4.35), it can be observed that ϕ_1 can be expressed in terms of ϕ_2. The next row of the matrix (4.35) for i =2, there is a relationship between ϕ_1, ϕ_2 and ϕ_3. However, since ϕ_1 can be expressed in terms of ϕ_2, this relationship

reduces to one between ϕ_2 and ϕ_3 (i.e. ϕ_2 can be expressed in terms of ϕ_3). This process of forward substitution is carried out through the last row of the matrix (4.35) when ϕ_{ni-1} is expressed in terms of ϕ_{ni}, which is known from the boundary conditions. This concept can be generally expressed using the following two expressions:

$$\phi_i = P_i \phi_{i+1} + Q_i \qquad\qquad \text{for } i = 1, \dots \; ni \qquad\qquad (4.36)$$

$$\phi_{i-1} = P_{i-1} \phi_i + Q_{i-1} \qquad\qquad \text{for } i = 2, \dots \; ni \qquad\qquad (4.37)$$

By combining Equations (4.29) and (4.37), we have the following redefined form for Equation (4.29):

$$\left(a_i - a_{W,i} P_{i-1} \right) \phi_i = a_{E,i} \phi_{i+1} + a_{W,i} \phi_{i-1} + d_i \qquad\qquad (4.38)$$

From Equation (4.38), we can see that the terms, P_i and Q_i, in Equation (4.36) can be written with the following expressions as:

$$P_i = \frac{a_{E,i}}{a_i - a_{W,i} P_{i-1}} \qquad\qquad (4.39)$$

$$Q_i = \frac{d_i + a_{W,i} Q_{i-1}}{a_i - a_{W,i} Q_{i-1}} \qquad\qquad (4.40)$$

These recurrence relations give P_i and Q_i in terms of P_{i-1} and Q_{i-1}. Since the value of $a_{W,\,i}$ is equal to 0 at the west face of the computational domain shown in Figure 4.5, the relationships given in (4.39) and (4.40) can be reduced to for i =1:

$$P_1 = \frac{a_{E,1}}{a_1} \qquad\qquad (4.41)$$

$$Q_1 = \frac{d_1}{a_1} \qquad\qquad (4.42)$$

After P_1 and Q_1 are calculated, the remaining values for P_2 and Q_2 through P_{ni} and Q_{ni} can be calculated from Equations (4.39) and (4.40), respectively. Furthermore, since the value of $a_{E,ni}$ is equal to zero, the value of the dependent variable, ϕ_{ni}, is equal to Q_{ni} from Equation (4.36). Using the calculated values for ϕ_{ni} and ϕ_{ni-1} from Equation (4.36), the values for all dependent variables shown in the row of

interest in Figure 4.5 can be calculated using back-substitution process. The general calculation procedure is:

1. Calculate the values of P_1 and Q_1 from Equations (4.41) and (4.42).
2. Use the recurrence relationships in Equations (4.39) and (4.40) to calculate all the values for P_i and Q_i for i = 2, …, ni.
3. Set ϕ_{ni} equal to Q_{ni}
4. Use Equation (4.36) and a back-substitution process to calculate the values for all dependent variables in the row of interest (i.e. ϕ_{ni-1}, …, ϕ_1 for i = ni-1, …, 1).

4.2.5.2 TDMA Applied to a Three-dimensional System

For a three-dimensional system, an individual grid point, P, will have six nearest neighbors as shown in Figure 4.4 rather than just two as for the case in one-dimension shown in Figure 4.5. As a result, the nonzero coefficients will not all align themselves along the three diagonals of matrix (4.35). Despite this complication, the TDMA process can still be used to solve a three-dimensional problem as for the modeling of laser-firing of Al-Si contacts. The three-dimensional discretization Equation (4.12) is re-written here without considering the value for the dependent variable at the previous time step:

$$a_P \, \phi_P = a_E \, \phi_E + a_W \, \phi_W + a_N \, \phi_N + a_S \, \phi_S + a_T \, \phi_T + a_B \, \phi_B + b \qquad (4.43)$$

In solving the three-dimensional problem, the process starts by first selecting one direction, such as the x-direction, for the TDMA process. Using this method, Equation (4.43) can be rewritten as:

$$a_P \, \phi_P - a_E \, \phi_E - a_W \, \phi_W = d \qquad (4.44)$$

where, the value d can be defined as:

$$d = a_N \, \phi_N + a_S \, \phi_S + a_T \, \phi_T + a_B \, \phi_B + b \qquad (4.45).$$

Equation (4.44) has the same structure as Equation (4.29) and can be followed in accordance with the TDMA process outlined above for one-dimension. In this model, the values for the dependent variable, ϕ, are first calculated starting at row j = 2 and k = nk-1 and proceeding in the x-direction for i = 2, …, ni-1. After the values are calculated, the program moves to row j = 3 and k = nk-1 and performs the TDMA in the x-direction for i = 2, …, ni-1 to obtain the values for ϕ. This process repeats itself until on the k = nk-1 plane until the row j = nj-1. After the values for ϕ are calculated in this row, TDMA moves down one plane to the index value k = nk-2 and TDMA is repeated at each row in the y-direction from j =2, …, nj-1.

This process is repeated along each plane in the z-direction until the plane k = 2 when all values for ϕ are obtained in the computational domain. This constitutes one cycle of iterations. Furthermore, TDMA is only performed on all interior grid point locations (i.e. i = 2, …, ni-1; j = 2, …, nj-1, k = 2, … nk-1) since boundary conditions for enthalpy and temperature are already specified on the grid point locations at the faces of the computational domain. In addition, when the boundary conditions are re-applied at the beginning of each iteration step, the heat flux due to the laser is used to recalculate boundary values on the top surface.

In order to arrive at a realistic solution, however, the values for ϕ at each grid point need to be updated in successive iterations. TDMA is then performed according to the procedure below throughout the computational domain, and the equations are solved repeatedly with updated coefficients. The iterations are stopped and the solution is deemed acceptable after the convergence criteria are met. The general TDMA solution procedure can be outlined as follows:

1. Assign initial values for the dependent variable, ϕ, at all grid point locations.
2. Apply enthalpy and velocity boundary conditions at all grid point locations.
3. Calculate the values for the coefficients in Equation (4.43) using Equations (4.14) to (4.16).
4. Select a plane perpendicular to the z-direction to start the calculations. Typically, calculations will start on the plane k = nk-1.
5. Perform TDMA in the x-direction on the plane perpendicular to the z-direction progressing from j = 2, …, nj-1.
6. Store the values the appropriate dependent variable matrix.
7. Index down one plane and repeat steps 4 and 5 until the dependent variables on plane k = 2 have been obtained.
8. Check convergence. If convergence criteria are not met, then repeat steps 2 through 7 until the maximum number of user-specified iterations is reached or convergence is obtained.

4.2.5.2 Convergence Criteria

In the mathematical model, there are two convergence criteria that are applied to evaluate the validity of the solution after each iteration step. An iterative process has converged when additional iterations will not result in changes in the calculated values of the dependent variables and the residual changes are minimized. Convergence criteria are applied to: 1) minimize the residual changes in the dependent variables (u, v, w and h); and 2) ensure overall heat balance ratio in the system (i.e. that the ratio of the accumulated heat in the system to the incoming heat from the laser heat source plus the outgoing heat

from the faces of the computational domain is equal to 1). To minimize the residual changes, the residue, R, at an individual grid point P can be calculated from Equation (4.12) as:

$$R_{\phi_P} = \frac{\sum a_{NN}\,\phi_{NN} + S_U\,\Delta V}{a_P} - \phi_p \tag{4.46}$$

where all terms have been previous defined. The residual values for all grid points within the entire computational domain can then be calculated as:

$$R_{\phi_{domain}} = \sum_{domain} \left| \frac{\sum a_{NN}\,\phi_{NN} + S_U\,\Delta V}{a_P} - \phi_p \right| \tag{4.47}$$

and should be equal to 0 for the entire domain. To speed up the rate of convergence, the residuals are normalized by the values of the dependent variables within the entire domain as follows:

$$R_{\phi_{domain,normalized}} = \frac{\displaystyle\sum_{domain} \left| \frac{\sum a_{NN}\,\phi_{NN} + S_U\,\Delta V}{a_P} - \phi_p \right|}{\displaystyle\sum_{domain} \left| \phi_P \right|} \tag{4.48}$$

The normalized residual values for each dependent variable (u, v, w and h) should be extremely small (on the order of 1×10^{-4}) for this convergence criterion to be met. In addition to the convergence criteria for the residuals, the heat balance criterion is utilized. The heat balance for the overall computational domain shown in Figure 4.1 can be expressed as:

$$F_i = Q + HA \tag{4.49}$$

where F_i is the heat input, Q is the heat output and HA is the heat accumulation. Heat input, F_i, is calculated from Equation (4.18) for the heat flux from the laser heat source. Heat output, Q, is calculated as:

$$Q = \iint q\,dA \tag{4.50}$$

where q is the heat flux through the area A and is calculated at the east, west, top, bottom, and north faces. The heat flux at the symmetry surface is zero based on the boundary condition (4.22). For the transient calculations used for the short pulse durations associated with the laser-firing process, it is necessary to account for the heat accumulation, HA, in Equation (4.49) at each time step, which is calculated for each grid point and summed over the entire domain as:

$$HA = \iiint\limits_{domain} \rho \frac{dH}{dt} dxdydz \qquad (4.51)$$

where H is the enthalpy. The heat balance ratio, θ, can then be calculated as:

$$\theta = \left| \frac{F_i}{Q + HA} \right| \qquad (4.52)$$

For convergence, the heat balance ratio should be close to 1. In the modeling performed, the criterion for the heat balance ratio is $0.999 \leq \theta \leq 1.001$. This allows for the convergence to be met without significant impact on the final solution while ensuring reasonable computation time.

4.2.6 Outputs

The directly-calculated outputs from the model are the values for dependent variables at each grid point. The sensible heat value is converted to temperature based on an Enthalpy-Temperature relationship [5]. Based on the temperatures calculated, the size of the laser-fired contact geometry can be obtained. Therefore, the values obtained from the model that are used for analysis of the laser-firing process are the contact geometry, temperature fields, and fluid flow velocities.

4.3 Summary

This chapter provides an overview for the framework of the heat transfer and fluid flow model used in this research to study the laser-fired contact formation process. Important aspects of the model, such as the inputs, governing equations and appropriate discretization schemes, boundary conditions, and solution procedure have been discussed in detail. The specific applications of the mathematical model and modifications to the model to simulate the laser-fired contacting process are discussed in Chapter 5.

4.4 References

1. S.V. Patankar, Numerical Heat Transfer and Fluid Flow, New York: Hemisphere Publishing Corporation, 1980.
2. M.A. Bramson, *Infrared Radiation: a Handbook for Applications*, New York: Plenum Press, 1968.
3. T. Reutzel, Applied Research Laboratory, Penn State University, Private communication, Measurement of IPG Photonics single mode fiber laser beam distribution using Precitec optics.
4. A.D. Brent, V.R. Voller and K.J. Reid, *Numer. Heat Transfer* **13**, 297 (1988).

5. G.G. Roy, W. Zhang, S. Mishra, X. He, Y. Fan, A. Kumar, T. DebRoy, A computer program to calculate fluid flow and heat transfer during fusion welding with free surface, Pennsylvania State Univeristy (2004).

6. J.L. Murray, A.J. McAlister, The Al-Si (aluminum-silicon) system, Bulletin of alloy phase diagrams, Springer (1984).

7. N. S. Tsai and T. W. Eagar, Metallurgical Transactions B, **16B**, pp. 841, (1985).

8. C. L. Chan, R. Zehr, J. Mazumder and M. M. Chen, Three-Dimensional Model for Convection in Laser Weld Pool, In: Modelling and Control of Casting and Welding Processes, Proceedings, 1986.

9. K. Mundra, T. DebRoy and K. M. Kelkar, Numer. Heat Transfer, Part A, 29, 115 (1996).

HEAT AND MASS TRANSFER AND FLUID FLOW DURING LFC FORMATION

5.1 Introduction

The majority of research on the laser-fired contact (LFC) process has focused on parametric optimization with little effort to understand the underlying physical processes that affect contact formation [1-10]. Developing an understanding of the contact formation process requires quantitative information about the substrate temperature profiles, the fluid flow fields, and the evolution of contact geometry. Unfortunately, due to the short pulse durations (less than a few milliseconds) and size of the contacts (tens of micrometers in diameter), there is not sufficient time to obtain accurate experimental data. Mathematical models for small-scale laser processing have been developed [11-18] to determine temperature profiles, thermal cycles, fluid flow velocities, and weld size as a function of processing parameters. It has been shown through numerical simulations that the interaction between the laser welding heat source and the material results in rapid heating, melting, vaporization, expulsion, variations in alloy composition, and changes in the solidification behavior based on the selection of different laser processing parameters, such as laser power, pulse duration, and beam diameter. However, most of these studies were performed considering substantially longer time scales (tens of milliseconds to steady state), larger beam sizes, and different material systems.

The LFCs under consideration are formed using short microsecond or millisecond pulse durations and high energy densities, which results in rapid heating and cooling cycles that will influence the contact geometries. The final contact geometry and the extent of Al alloying can significantly impact the total contact resistance as shown in Chapter 3. The objective of this chapter[2] is to analyze the role that various laser processing parameters have on the physical phenomena governing contact formation. In order to achieve this objective, the evolution of temperature and velocity fields during laser-firing is studied using a transient numerical heat transfer and liquid metal flow model. A novel method is developed based on the Al-Si phase diagram to account for the melting and mixing of the Al and Si during laser-firing to accurately predict contact geometry and Al concentration profiles. Using the validated model, the impact of changes in laser power, laser beam radius, and pulse duration on thermal cycles, contact geometry, and dopant concentration profiles is analyzed to understand the mechanisms that affect heat and mass transfer,

---

[2] Portions of this chapter are directly excerpted from the following two published manuscripts:
1. A. Raghavan, T. A. Palmer, T. DebRoy, Evolution of laser-fired aluminum-silicon contact geometry in photovoltaic devices, J. Appl. Phys. 111, 2012. ©
2. A. Raghavan, T. A. Palmer, T. DebRoy, Mathematical modeling of laser micro-welding for photovoltaic devices, Proceedings of Trends in Welding Research, 2013. ©

and fluid flow. The model is also updated to include a secondary laser heat source to simulate the processing of multiple contacts simultaneously, as would be done in a high throughput environment. The influence of LFC pitch distance on temperature profiles, fluid flow velocity, and contact geometry is analyzed to determine acceptable contact spacing. The results generated here provide a quantitative framework and understanding of the LFC process that are important for future process development.

5.2 Experimental Procedure

The majority of experimental data used for model validation was obtained from the literature [9] for contacts that exhibited little to no metal expulsion during processing. The laser-fired contacts were processed on a 275 µm thick, double-side polished, (100), p-type, float zone (FZ) Si wafers with resistivities between 1 and 5 Ω-cm. The substrate had a dual stack passivation with 10 nm hydrogenated amorphous Si (a-Si:H) and 100 nm silicon dioxide (SiO_2) deposited by plasma-enhanced chemical vapor deposition (PECVD) and a 0.5 µm thick layer of Al deposited on both sides using electron-beam deposition. Figure 5.1(a) shows a schematic diagram of the experimental sample structure. Contacts were generated using an IPG Photonics 1070 nm single mode fiber laser with a 25 µm beam at focus. The laser consists of an ytterbium-doped fiber medium that outputs a collimated, near-Gaussian beam operating in the TEM_{00} mode through a fiber-optic delivery system and operates continuously up to 200 W or in pulsed mode up to 500 W. A schematic diagram of the beam profile is shown in Chapter 3. The exposure times can vary from 50 µs to over 1000 ms and are modulated using a National Instruments LabVIEW® program.

Contacts were processed with laser powers varied from 18 W to 50 W and pulse durations from 4 ms to 19 ms. Figure 5.2 [9] shows the top surface of various LFCs processed as a function of pulse duration and power level. The fluence (or energy density, J/cm^2) levels for each contact are identified on the SEM micrographs and are calculated using a beam waist measurement method developed by Zou, et al. [19]. Additional details about laser- firing and sample preparation can be found in the literature [9]. LFCs that did not exhibit metal expulsion, which were processed using the conditions given in Chapter 3, were also used for model validation.
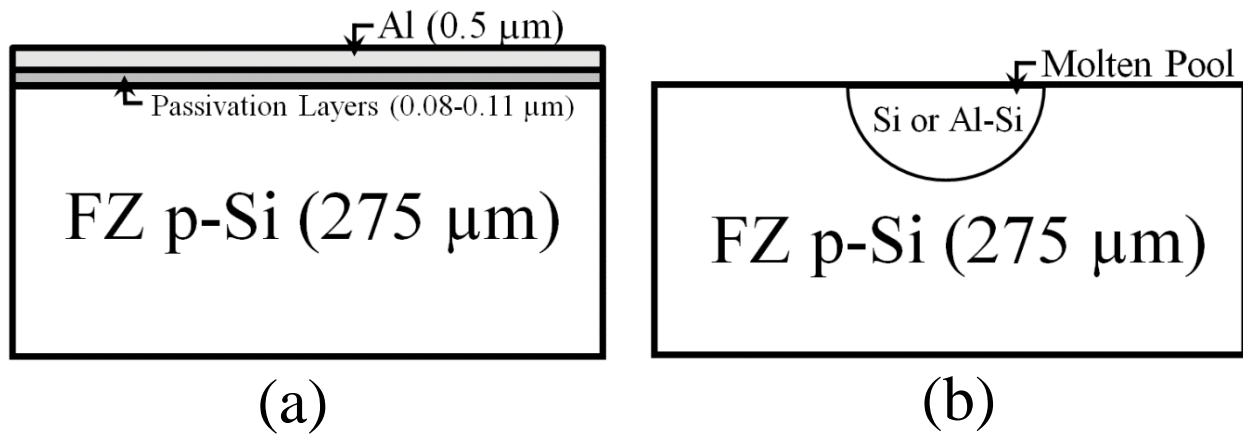
Figure 5.1. Schematic diagram of (a) experimental substrate, and (b) modeled substrate that uses Si material properties in bulk substrate and Si or Al-Si properties within molten region depending on the alloy concentration. Substrate thickness is 275 μm.
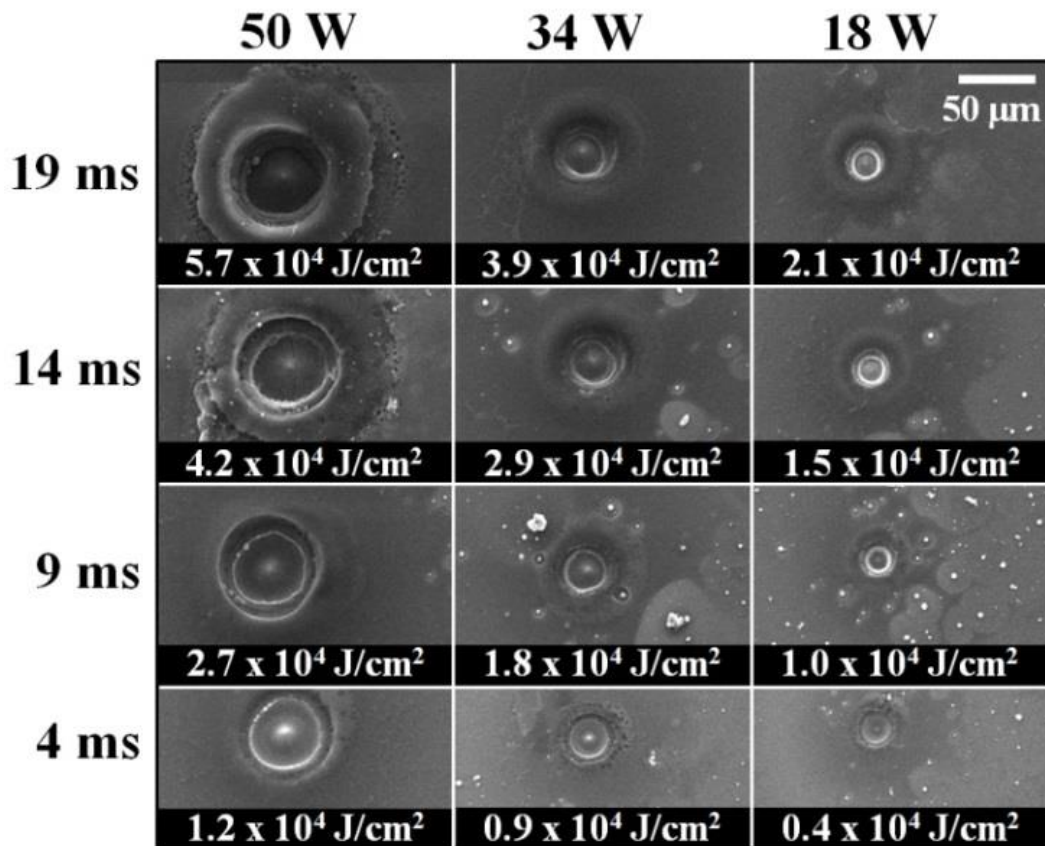
Figure 5.2. SEM micrographs of LFCs processed with IPG 1070 nm single mode fiber laser on dual stack passivation sample. The images shown above are of the LFC top surface.

5.3 Influence of Al-Si Mixing on LFC formation

5.3.1 Modeling of Al-Si Alloying during LFC Formation

Despite the thinness of the Al metallization layer (0.5 µm), if one were to only consider the melting of pure Si, it would not be possible to accurately predict the contact geometry. A comparison between experimental spot size inner crater diameter and the computed molten pool size when considering a pure Si substrate processed with 18 W laser power and a 19 ms pulse duration is shown in Figure 5.3. It is observed that the size of the computed molten pool is significantly over-predicted when assuming a pure Si substrate when compared to the experimental inner LFC diameter. Therefore, it is important to consider the alloying of Al and Si that will occur during laser-firing to accurately calculate the amount of energy required for heating and melting of the LFC in order to predict the contact geometry.

Figure 5.4(a) shows a schematic diagram of how changes in contact geometry with time can influence the amount of dissolved Al in the molten pool (where $t_1 < t_2 < t_3$). As the molten pool size changes with variations in laser processing parameters, the concentration of Al in solution will change, since Al will be melted into a predominantly molten Si pool as it grows. Therefore, in the modeled substrate, shown in Figure 5.1(b), the molten pool is considered as an Al-Si alloy. The passivation layer is not considered because of its extremely small thickness. As the amount of Al in solution changes with contact geometry, the melting and solidification behavior will also be affected because the liquidus temperature and the amount of liquid present in the two-phase region will change.

The size of the two phase region that will exist due to alloying of Al and Si can be predicted based on the binary Al-Si phase diagram, which is shown in Figure 5.4(b). Using the Al-Si phase diagram, the liquidus temperature and liquid fraction at various compositions and temperatures can be calculated at any given instant in time. With changes in Al concentration, the difference between both the liquidus and eutectic temperatures will also change based on the phase diagram. Depending on the concentration of Al in the binary alloy, the difference between both the eutectic transformation and liquidus temperatures can be greater than 800K. Since experimental results confirm the formation of a two-phase microstructure, considering Al-Si alloying allows for an accurate determination of the amount of energy required to raise the temperature of the material and melt an incremental fraction of solid in the two-phase region, which is critical to accurately calculating the thermal cycles and spot size.
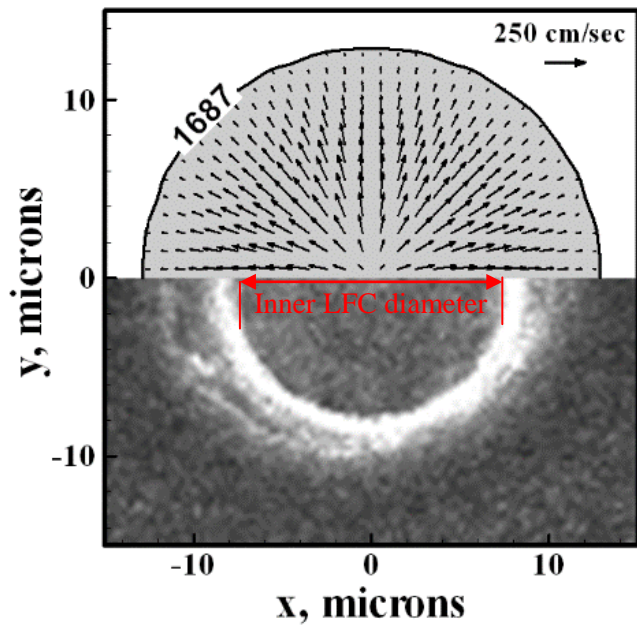
Figure 5.3. Comparison between the experimental and computed sizes of the molten region when modeling laser melting of pure Si.
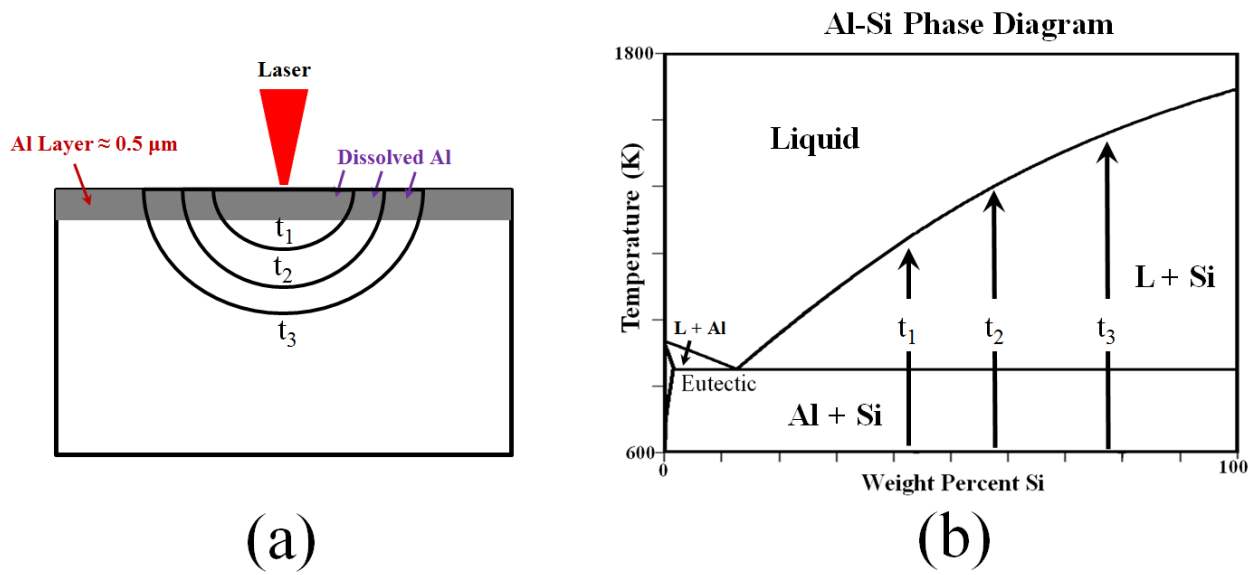
Figure 5.4. (a) Change in LFC size and resulting Al concentration with as a function of time ($t_1 < t_2 < t_3$), and (b) Al-Si phase diagram showing change in liquidus temperature as a function of time.

Depending on the alloy composition, the total enthalpy in the system, H, can vary widely over the two-phase (Liquid + Si) region. The relationship between the sensible heat, h, and latent heat content, ΔH, and total enthalpy is defined as:

$$H = h + \Delta H \qquad (5.1)$$

The sensible heat, h, is calculated as:

$$h = \int C_p dT \qquad (5.2)$$

where C_p is the specific heat of the solid or liquid and T is the temperature. The latent heat content, ΔH, is calculated as:

$$\Delta H = f_L \times L \qquad (5.3)$$

where f_l is the liquid fraction and L is an approximated latent heat of fusion for a Al-Si alloy. The liquid fraction in the two phase region can be calculated using the lever rule for binary phase diagrams as:

$$f_L = \frac{100 - \%Si_a}{100 - \%Si_l} \qquad (5.4)$$

where, f_L is the liquid fraction, $\%Si_a$ is the concentration of Si in the alloy, and $\%Si_l$ is the concentration of Si in the liquid at temperature T. In order to accurately determine the amount of liquid present at any given temperature, it is necessary to determine the alloy composition, $\%Si_a$. The concentration of Si in the Al-Si molten pool can be calculated assuming that the Al directly above the molten region dissolves into the melt pool as:

$$\%Si_a = \frac{V_{Si}\rho_{Si}}{V_{Si}\rho_{Si} + V_{Al}\rho_{Al}} \times 100 \qquad (5.5)$$

where V_{Si} and V_{Al} are the volumes of Si and Al in the molten region, respectively, and ρ_{Si} and ρ_{Al} are the densities of liquid Si and liquid Al, respectively. Using the alloy composition, the composition of the liquid, $\%Si_l$, at temperature T can be calculated using a relationship between Si composition and the liquidus line on the phase diagram shown in Figure 5.4(b). These functions were obtained by fitting two curves to the liquidus line on the Al-Si phase diagram:

$$\%Si_l = \begin{cases} (T/145.62 - 2.25)^2 - 0.345279 & \text{for } T_{eutectic} \leq T < 1404 \\ 1.73 \times 10^{-9} \, T^{3.335} & \text{for } 1404 \leq T \leq T_{liquid} \end{cases} \tag{5.6}$$

Equation (5.6) is used to determine the concentration of Si in the liquid at any given temperature over the two-phase region. Using Equations (5.5) and (5.6), the liquid fraction can be approximated for an alloy with a given concentration of Si. After calculating the liquid fraction based on Equation (5.4), the latent heat content can be calculated over the two-phase region per Equation (5.3) to determine the total enthalpy for any given alloy system. A comparison of the sensible heat and enthalpy for three systems with varying alloy concentrations is shown in Figure 5.5. This figure shows the total enthalpy versus temperature for alloys with 30wt. % Si, 60 wt. % Si and 90 wt. % Si. The area under the curve represents the total energy required for melting. Based on the alloy composition, the amount of energy required for melting will change. For the alloy with 30 wt. % Si, there will be more energy required for the phase change at the eutectic temperature than that for an alloy with 60 or 90 wt.% Si. By accounting for these changes, modeling proceeds in time and can more accurately represent the ongoing physical processes. When the material is a pure liquid or pure solid (i.e. the sensible hat thresholds are exceeded), the liquid fraction in Equation (5.4) will be 1 or 0, respectively.
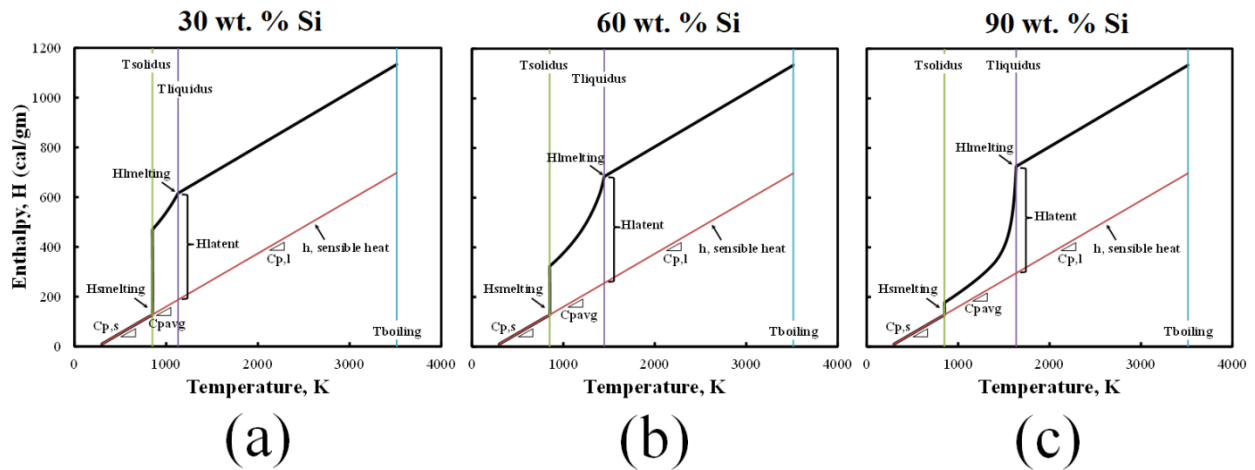
Figure 5.5. Enthalpy temperature diagrams used in the model for Al-Si alloys with (a) 30 wt% Si, (b) 60 wt. % Si, and (c) 90 wt. % Si.

Non-uniform grid spacing, typically 135 x 70 x 55 grids and 50 microsecond time steps were used to maintain computational accuracy when modeling the millisecond pulse durations. Shorter time steps (1-10 μs) were used for modeling of microsecond pulse durations. The solution domain had dimensions in the *x*-, *y*- and *z*- directions of 800 μm, 400 μm and 275 μm, respectively. Finer grid spacing was used in the area below the laser beam to achieve maximum resolution of variables, and the minimum grid spacing

was approximately 1 µm in the x, y, and z directions. Figure 5.6 shows a schematic diagram of the boundary conditions used in the solution of these equations, which are explained in detail in the previous chapter. Table 5.1 shows the material properties used for both pure Si and the binary Al-Si alloy.

Top Surface:

$$\mu \frac{\partial u}{\partial z} = f_L \frac{d\gamma}{dT} \frac{dT}{dx}$$

$$\mu \frac{\partial v}{\partial z} = f_L \frac{d\gamma}{dT} \frac{dT}{dy}$$

w = 0 cm/sec

Other Surfaces:

T = 298K

u = v = w = 0 cm/sec

Symmetry Surface:

$$\frac{\partial u}{\partial y} = 0 \qquad \frac{\partial w}{\partial y} = 0$$

v = 0 cm/sec

Heat Input and Loss:

$$H_{in} = \frac{Qf\eta}{r_b^2} \exp\left(-\frac{f\left(x^2+y^2\right)}{r_b^2}\right)$$

$$-h_c\left(T-T_a\right) - \sigma\varepsilon\left(T^4-T_a^4\right)$$

convective   radiative
loss   loss
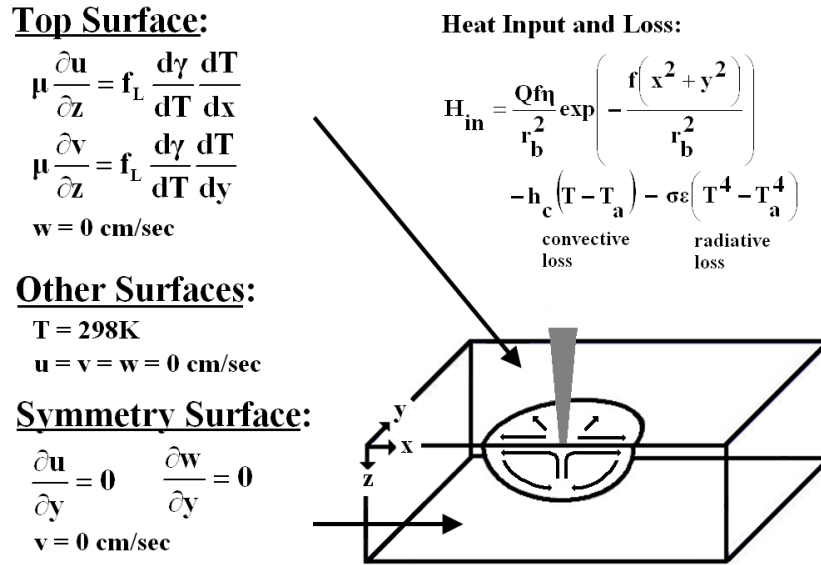
Figure 5.6. Boundary conditions applied to solve conservation equations.

Table 5.1. Data used for calculations [20-30].

Property	Value
Density of liquid Si $(kg\ m^{-3})$	2510
Density of liquid Al $(kg\ m^{-3})$	2390
Absorptivity of solid Al	0.1 - 0.4
Absorptivity of liquid Si	0.223
Effective viscosity $(kg\ m^{-1}\ s^{-1})$	0.0088
Melting Temperature (K), Pure Si	1687
Solidus Temperature (K), Al-Si Alloy	850
Liquidus Temperature (K), Al-Si Alloy	1551-1664
Enthalpy of solid at melting point $(kJ\ kg^{-1})$, Pure Si	1286
Enthalpy of solid at solidus $(kJ\ kg^{-1})$, Al-Si Alloy*	536
Enthalpy of liquid at melting point $(kJ\ kg^{-1})$, Pure Si	3085
Enthalpy of liquid at liquidus $(kJ\ kg^{-1})$, Al-Si Alloy*	2961-3064
Specific heat of solid $(kJ\ kg^{-1}\ K^{-1})$	0.895
Specific heat of liquid $(kJ\ kg^{-1}\ K^{-1})$	0.908
Specific heat of two-phase region $(kJ\ kg^{-1}\ K^{-1})$*	0.895
Thermal conductivity of solid $(J\ m^{-1}\ s^{-1}\ K^{-1})$	36
Effective thermal conductivity of liquid $(J\ m^{-1}\ s^{-1}\ K^{-1})$	218
Thermal coefficient of surface tension $(mN\ m^{-1}\ K^{-1})$	-0.13
Coefficient of thermal expansion	2.3×10^{-6}

5.3.2 Contact Geometry and Thermal Cycles

In order to accurately determine the molten pool geometry, the temporal variation of Al concentration is calculated using Equation (5.5). Figure 5.7 shows how the Al concentration can change as a function of time. The Al concentration experiences the most change during the first 200 μs and becomes constant thereafter for the three power levels considered. The molten pool dimensions experience little change after 200 μs, and the Al concentration reaches a steady state concentration at 24.6, 7.8 and 4.6 wt. % for laser powers of 18 W, 34 W and 50 W, respectively. Therefore, changes in Al concentration with increases in molten pool size should reach a minimum with longer pulse durations.

By considering the time-dependent concentration of Al in the molten pool, excellent agreement in the contact geometry between the calculated and experimental values is observed. For an LFC processed with 18 W laser power and a pulse duration of 19 ms, as shown in Figure 5.8, good agreement is observed between the experimental fusion zone boundary and the liquidus temperature contour. Figure 5.9 shows the calculated spot sizes for a binary Al-Si alloy at a power level of 50 W and pulse durations of 4 ms and 19 ms. In Figure 5.8(b), the alloy contains 24.6 wt.% Al, based on the molten pool size and the dissolved Al content, which corresponds to a liquidus temperature of 1551K. For the contact processed with the 50 W laser power, the concentration of Al is approximately 4.6 wt. %, which corresponds to a liquidus temperature of approximately 1663K. Figure 5.10 also shows excellent agreement between the calculated and experimental top surface and cross-sectional region when using a 65 W laser power, a 500 μs pulse duration and a 50 μm beam diameter. In this case, the liquidus temperature is approximately 1638K for an Al concentration of approximately 10 wt. %. Table 5.2 shows that excellent agreement was obtained for the top surface LFC diameters for a wide range of processing conditions when considering the microsecond data presented in Chapter 3.

For a wide range of processing parameters, accounting for the alloying between Al and Si allows for accurate determination of the contact geometry. When accounting for Al, the total enthalpy for the system immediately increases at the eutectic temperature due to the energy required to melt a portion of the solid material. Therefore, a larger fraction of the supplied laser energy is used to melt some solid material, and the temperature does not rise as rapidly as it would for pure Si and the molten pool does not grow as large for the alloy. By accounting for this additional energy expenditure, the molten pool can be calculated with greater accuracy. As the molten pool size changes, it is therefore important to determine the Al concentration to understand the influence that alloying will have on molten pool geometry. The fluid flow as expressed by the velocity vectors on the top surface of the melt pool is due to Marangoni convection, which results from the spatial variation of surface tension along the surface of the pool. The surface tension of Si strongly decreases with an increase in temperature, which causes the fluid to flow

from the center (high temperature region) to the periphery (low temperature region). Depending on the selection of processing parameters, the stress on the surface will influence the fluid flow velocities.
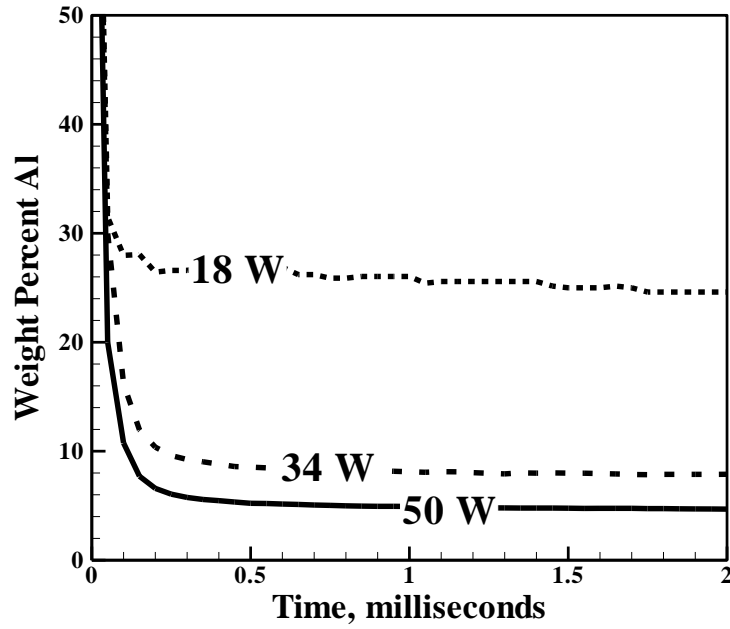
Figure 5.7. Concentration of Al in molten pool approaches constant value within 0.2 ms for all laser powers.
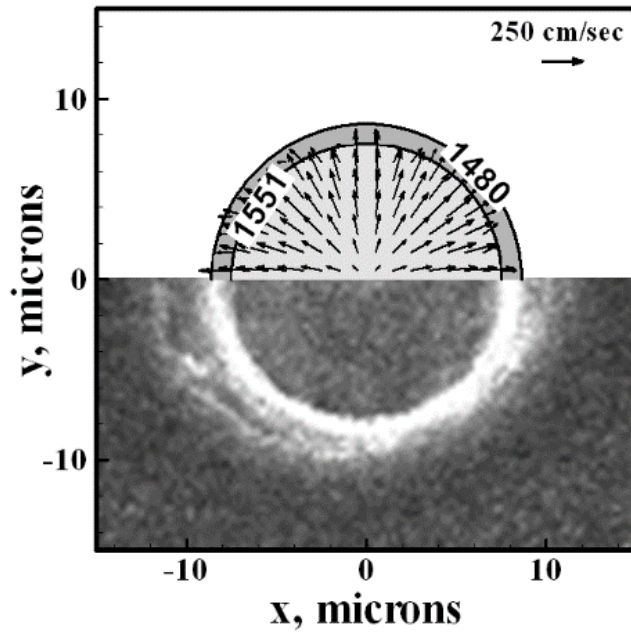
Figure 5.8. Comparison of calculated and experimental results for LFC processed with 18 W, 25 μm beam size, and a 19 ms pulse duration. 1551 K represents liquidus temperature contour and 1480 K is passivation layer melting temperature.
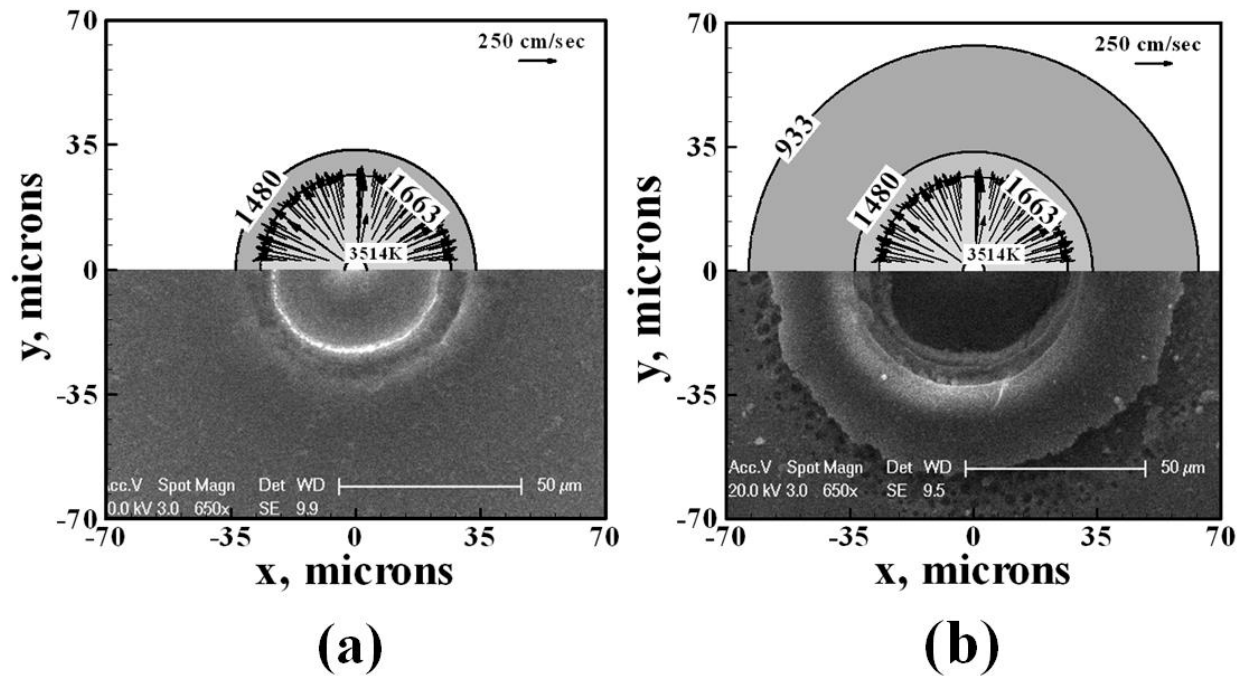
Figure 5.9. Comparison of calculated and experimental [9] molten pool sizes for Al-Si shows improved fit for molten zone for (a) 50W, 4.6 wt.% Al, 4 ms pulse duration and (b) 50W, 4.6 wt.% Al, 19 ms pulse duration. Contours identified on the plot are: Al melting temperature (933K), α-Si:H (1480K) and liquidus temperatures (1663K).
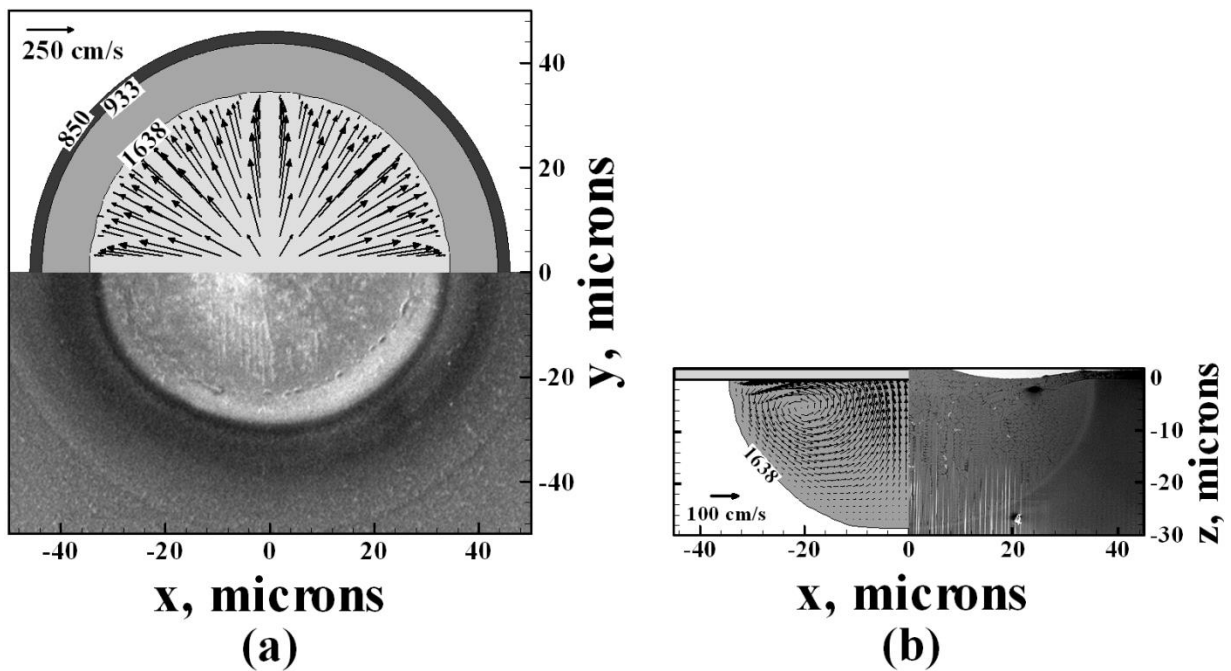
Figure 5.10. Comparison of calculated and experimental molten pool sizes for (a) top surface and (b) cross-section for LFC processed 65 W laser power, 500 μs pulse duration and 50 μm beam diameter.

137

Table 5.2. Comparison between experimental (exp.) and calculated (cal.) top surface LFC diameters.

LFC No.	Power (W)	Pulse Duration (µs)	LFC Diameter (µm)	
			Exp.	Cal.
1*	65	500	64	67
2	112	200	83	85
3	112	500	97	101
4	159	50	63	66
5	159	100	83	86
6	159	200	104	102

*Processed with 50 µm beam diameter

Figure 5.11(a) and Figure 5.11(b) show the thermal cycles for a pure material and an Al-Si alloy processed with 50 W laser power, a 200 µs pulse duration, and a 25 µm beam size, respectively. In Figure 5.11(a), a long thermal arrest is observed on cooling at the melting point of Si due to the large difference in the enthalpy at the melting temperature between solid Si (1286 kJ kg^{-1}) and liquid Si (3085 kJ kg^{-1}). Despite the large latent heat of fusion for pure Si, the amount of energy supplied from the laser is sufficient to induce rapid phase change from solid to liquid on heating. The heating rate within the molten pool is on the order of 10^7 K sec^{-1}, and the elevated temperatures within the pool are maintained for the entire 200 µs pulse duration with minimal increase. The temperature varies from 3832K at the center of the pool to 1687K at the solid/liquid interface over a distance of approximately 22.8 µm.

(a)

(b)
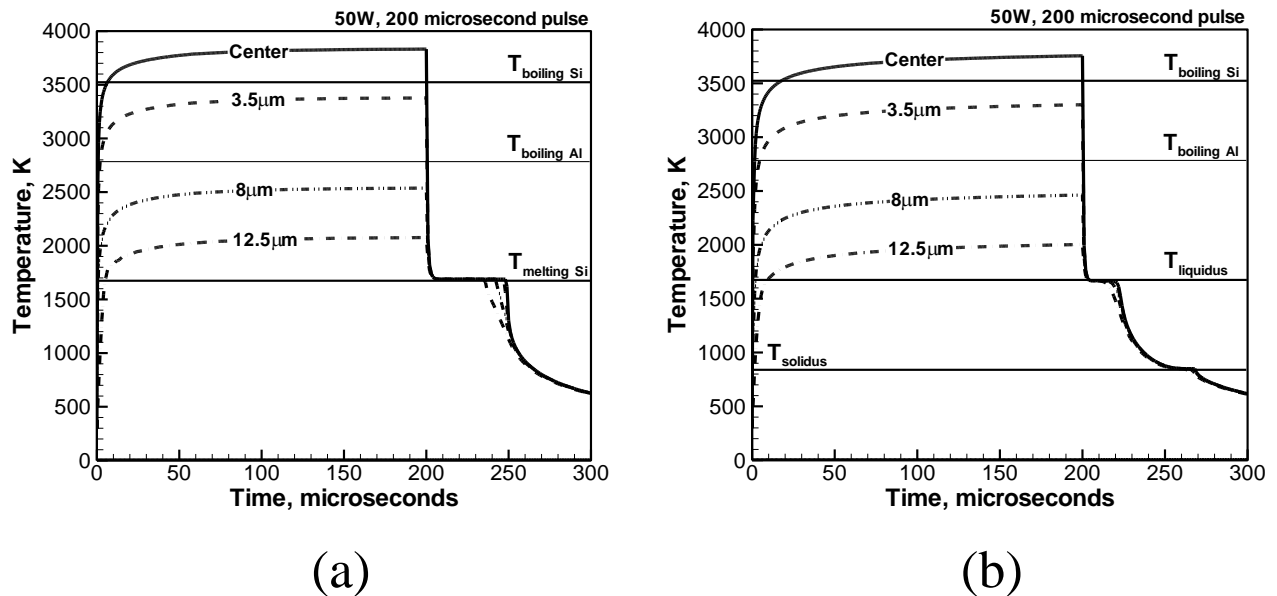
Figure 5.11. Thermal cycles for (a) pure versus (b) Al-Si alloy with 50 W laser power and 200 µs pulse duration exhibit different heating and cooling behavior due to the presence of Al in the melt. The distance values shown on different lines indicate the distance from the center of the molten pool.

Due to the large Maragnoni shear stress and its impact on the spatial variation of surface tension, the maximum velocities are approximately 5.2 m sec^{-1}. With such high velocities, substantial mixing within the molten pool is expected at this pulse duration. When comparing the thermal cycles in Figure 5.11(a) and Figure 5.11(b), it is evident that the temperatures in the molten region are lower for the binary alloy than that for pure Si over the entire course of the laser pulse. The peak temperatures within the molten pool are about 100K higher for the pure material during the first 200 μs. The cooling curves shown in Figure 5.11(b) are substantially different from that for pure Si. Specifically, there are two discernable thermal arrests for the alloy located at the liquidus and eutectic temperatures.

As the power level is varied and the concentration of Al in the molten pool changes, the observed cooling cycles change as well, since the liquid to solid transformations that take place at the liquidus and eutectic temperatures will be composition dependent, as shown in Figure 5.5. As the concentration of Al is increased, a larger fraction of the transformation will take place at the eutectic temperature because the initial fraction of solid Si in the melt will be greater immediately above the eutectic temperature. However, as the concentration is decreased and the liquid alloy more closely resembles a pure material, a significant portion of the liquid to solid transformation will take place at the liquidus temperature. As a result, the substrate time at elevated temperatures. In both cases (pure vs. binary alloy), the cooling cycles are similar after the eutectic temperature is reached. The rate of cooling, however, is much greater for pure Si than for the binary alloy since the entire liquid to solid transformation takes place at the melting temperature (1687K). With higher rates of cooling, it can be expected that there will be different solidification morphologies observed within the LFC.

Since the temperatures within the pool are above the boiling point of both Si (3514K) and Al (2792K) for the LFC processed with 50 W laser power, it can be expected that substantial vaporization of alloying elements will take place. The impact of excessively high processing temperatures can be confirmed in Figure 5.9(b), where noticeable substrate damage is observed as the pulse duration is increased from 4 ms to 19 ms. The alignment of important temperature contours for the molten region (1663K) and the melting temperature of Al (933K) shows fair agreement with the regions of delamination observed in the experimental results. Depending on the critical temperature and radius for liquid metal expulsion, it is important to maintain temperatures significantly below the boiling point of Si to ensure that alloy elements are not lost during processing.

Small differences between the computed molten pool sizes and experimental results can be attributed to errors in the estimation of the actual amount of dissolved Al. Here, the estimated concentration of Al assumes that the Al content present in the molten pool comes solely from the melting of the thin-film

layer directly above the molten region. However, the actual amount of Al in the molten region may be slightly higher than the computed values, since the thin-film covers the entire substrate and the surface temperatures away from the molten region will also be above the melting temperature of Al. Furthermore, as observed in the EDS mapping for cross sections shown in Chapter 3, there can be significant interdiffusion of Si and Al, which may influence the actual concentration.

5.4 Heat Transfer and Mass Transfer

The mechanism of heat transport within the molten pool determines the molten pool width and depth, whereas the mass transport mechanisms will influence the dopant density through the pool. Since these factors influence contact formation and device performance, it is important to quantity the dominant mechanisms to understand what physical phenomena govern the process.

5.4.1 Modeling Al Concentration Profiles

In order to predict the mass transfer behavior associated with contact formation under microsecond pulses, the model was modified to also iteratively solve the conservation of mass equation for a dopant species to calculate Al concentration profiles within the molten pool. The conservation equation is:

$$\rho\frac{\partial(C)}{\partial t} + \frac{\partial(\rho u_i C)}{\partial x_i} = \frac{\partial}{\partial x_i}\left(\rho D \frac{\partial C}{\partial x_i}\right) \tag{5.7}$$

where ρ is the density of the material, C is the dopant concentration, t is time, u_i and x_i are the velocity and distance components in the ith orthogonal direction (where $i = 1$, 2, or 3), and D is the diffusion coefficient of Al in liquid Si, taken here as 7×10^{-4} cm/s [31].

The Al surface concentration, C_s, is set equal to 100 wt. % Al along the entire top surface of the substrate at the start of processing at $t = 0$ μs, as shown in Figure 5.12(a). After a molten pool first forms at time t_1, as shown in Figure 5.12(b), the surface concentration is maintained at 100 wt. % to allow Al to dissolve into the molten pool, as should be expected during initial melting and dissolution of the Al metallization layer. At time t_2, the surface concentration, $C_{s,m}$, above the molten pool region that was formed during the previous time step t_1 is significantly reduced to maintain an average molten pool concentration, C_{avg}, equal to:

$$C_{avg} = \frac{\rho_{Al} V_{Al}}{\rho_{Al} V_{Al} + \rho_{Si} V_{Si}} \times 100\% = \frac{\rho_{Al} (2\,\mu m)\pi\, r^2}{\rho_{Al} (2\,\mu m)\pi\, r^2 + \rho_{Si}\left(\frac{2}{3}\pi\, r^2 d - V_{Al}\right)} \times 100\% \tag{5.8}$$

where ρ_{Al} is the density of liquid Al, r is the top surface radius of the LFC, ρ_{Si} is the density of liquid Si, and d is the depth of the molten pool. The quantity in Equation (5.9) reflects the average concentration of Al in the molten region assuming the Al metallization layer directly above the molten pool has completely dissolved into the contact.

The surface concentration, C_s, is maintained at 100 wt. % Al above the regions that melt at time t_2, as shown in Figure 5.12(c), to allow additional Al to enter the pool such that the average pool concentration is equal to that calculated from Equation (5.9). This approach is utilized for each time step after time t_2 so that more Al is incorporated into the pool as it grows. In order to simplify the problem, the model does not consider the solid-state diffusion of Al into the Si outside the fusion zone. Therefore, the bulk aluminum concentration, C_b, outside the molten region is maintained at 0 wt. %, as shown in Figure 5.12. Although solid-state diffusion is not considered here, the formation of a p+ back surface field near the LFC interface due to solid-state diffusion of Al into the Si crystal has been observed experimentally [1] and is required to significantly reduce the recombination velocities.
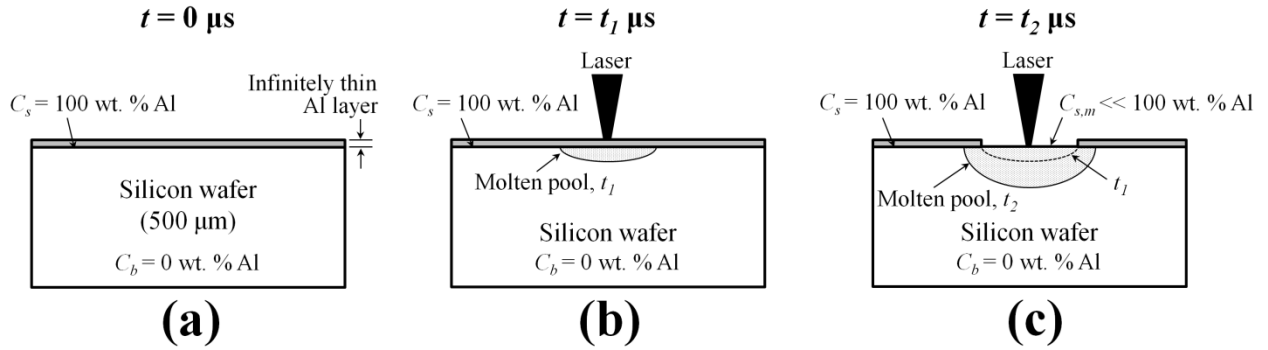
Figure 5.12. Schematic diagram of modeled substrate accounting for dissolution of Al into molten pool (a) prior to laser processing, (b) at time, t_1, when a molten pool has just formed, and (c) at time, t_2, which is greater than t_1. C_s is surface concentration, $C_{s,m}$ is surface concentration above the molten pool, and C_b is Al concentration in the bulk material.

5.4.2 Heat and Mass Transfer Mechanisms

The change in contact geometry in response to changes in process parameters is driven by a combination of convection and conduction heat transfer mechanisms. The relative importance of each in the overall heat transport can be evaluated using the heat transfer Peclet number, Pe_h:

$$Pe_h = \frac{\rho C_p U L}{k} = \frac{\rho C_p \, r\,(u_{max}/4)}{k} \tag{5.9}$$

where ρ is liquid density, C_p is specific heat of the liquid, k is the thermal conductivity, U is characteristic velocity taken as a quarter of the maximum velocity along the surface, and L is characteristic length taken

as the radius, r, of the molten pool. When the Pe_h is greater than 1, convection is the dominant heat transfer mechanism and when it is less than 1, conduction dominates heat transport.

Figure 5.13(a) shows a plot of Pe_h as a function of time for various laser powers and beam diameters. In all cases shown, the Pe_h rapidly exceeds 1 at the onset of contact formation and remains well above 1 over the course of processing. Therefore, heat transfer will be dominated by convection when generating LFCs with microsecond pulse durations. Furthermore, an increase in laser power from 50 W to 80 W when using a 50 μm beam diameter causes Pe_h to dramatically increase throughout the processing time. The influence of heat transfer by convection is driven by an increase in fluid flow velocities due to the higher temperature gradients within the molten pool.
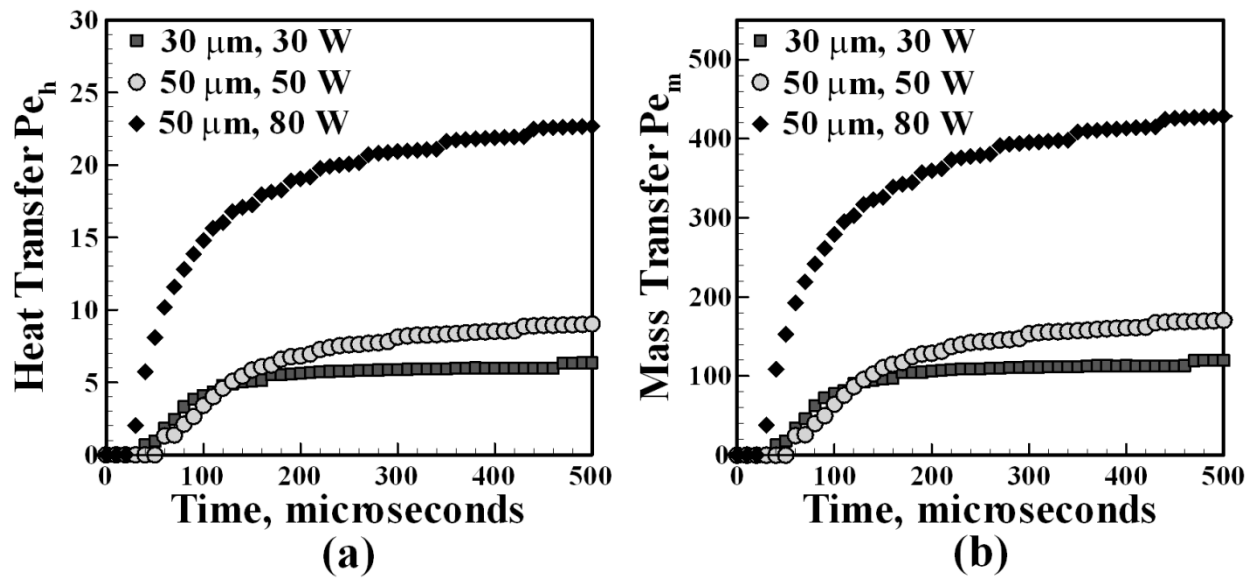
Figure 5.13. (a) Heat transfer Pe_h, and (b) Mass transfer Pe_m as a function of power, beam diameter, and pulse duration.

In addition to heat transfer, the fluid flow is important in mixing Al within the molten pool. Aluminum will be distributed by a combination of diffusive and convective mass transfer mechanisms. The dimensionless mass transfer Peclet number, Pe_m, can be used to identify the dominant mass transfer mechanism, and is calculated as:

$$Pe_m = \frac{U\,L}{D} = \frac{(v_{max}/4)(r)}{D} \tag{5.10}$$

where D is the diffusion coefficient of Al in Si and is taken as 7 x 10^{-4} cm/s [31]. If Pe_m is greater than 1, convection dominates mass transfer, and if Pe_m is less than 1, diffusion dominates. Figure 5.13(b) shows a plot of the mass transfer Pe_m as a function of time for the same processing conditions shown in Figure 5.13. Similar to the heat transfer Pe_h, the mass transfer Pe_m rapidly increases above 1 at the onset of

contact formation. In addition, an increase in laser power from 50 W to 80 W when using a 50 μm beam diameter causes the Pe_m to increase from approximately 150 at the end of the pulse to over 400. From Equation (5.11), it can be seen that increases in the radius and fluid flow velocities will directly increase Pe_m. At 80 W laser power and a 50 μm beam, the calculated LFC radius is 39 μm and the maximum fluid flow velocity is 305 cm/s in comparison to a 28 μm radius and 171 cm/s fluid flow velocity at 50 W. Therefore, the Pe_m increases significantly with an increase in power. In all cases, the mass transfer Pe_m is significantly greater than 1, indicating that convection will dominate mass transfer of Al within the pool.

Figure 5.14 shows a comparison between two concentration profiles calculated for an LFC that was processed with 65 W laser power, a 50 μm beam radius, and a 500 μs pulse. The lowest Al concentration of 0.017 wt. % corresponds to a dopant density of approximately 1×10^{19} cm^{-3} and represents a heavily Al-doped Si region [32]. Figure 5.14(a) shows the concentration profiles for Al within the contact when convection is not considered. This profile is obtained by not considering fluid flow in the numerical solution. The Al is not well distributed within the contact with extremely high concentrations observed near the surface of the melt pool. These high concentrations are due to the fact that as the pure Al metallization layer melts, it is incorporated into the pool only by diffusion. Although the results indicate that the Al concentration profiles are highly non-uniform throughout the pool, the LFC is nevertheless heavily doped since only a small Al concentration is necessary to achieve sufficiently high doping levels. Figure 5.14(b) shows the LFC when considering mass transfer by both diffusion and convection. The Al is more uniformly distributed throughout the pool due to the high fluid flow velocities associated with the process.
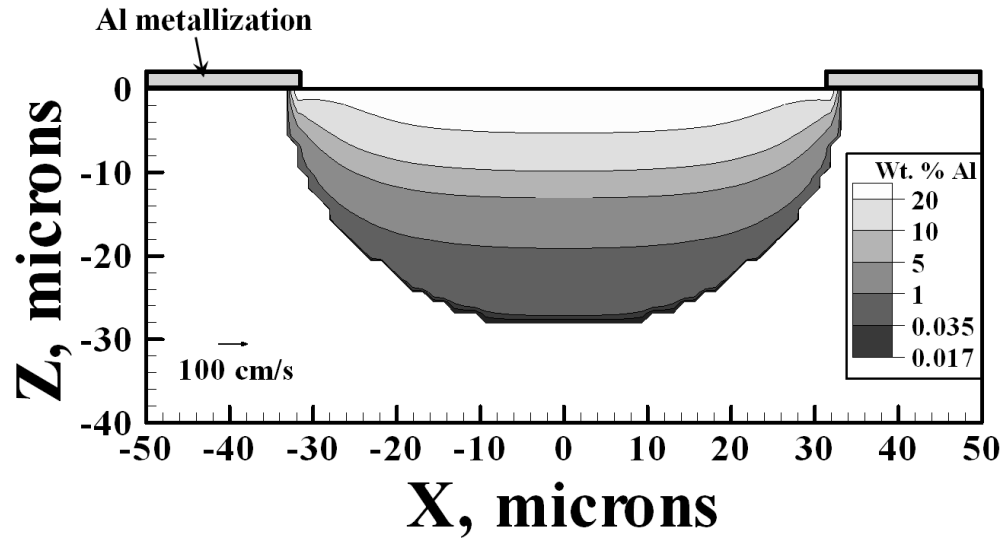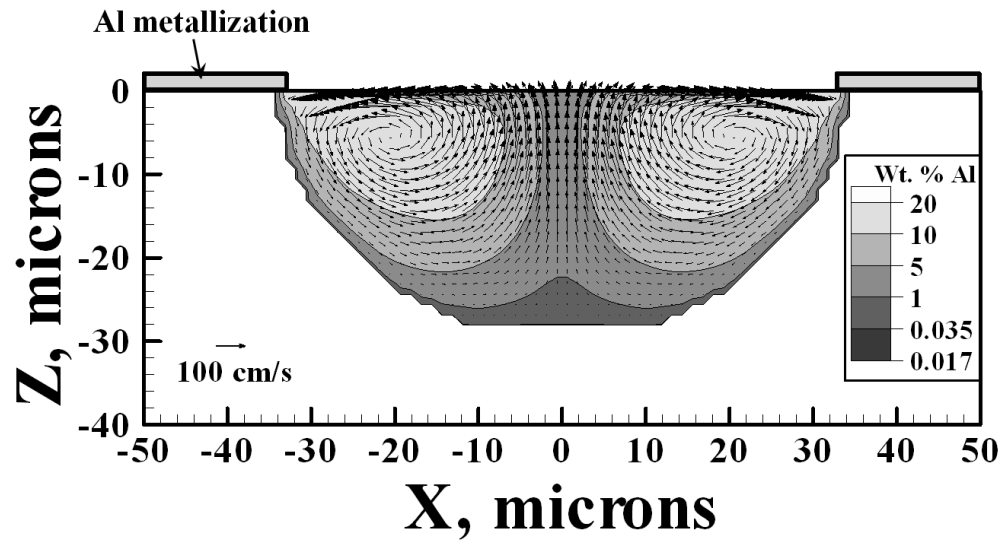
Figure 5.14. Concentration profiles at the end of the pulse duration through center of an LFC processed with 65 W laser power, a 500 µs pulse duration, and 50 µm beam diameter considering (a) diffusion only, and (b) both convection and diffusion.

Figure 5.15 shows a comparison between the calculated concentration profiles and the experimental results for a contact processed with 65 W laser power, a 50 µm beam radius, and a 500 µs pulse. Figure 5.15(a) shows the horizontal concentration profile for Al from the center to the end of the visible fusion boundary at locations 2 µm below the passivation layer. Figure 5.15(b) shows the Al concentration profile through the depth at the center of the pool starting at a location 2 µm below the passivation layer and ending within the Si wafer close to the fusion boundary, where the Al concentration goes to 0 wt. %.

The calculations when considering mass transfer by both convection and diffusion exhibit much better agreement along the top surface of the pool as shown in Figure 5.15(a).

Figure 5.15(b) shows the concentration profile through the depth of the pool at the center of the contact. The calculated results considering convection and diffusion under-predict the actual concentration profiles. Since the calculations are taken at the end of the pulse, they do not account for solute segregation during solidification, which will be reflected in the experimental results taken after complete solidification. During solidification, the Si, which has an extremely low solid solubility for Al [33], will reject Al to the liquid phase and the concentration of Al in the liquid will increase. In addition, the liquid with higher Al concentration will be pushed towards the center of the contact since solidification will progress from the fusion boundary towards the center [12]. Therefore, it can be expected that the experimental concentrations at the center will be higher than the calculated results. In both cases, considering only conduction leads to much steeper concentration profiles within the pool, which are not reflected in the experimental data. The experimental data suggest the presence of a well-mixed pool as observed in the data where the concentration is around 10 wt. % Al throughout the pool. The fair agreement between the experimental data and the calculations confirm that convection is the dominant mass transfer mechanism during LFC formation.
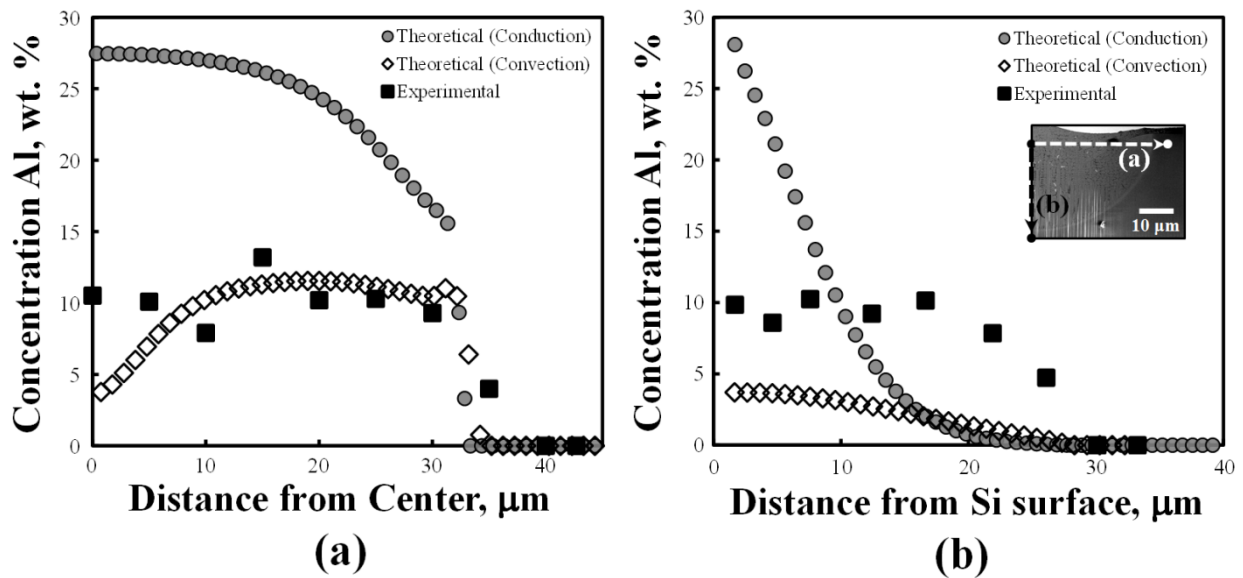
Figure 5.15. Comparison between the calculated (considering diffusion only versus convection and diffusion) and experimental Al concentrations (a) along top surface of contact 2 μm below surface of aluminum metallization layer, and (b) through center of contact.

Figure 5.16 shows the impact of changes in pulse duration and beam diameter on Al concentration profiles for a contact processed with 65 W laser power. At 50 μs, the contact produced with the larger 50

µm beam diameter exhibits a smaller pool size with a less well-mixed pool than the one formed with a 30 µm beam. In addition, the contact size is more hemispherical when using the smaller 30 µm beam diameter. The use of the smaller 30 µm beam diameter, however, results in a peak temperature of 3184K versus 2269K for the larger 50 µm beam diameter. When the pulse duration is increased to 100 µs, the dissolution of aluminum from the periphery of the molten region where the metallization layer has just melted can be clearly visualized when using the 50 µm beam diameter, as shown in Figure 5.16(b). As the metallization layer is incorporated into the melt, the circulation patterns of the molten material result in regions with Al concentration greater than 20 wt. % aluminum within the pool. In order to increase the uniformity of the mixing when using a larger beam diameter, a longer duration pulse is required. More time allows for the Al that has just been incorporated into the molten contact to be more uniformly distributed throughout the pool by convection. At 200 µs, for instance, the Al concentration within the pool is more uniform as shown in Figure 5.16(c).

When using the smaller 30 µm beam diameter, aluminum is more rapidly incorporated and distributed within the pool due to higher fluid flow velocities. At 100 µs, the maximum fluid flow velocity when using the 30 µm beam diameter is approximately 470 cm/s in comparison to 199 cm/s for the larger 50 µm beam diameter. Increasing the pulse duration leads to greater mixing and more uniform concentration profiles within the melt pool for both cases, although very limited mixing of Al into the Si is required to achieve the required level of Al doping within the contact. Therefore, the results suggest that the use of microsecond pulses can allow for incorporation of Al into the melt pool to much greater depths (nearly 30 µm in both cases shown here) than the use of shorter nanosecond duration pulses, which reach depths on the order of only 1 µm [12]. Furthermore, by using longer pulse durations, enhanced mixing can be promoted to form larger alloyed regions and a greater interfacial area between the LFC and wafer, which can reduce the total contact resistance.

50μm beam

30μm beam

50μs

(a)

(d)

100μs

(b)

(e)

200μs

(c)

(f)
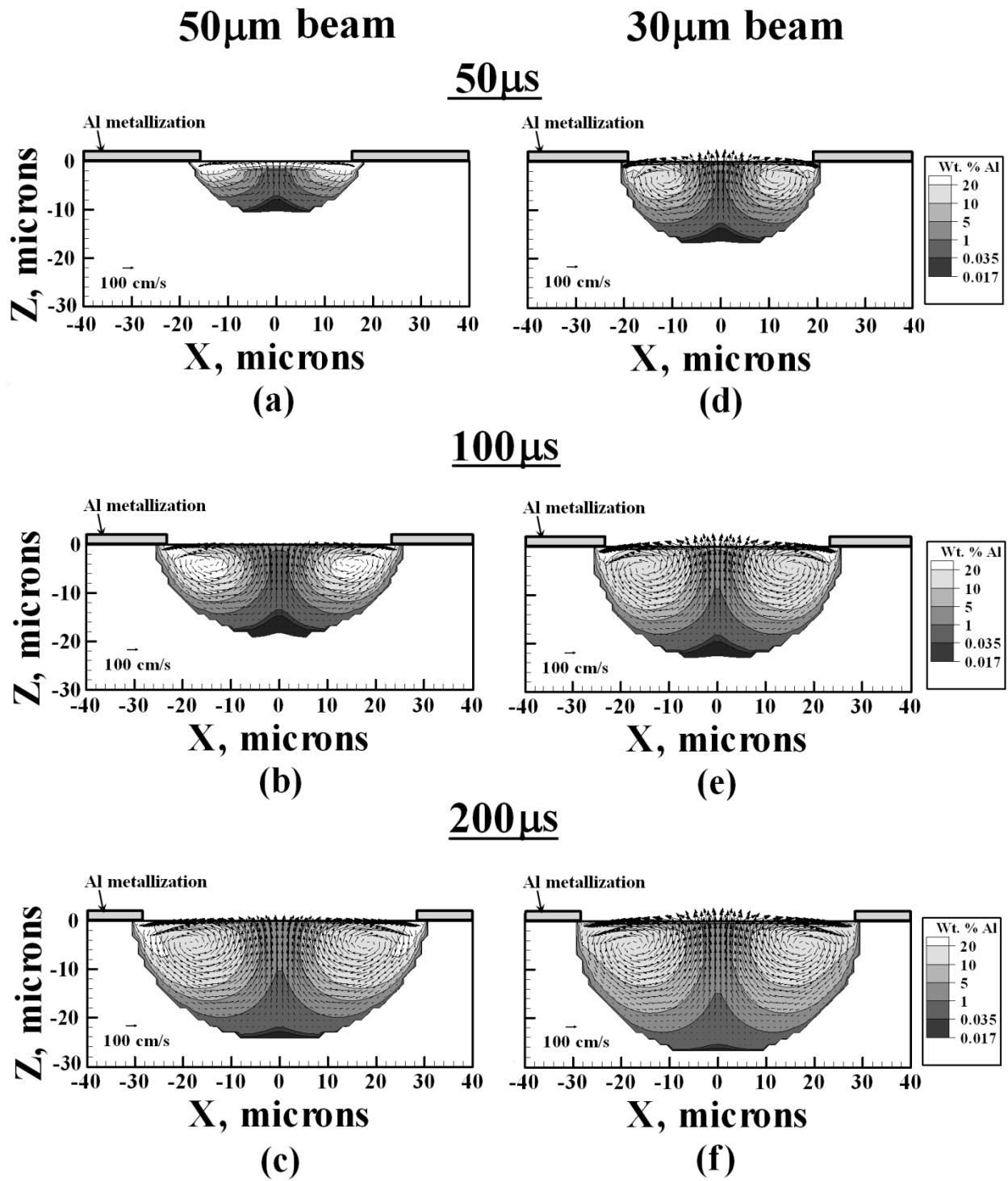
Figure 5.16. Change in concentration profiles as a function of pulse duration for (a)-(c) a 50 μm beam diameter and (d)-(f) a 30 μm beam diameter.

5.5 Process Maps for Contact Geometry

The influence of the LFC radius and hemispherical geometry on total contact resistance can also be seen in Figure 5.17. Additional data points are shown for LFCs processed with the exact same processing conditions on a different passivation stack (80 nm a-Si:H instead of 10 nm a-Si:H and 100 nm SiO_2) [9]. As the LFC radius increases as a result of increasing laser power from 18 W to 50 W, the total contact resistance decreases for all conditions. It can be seen that when maintaining a constant power level, an increase in the pulse duration also leads to a reduction in the total contact resistance, which will be due to an increase in radius. For both passivation stacks, the experimental data exhibits much greater fit with the three-dimensional calculations than the contact resistances calculated for planar contacts based on the empirical Cox-Strack relationship [34]. The results indicate that the ability to predict the contact geometry as a function of processing parameters can provide a means to reliably estimate total contact resistance. Therefore, the validated heat transfer and fluid flow model can be used over a wide range of processing conditions to predict the required contact geometry.
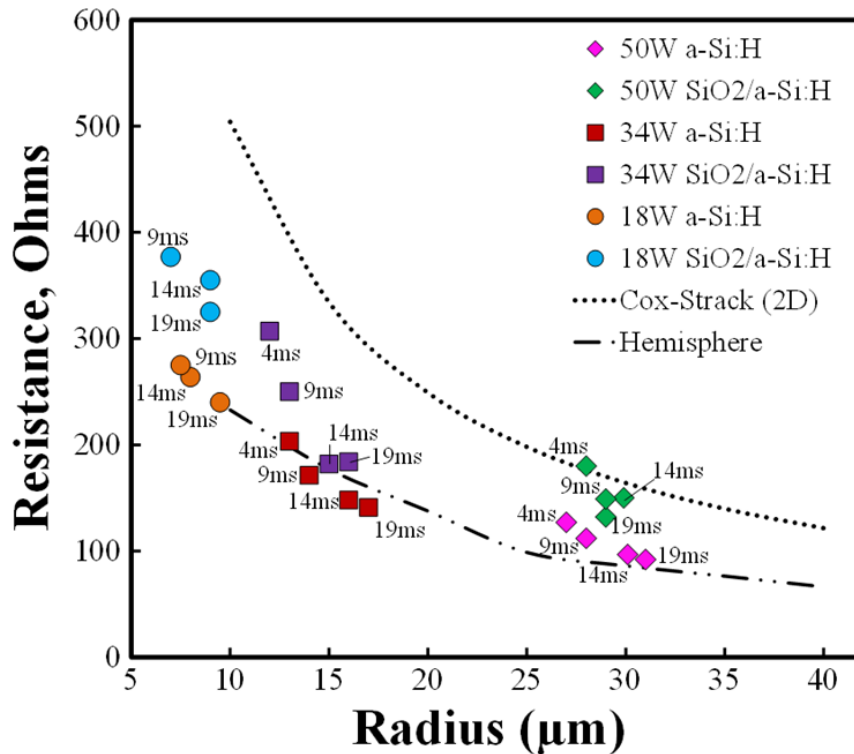
Figure 5.17. Contact resistance versus LFC top surface radius for measured and simulated data assuming Al dopant density of 2 x 10^{19} cm^{-3}. Experimental data shown identified with symbols and pulse duration.

Process maps have been developed to identify safe operating regimes where substrate peak temperatures will not exceed the boiling point for the alloys. Figure 5.18(a) through Figure 5.18(f) show process maps for the contact width and contact depth as a function of power levels up to 80 W and laser

beam diameters between 10 μm and 30 μm for pulse durations of 20 μs, 200 μs and 2 ms. Using these maps can be of great benefit since it has been demonstrated that accurately predicting the contact geometry can allow for improved prediction of the total contact resistance. These pulse durations were selected because noticeable differences in the processing windows are observed over this range. Since alloy formation between the Si and Al is critical to achieve the ohmic contact, the peak temperature should remain between the melting and boiling points for the material under consideration. The melting temperature of Si (1687K), the boiling temperature of Al (2792K) and the boiling temperature of Si (3514K) have been used to define safe operating windows for the process. The upper limits have been selected to avoid significant metal loss through vaporization of Al and Si and ejection of particulates. The computed results in Figure 5.18 show that the practical range of appropriate laser powers becomes rather narrow when a smaller beam radius is selected for all pulse durations. This behavior is consistent with the fact that an increase in the power density will lead to a rapid rise in the peak temperature above the boiling point of both Al and Si.

At 20 μs pulse durations, the process window is substantially larger for larger beam diameters since the peak temperatures do not exceed the boiling point of Al and Si within this time frame. As the pulse duration is increased, however, the processing window shrinks as the process trends towards minimal increase in peak temperature and spot growth. At 20 μs, the spot size is considerably smaller for the same processing parameters. For instance, the spot width is only 30 μm when using a power of 50W and beam diameter of 30 μm. For the same parameters, the spot width grows to 40 μm at 200 μs and 50 μm at 2 ms. In addition, the contact width and depth remain fairly constant with changes in beam diameter at the same power level. For instance, at 40 W laser power, one can achieve similar contact geometry for a 200 μs pulse with both a 20 μm and a 30 μm beam diameter. By utilizing a 30 μm beam diameter, one can ensure that the processing temperatures do not exceed the boiling point of Al and thereby eliminate the possible loss of important alloying elements. The computed results in Figure 5.18 provide guidance as to how the depth and width of the weld pool can vary during laser processing as a function of beam radius and laser power. An important feature of the results in Figure 5.18 is that a particular contact size can be achieved through multiple combinations of processing parameters. Such flexibility can be worthwhile in determining what parameters to use to obtain a specific contact size while minimizing high temperature exposure to substrate.

A desired molten pool size can be obtained from various combinations of laser processing variables. However, the computed peak temperatures and thermal cycles may vary resulting in one processing condition being more desirable than others. Figure 5.19 shows the changes in the computed temperatures along the top surface within the molten region for two conditions that produce the same geometry (20 μm

and 30 μm laser beam diameters for 40 W laser power and 200 μs pulse duration). In these two cases, the diameters of the molten pool are the same (30 μm). With a laser beam diameter of 20 μm, the computed peak temperature reaches 3225K, while that for a 30 μm beam diameter reaches only 2546K. Since the pool width is approximately the same for both beam diameters, the temperature gradient using a smaller beam diameter is much greater. As a result, the calculated fluid flow velocities are approximately two times larger for the smaller beam diameter. Although these elevated temperatures can lead to greater mixing of the molten region, they can also lead to a significant loss of alloying elements.
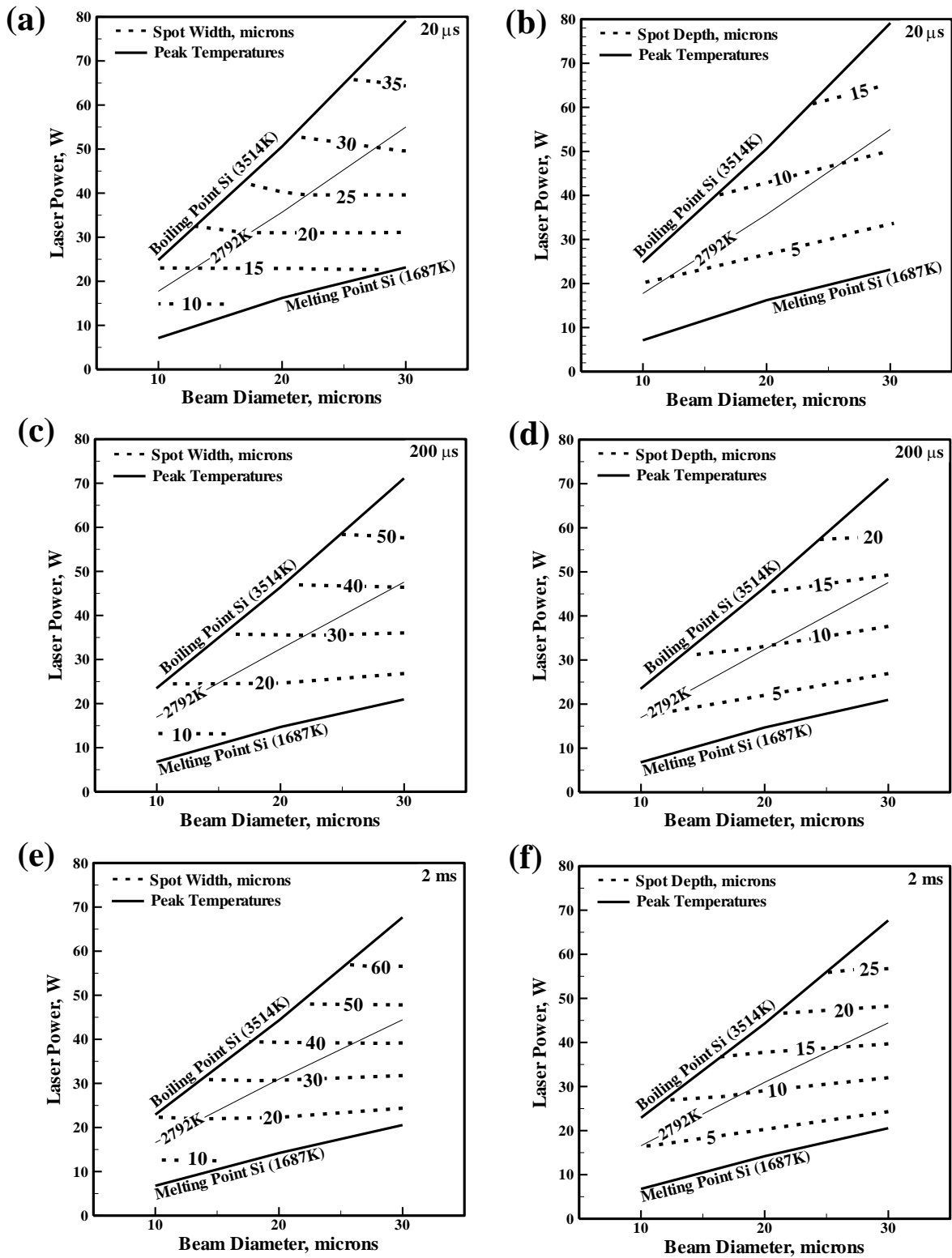
Figure 5.18. Computed molten pool width and depth are shown as a function of laser power and beam diameter for assistance in selection of appropriate processing parameters at (a)-(b) 20 μs, (c)-(d) 200 μs and (e)-(f) 2 ms.

151
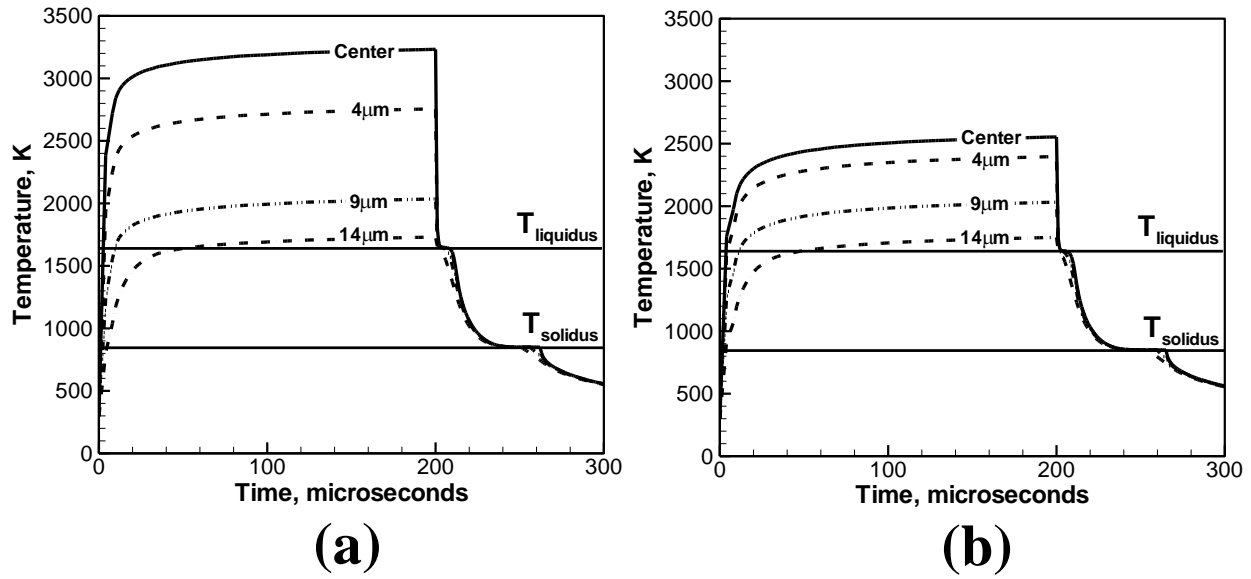
Figure 5.19. Thermal cycles for top surface of molten pool with 40 W laser power and 200 μs pulse duration for (a) 20 μm beam diameter and (b) 30 μm beam diameter. The distance values shown on different lines indicate the distance from the center of the molten pool.

When the power level is kept constant but the pulse duration is increased, the peak temperature increases most rapidly during the first hundred microseconds before leveling off. As a result, the Marangoni shear stress on the surface of the melt pool, which is driven by the temperature gradient across the surface, will not increase substantially, and there will be less pronounced growth when only changing the pulse duration. However, when the power level is increased from 18 W to 50 W, as done in these experiments, the molten pool temperatures will increase significantly. Calculations show that when using a laser beam diameter of 30 μm and a 2 ms pulse, the peak temperature can increase over 1000K. Therefore, there will be a much larger temperature gradient on the surface with small changes in power, which will drive fluid from the center of the melt to the periphery at much greater velocity and lead to larger contact sizes when changing power in comparison to pulse duration as seen in Figure 5.2. Being able to predict the contact geometry as a function of processing parameters as shown in Figure 5.18 and control processing temperatures provides an additional benefit in terms of offering an ability to estimate total contact resistance for a given contact geometry.

Figure 5.20 shows how transitions in contact geometry between planar, half-ellipsoidal and hemispherical with increasing pulse duration influence total contact resistance for various beam diameters. The total contact resistance is plotted as a function of LFC diameter based on the Sentaurus simulation results from Chapter 3. Data for extremely small contact diameters (less than 30 μm) was extrapolated from the simulated data. The three lines on the plots without symbols correspond to the

152

contact resistance for the following contact geometries: planar, half ellipsoidal (with contact depth, *c*, equal to one-fourth the contact diameter, *a*), and hemispherical (with *c* equal to one-half *a*). For a planar contact, the contact resistance is calculated using the empirical Cox-Strack relationship [34]. The laser power selected for each case gives a peak temperature slightly less than the boiling point of Al (2792K).

(a)

(b)

(c)
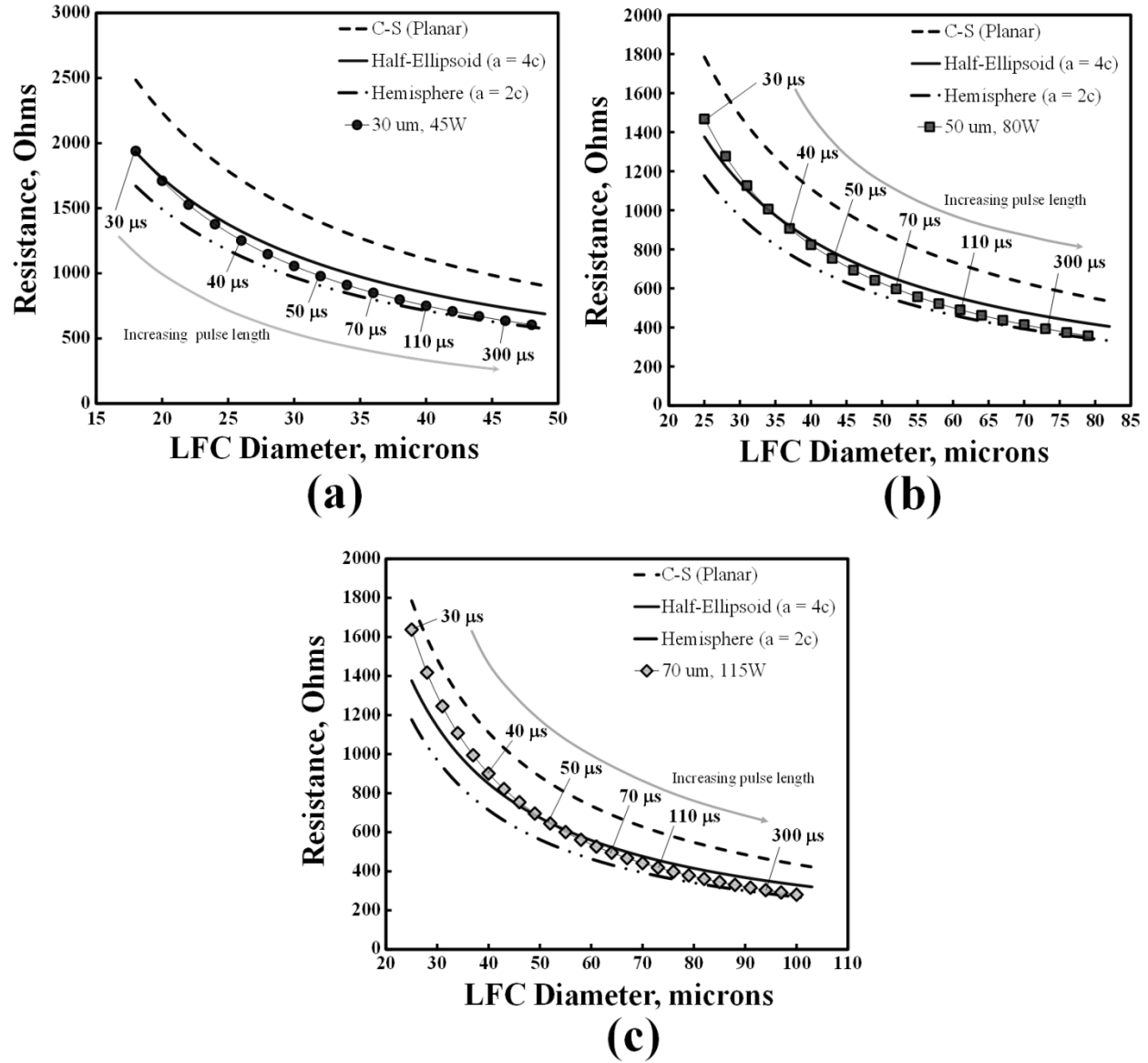
Figure 5.20. Plots of total contact resistance versus LFC inner crater diameter for various contact geometries (planar, half-ellipsoidal, and hemispherical). Symbols correspond to LFC diameters as a function of increasing pulse duration for (a) 45 W laser power and a 30 μm beam diameter, (b) 80 W laser power and a 50 μm beam diameter, and (c) 115 W laser power and 70 μm beam diameter. Device simulation results used from Chapter 3 assuming an aluminum doping density of 2×10^{19} cm^{-3}.

Figure 5.20(a) shows results for a contact processed with a 30 μm beam diameter and 45 W laser power. At 30 μs, the contact has a diameter and depth of approximately 18 μm and 5 μm, which corresponds to a depth/radius ratio close to 0.54. As a result, the contact is half-ellipsoidal (with $a \approx 4c$) and its total contact resistance will be almost 2000 Ω. For a planar contact of the same LFC diameter, the total contact resistance would be close to 2500 Ω, demonstrating the benefit of forming a three-dimensional contact. At 40 μs, the LFC diameter is close to 26 μm with a depth of 19 μm, which results in a half-ellipsoid contact with a depth/radius ratio of 0.71. By increasing pulse duration, the growth in both contact diameter and depth result in the depth/radius ratio increasing towards 1 and the total contact resistance approaching that for a hemispherical contact. Since a contact processed with a 30 μm beam diameter rapidly takes on a hemispherical shape at the onset of processing, the reduction in total contact resistance is largely driven by an increase in the hemispherical shape, rather than a marked transition in the contact geometry from planar to hemispherical as a result of longer processing times.

Figure 5.20(b) shows the evolution of total contact resistance as a function of LFC diameter and pulse duration for a contact processed with a 50 μm beam diameter and 80 W laser power. When the contact initially forms at 30 μs, its depth and diameter are approximately 6 μm and 25 μm, which results in a half-ellipsoidal contact shape with a slightly greater than $4c$. The total contact resistance will be approximately 1450 Ω, in comparison to nearly 1800 Ω for a purely planar contact. An increase in the pulse duration from 30 μs to 40 μs results in a contact diameter of 36 μm with a depth/radius ratio around 0.6, lowering the contact resistance almost 500 Ω. However, significantly more time is required for the shape to transition from half-ellipsoidal to hemispherical than for the smaller 30 μm beam diameter. At 110 μs, the depth/radius ratio is 0.79 and increases to 0.86 at 300 μs. Although the transition in contact geometry will lead to a reduction in total contact resistance, the influence of shape on contact resistance is less pronounced at larger LFC diameters. Therefore, after the initial transition in contact geometry from planar to hemispherical, the reduction in total contact resistance is largely driven by an increase in LFC diameter, and the influence of a forming a hemispherical contact on reducing total contact resistance is less influential.

Figure 5.20(c) shows the most pronounced effect of contact geometry evolution on total contact resistance for an LFC processed with a 70 μm beam diameter and 115 W laser power. At the onset of processing when the contact forms at 30 μs, it possesses a highly planar geometry and the resistance is best approximated by the Cox-Strack relationship. By 40 μs, however, the geometry takes on a near half-ellipsoidal geometry with $a \approx 4c$, which will lead to a reduction in total contact resistance of 200 Ω versus a planar contact with the same LFC diameter. By 70 μs, the contact has a diameter that is approximately 2.7 times the depth, which will lead to further reductions in total contact resistance. Furthermore, the

total achievable contact size with a 70 μm beam diameter is much larger than that for contacts formed using the smaller beam diameters. However, the time required to form a completely hemispherical geometry can be longer, which may impact the choice of processing parameters.

In all cases, tens of microseconds are required after initial contact formation for the shape to transition from planar to hemispherical. This transition in shape occurs more rapidly for a smaller beam diameter, which results in lower contact resistances for a given LFC diameter when compared to planar contacts. As the beam size is increased, the transition in contact shape is more pronounced. For a 70 μm beam diameter, both the transition in contact geometry from planar to hemispherical with longer processing times and the growth in the LFC diameter drive a reduction in the contact resistance. For the smaller 30 μm beam, however, since the contact takes on a hemispherical shape more rapidly, the growth in the LFC diameter is the primary driver for a reduction in total contact resistance. Therefore, if a larger contact size is required for a desired rear contacting scheme, a larger beam diameter with a longer pulse duration should be used to form a large hemispherical shape. The shape that a contact achieves will be driven by the heat transport mechanisms acting within the pool. In addition, sufficient Al doping within the entire molten region is required for an ohmic contact to form, which will be governed by mass transport of the Al within the Si.

5.6 Impact of Pitch on Temperature Fields and Contact Geometry

Multiple LFCs are generated on the backside of the device to maximize device performance efficiency by reducing current crowding. The selection of the spacing between adjacent spots is critical because cell efficiency is directly related to LFC pitch distance [35,36]. In a laboratory environment, these spot welds are generated using a rastering approach in which each laser pulse generates one spot weld. In order to achieve high production rates, however, diffractive optical elements in conjunction with high powered-lasers and fast-scanning methods are being investigated to produce multiple spots simultaneously [37]. Depending on the pitch distance, the substrate surface temperatures can change drastically depending on thermal interaction of adjacent spots. Furthermore, microstructural defects, such as dislocations and grain boundaries, can form during welding that can lead to high recombination velocities of electrons and holes, which can adversely affect device performance. Therefore, careful selection of pitch distance based on processing parameters is required to ensure that the spot welds are generated as expected.

Numerical simulations were used to evaluate how changes in pitch distance and processing parameters impact spot weld size and substrate thermal profiles. In addition, surface temperatures were calculated as a function of pitch distance and laser processing parameters to demonstrate the thermal

impact on the substrate, the Al contact layer and passivation layers as spot welds are processed within close proximity of one another. Processing regimes are identified to minimize thermal interaction between adjacent spot welds. In order to consider the effect of varying pitch, a second heat source was introduced to the model to simulate the process of simultaneous laser processing of LFCs. A comparison between experimental results and modeled results is shown in Figure 5.21 for a contact processed with 45 W laser power, a 4 ms pulse duration and a 20 μm beam diameter at focus. Good agreement is observed between the calculated and experimental results in size and alignment of important temperature contours for the alloy liquidus temperature of 1664K and for an α-Si:H passivation layer melting temperature, 1480K. This passivation layer melting temperature represent the lowest extreme under which processing conditions should be evaluated since more robust passivation layers, such as SiO_2 and Al_2O_3, will have much higher melting temperatures than both pure Si and pure Al. In this case, the contact sizes resulted in contacts with an approximate concentration of 90 wt. % Al, which corresponds to a liquidus of 1664K. Since the model only considers two heat sources, the thermal interaction is evident solely between the two spots. This effect can also be observed in the slight elongation of the molten pool size between the two spot welds.
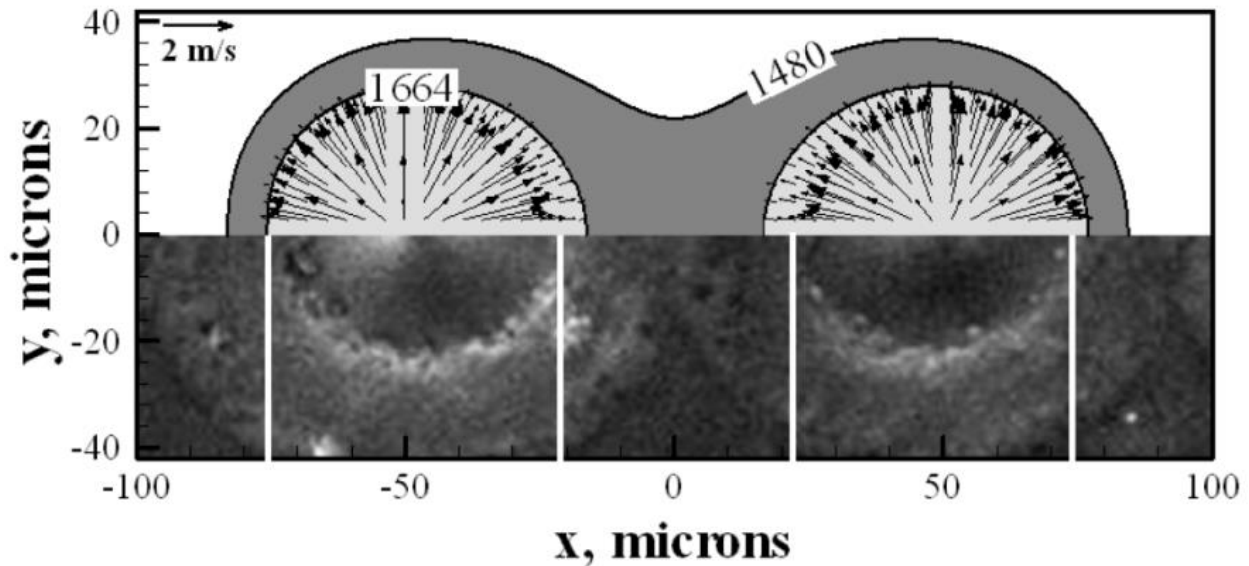
Figure 5.21. Comparison between experiments and modeling when considering 45 W laser power with 4 ms pulse duration.

With insufficient pitch, adjacent pools can combine to form large pools. This effect can be observed in Figure 5.22, where modeling is performed using 50 W laser power, a 20 μm beam diameter, and pitch distances of 25 μm, 50 μm, and 75 μm with a 50 μs pulse duration. It can be observed that at 25 μm, the molten pools combine to form one large hemispherical pool with a width of 65 μm and depth of 21 μm. When the pitch is increased to 50 μm, there is one pool that is observed with two separate regions of

circulating molten material. The molten pool width is 86μm along the top surface, and the depth is approximately 14μm. When these types of large pools form, all locations on the substrate surface will be subject to melting and solidification as laser firing is performed across the entire substrate. However, when the pitch is increased to 75μm, it is observed that the molten pools are distinctly separated.

The LFC sections shown in Figure 5.22 show that the liquidus temperature for each case is slightly different, which is attributed the Al concentration calculated for each case. The amount of Al in solution varies little despite changes in the pitch, due to the fact that the relative concentration of Al in the pool remains consistent regardless of the spot size. As the volume of the spot grows, the amount of dissolved Al in solution also grows. Thus, for a larger spot, the relative concentration is similar to two smaller spots. Selection of pitch is important to avoid situations where coalescence of adjacent spots takes place. In addition, selection of pitch is important to maintain a sufficiently low metallization fraction and high passivation fraction. In order to avoid the coalescence of adjacent LFCs, careful consideration of the surface temperature is required. It is imperative to ensure that specific locations across the substrate surface do not exceed the melting temperature of both Al and the passivation layers. The melting temperature of Al is 933K and the melting temperature of the passivation layers is approximately 1480K for a-Si:H. The temperature can be high for SiO_2 or other dielectric passivation layers. A higher melting temperature oxide would allow for higher operating temperatures without damage to the passivation. Furthermore, in these cases, extremely close pitch distances were used to demonstrate the impact of pitch on temperature profiles. For larger pitch distances, it can be expected that the laser energy associated with longer pulse durations will have little effect on the passivation layer and overall substrate between contacts.
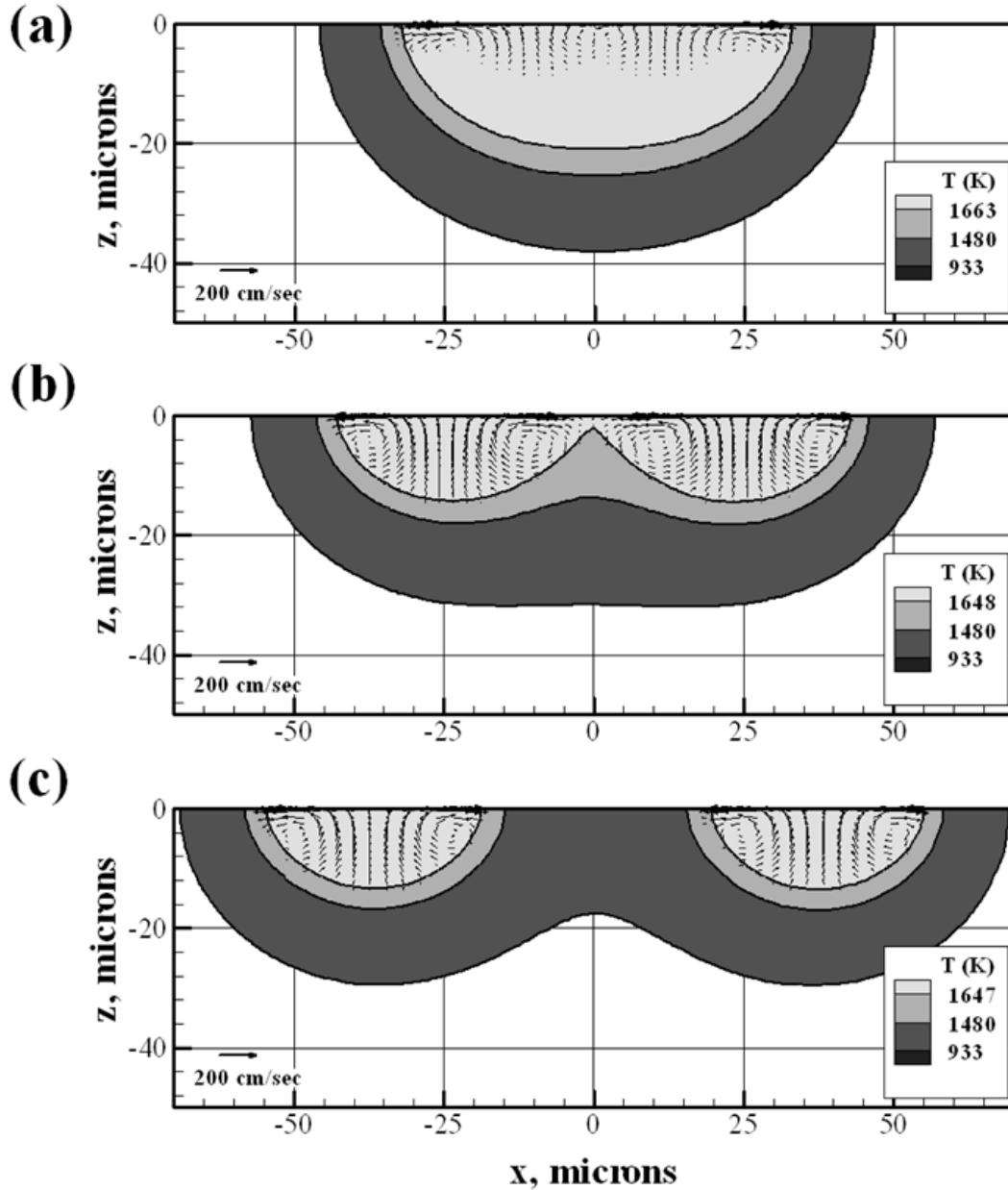
Figure 5.22. Shows how selection of pitch can affect molten pool geometry for: (a) 25μm, (b) 50μm, and (c) 75 μm pitch.

Figure 5.23 shows a plot of the ratio of the temperature at the midpoint between two adjacent spots to the liquidus temperature ($T_{liquidus}$) versus the ratio of pitch ($D_{separation}$) to laser beam diameter (D_{beam}), which is 20 μm, for 30 W laser power. The ratio of the melting temperature of the passivation layer to the liquidus temperature ($T_{a-Si:H}/T_{liquidus}$), which is ~0.9, and the ratio of the melting temperature of Al to the liquidus temperature ($T_{Al}/T_{liquidus}$), which is ~0.56, are indicated on the plots with dashed lines. The contours represent the time. It can be observed that as the pitch is decreased, the temperature ratio increases. As a result, the ratio begins to approach 1, which is when the temperature at the midpoint between two adjacent spots equals the liquidus temperature. For this particular system, as ratio of pitch to

beam diameter is increased above 2.2 for a 150 μs pulse, it can be seen that the midpoint temperature will not exceed the melting temperature since the ratio will be less than 1.

As the time is increased, which is shown by the contours on the plots, the ratio of temperatures also increases for the same separation distance. Thus, the midpoint location will ultimately exceed the important temperature ratios indicated above depending on the parameters selected. Using a plot like this one, processing parameters can be selected to ensure that for a combination of beam separation and pulse duration, the midpoint temperature does not exceed important temperature thresholds where unintended surface melting takes place that can reduce performance efficiency. If the surface temperatures exceed the melting temperatures of Al and the passivation layers, then the entire substrate surface can be cycled through melting and solidification processes, which can lead to the formation of defects that will adversely affect the substrate due to an increased number of sites where minority carriers can recombine.
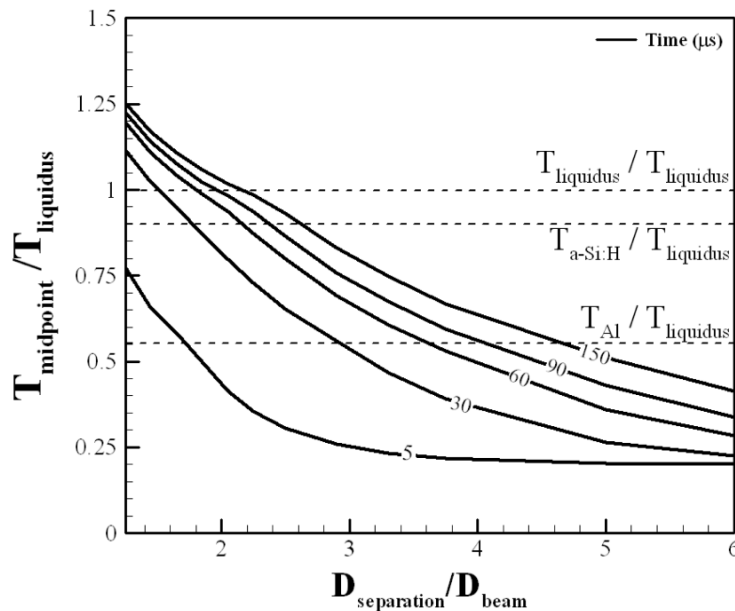
Figure 5.23. Variation in midpoint temperature between adjacent spot with increasing pitch and increasing pulse duration.

Process maps can be generated to assist in the selection of appropriate pitch distances. Figure 5.24 shows process maps of spot width as a function of laser power and the ratio of pitch to laser beam diameter. The graphs show how the LFC diameter (width) varies as the pulse duration is increased from 50 μs in Figure 5.24(a) to 150 μs in Figure 5.24(b). For shorter pulses, the LFC diameter reaches a plateau at lower power levels as the pitch increases to 4 times the laser beam diameter. However, for longer pulse durations, the pool size continues to grow slightly for higher power levels as the ratio approaches 6. The gray colored area represents regions where two adjacent spot welds are expected to

combine for a given ratio of pitch to beam diameter and represents the parameters where processing should definitely be avoided.

As the power level increases, this region becomes larger since more heat is imparted to the system and the thermal interaction of adjacent spots increases as heat is drawn away from the laser affected region at a slower rate. Thus, larger pitch distances are required for higher powers and longer pulse durations to avoid the thermal effects associated with adjacent two spots welds. In practice, larger pitch distances (i.e. on the order of 500 μm and greater) are typically used to maintain high passivation fractions and maintain device performance efficiencies. The results suggest that with a 50 μm beam diameter, approximately 200 μm pitch distance is required to have a Pitch/D_{beam} ratio of 4 to avoid coalescence of the contacts with higher power levels. Therefore, for larger pitch distances, there will little impact on the substrate temperatures since the thermal interaction occurs only within close proximity of the contact for shorter microsecond pulse durations.
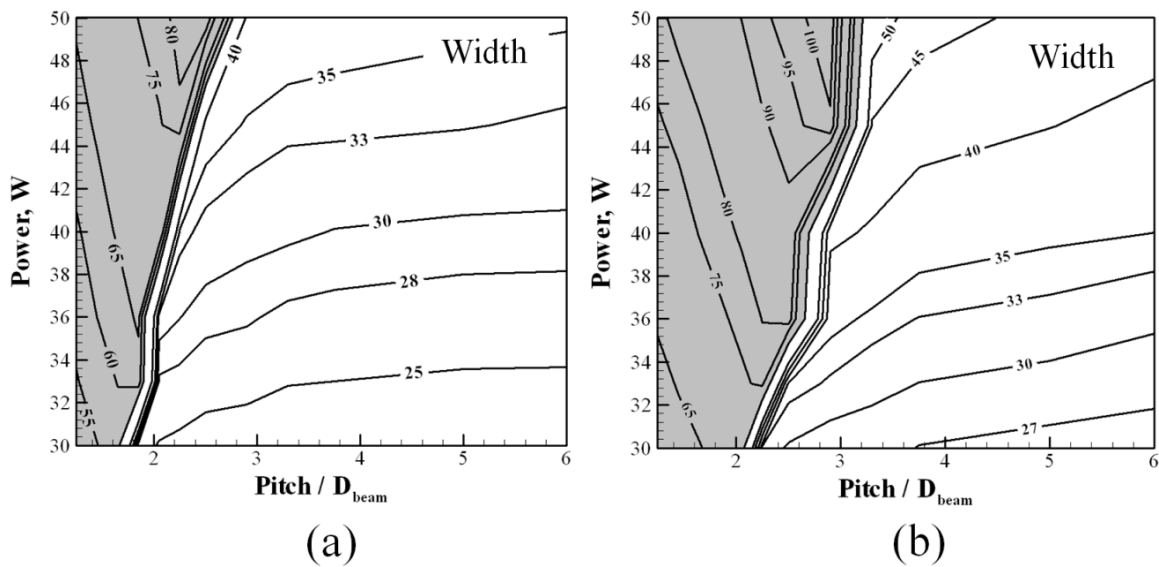
Figure 5.24. Process maps for spot width show that pitch distance must be increased as pulse duration is increased from (a) 50μs to (b) 150μs to ensure that adjacent spots remain distinctly separated during laser spot welding.

The impact of the thermal interaction between two adjacent spot welds can be observed when considering how the LFC diameter (width) varies with the pitch distance. Figure 5.25 shows plots of width versus the ratio of pitch to beam diameter for laser powers of 30 W and 50 W using a beam diameter of 20 μm. For both cases, the weld width grows despite an increase in the LFC pitch separation distance. This is due to joining and coalescence of adjacent spots that occurs if the pitch distance is too small. However, after the initial region of increasing weld width, it rapidly drops off and begins to reach a specific value, which will correspond to the nominal geometry when processing a singular LFC without

160

two interacting beams. For 30 W laser power, the single spot LFC size at 50μs, 100μs and 150μs is 22.5μm, 24.6μm and 25.4μm, respectively. For 50 W laser power, the single spot weld size at 50μs, 100μs and 150μs is 35.8μm, 38.9μm and 41.9μm, respectively. These values are indicated by the horizontal dashed lines. The plots suggest that the thermal interaction between spot welds is substantially less for lower power levels. Furthermore, as the pulse durations are lowered, shorter separation distances can also be used if a larger metallization fraction is required.

Although the results suggest that it may be advantageous to use lower power levels and shorter pulse durations to process more contacts within close proximity to one another, it is important to consider the amount of mixing that takes places between the Al thin film and Si substrate during contact formation and the passivation fraction. The amount of mixing will play a role in dictating performance if insufficient Al doping is achieved. Increasing the power level from 25 W to 50 W laser power can lead to fluid flow velocities within the molten pool that are 5 times larger. As a result, more thorough mixing will take place despite a lower Al concentration due to a much greater influence of mass transfer by convection. Furthermore, the total contact resistance will decrease significantly as higher power levels are used. Figure 5.26 shows the total contact resistance measurements for LFCs processed on two passivation stacks [9] and millisecond pulse durations as a function of pulse duration and laser power. For both passivation layer configurations, there is a trend of decreasing total contact resistance with increasing laser pulse duration and power.

The total contact resistance has been shown to be dependent on the contact geometry since the spreading resistance will vary as the contact geometry changes. With changes in contact geometry, the interfacial area between the LFC and the wafer will change and the doping density may vary depending on pulse duration and power level. Therefore, it is important to understand that despite the ability to process contacts within close proximity with lower power levels and shorter pulse durations due to lower processing temperatures and higher Al concentrations in a smaller pool, only a little Al is required (on the order of 0.017 wt.%) within the contact for sufficiently high doping levels to be achieved. Furthermore, the passivation fraction must be maximized to ensure high device performance efficiencies. From a device performance standpoint, the balance between ohmic losses and recombination losses through optimization of the metallization fraction and passivation fraction is important. An increase in contact density will reduce current crowding but also lead to higher recombination rates since the recombination velocities at the LFC/wafer interface is much higher than at the passivation/wafer interface. Therefore, although many contacts can be processed with minimal thermal interaction between contacts at small pitch distances, the overall device performance may suffer.
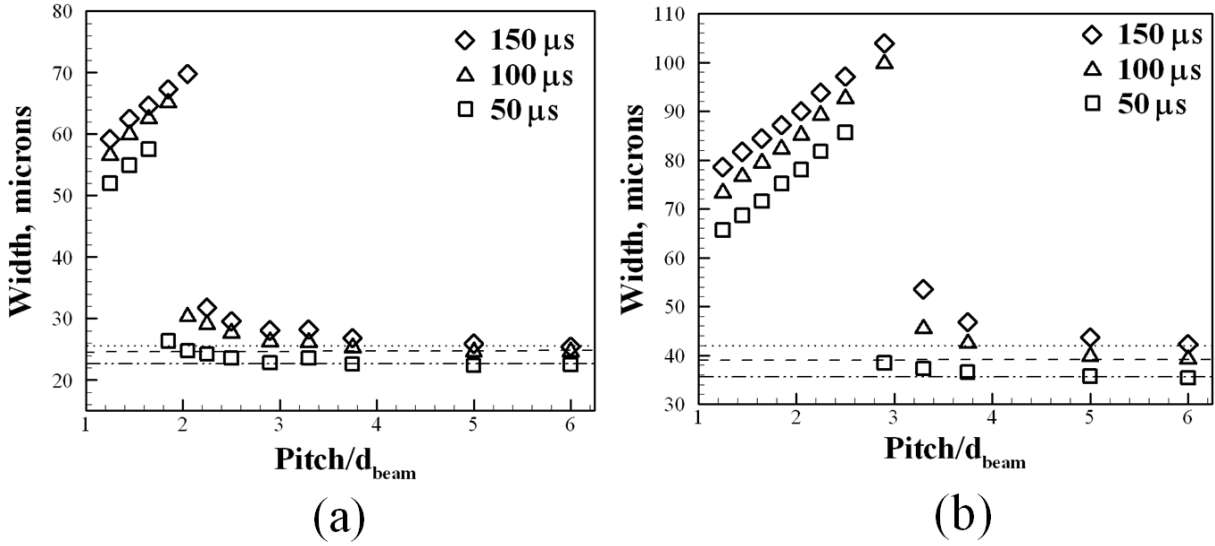
Figure 5.25. Weld width as a function of pitch distance divided by beam diameter for (a) 30 W laser power, and (b) 50W laser power.
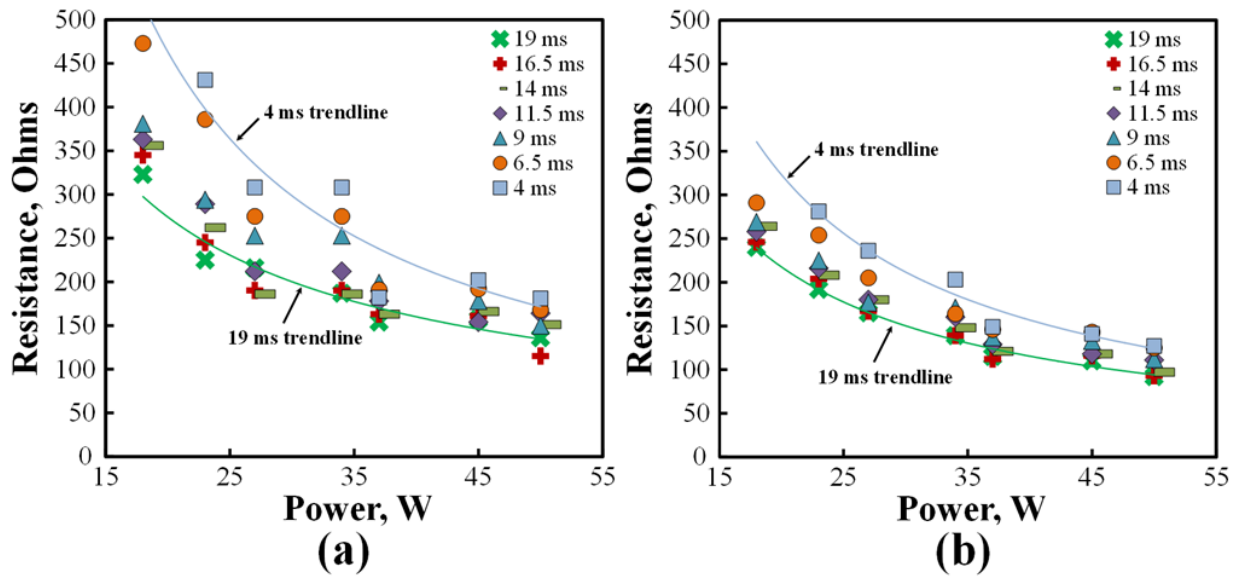
Figure 5.26. Resistance trends based on power and pulse duration for LFCs processed with IPG 1070 nm single mode fiber laser on (a) dual stack passivation of a-Si:H and SiO$_2$, and (b) a single a-Si:H passivation stack.

Figure 5.27 shows process maps of Si concentration in the molten pool as a function of laser power and the ratio of pitch to laser beam diameter. The shaded region represents where adjacent spots combine to form one large spot as shown in Figure 5.24. The graphs show how the Si concentration varies with time as pulse duration is changed from 50 µs to 150 µs. The concentration of Si is primarily affected by the laser power with larger pitch distances. This effect is most pronounced at lower pulse durations where the concentration levels off with increases in pitch distance. At the longer pulse duration, it can be

162

observed that the alloying does not reach a plateau at higher power levels since the molten pool size will continue to grow and Al will be added to the system.

As the power level is increased for the same pitch distance, the amount of alloying also increases. This is particular evident at the highest power level. In general, however, there is little observable change in concentration as the ratio of pitch to laser beam diameter is increased above 3 since the amount of Al added will be relatively insignificant compared to the size of the contact. This suggests that the thermal interaction between adjacent spots does not enhance the amount of alloying that takes place in a single spot. Furthermore, since the dopant density of Al in the Si will be sufficiently high even with a Si concentration of 90 wt. % in the molten region, the results suggests that the LFC will form with relative ease in all situations.
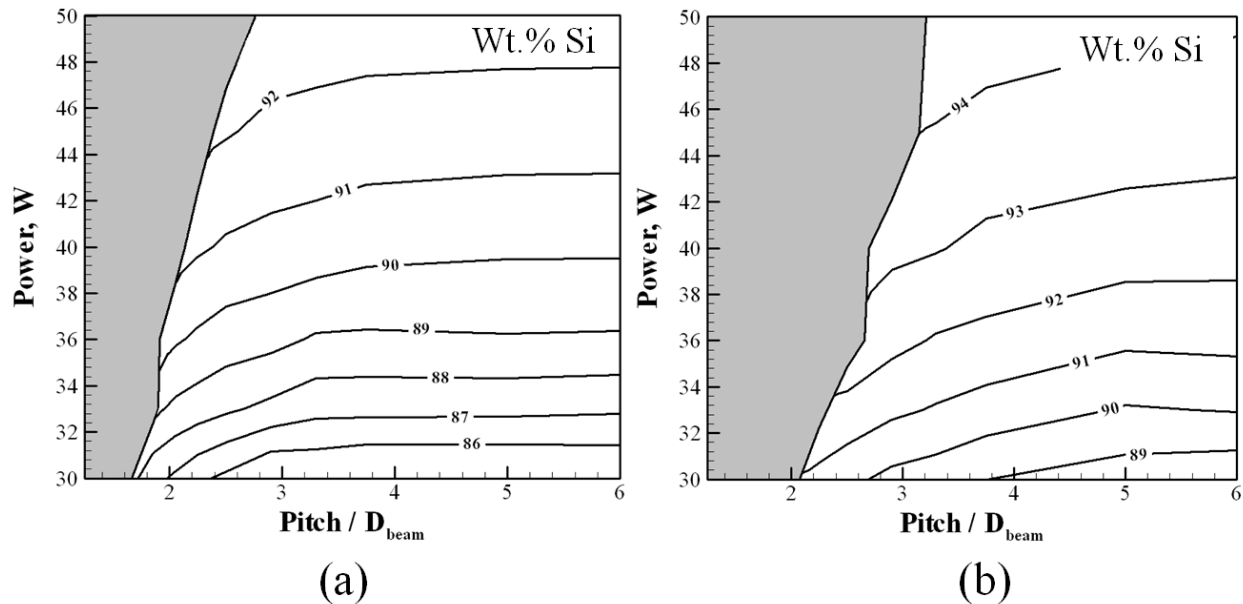
Figure 5.27. Process maps for Si concentration as a function of pitch distance and power level at (a) 50 μs and (b) 150 μs.

5.7 Summary and Conclusions

In order to develop a fundamental understanding for the influence of laser processing parameters on the LFC formation process, mathematical modeling was employed. The mathematical models were used to calculate the contact geometry, temperature and velocity fields, and thermal cycles. In addition, dimensionless numbers were used to determine the dominant mechanisms governing heat and mass transfer during laser processing of contacts. Finally, the model was updated to incorporate a secondary heat source to evaluate how temperature fields and contact geometry are impacted when simultaneously processing two LFCs. The major conclusions are:

1. By accounting for the time-dependent variation in Al concentration within the molten pool, the accuracy of the computed LFCs widths were significantly improved and agreed well with experimental results over a wide range of laser processing parameters. In order to consider the formation of a binary Al-Si alloy, it is necessary to calculate the liquid fraction within the large two-phase region based on the Al-Si phase diagram and to modify the Enthalpy-Temperature relationship used in the model. Considering the liquid fraction allows for correct determination of the amount of laser energy required for heating and melting of the binary Al-Si alloy.

2. The addition of Al to the molten region significantly alters the thermal cycles. As the amount of Al is increased, the temperatures within the molten region can decrease substantially for the compositions considered because there will be a larger phase transformation that occurs at the eutectic temperature. For pure Si, a thermal arrest is observed on cooling during the transformation of liquid to solid due to the evolution of the latent heat of fusion. The cooling cycles are drastically different when Al is present since the liquid-to-solid transformation occurs over a very large two-phase region.

3. Convection plays a dominant role in heat transfer and mass transfer during LFC formation. Due to high fluid flow velocities, Al is well distributed throughput the molten pool, leading to heavy doping of the Si and indicating that the entire molten area comprises the ohmic contact. A reduction in beam size from 50 μm to 30 μm will lead to more uniform concentration profiles within the molten pool when using shorter pulses because the fluid flow velocities will increase significantly. However, the results suggest that sufficiently high Al doping levels can be achieved in a less well-mixed pool.

4. Numerically computed process maps demonstrate that the safe operating regime for selection of laser power is restricted as spot size is reduced. As the pulse duration is increased from tens of microseconds to hundreds of microseconds, the operating window shrinks to avoid peak temperatures exceeding the boiling point of Al and Si, which can result in significant metal expulsion. The process maps demonstrate that multiple combinations of laser power, spot size, and pulse duration exist to obtain a given contact size. For example, the use of a large beam diameter can achieve a similar LFC size while substantially reducing the temperature gradients within the pool.

5. The thermal interaction between adjacent spot welds is largely dependent on the laser power level. When using 30 W laser power, a contact spacing of 3 times the beam diameter is required to ensure that spot weld size is not affected by a neighboring spot. For 50 W laser power, the pitch distance must be 6 times the beam diameter to achieve the same effect. Since beam sizes are on the order of tens of microns, however, pitch distance can be selected to maintain a desired contact area fraction,

which usually requires pitch distances of hundreds of microns, without little concern for thermal interaction between simultaneously processed LFCs when using microsecond pulse durations.

5.8 References

1. U. Zastrow, L. Houben, D. Meertens, A. Grohe, T. Brammer, E. Schneiderlöchner, Characterization of Laser-Fired Contacts in PERC Solar Cells: SIMS and TEM Analysis Applying Advanced Preparation Techniques. Applied Surface Science 252, 2006, pp 7082–7085.

2. E. Schneiderlochner, R. Preu, R. Ludemann, S.W. Glunz, Laser-fired rear contacts for crystalline silicon solar cells, Prog. in Photovoltaics 10, 2002, pp 29-34.

3. B. Sopori, V. Mehta, d. Guhabiswas, R. Reedy, H. Moutinho, B. To, A. Shaikh, A. Rangappan, Formation of a back contact by fire-through

4. W. Brendle, V.X. Nguyen, A. Grohe, E. Schneiderlochner, U. Rau, G. Palfinger, J.H. Werner, 20.5% efficient silicon solar cell with a low temperature rear side process using laser-fired contacts, Prog. In Photovoltaics Research Applications 14(7), 2006, pp 653-62.

5. R. Preu, E. Schneiderlöchner, A. Grohe, S.W. Glunz, G. Willeke. Laser-Fired Contacts - Transfer of a Simple High Efficiency Process Scheme to Industrial Production. Photovolt. Spec. Con.: Conf. Record of the Twenty-Ninth IEEE. 29, 2002, pp 130-133.

6. M. Tucci, E. Talgorn, L. Serenelli, E. Salza, M. Izzi, P. Mangiapane. Laser Fired Back Contact for Silicon Solar Cells, Thin Solid Films 516, 2008, pp 6767-6770. DOI: 10.1016/j.tsf.2007.12.079.

7. C. Molpeceres, M.I. Sanchez-Aniorte, M. Morales, D. Munoz, I. Martin, P. Ortega, M. Colina, C. Voz, R. Alcubillia, Influence of wavelength on laser doping and laser-fired contact processes for c-Si solar cells, Proc. Of SPIE 8473, DOI: 10.1117/12.929456.

8. P. Ortega, A. Orphella, I. Martin, M. Colina, G. Lopez, C. Voz, M.I. Sanchez, C. Molpeceres, R. Alcubilla, Laser-fired contact optimization in c-Si solar cell, Prog. in Photovoltaics 2012; 20 (2): 173-180, DOI: 10.1002/pip.1115

9. B. DeCesar, M.S. Thesis, Penn State University, 2011.

10. B. Hedrick, M.S. Thesis, Penn State University, 2011.

11. X. He, J.W. Elmer, T. DebRoy, Heat transfer and fluid flow in laser microwelding, J. Appl. Phys. 97, 2007, DOI: 10.1063/1.1873032.

12. X. He, T. DebRoy, P.W. Fuerschbach, Alloying element vaporization during laser spot welding of stainless steel, J. Phys. D.: Appl. Phys, 36, 2003, pp 3079-3088.

13. X. He, PhD Thesis, Pennsylvania State University, 2006.

14. J.J. Blecher, T.A. Palmer, T. DebRoy, Laser-silicon interaction for selective emitter formation in photovoltaics, I. Numerical model and validation, J. Appl. Phys. 112, 2012.

15. J.J. Blecher, T.A. Palmer, E.W. Reutzel, T. DebRoy, Laser-silicon interaction for selective emitter formation in photovoltaics, II. Model applications, J. Appl. Phys. 112, 2012.

16. X. He, T. DebRoy, P.W. Fuerschbach, Composition change of stainless steel during microjoining with short laser pulse, J. Appl. Phy. 96, 2004, 4547.

17. X. He, J.T. Norris, P.W. Fuerschbach, T. DebRoy, Liquid metal expulsion during laser spot welding of 304 stainless steel, J. Phys. D.: Appl. Phys. 39, 2006, pp 525-534.

18. X. He, P. Fuerschbach, T. DebRoy, Heat transfer and fluid flow during laser spot welding of 304 stainless steel, J. Phys. D: Appl. Phys. 36, 2003, pp 1388-1398.

19. L. Zou, W. Lei, Measurement of focused beam waist of UV pulse laser and material processing threshold, 21st International Congress of Applications of Laser and Electro-Optics, Scottsdale, AZ, October 14-17, 2002.

20. G.E. Jellison, Optical and Electrical Properties of Pulse Laser Annealed Silicon

21. Smithells Metals Reference Book, 7th Edition, 1992

22. J.F. Ready, D.F. Farson. LIA Handbook of Laser Materials Processing, 2001

23. W.K. Rhim and K. Ohsaka, Thermophysical properties measurement of molten silicon by high-temperature electrostatic levitator: density, volume expansion, specific heat capacity, emissivity, surface tension and viscosity, J. Crystal Growth 208, 200, pp. 313-321.

24. A. De, T. DebRoy, Improving Reliability of Heat and Fluid Flow Calculations during Conduction Model Laser Spot Welding by Multi-variable Optimization, Sci. Tech. Weld. and Joining 11 (2), 2006, pp. 143-144

25. A. De, T. DebRoy, A Smart Model to Estimate Effective Thermal Conductivity and Viscosity in Weld Pool, J. Appl. Phys 95 (9), 2004, pp. 5230-5240.

26. J.L. Murray, A.J. McCalister, Bulletin of Alloy Phase Diagrams 5 (1), 74-84 (1984)

27. L.B. Pakratz, Thermodynamic Properties of Elements and Oxides, 1982

28. C.J. Glassbrenner, G.A. Slack, Thermal conductivity of silicon and germanium from 3K to the melting point, Physical Review 134 (4A), 1964, A1058-A1069.

29. E. Yamasue, M. Susa, H. Fukuyama, K. Nagata, Thermal conductivities of silicon and germanium in solid and liquid states measured by non-stationary hot wire method with silica coated probe, J. of Crystal Growth 234, 2002, 121-131.

30. D.F. Gibbons, Physical Review 112 (1), 136-140 (1958)

31. H. Kodera, Japan. J. Appl. Phys. 2, 212 (1963).

32. T. Hara, H. Suzuki, M. Furukawa, K. Ameyiya, K., Jap. J. Appl. Phys 22(6) (1983).

33. J. L. Murray and A. J. McCalister, Bull. Alloy Phase Diagrams 5(1), 74 (1984).

34. R.H. Cox, H. Strack, Ohmic Contacts for GaAs Devices, Solid State Electronics 1967; 10: 1213-1218, DOI: 10.1016/0038-1101(67)90063-9.

35. S. Sterk, J. Knobloch and W. Wettling, "Optimization of the Rear Contact Pattern of High-Efficiency Silicon Solar Cells With and Without Local Back Surface Field", Prog. In Photovoltaics, Vol. 2 (1994), pp. 19-26

36. S.W. Glunz, A.Grohe, M. Hermle , E. Schneiderlochner, J. Dicker, R. Preu, H. Mackel, D. Macdonald, A. Cuevas, "Analysis of Laser-Fired Local Back Surface Fields Using n+np+ Cell Structures", 3rd World Conference on Photovoltaic Energy Conversion, 2003, pp 1332-1 335

37. Z. Hua, "Beam Delivery System for Lase Fired Contact", MS Thesis Pennsylvania State University, 2010.

Chapter 6

IMPLICATIONS OF LFC GEOMETRY ON DEVICE DESIGN

6.1 Introduction

Similar to conventional contacting methods [1,2], an LFC processed with nanosecond pulses exhibits a planar, two-dimensional geometry with the Al-alloyed region contained within a small circular area at the center of the contact [3, 4]. The size of the contact region is of critical importance because it strongly influences various device performance metrics, such as the rear surface recombination velocities, S_{eff}, and the rear side series resistance, $r_{s,rear}$ [5].

Several researchers [5-9] have sought to understand the influence that LFC size has on device performance to optimize the rear contacting scheme. Fischer [5] developed an analytical model to predict S_{eff} for point-contacted structures considering various device design factors, such as pitch distance, contact area fraction, and surface recombination velocities (SRVs) at both the contacted and passivated regions. Kray *et al* [6] validated Fischer's model on oxide-passivated wafers contacted with the LFC process and showed a strong dependence of S_{eff} on contact size and doping density. Wolf *et al* [7] also utilized Fischer's model to predict the energy conversion efficiency for solar cells and demonstrated that S_{eff} is highly sensitive to the size of the Al-doped region formed during laser firing. Ortega *et al* [8,9] used the same model to predict $r_{s,rear}$ for point-contacted devices based on the spreading resistance for planar contacts estimated from the empirical Cox-Strack relationship [10], showing good agreement with experimental measurements. All of these studies made clear the importance of LFC size on device performance. However, they only considered planar contact geometries.

In Chapters 3 and 5, it was shown that the use of longer microsecond pulses produces heavily-alloyed half-ellipsoidal or hemispherical Al-Si contacts. These three-dimensional contacts [11] have larger interfacial areas between the LFC and the Si wafer, which yield significantly lower contact resistances [12,17]. As a result of the larger interfacial area, it should be possible to reduce the number of contacts while maintaining a target contact area fraction to optimize device performance. Furthermore, since no visible damage to the passivation layer surrounding the LFC has been observed with the use of longer pulse durations [13,14], fewer contacts should translate to a higher passivation area fraction. A higher passivation area fraction can have a positive influence on S_{eff}. Therefore, it is important to evaluate how the use of three-dimensional contacts can impact the rear contacting scheme and device performance.

In this chapter, the impact of employing different contact geometries on the backside LFC array design is analyzed. Known relationships between LFC array area, contact pitch distance, and contact area fraction for planar contacts are modified to account for three-dimensional contact geometries. Using these geometric relationships, the impact of three-dimensional geometries on the pitch distance and the number of contacts required for a given contact area fraction is determined. In addition, the analytical models developed by Fischer [5] are modified to account for three-dimensional contact geometries to predict the rear side series resistances and the effective rear surface recombination rates. The models are used to determine if performance benefits can be realized by employing half-ellipsoidal or hemispherical contacts. The results presented here provide a new perspective on how LFC geometries can be tailored to optimize the rear contacting scheme for high efficiency, Si-based solar cells.

6.2 LFC Geometries and Analytical Model

Geometric relationships from the literature [6-9] between contact pitch distance, LFC array area, and contact area fraction for planar contacts are modified to consider the interfacial area between the LFC and Si wafer to understand how the rear contacting scheme will change by employing three-dimensional contacts. The contact geometries considered are shown in Figure 6.1. A planar contact, as shown in Figure 6.1(a), is one in which the contact radius, a, is substantially larger than the contact depth, c. The three-dimensional contacts considered here are shown in Figure 6.1(b), Figure 6.1(c), and Figure 6.1(d). These geometries exhibit different c/a ratios and form based on the laser processing parameters used [11,12,15].

Fischer's analytical models for S_{eff} and $r_{s,rear}$, which were originally developed for point-contacted structures assuming planar contact geometries [5], are modified to evaluate the impact of LFC dimensionality on device performance. The specific details of the model and applicable assumptions are described later in this chapter. In order to employ modified versions of Fischer's models, the simulated data for total contact resistance as a function of three-dimensional contact geometry in Chapter 3 are used. In addition to the total contact resistance data, the Si wafer thickness (500 μm) and the wafer resistivity (9 Ω-cm) are used to predict S_{eff} and $r_{s,rear}$. Additional details on the experiments and device simulations can be found in the Chapter 3.
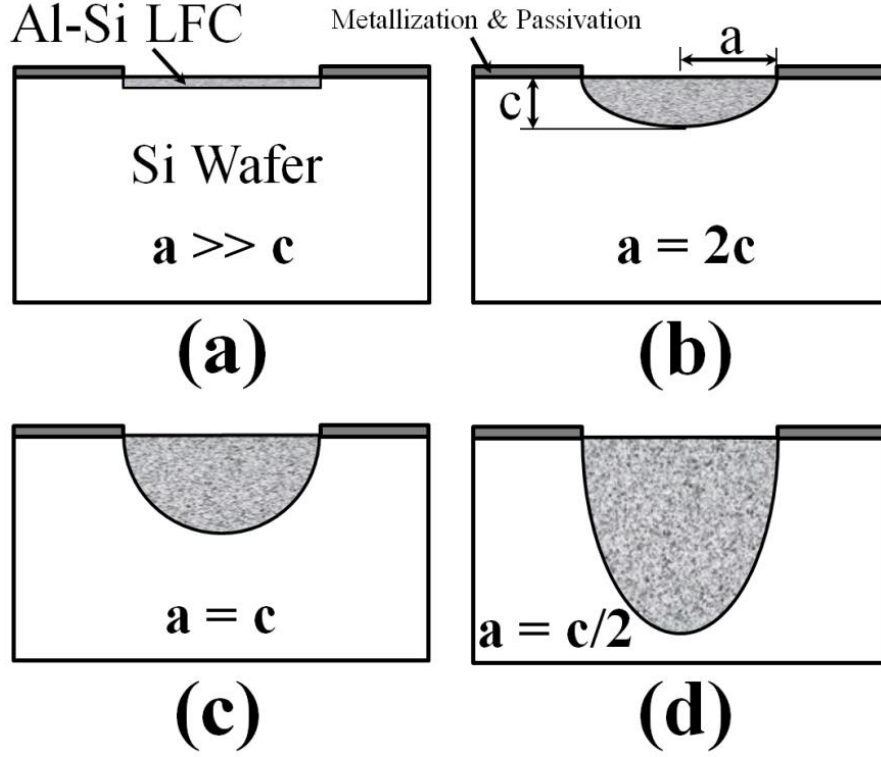
Figure 6.1. Schematic diagrams of various LFC geometries: (a) planar, (b) half-ellipsoidal with $a = 2c$, (c) hemispherical, and (d) half-ellipsoidal with $a = c/2$. Here, a and c are LFC radius and depth, respectively.

6.3 Influence of Contact Geometry on Rear Side Contacting Scheme

The number of contacts used on the rear of a device depends on the contact area fraction required to optimize energy conversion efficiencies [9]. As the interfacial contact area between the Si wafer and LFC increases with increasing contact dimensionality, the rear contacting scheme will have to change to maintain a target contact area fraction. Therefore, it is important to understand how changes in contact geometry will influence the rear contacting scheme.

A schematic diagram of a backside LFC array is shown in Figure 6.2, where L_p is the LFC pitch distance and N is the number of contacts. The array area, A, can be calculated as:

$$A = L_p^2 \times N \tag{6.1}.$$

When assuming a planar contact, the pitch distance can be calculated as:

$$L_p = \sqrt{\frac{\pi a^2}{f}} \tag{6.2}$$

where f is the contact area fraction. The contact area fraction is equal to the total contacted area divided by the total array area. For an individual planar contact, the interfacial area between the Al-alloyed, p-doped region and the Si wafer can be approximated as that of a circle, as shown in Figure 6.3 [8]. Approximating the interfacial area as a circle yields good agreement between experimental measurements of contact resistance and predicted values from the empirical Cox-Strack relationship [8]. Based on the required contact area fraction, the pitch distance can be calculated from Equation (6.2) for a specific planar contact radius.
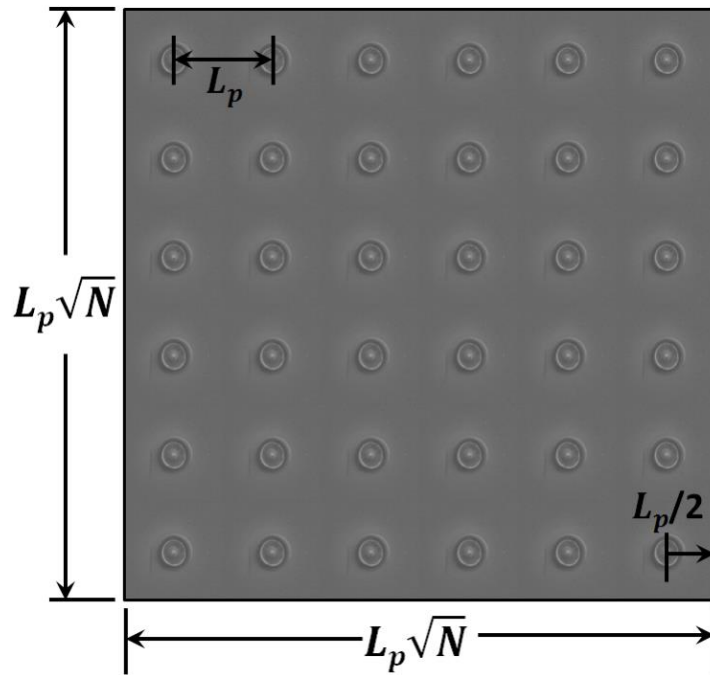
Figure 6.2. LFC array comprised of N LFCs (here $N = 36$) separated by pitch distance, L_p.
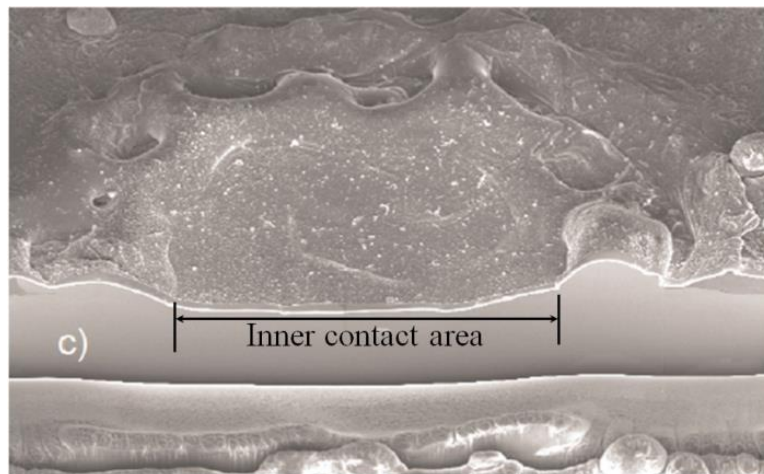
Figure 6.3. SEM micrograph of planar contact formed using nanosecond pulses, Adapted from [12].

The interfacial area for three-dimensional contact geometries, however, will be different since the interface between the LFC and the wafer is contained within the bulk wafer, as shown in Figure 6.1 and explained in Chapters 3 and 5. Consider a three-dimensional contact formed using 112 W laser power, a 50 µm beam diameter, and a 50 µs pulse, as shown in Figure 6.4. In the cross-sectional micrograph, the dark-colored regions are the primary Si-rich phase and the lighter-colored regions are a secondary Al-rich phase. The interfacial area between the LFC and the wafer is governed by the surface area of the heavily-alloyed Al-Si region.
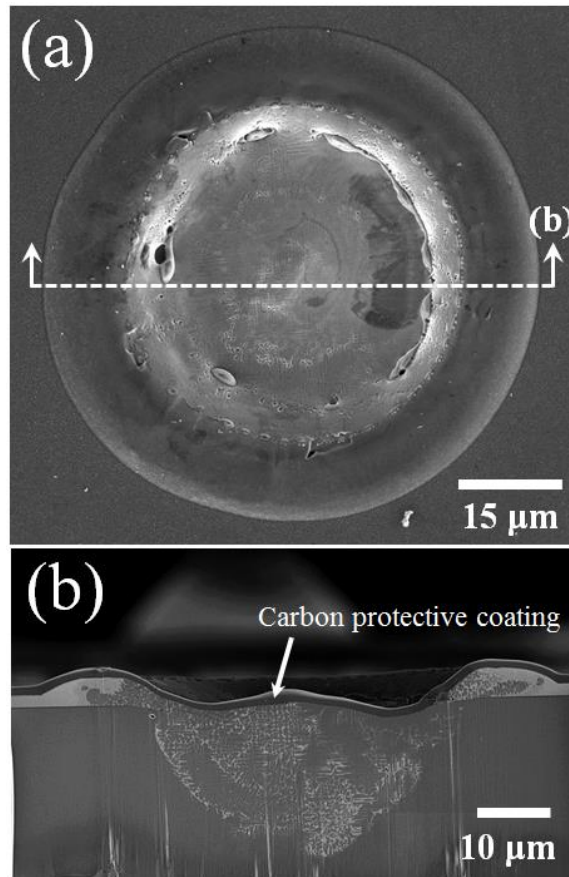
Figure 6.4. SEM micrograph of three-dimensional, hemispherical contact formed using microsecond pulses for (a) top surface and (b) cross-section.

By carefully selecting laser processing parameters, the various contact geometries shown in Figure 6.1(b), Figure 6.1(c), and Figure 6.1(d) can be obtained to tailor the total interfacial contact area. Increases in laser power or pulse duration or a reduction in laser beam diameter will result in a transition in the contact geometry from half-ellipsoidal ($a \approx 2c$) at the onset of laser exposure to a more hemispherical shape ($a \approx c$) after tens of microseconds [19]. The two LFC geometries shown in Figure 6.1(b) and Figure 6.1(c) are indicative of conduction-mode laser processing [16,17], whereas the half-

ellipsoidal shape shown in Figure 6.1(d) ($a = c/2$) is caused by keyhole-mode laser processing and will form under much higher power densities [18]. Keyhole-mode processing of LFCs may not be desirable since it will be accompanied by excessively high substrate temperatures, and significant alloying element vaporization and metal expulsion [12,13].

Since the interfacial area between the LFC and the wafer is contained within the wafer for a three-dimensional contact, it is necessary to account for the contact geometry to predict the required pitch distance for a specific contact area fraction. A modified pitch distance, $L_{p,m}$, can be calculated to account for any contact geometry as:

$$L_{p,m} = \frac{S}{\pi a^2} L_p \tag{6.3}$$

where S is the approximate LFC/wafer interfacial area for a three-dimensional contact. The interfacial area, S, is calculated as the surface area of a three-dimensional half-ellipsoid or hemisphere using the modified Knud-Thomsen approximation [19]:

$$S = 2\pi \left[\frac{a^{2p} + 2a^p c^p}{3} \right]^{1/p} \tag{6.4}$$

where p is a constant valued at 1.6075 that yields less than 1% error in the calculation. When a and c are equal, the interfacial area will be that of a hemisphere. It can be observed from Equations (6.3) and (6.4) that as S increases above that of a planar contact, the pitch distance will increase to maintain the target contact area fraction. Therefore, the term $S/\pi a^2$ can be viewed as a pitch distance multiplier (PDM) relative to the pitch distance required for a planar contact.

The PDM is plotted on the left hand axis in Figure 6.5 as a function of the contact c/a ratio. When the c/a ratio is 0 and the contact is planar, the PDM value is 1. As the depth of a contact is increased while maintaining the same top surface LFC radius, the surface area increases and the PDM is also greater than 1. Therefore, the pitch distance required to maintain the same contact area fraction increases with higher contact dimensionality. For example, a hemispherical contact with a c/a ratio of 1 produces a PDM value of 2. Since the surface area of a hemispherical contact is twice that of a planar contact, the pitch distance can be doubled to maintain the same contact area fraction. As the surface area increases with larger three-dimensional contacts, the pitch distance will increase the PDM value.

As a result of increasing the pitch distance for higher surface area contacts, fewer contacts can be used to maintain the target contact area fraction for a given array area. Combining Equations (6.1) and (6.3) gives a modified number of contacts, N_m, for any contact geometry:

$$N_m = \frac{N}{PDM^2}$$
(6.5).

The percentage of contacts required relative to that required for planar contacts is plotted on the right hand axis in Figure 6.5 as a function of the c/a. At a c/a ratio of 0, the value is 100%, corresponding to the total number of planar contacts required. As the c/a ratio is increased, the percentage of contacts required to maintain the same contact area fraction drops significantly. For instance, when a hemispherical contact forms and the c/a ratio is 1, the percentage of contacts falls to 25% of those required for planar contacts. Table 6.1 provides a summary of the PDM values and the number of contacts required as a percentage of the number of planar contacts for various c/a ratios.
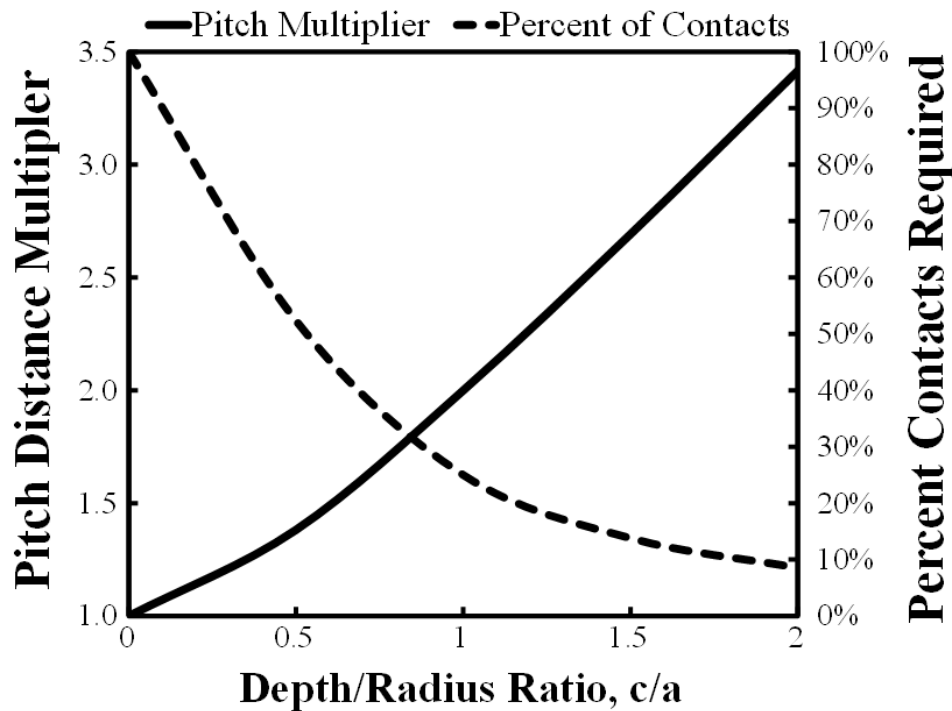
Figure 6.5. Percent of contacts required and pitch distance multiplier versus depth/radius ratio. Percent of contacts required and pitch distance multiplier calculated assuming that a planar contact size is the baseline value.

Table 6.1. Calculated design consideration parameters for various LFC depth/radius ratios. All values are calculated with respect to requirements for a planar contact.

Aspect Ratio, c/a	Fraction of Required Contacts	Pitch Distance Multiplier	Passivation fraction, f_p		
			3% Contact Area	5% Contact Area	7% Contact Area
0	1.00	1.00	97.0%	95.0%	93.0%
0.5	0.52	1.38	98.4%	97.4%	96.3%
1	0.25	2.00	99.3%	98.8%	98.3%
1.5	0.14	2.69	99.6%	99.3%	99.0%
2	0.09	3.42	99.7%	99.6%	99.4%

The modified pitch distance is directly proportional to the PDM value and the contact radius, and indirectly proportional to the contact area fraction. In many cases, the contact radius used for a device is largely dictated by the selection of laser processing parameters [8,9,11]. In order to consider the influence of contact radius and contact geometry on the pitch distance, the product of the modified pitch distance and the square root of the contact area fraction is plotted in Figure 6.6 as a function of contact radius. Rather than plot the pitch distance as a function of radius, the product of the modified pitch distance and the square root of the contact area fraction is plotted since different contact area fractions will require different pitch distances. By removing dependence of pitch distance on the contact area fraction, the general trends for pitch distance as a function of radius and contact geometry can be observed. As the LFC radius is increased, the pitch distance required for three-dimensional contacts is substantially larger than that required for planar contacts. Although the modified pitch distance can be significantly increased through the formation of more three-dimensional contacts, the wafer thickness will impact the allowable depth of penetration for a given device design. For instance, a hemispherical LFC with a radius of 60 μm will also require a 60 μm depth of penetration. Therefore, as wafer thicknesses are reduced to decrease material costs, the practicality of a three-dimensional contact must also be considered.
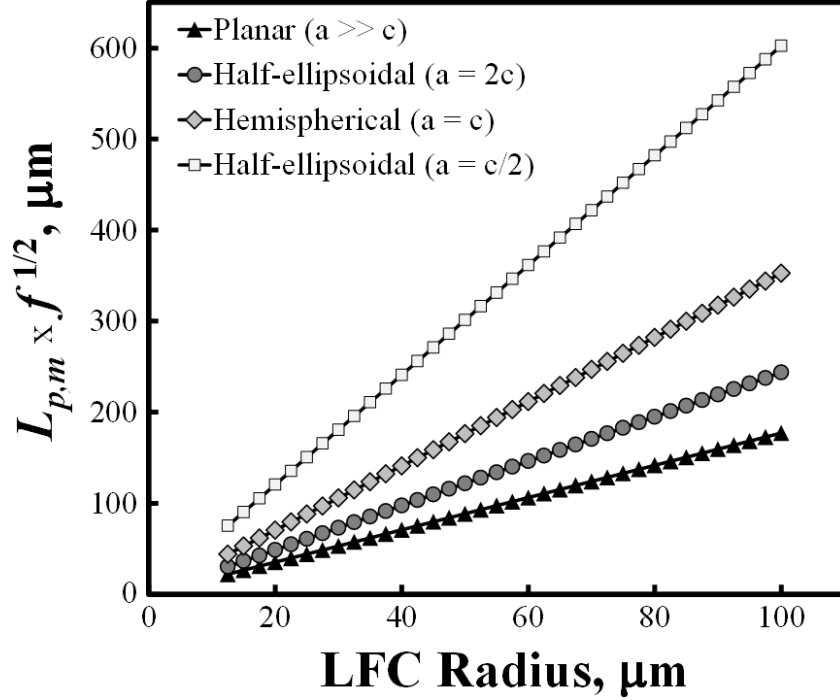
Figure 6.6. Product of modified pitch distance and square root of contact area fraction ($L_{p,m} \times f^{1/2}$) as a function of LFC radius for various contact geometries. Considering $L_{p,m} \times f^{1/2}$ rather than $L_{p,m}$ allows for visualization of impact of LFC radius on pitch distance independent of contact area fraction.

As a device design example, consider a standard wafer size of 12.5 cm x 12.5 cm [24], an LFC top surface radius of 50 µm, and a contact area fraction of 7%. The 7% contact area fraction has been extrapolated based on the 9 Ω-cm wafer resistivity considered here [12] using literature results [9] that showed the optimal contact area fraction for a range of wafer resistivities. Using Equations (6.1) and (6.2), 140,000 planar contacts are required with a pitch distance of 335 µm for a 7% contact area fraction. On the other hand, only 35,000 hemispherical contacts are required with a pitch of 670 µm. As the pitch distance increases with higher c/a ratios, the total number of required contacts can be reduced considerably. However, the formation of three-dimensional contacts requires the use of longer microsecond pulse durations [11,12,14,15]. Therefore, it is important to consider the implications of longer pulses on rapid fabrication of LFCs when compared to conventional processing with nanosecond pulses.

Contacts formed with nanosecond pulses typically have pulse durations on the order of tens of nanoseconds, but are processed with laser systems that have repetition rates ranging from 8-20 kHz [25,26]. Many studies also utilize multiple pulses per contact to form an LFC [8,21,22]. With a repetition rate of 20 kHz, 50 µs are still required per pulse to process one LFC, assuming only one pulse per contact. If multiple pulses are required, which is often the case [9,20-24], the processing time will

increase accordingly. It should also be noted that researchers are currently investigating the use of Al foil metallization to significantly reduce costs associated with metallizing the wafer surface [22,23]. The Al foil used in the experiments can be as thick as 8 μm, requiring at least 70 pulses per contact (when using nanosecond pulse durations) to penetrate the foil and form the LFC [22]. At a repetition rate of 20 kHz, 70 pulses translates to 3.5 ms per contact. Therefore, even with high speed scanning methods [20], processing times required per contact can be significantly greater than those required to process one contact with a singular microsecond pulse.

Fiber laser systems similar to the one used for the microsecond-pulsed processing experiments [12] are commercially available with output powers in excess of 10 kW that can be delivered through multiple fiber outputs. These high-powered lasers can also be integrated with diffractive optics and fast scanning methods to simultaneously produce multiple contacts [24]. Therefore, when considering a rear contacting scheme with hemispherical contacts, the processing time can be significantly reduced through existing fiber laser technology. For the contact shown in Figure 6.3 that is processed with 112 W laser power and a 50 μs pulse, it is conceivable that a 2 kW fiber laser with 15 output fibers can be retrofitted with diffractive optic elements to split each beam into 5 separate beams to process over 75 contacts at a time. Therefore, in addition to the 75% reduction in the total number of contacts required, the processing time can be further reduced 75 fold. As the laser output power is increased and/or more fibers are utilized, processing times can be reduced further. Furthermore, since it has been shown that the passivation layer surrounding the LFC remains intact even with the use of longer pulse durations [12-15], microsecond-pulsed processing to form three-dimensional contacts may be an attractive alternative that has not been considered.

6.4 Device Performance Considerations

6.4.1 Rear Side Series Resistance

In considering the viability of three-dimensional LFCs for the Si-based solar cells, it is also important to evaluate the potential impact on device performance. The rear contacting scheme has been shown to influence the rear side series resistance and the effective rear surface recombination rate [5-9]. Both metrics must be optimized for a point-contacted structure to generate higher energy conversion efficiencies. A low rear side series resistance is required to minimize internal losses of current and maximize the fill factor, and low recombination rates are necessary to achieve higher open circuit voltages and short circuit currents. The rear surface series resistance, $r_{s,rear}$ (in Ω-cm^2), can be calculated for a point-contacted structure that employs planar contacts [5,7,9] as:

$$r_{s,rear} = \frac{R_{LFC}\,S}{f} + \rho_b\,W\left(1 - e^{-W/L_p}\right) \tag{6.6}$$

where R_{LFC} is the total contact resistance, ρ_b is the wafer resistivity, W is the wafer thickness, and S is the planar contact area (taken as πa^2). Equation (6.6) can be modified using Equation (6.3) and the PDM to determine $r_{s,rear}$ for any contact geometry as:

$$r_{s,rear} = R_{LFC} \times PDM \times L_p{}^2 + \rho_b\,W\left(1 - e^{-W/PDM \times L_p}\right) \tag{6.7}.$$

When considering a planar contact, the PDM value is 1 and the original equation is maintained. The total contact resistance, R_{LFC}, can be approximated by the spreading resistance, R_S, when assuming a low specific contact resistance, i.e., $R_{LFC} \approx R_S$ [8]. The spreading resistance for a planar contact can be calculated as [10]:

$$R_S \cong \frac{\rho_b}{2\pi a}\,arctan\left(\frac{2W}{a}\right) \tag{6.8}.$$

The total contact resistance, R_{LFC}, is plotted in Figure 6.7(a) as a function of LFC top surface radius for various contact geometries. The total contact resistance for a planar contact is calculated from Equation (6.8) using 9 Ω-cm and 500 μm for ρ_b and W, respectively [12]. The R_{LFC} values for the three-dimensional contact geometries were obtained from device simulation data from Chapter 3. It can be observed that contact geometry strongly influences the total contact resistance, R_{LFC}. Since three-dimensional contacts possess higher LFC/wafer interfacial areas, they exhibit significantly lower total contact resistances. Table 6.2 shows the total contact resistance values for various LFC radii as a function of the c/a ratio.
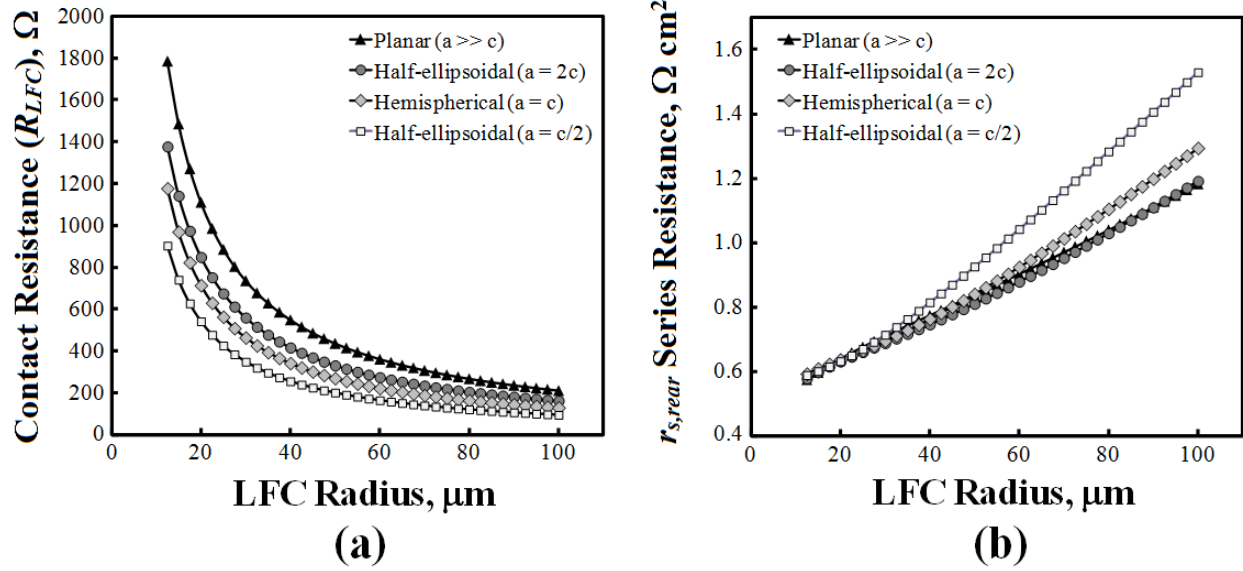
Figure 6.7. Plots of (a) Contact resistance and (b) the rear side series resistance ($r_{s,rear}$) versus LFC radius for various contact geometries.

Table 6.2. Simulated values for total contact resistance (Ω) for various LFC radii and depth/radius (c/a) ratios.

Aspect Ratio, c/a	Total Contact Resistance (Ω)			
	LFC Radius (μm)			
	25	50	75	100
0	886	436	286	211
0.5	674	330	218	162
1	563	269	175	129
2	425	200	129	94

The impact of contact geometry and contact radius on the rear side series resistance is shown in Figure 6.7(b). The $r_{s,rear}$ is calculated assuming a contact area fraction of 7%. The rear side series resistance increases for all contact geometries as the contact radius is increased because a larger contact pitch distance is required to maintain the same contact area fraction. When a larger pitch distance is used, the majority carriers at the rear surface have to travel longer lateral distances to reach the rear contacts. Therefore, as the pitch distance is increased to maintain the same contact area fraction for larger contact radii, $r_{s,rear}$ also increases for all contact geometries.

The rear side series resistance is also strongly dependent on the contact dimensionality, especially at contact radii greater than 50 μm and c/a ratios greater than 1. Despite the fact that contacts with larger c/a ratios exhibit lower R_{LFC}, as shown in Figure 6.7(a), the contribution of the *PDM* value results in a much larger $r_{s,series}$ values as the c/a ratio increases. For instance, for the contact radii values shown in

Table 6.2, R_{LFC} is nearly 55% lower for a half-ellipsoidal contact with $a = c/2$ than for a planar contact. However, since the *PDM* is 3.42 for a contact with a c/a ratio of 2, the benefits associated with a lower individual R_{LFC} for contacts with higher dimensionality are offset by the higher pitch distance required since contacts with larger c/a ratios require greater pitch distances to maintain the same contact area fraction.

The influence of the *PDM* value on $r_{s,rear}$ is more pronounced at larger contact radii, especially for the half-ellipsoidal contact with $a = c/2$. The difference in $r_{s,rear}$ between a hemispherical and planar contact is most impacted at extremely large contact radii, close to 100 µm. At radii less than 75 µm, the difference in $r_{s,rear}$ between hemispherical contacts and planar contacts is less than 5%. Therefore, for a wide range of contact radii and c/a values less than or equal to 1, the contact geometry has little impact on rear surface series resistance despite significantly lower individual total contact resistances for more three-dimensional contacts. The predicted results suggest that comparable rear side series resistances are achievable when employing three-dimensional contacts in comparison to planar contacts depending on the LFC top surface radius and dimensionality.

6.4.2 Effective Rear Surface Recombination Velocity

In addition to considering the ohmic losses, it is important to consider the recombination losses associated with different geometries. Rear side recombination losses can be predicted based on the effective rear surface recombination velocity, S_{eff}. An analytical model for S_{eff} was developed by Fischer [5] for a point-contact scheme using planar contacts. The analytical model assumes low-injection levels (i.e., the number of carriers generated is substantially smaller than the majority carriers in the material), no recombination in the base, and decoupling of the contacted and passivated regions on the rear side. In applying the model originally developed for planar contacts to the case of three-dimensional LFCs, it is assumed that recombination only occurs at the LFC/wafer interface, rather than within the contact. Although this assumption has not been experimentally validated, the heavy alloying of Al and Si within the contact is expected to result in the LFC volume behaving similar to the Al metallization layer where significant recombination is not a concern. The modified form of the model can be expressed as:

$$S_{eff} = \frac{D}{W}\left(\frac{r_{s,rear}}{\rho W} + \frac{D}{fWS_{met}} - 1\right)^{-1} + \frac{S_{pass}}{f_p} \tag{6.9}$$

where D is the minority carrier diffusion constant taken as 10.6 cm^2/s [6], W is the wafer thickness taken as 500 µm [12], and S_{met} and S_{pass} are the surface recombination velocities at the metallized and passivated areas, respectively, and f_p is the passivation fraction. Although S_{met} has not been derived for

three-dimensional LFCs formed under microsecond pulsed processing, it can be approximated from the following empirical relationship [10] based on the known doping density, N_A:

$$S_{met} = S_0 + \alpha \exp[\beta(N_A + N_0)] \tag{6.10}$$

where S_0 is -900 cm/s, α is 22.1 cm/s, β is 1.29 x 10^{-16} cm^3, and N_0 is 3.4 x 10^{16} cm^{-3} [6]. N_A is estimated as 1.5 x 10^{15} cm^{-3} based on the 9 Ω-cm wafer resistivity [25]. S_{met} is highly dependent on the doping density and the size of the active recombination area (i.e., LFC) [11]. A higher doping density will lead to lower recombination rates at the contact as a result of a reduced $N_A/N_{A,BSF}$ ratio at the back surface field (BSF) of the contact [6,7], and an increase in the active recombination area will reduce the SRV at the metallization layer [7]. Since the size of this region is unknown for the three-dimensional contact geometries, a constant value of 1254 cm/s is calculated. For a comparison of the impact of changing S_{met} on S_{eff}, an extremely high value of 1 x 10^5 cm/s was also used [6]. S_{pass} is significantly lower than S_{met} and is taken here as 13 cm/s [9]. The passivation fraction, f_p, in Equation (6.9) is normally calculated as (1-f) for planar contacts. However, since the contact area fraction for three-dimensional contacts is contained within the substrate, the passivation fraction is calculated as:

$$f_p = 1 - \frac{\pi a^2}{L_{p,m}^2} \tag{6.11}.$$

From Equation (6.11), it can be observed that for a planar contact, when $L_{p,m}$ is equal to L_p the passivation fraction will be equal to (1-f). For instance, when the contact area fraction f is 0.07, the passivation fraction will be 0.93 for planar contacts. As the contact dimensionality is increased through higher depth/radius ratios, fewer contacts are required to obtain a particular metallization fraction. Therefore, the passivation fraction will increase, as shown in Table 6.1. When employing a hemispherical contact with a c/a ratio of 1, the passivation fraction is 0.983, which is nearly a 6% increase over that obtained for planar contacts. Table 6.1 also shows passivation fractions for various other contact area fractions that are typically used in device fabrication [7,26]. Lower contact area fractions are typically used for highly doped wafers with lower wafer resistivities to achieve higher energy conversion efficiencies [9]. The increase in f_p is less pronounced when employing lower contact area fractions since fewer backside contacts are required and the pitch distance is greater. The gains associated with increasing the passivation area fraction will be greater at lower S_{eff} values since the overall contribution of S_{pass} to S_{eff} in Equation (6.9) is generally much smaller than that from S_{met}.

The effective rear surface recombination rate calculated from Equation (6.9) is plotted as a function of contact radius and contact geometry in Figure 6.8 assuming a contact area fraction of 7%. Since S_{eff} is

inversely proportional to the $r_{s,rear}$, S_{eff} decreases for all the contact geometries as the contact radius is increased regardless of S_{met}. For the case where S_{met} is taken as 1254 cm/s, as shown in Figure 6.8(a), the S_{eff} values for all contact geometries are fairly equal at smaller contact radii since the rear surface series resistances for the various contact geometries are approximately equal. With increasing contact radius, the three-dimensional contacts exhibit slightly lower effective rear surface recombination rates since the pitch distance increases as the dimensionality increases. For example, for a planar contact with an LFC top surface radius of 75 μm, S_{eff} is 71.9 cm/s in comparison to 64.4 cm/s for a half-ellipsoidal contact with c/a ratio of 2. In this case, however, $r_{s,rear}$ is 1.011 Ω-cm^2 for the planar contact in comparison to 1.223 Ω-cm^2 for the planar contacts. When using a 75 μm hemispherical contact, $r_{s,rear}$ is 1.059 Ω-cm^2 and S_{eff} is 69.5 cm/s. Therefore, there will be a clear tradeoff in these two device performance metrics when employing one geometry over another.

When assuming a S_{met} value of 10^5 cm/s, as shown in Figure 6.8(b), S_{eff} values will be significantly higher since the contribution of S_{met} will have a greater influence on S_{eff}. However, the same general trends can be observed where S_{eff} is lower for contacts with higher c/a ratios and larger contact radii. The reduction in S_{eff} is primarily driven by the increase in pitch distance required for three-dimensional contacts with larger LFC/wafer interfacial areas. Furthermore, the influence of an increase in the passivation fraction due to higher contact dimensionality is lower since the recombination rates at the LFC/wafer interface are substantially higher than those at the passivation/wafer interface. Although the passivation fraction is increased through the use of contacts with higher dimensionality, as shown in Equation (6.11), the passivation term in Equation (6.9) has little impact on S_{eff} when it is extremely high.
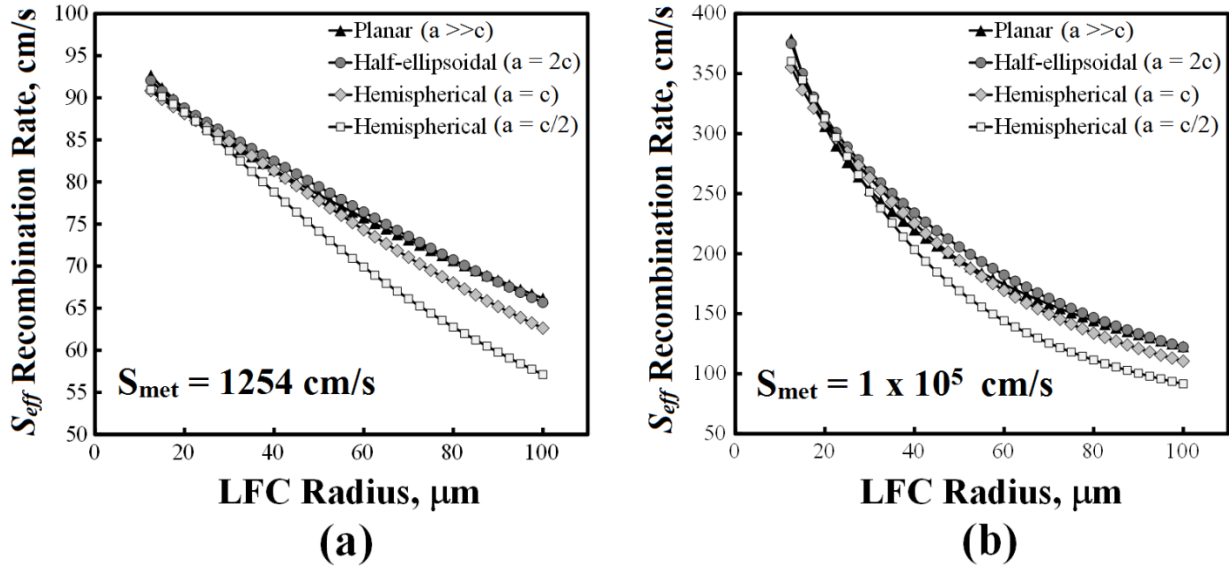
Figure 6.8. Plots of effective rear surface recombination rates, S_{eff}, as a function of LFC radius and contact geometry assuming S_{met} to be (a) 1,254 cm/s and (b) 1 x 10^5 cm/s.

From the plots of $r_{s,rear}$ and S_{eff}, it is clear that there are tradeoffs associated with using contacts with higher dimensionality over planar contacts from a device performance standpoint. The reduction in S_{eff} is offset by an increase in $r_{s,rear}$ when the contact radius is greater than 50 µm and the c/a ratio approaches 2. For more hemispherical contacts, however, both the $r_{s,rear}$ and S_{eff} values are comparable to those obtained when using planar contacts. Therefore, along with a significant reduction in the total number of contacts required to maintain a desired metallization fraction, the results suggest that device performance can be maintained when employing hemispherical contact geometries.

6.5 Summary and Conclusions

In order to determine how manufacturing efficiency and device performance are affected by increasing the contact volume, various well-established geometric relationships and analytical models have been employed. Geometric relationships between contact pitch, contact radius, and contact area fraction have been developed to account for LFC geometry to determine the number of contacts required to maintain a target contact area fraction. In addition, the analytical models developed by Fischer [9] to predict the $r_{s,rear}$ and S_{eff} for point-contacted structures have been modified to determine if performance benefits can be achieved through by increasing the interfacial LFC area. The following conclusions can be drawn from the work:

1. The number of LFCs required on the rear side can be reduced considerably by increasing the contact volume. Since an increase in the contact volume leads to higher interfacial contact area between the

LFC and wafer, fewer contacts can be used to maintain a specific contact area fraction. By employing fewer contacts on the rear surface, the LFC process can be significantly streamlined.

2. Theoretical calculations for the values of $r_{s,rear}$ and S_{eff} are comparable over a wide range of LFC radii and contact geometries, suggesting that current energy conversion efficiencies can be maintained by employing more three-dimensional contacts. The predicted values for $r_{s,rear}$ and S_{eff} are comparable when employing depth/radius ratios less than or equal to 1 and LFC radii less than 50 μm. As both the LFC aspect ratio and radius are increased above these values, there will be a negative impact on $r_{s,rear}$ and a positive impact on S_{eff}.

3. A larger fraction of the backside passivation layer can be preserved by increasing the contact dimensionality. Since a larger portion of the interfacial area between the LFC and the wafer is contained within the wafer as the contact dimensionality is increased, less passivation is removed during contact formation. The impact that increasing the passivation fraction has on the effective rear surface recombination rates will depend on the contact area fraction and the recombination rates at the metallized region.

4. By employing hemispherical LFCs over planar LFCs, the number of contacts required on the rear side can be reduced 75%. Furthermore, the predicted values for $r_{s,rear}$ and S_{eff} vary less than 5% between planar and hemispherical LFC geometries when the contact radius is less than 50 μm, suggesting that device performance levels will be similar. As an additional benefit, reducing the total number of contacts required leads to an increase in the passivation fraction by 6% from 0.93 to 0.983 for a contact area fraction of 0.07.

6.6 Limitations

There are a several limitations associated with this analysis that can only be evaluated through directed experimentation. In this work, constant recombination rates were assumed at the metalized and passivated surfaces. Although this assumption is valid for illustrative purposes, it would be necessary to conduct carrier lifetime experiments to accurately determine the actual recombination rates at the metallized surface for LFCs formed with longer pulse durations. Although there is no clear presence of a back-surface field, the longer pulse durations may promote solid-state diffusion of Al into the crystalline Si which can improve recombination rates at this LFC/wafer interface. In addition, although the results suggest that device performance can be maintained when using higher dimensionality contacts, this idea needs to be further evaluated. For instance, it is unclear how larger LFCs will influence carrier lifetime. Since the LFCs will more deeply penetrate the substrate, the distance that carriers have to travel may be reduced since the required diffusion length will be shorter. However, if fewer contacts are used on the

back surface to maintain a specific contact area fraction and to improve throughput times, these benefits may not exist. Although this work introduces novel concepts through the use of modified analytical expressions, the concepts need to be tested.

6.7 References

1. E. Urrejola, K. Peter, H. Plagwitz, G. Schubert, Silicon diffusion in aluminum for passivated rear solar cells, Appl. Phys. Lett. 98, 153508 (2001).

2. B. Sopori, V. Mehta, D. Guhabiswas, R. Reedy, H. Moutinho, Bobby To, A. Shaikh, A. Rangappan, Formation of a back contact by fire through process of screen-printed silicon solar cells, 2009 IEEE, pp 1963-1968, 978-1-4244-2950-9/09. .

3. U. Zastrow, L. Houben, D. Meertens, A. Grohe, T. Brammer, E. Schneiderlöchner. Applied Surface Science 252, (2006).

4. A. Grohe, U. Zastrow, D. Meertens, L. Houben, W. Brendle, G. Bilger, E. Schneiderlochner, S.W. Glunz, R. Preu, G. Willeke, Proc. 20th European Photovoltaic Solar Energy Conference, Barcelona, (2005).

5. B. Fischer, Loss analysis of crystalline silicon solar cells using photoconductance and quantum efficiency measurements, PhD Thesis, University of Konstanz, 2003.

6. D. Kray, S. Glunz, Investigation of laser-fired rear-side recombination properties using an analytical model, Prog. In Photo. 14, pp. 195-201, 2006.

7. A. Wolf, D. Biro, J. Nekarda, S. Stumpp, A. Kimmerle, S. Mack. R. Preu, Comprehensive analytical model for locally contacted rear surface passivated solar cells, J. Appl. Phys. 108, 124510, 2010.

8. P. Ortega, A. Orphella, I. Martin, M. Colina, G. Lopez, C. Voz, M.I. Sanchez, C. Molpeceres, R. Alcubilla, Laser-fired contact optimization in c-Si solar cells, Prog. In Photo. 20, pp 173-180, 2012.

9. P. Ortega, A. Orpella, G. López, I. Martín, C. Voz, R. Alcubilla, I. Sanchez-Aniorte, M. Colina, F. Perales, C. Molpeceres, Optimization of the rear point contact scheme of crystalline silicon solar cells using laser-fired contacts, Proc. of 25th EUPVSEC, 6-10, (2010).

10. R.H. Cox, H. Strack, Ohmic Contacts for GaAs Devices, Solid State Electronics 1967; 10: 1213-1218, DOI: 10.1016/0038-1101(67)90063-9.

11. A. Raghavan, T.A. Palmer, T. DebRoy, Evolution of laser-fired aluminum-silicon contact geometry in photovoltaic devices, J. Appl. Phys. 2012; 111 (2), DOI: 10.1063/1.3675442.

12. A. Raghavan, T.A. Palmer, K.C. Kragh-Buetow, A. Domask, E.W. Reutzel, S.E. Mohney, T. DebRoy, Employing microsecond pulses to form laser-fired contacts in photovoltaic devices, submitted for publication in Prog. In Photovoltaics, 2013.

13. A. Raghavan, B. Hedrick, B. DeCesar, B.P. Downey, J. Flemish, L. Zou, T.A. Palmer, T. DebRoy, S.E. Mohney, E.W. Reutzel, Impact of millisecond pulses on laser-fired contact geometry and photovoltaic device performance, submitted for publication in Solar Energy Materials and Solar Cells, 2014.

14. A. Raghavan, T.A. Palmer, T. DebRoy, Passivation layer breakdown during laser-fired contact formation for photovoltaic devices, prepared for Appl. Phys. Letters, 2014.

15. A. Raghavan, K.C. Kragh-Buetow, T.A. Palmer, S.E. Mohney, T. DebRoy, Heat and mass transfer during laser-fired contact formation for photovoltaic devices, submitted to J. Appl. Phys., 2014.

16. X. He, P.W. Fuerschbach, T. DebRoy, Heat transfer and fluid flow in laser spot welding of 304 stainless steel, J. Phys. D: Appl. Phys. 36 (12), 2003, pp. 1388. DOI: 10.1088/0022-3727/36/12/306.

17. X. He, J.W. Elmer, T. DebRoy, Heat transfer and fluid flow in laser microwelding, J. Appl. Phys. 97, 2007, DOI: 10.1063/1.1873032.

18. R. Rai, J.W. Elmer, T.A. Palmer, T. DebRoy, Heat transfer and fluid flow during keyhole mode welding of tantalum, Ti-6Al-4V, 304L stainless steel, and vanadium, J. Phys. D: Appl. Phys, 40, 2007, pp 5753-5766.

19. D. Xu, J. Cui, R. Bansal, X. Hao, J. Liu, W. Chen, B.S. Peterson, The ellipsoidal area ratio: an alternative anisotropy index for diffusion tensor imaging, Magnetic Resonance Imaging 27 (2009); 311, DOI: 10.1016/j.mri.2008.07.018

20. R. Preu, E. Schneiderlochner, A. Grohe, S.W. Glunz, G. Willeke, Laser-fired contacts – transfer of a simple high efficiency process scheme to industrial production, 2002 IEEE, 0-7803-7471-1/02

21. C. Molpeceres, M. Isabel Sanchez-Aniorte, M. Morales, D. Munoz, I. Martin, P. Ortega, M. Colina, C. Voz, R. Alcubilla, Influence of wavelength on laser doping and laser-fired contact processes for c-Si solar cells, Proceedings of SPIE Conference 2014. #847308-1.

22. L. Wang, D.E. Carlson, M.C. Gupta, Investigation of metal contacts for silicon solar cells using laser processed 8 μm thick Al foils, SPIE Conference, #882604-1.

23. J.F. Nekarda, F. Lottspeich, A. Wolf, R. Preu, Silicon solar cells using aluminum foils as rear side metallization reaching 21% efficiency, 25th European Photovoltaic Solar Energy Conference and Exhibition, 2010, Valencia, Spain, pp 2211-2214.

24. Z. Hua, E.W. Reutzel, L. Zou, Beam delivery techniques for laser fired contacts, ICALEO 2010, #M1101.

25. Sze, S.M., K.NG, Kwok, Physics of Semiconductor Devices, 3rd Ed., John Wiley & Sons, Hoboken, NJ (2007).

26. S. Gatz, T. Dullweber, R. Brendel, Evaluation of series resistance losses in screen-printed solar cells with local rear contacts, IEEE J. Photo. 1(1), 2011. pp 37-42.

Chapter 7

CONCLUDING REMARKS

7.1 Summary and Conclusions

Lasers offer a non-contact method to fabricate Al-Si ohmic contacts on the rear side of dielectrically passivated Si-based photovoltaic devices [1]. Research to date has focused on parametric optimization of the process using nanosecond pulse durations despite liquid metal expulsion [2], spatter, and crater formation [3], which typically accompany the process and can adversely impact contact quality [4]. The use of longer microsecond pulses may offer a means to mitigate these issues. However, the impact of microsecond pulses on laser-fired contact (LFC) quality has not been evaluated. Researchers have likely avoided this processing regime based on two unconfirmed beliefs: 1) longer pulses will structurally damage the passivation layer and crystalline silicon wafer outside the LFC, and 2) microsecond pulses translate to longer processing times. The second item has been addressed in separate studies [5,6], which suggest that laser processing methods exist to simultaneously process multiple LFCs to meet throughput requirements with longer pulses. The first concern, however, has not been systematically evaluated. Therefore, a gap exists in this field of study concerning the impact of fabricating LFCs with microsecond pulses.

This study explores the impact of using microsecond pulse durations on various aspects of contact formation using experimental and theoretical methods. Through this work, the effects of laser processing parameters on contact morphology, passivation layer quality, alloying between Al and Si, and total contact resistance have been evaluated. In addition, several important phenomenological issues involving LFC formation have been addressed, such as heat and mass transfer, fluid flow, thermal cycles, and liquid metal expulsion. Finally, the effect of producing three-dimensional contacts with increased interfacial LFC area on device performance metrics has been analytically determined. The findings provide valuable information in determining the applicability of this LFC processing approach to solar cell fabrication.

Laser-fired contacts were produced over a wide range of laser processing parameters on a Si wafer substrate that was passivated with a 100 nm thick SiO_2 layer and metallized with a 2 μm thick Al layer. The LFCs were systematically analyzed using advanced materials characterization tools and device simulations to determine the influence of laser processing parameters on LFC surface morphology, cross-sectional geometry, passivation layer quality, alloying element concentration, and total contact resistance. LFCs that form when using microsecond pulses are three-dimensional and heavily alloyed with Al and Si, and typically exhibit three distinct features: a central peak, an inner contact region and an outer ring. The resulting contact morphology is largely dependent on pulse duration, laser power, and beam diameter.

The outer ring region that forms during processing is due to liquid metal expulsion, which occurs when the vapor recoil force on the surface of the melt pool exceeds the surface tension force of the liquid metal at the periphery of the melt pool. Changes in the irradiated material from solid Al to molten Si during laser processing lead to a significant increase in the amount of absorbed laser energy, which can rapidly raise the molten pool surface temperatures. The critical peak temperature and critical radius for metal expulsion were found to be largely dependent on the laser beam diameter. By increasing laser beam diameter from 50 µm to 70 µm, the critical radius for metal expulsion increases from approximately 20 µm to 39 µm, whereas the critical peak temperature decreases from 3359K to 3216K. In most cases, liquid metal expulsion took place within the first 10 µs of initial contact formation. In order to avoid expulsion, lower power levels and longer processing times are required.

By processing with lower power levels, the pulse duration operating regime is also much larger. When processing with a 70 µm beam diameter, for instance, the use of a power levels less than 112 W allows for contact formation with no metal expulsion at all pulse durations tested. Increasing the power level to 159 W, however, results in observable metal expulsion within 500 µs. Further increasing power can significantly reduce the operating regime. Using 210 W laser power, liquid metal expulsion initiates within 10 µs after initial contact formation. Similarly, when using a 50 µm beam diameter, contacts can be processed with 65 W laser power with no observable metal expulsion. However, an increase in laser power to 112 W results in metal expulsion within 10 µs after initial contact formation. Therefore, careful selection of laser processing parameters when considering microsecond pulse durations can promote the formation of large contact dimensions without liquid metal expulsion.

In order to determine the impact of laser processing on the contact formation, FIB milling was employed to polish various cross-sectioned surfaces. The cross-sections show that the amount of Al dissolved into the molten pool is much greater than the solid solubility of Si. Therefore, a two-phase microstructure composed of a Si-rich phase and a second phase with higher Al concentration is observed. The LFCs exhibit half-ellipsoidal or hemispherical contact geometries depending on the selection of processing parameters, and a reduction in the beam size will result in larger penetration depths and larger interfacial contact areas between the LFC and the Si wafer. Furthermore, the formation of these heavily-alloyed three-dimensional regions suggests that the entire region constitutes the electrically active region and that the ohmic contact is governed by the interfacial contact area.

The sample cross-sections also reveal that the SiO_2 passivation layer is extremely robust due to its high melting temperature and does not melt outside the resolidied LFC even when significant metal expulsion occurs. Although accelerated breakdown of SiO_2 passivation layers has been observed

experimentally due to a reduction reaction involving the Al metallization layer, the results indicate that the removal of SiO_2 during LFC formation is driven by direct melting of the SiO_2 by the laser energy. As the LFC grows radially outward during processing, free O_2 that forms due to the dissociation of SiO_2 reacts with the Al metallization layer to form a stable Al_2O_3 at the LFC/passivation layer boundary. The impact of this Al_2O_3 byproduct on device performance is unclear. However, since the passivation layer is preserved outside of the LFC region, the benefits of reduced recombination rates at the wafer/passivation layer interface should not be severely impacted.

Electrical measurements of total contact resistance demonstrate that a reduction in the laser beam diameter, an increase in laser power, and/or an increase in pulse duration can result in lower contact resistances when the top surface LFC radius is the same. This reduction in total contact resistance is due to the existence of a larger interfacial contact area between the LFC and the wafer which reduces the spreading resistance. Device simulations performed considering half-ellipsoidal (with the LFC top surface diameter = LFC depth) and hemispherical contact geometries validated this finding. Regardless of LFC top surface radius, the total contact resistance is 37% less for hemispherical contacts and 53% less for half-ellipsoidal contacts than that predicted for planar contact geometries from the empirical Cox-Strack relationship. Therefore, laser processing parameters can be selected accordingly to maximize the three-dimensional LFC size to reduce the total contact resistance when designing a device.

In order to investigate the physical phenomena governing LFC formation, a comprehensive mathematical model was developed to evaluate contact geometry, heat and mass transfer, and fluid flow. An accurate prediction of LFC contact geometry was obtained by accounting for the dissolution of Al into the molten pool despite the thinness of the Al metallization layer. Incorporating the Al-Si phase diagram into the model to calculate the liquid fraction within the large two-phase region allowed for an accurate calculation of the amount of laser energy required to heat and melt a binary Al-Si alloy. Since the total contact resistance is directly dependent on the contact geometry, being able to predict the shape can allow for tailoring of process parameters to determine the appropriate shape for a particular application.

Numerically computed process maps show how various combinations of processing parameters can be used to arrive at a given contact geometry within a safe operating regime to avoid metal expulsion. The results show that the allowable laser power levels are greatly restricted as spot size is reduced by the limitation of the upper and lower limits of the peak temperature values between the melting and boiling points of the alloy. In addition, as the pulse duration is increased from tens of microseconds to hundreds of microseconds, the operating window shrinks to prevent the peak temperatures from exceeding the boiling point of Al and Si. The process maps provide a beneficial roadmap to arrive at a given contact

geometry and demonstrate that multiple combinations of laser power, spot size, and pulse duration exist to obtain a given contact size. For example, a large beam diameter can be used to achieve a similar LFC size to that obtained with a smaller beam diameter while substantially reducing the temperature gradients and processing temperatures within the pool.

The contact geometry and concentration profiles achieved during processing with microsecond pulses are largely driven by convection, as evidenced through calculations of the heat and mass transfer Peclet numbers. The values for each of these dimensionless numbers rapidly exceed 1 within tens of microseconds after contact formation. Due to high fluid flow velocities, Al is well distributed throughout the molten pool, leading to heavy doping of the Si and indicating that the entire molten area comprises the ohmic contact. A reduction in beam size from 50 µm to 30 µm will lead to more uniform concentration profiles within the molten pool when using shorter pulses because the fluid flow velocities will increase significantly. However, since Si has an extremely low Al solid solubility, the results indicate that sufficiently high Al doping levels can be achieved in a less well-mixed pool regardless of beam diameter.

The dissolution of Al into the molten pool also has a noteworthy impact on the thermal cycles and peak temperatures. As the amount of Al in the molten pool increases based on the contact size, the temperatures within the molten region can decrease substantially because more energy is consumed during a larger phase transformation of solid to liquid at the eutectic temperature. Due to the presence of a two-phase (Liquid + Si) region within the molten pool, the cooling cycles are significantly different than those predicted for pure Si. Thermal arrests are observed on cooling at both the liquidus and eutectic temperatures during the initial formation of a solid and complete solidification of the liquid, respectively.

Calculations of the temperature profiles for simultaneously processed contacts allow for a determination of how contact spacing will impact parameter selection. The thermal interaction between adjacent spot welds is largely dependent on the laser power level. When using 30 W laser power, a contact spacing of 3 times the beam diameter is required to ensure that spot weld size is not affected by a neighboring spot. For 50 W laser power, the pitch distance must be 6 times the beam diameter to achieve the same effect. In practice, optimal pitch distances are on the order of hundreds of microns to two millimeters to achieve a desired contact area fraction. Since beam diameters are on the order of tens of microns, the thermal interaction between simultaneously processed LFCs when using microsecond pulse durations should have little impact on the substrate.

Pitch distance also influences the rear contacting scheme and important device performance metrics. Considering the higher dimensionality contacts produced using microsecond pulse durations, it was shown that the number of LFCs required on the rear side can be reduced considerably due to an increase

in contact spacing required to maintain a constant contact area fraction. Since an increase in the contact dimensionality leads to higher interfacial contact area between the LFC and wafer, fewer contacts can be used to maintain a specific contact area fraction. For instance, by employing hemispherical LFCs over planar LFCs, the number of contacts required on the rear side can be reduced 75%. By employing fewer contacts on the rear surface, the LFC process can be significantly streamlined. As an additional benefit, reducing the total number of contacts required leads to an increase in the passivation fraction. The amount of increase in the passivation fraction will be dependent on the required contact area fraction.

Experimentally validated [7-10] analytical expressions used to determine rear side series resistance ($r_{s,rear}$) and effective rear surface recombination rates (S_{eff}) were modified to consider higher dimensionality contacts. The results indicate that comparable values of $r_{s,rear}$ and S_{eff} can be obtained over a wide range of LFC radii and contact geometries, suggesting that current energy conversion efficiencies can be maintained by employing more three-dimensional contacts. Specifically, the predicted values for $r_{s,rear}$ and S_{eff} vary less than 5% between planar and hemispherical LFC geometries when the contact radius is less than 50 μm. As the LFC dimensionality and radius are increased above these values, there will be a negative impact on $r_{s,rear}$ and a positive impact on S_{eff}. The analytical findings coupled with the geometric considerations suggest that device performance can be maintained while dramatically streamlining the overall manufacturing process.

The research performed in this thesis has generated a comprehensive understanding of the physical processes governing laser-fired contact formation. The experimental results make clear that the passivation layer outside of the LFC remains intact after processing, and that the use of longer pulse durations results in heavily Al-alloyed, three-dimensional contacts that exhibit significantly lower contact resistances than their planar counterparts. These results have important implications on device design and performance. Heat transfer and fluid flow modeling was developed to quantitatively relate processing parameters to the physical phenomena occurring during contact formation. A reliable mathematical model eliminates the need for conventional trial and error in tailoring contact geometry for a specific device design. The results from this study significantly expand the existing knowledge base governing LFC formation for Si-based PV devices by developing an experimental and theoretical foundation for the laser firing process.

7.2 Future Work

In order to determine whether LFC formation with microsecond pulse durations is a viable long-term option, additional research avenues should be explored.

In this study, lifetime measurements were not conducted. Since devices fabricated with LFC technology should exhibit low effective rear surface recombination rates, it is important to quantify recombination rates associated with the three-dimensional contacts formed when employing microsecond pulses. Arrays of LFCs should be generated using appropriate contact area fractions and carrier lifetimes should be measured. Lifetime measurements can be performed using a technique such as microwave detected photoconductive decay. Carrier lifetimes can be correlated back to process parameters to determine the influence that three-dimensional LFCs will have on device performance.

Various solidification structures were observed in the experimental results as a function of processing parameters. It is unclear how the morphology of these structures will affect recombination rates. Therefore, the morphologies of the solidification structures should be compared with the lifetime measurements to identify any correlations. In addition, the numerical heat transfer and fluid flow model should be utilized to predict the solidification morphologies by calculating the solidification rate and cooling rate. If solidification structure impacts device performance, the phenomenological model can be used to predict the solidification behavior as a means to optimize contact morphology and performance.

Fully-functioning solar devices should be fabricated to evaluate the effect of using three-dimensional LFCs produced with microsecond pulses. The analytical calculations performed in this thesis provide a framework for what LFC geometries should be employed. A baseline structure should be generated using traditional contacting methods (i.e., photolithography and Al deposition). Then, a device that employs the LFC technology using microsecond pulse durations should be fabricated. Energy conversion efficiencies should be determined to evaluate the device capabilities. Only by fabricating devices with this approach can a conclusive stand be made on the advantages of using LFCs produced with microsecond pulses.

LFCs should be fabricated on samples that possess different passivation stacks, such as SiN_x and Al_2O_3, to determine what influence passivation plays on contact formation with microsecond pulses. Numerical simulations using heat transfer and fluid flow modeling and advanced materials characterization can be further employed to study the influence of passivation on contact formation. Calculations of temperature fields will be important since these passivation layers have different melting temperatures and the degradation may be more severe for one versus another. Numerical simulations can help determine which passivation layers may be the best candidates for device fabrication.

The LFCs produced here exhibit characteristic surface features, such as a central peak and a raised lip, which result from changes in molten pool concentration and temperature. The mathematical models should be developed to predict the impact of laser processing parameters on these features. Predicting these features will allow for a better predictive capabilities of the overall contact formation process.

7.3 References

1. E. Schneiderlochner, R. Preu, R. Ludemann, S.W. Glunz, Laser-fired rear contacts for crystalline silicon solar cells, Prog. in Photovoltaics 10, 2002, pp 29-34.
2. I. Sanchez-Aniorte, R. Barrio, A. Casado, M. Morales, J. Carabe, J.J. Gandia, C. Molpeceres, Optimization of lase-rfiring processes for silicon-heterojunction solar-cell back contacts, Appl. Surf. Sci. 258, 2012, pp 9443-9446.
3. P. Ortega, A. Orphella, I. Martin, M. Colina, G. Lopez, C. Voz, M.I. Sanchez, C. Molpeceres, R. Alcubilla, Laser-fired contact optimization in c-Si solar cell, Prog. in Photo. 2012, 20 (2): pp 173-180.
4. D.W. Cunningham, BP Solar International, Reaching Grid Parity Using BP Solar Crystalline Silicon Technology A Systems Class Application, DOE Award Number: DE-FC36-07GO17049.006.
5. Z. Hua, E.W. Reutzel, L. Zou, Beam delivery techniques for laser fired contacts, ICALEO 2010, #M1101.
6. V. Schutz, A. Horn, U. Stute, High-throughput process parallelization for laser surface modification on Si-Solar cells: determination of the process window, Proceedings of SPIE Vol. 8244 (2013).
7. B. Fischer, Loss analysis of crystalline silicon solar cells using photoconductance and quantum efficiency measurements, PhD Thesis, University of Konstanz, 2003.
8. D. Kray, S. Glunz, Investigation of laser-fired rear-side recombination properties using an analytical model, Prog. In Photo. 14, pp. 195-201, 2006.
9. A. Wolf, D. Biro, J. Nekarda, S. Stumpp, A. Kimmerle, S. Mack. R. Preu, Comprehensive analytical model for locally contacted rear surface passivated solar cells, J. Appl. Phys. 108, 124510, 2010.
10. P. Ortega, A. Orphella, I. Martin, M. Colina, G. Lopez, C. Voz, M.I. Sanchez, C. Molpeceres, R. Alcubilla, Laser-fired contact optimization in c-Si solar cells, Prog. In Photo. 20, pp 173-180, 2012.
11. B. DeCesar, Investigation of process parameter optimization of laser-fired back contact silicon solar cells, MS Thesis Penn State University, 2010.

VITA

Ashwin S. Raghavan

Ashwin S. Raghavan completed his Bachelor of Science degree in Welding Engineering from the Ohio State University (OSU) in 2000, graduating Magna Cum Laude with Distinction. Upon graduation, he joined General Electric (GE) Aviation in 2004 as a manufacturing engineer, completing various rotational assignments focused on welding and joining, laser processing, and coatings development. While at GE, Ashwin completed his Master of Science degree in 2007 in Materials Science and Engineering (MSE) from the OSU. Upon graduation, he joined Ameron International as a Welding Engineer, leading welding development and the implementation of an ISO 9001:2008-based quality management system. Ashwin came to the Pennsylvania State University in 2010 to obtain a doctorate degree in MSE. A list of his publications and manuscripts submitted for publication is shown below:

1. A. Raghavan, T.A. Palmer, T. DebRoy, Heat and mass transfer during laser-fired contact formation in photovoltaic devices, *submitted for publication* in J. Appl. Phys., 2014.

2. A. Raghavan, T.A. Palmer, T. DebRoy, Passivation layer breakdown during laser-fired contact formation, *submitted for publication* in Appl. Phys. Letters, 2014.

3. A. Raghavan, B. Hedrick, B. DeCesar, B.P. Downey, J. Flemish, L. Zou, T.A. Palmer, T. DebRoy, S.E. Mohney, E.W. Reutzel, Impact of millisecond pulses on laser-fired contact geometry and photovoltaic device performance, *submitted for publication*, J. Elec. Mat. 2014.

4. A. Raghavan, T.A. Palmer, K.C. Kragh-Buetow, A. Domask, E.W. Reutzel, S.E. Mohney, T. DebRoy, Employing microsecond pulses to form laser-fired contacts in photovoltaic devices, Progress in Photovoltaics, *in press* 2014.

5. A. Raghavan, T. A. Palmer, A. Domask, S. Mohney, E. W. Reutzel, T. DebRoy, Role of processing parameters on morphology, resistance and composition of laser fired contacts, Proc. SPIE, Laser Material Processing for Solar Energy Devices II, 882606, 2013.

6. A. Raghavan, H.L. Wei, T.A. Palmer, T. DebRoy, Heat transfer and fluid flow in additive manufacturing, J. Laser Appl., 5(5), 2013.

7. A. Raghavan, J. J. Blecher, T. A. Palmer, E. W. Reutzel, T. DebRoy, Modeling of contact geometry and dopant profile during laser-silicon interaction, Proc. SPIE 8473, Laser Material Processing for Solar Energy, 847304, 2012.

8. A. Raghavan, T.A. Palmer, T. DebRoy, Mathematical Modeling of Laser Micro-Welding for Photovoltaic Devices, 9th International Conference on Trends in Welding Research, Chicago, IL, 2012, pp 635-640.

9. A. Raghavan T.A. Palmer, T. DebRoy, Evolution of laser-fired aluminum-silicon contact geometry in photovoltaic devices, J. Appl. Phys. 111, #024903, 2012.